MEASUREMENT OF THE PRODUCTION CROSS SECTION OF CHARM MESONS AT HIGH TRANSVERSE MOMENTUM IN 515 GeV/c π^--NUCLEON COLLISIONS

by

Steven R. Blusk
B.A., Potsdam College, 1988
M.S., University of Pittsburgh, 1989

Submitted to the Graduate Faculty of
Arts and Sciences in partial fulfillment
of the requirements for the degree of
DOCTOR OF PHILOSOPHY

Department of Physics and Astronomy
College of Arts and Sciences

University of Pittsburgh
Pittsburgh, Pennsylvania
1995

UNIVERSITY OF PITTSBURGH

FACULTY OF ARTS AND SCIENCES

This dissertation was presented

by

Steven R. Blusk

It was defended on

August 7, 1995

and approved by

Dr. Paul Shepard, Dept. of Physics & Astronomy

Dr. Eugene Engels, Dept. of Physics & Astronomy

Dr. Tony Duncan, Dept. of Physics & Astronomy

Dr. Regina Schulte-Ladbeck, Dept. of Physics & Astronomy

Dr. Joel Falk, Dept. of Electrical Engineering

Committee Chairperson

MEASUREMENT OF THE PRODUCTION CROSS SECTION OF CHARM MESONS AT HIGH TRANSVERSE MOMENTUM IN 515 GeV/c π^--NUCLEON COLLISIONS

Steven R. Blusk, Ph.D.

University of Pittsburgh, August 1995

This thesis presents the results from an investigation of the production of charmed mesons at high transverse momentum in collisions of 515 GeV/c negative pions with copper and beryllium targets. The data were taken during the 1990 fixed target run at Fermilab using the E706 spectrometer. The E706 detector consisted of a high precision charged tracking system and a finely segmented liquid argon calorimeter. The tracking system was used to reconstruct the charged particles in the event, as well as the associated vertices. The electromagnetic section of the calorimeter (EMLAC) provided precise measurements of the position and energy of the photons, as well as forming the basis for the high p_T trigger. Events which produced localized high p_T showers in the EMLAC were selected by the trigger and written to tape.

The events which were recorded are enriched with direct photons and high p_T jets. From the 1990 data, a sample of ~150 charmed hadrons have been fully reconstructed via their displaced vertices. Due to the high p_T trigger, these charm particles are also at high transverse momentum. The intent of this thesis is to present a measurement of the differential cross section of charmed particles in the p_T range from 1-8 GeV/c. By extrapolating below 1 GeV/c, we also present a measurement of the total inclusive $D^{\pm}$ production cross section. These results are compared with the NLO theoretical calculations, as well as with the predictions from the Pythia Monte Carlo.

ACKNOWLEDGEMENTS

First and foremost, I would like to thank my family for their encouragement and support throughout my *graduate career*. There were many times when the *going got tough*, and, in response, *the tough called home*. Well, what would you do? My family always opened their hearts and ears to listen to my problems, despite the fact that physics is nearly a foreign language to them. A difficult transition to graduate school was cushioned by my parents, Samuel and Gloria, and my brother Eric and sister Debra. With the passing of my father in the middle of my MWEST tenureship, I was turned inside out. It was a few weeks later that I could hear his voice in my dreams, encouraging me to continue on with what I had begun. Although I never told anyone, it was often these dreams which gave me the determination and motivation that I couldn't muster up myself. For all his encouragement and support, I dedicate this thesis to my late father, Samuel Blusk, whom without, I would not be where I am today.

I also owe a great deal of thanks to my extended family, who have also supported me throughout. Topping the list is a special thanks to my grandparents, Max and Claire, who, have always maintained their confidence in my decisions, as if I really knew what I was doing ! I also wish to express my deepest thanks to my Aunt Joan, Marty, my cousins Lisa, Randi, and Todd; my Uncle Al (the paddleball guru), Aunt Saundy, Marcy and Amy. Although I have not been able to see you all too often, you're always in my heart.

My interest in physics was sparked by my high school physics teacher, who oddly enough, was a bartender on the weekend. I thought "Wow, so this is the life of a physicist; what a great job" ! It wasn't until after wasting a year in college

that I realized two things. First, most physicists are not also bartenders. Second, physics was intellectually stimulating, even without any alcohol. I owe much thanks to a fantastic group of teachers at Potsdam College who conveyed their enthusiasm for the subject in their lectures. Among those professors were, Professors Jekeli, McRobbie, Kruezer, and Islam. I'd especially like to thank Prof. Azad Islam for his guidance throughout my college years. During my final year at Potsdam, he escorted me to two undergraduate symposiums, where I had the opportunity to present our studies of the Faraday Effect. He also helped direct me toward graduate school, which I believe was the right choice. I was delighted to recently hear from him, and look forward to keeping in touch with him in the future. I'd also like to thank my Mathematics advisor, Prof. Irene Schensted, who had a special flair for teaching. There are few professers which have the ability to pass on their enthusiasm for a subject; I was fortunate enough to have been exposed to a few of them at Potsdam College, and for that I am grateful.

Almost exactly seven years ago, as chairman of the Department of Physics and Astronomy, Gene Engels welcomed a new class of graduate students aboard. It was my good fortune to be one of the graduate students in that bunch, since it was that same day which Gene announced that there were two openings for GSR's in his group. Acting on advice given to me by my undergraduate advisor, Dr. Azad Islam (Potsdam College), I siezed the opportunity to begin doing research. Over the past 7 years, I've enjoyed working with Paul and Gene not only as a student, but as a pier. They promote an environment of mutual respect, giving their students the room to learn on their own, while also staying actively involved. It seems just like yestarday that I was making wire bonds from the silicon wafers to the fine line PC boards (with Luke). Seven years later, the fruits of our labor have payed off, achieving what some thought could not be done. To both Gene and Paul, I thank you for your encouragement and vote of confidence along the way. It has been my pleasure to work with both of you, and I look forward to continuing to do so in the future.

Soonafter arriving at MWEST, I met up with the other people from Pittsburgh, including Dhammika, Mani, and Woohyun. During my first 6 months at MWEST, we worked nearly around the clock in order to have the SSDs ready for the beam which was, by definition, due at any minute. During that time, there were many late nights and early mornings where I got to know the three of them fairly well. Sometimes those late nights ended at the Users Center where we would kick back for a few cold ones. Soonafter, I got to know Rob Roser and Brajesh Choudhary (the odd couple). I want to thank you two for many memorable experiences (JD) along this long and bumpy road. Especially memorable, were the infamous games of *Liar's poker*, where only the *Hindu truth* was spoken. Brij, you're the ping pong champ, even though I let you win (only joking, pal) ! A year or so after, we all met up with Len Apanasevich (Mr. Saturday morning), whom was usually ready, willing, and able, to take a break to indulge in some beverages (thanks, pal). I also want to thank my good friend, Vijay Kapoor for many fun times over the last few years. I'd also like to thank a dedicated crew of people have been convening once a week to play hoops; they include Len (Patrick Ewing) Apana, Rob (Spudd) Roser, Mark (Mugsy) Shaw, Carlos Yosef, Paoti ("his air-ness") Chang, John Bacigalupi, and Rick (Charles Barkley) Jesik and Tony Frelo, and others. I'd like to thank you guys for some intense, but yet always friendly games of hoops. Other people who deserve special mention are Judy, Doug, Rich, Sue Winchester, Jean Guyer, and Michele, who always made the Users Center a relaxing and enjoyable atmosphere for retreat from the daily routine.

Early on, it was Mani who stimulated my interest in the subject of charm physics. Much of the credit belongs to him, for he provided invaluable insights into the procedures of secondary vertex finding. As I became more involved with charm, Carl Bromberg also provided valuable suggestions (in his own special way) which usually proved to be fruitful. I would also like to give a special thanks to all the members of the tracking group, who spent countless hours on Thurdsay mornings, hashing out details which few had patience for. These people include Sudindra

Mani, George Ginther, Jim Dunlea, Casey Hartman, Phil Gutierrez, Carl Bromberg, Dhammika Weerasundara, WooHyun Chung, Andre Maul, Paoti Chang, Lenny Apanasevich, and John Bacigalupi. I'd like to also thank Rob Roser, Nikos Varelas, Wiesek Dlugosz, George Ginther, and Lee Sorrell for their valuable discussions regarding the operation of the EMLAC and the trigger. I am grateful to George Ginther, Sudindra Mani and Marek Zielinski, for many enlightening conversations on a variety of physics issues. In addition, I'd like to thank Gene Engels and Paul Shepard for their guidance throughout. I'd also like to thank Paul Slattery and Tom Ferbel for their advice over the last 5 years. There were a number of other people who contributed indirectly to this thesis, and I'd like to thank them as well. Special mention goes to Dan (give me more chile peppers) Ruggiero, who was an unsung hero over the last few years. Finally, I'd like to thank Michael Begel for his help in formatting with TEX.

I though that George Ginther deseved his own paragraph, since he has been integral not only to this analysis, but essentially every analysis project which is being done at E706. He has helped guide all of the graduate students through a learning process which we are all indebted to him for. When people asked whether or not I was worried about my defense, I replied, "No, not really, I've already gone through one of the toughest critics of all!" Consequently, I felt prepared for what was to come. George was also instrumental in helping clarify a number of issues regarding this analysis. For all his dedicated efforts, I'd like to give him my sincerest thanks.

While being a graduate student, I was able to maintain my friendship with some great friends. From my undergraduate years, my frateral brothers Anthony Gasteiger and Martin Coppola have been true friends in every sense of the word. In addition, my roommate and great friend from college, Shawn Skafelstad has always been there for me and my family, and for that I am eternally grateful. I have been fortunate enough to keep in touch with some quality friends back at Pitt, including Mike MacMillan, Chris Sirola, Ertu (where are you) Sorar and Paula Pomianowski.

Thanks to you all for making graduate school alot more fun. I'd also like to thank my housemate, Stefan Vandenbrink who has been a good friend over the last year. I'm looking forward to working with hime in the near future.

During the preparation of this thesis, communications with Torbjörn Sjöstrand (author of Pythia) and Brain Webber and Mike Seymour (authors of Herwig) were beneficial to my understanding this subject. I'd also like to thank Michelangelo Mangano for making the NLO QCD program available to me, and to Rick Jesik for helping me to get started with them. I'd also like to thank Simon Kwan (Fermilab) for several enlightening discussions on charm physics.

Finally, I'd like to thank the staff at the Physics Department Office, who were more helpful than they can imagine. I'd like to give a special thanks to Meriam Green who recently retired. The students and staff were to lucky to have worked and been around such a fine person. In the last few years while at Fermilab, Duane Hovanec and Kate Connoly have made my dealings with the University simpler, and for that, I thank them both.

TABLE OF CONTENTS

LIST OF TABLES

LIST OF FIGURES

Chapter 1 Introduction

1.1 A historical introduction to particle physics

For hundred's of years, man has been trying to understand the world we live in. One of the main efforts of scientists during the last century or so has been to understand the fundamental structure of matter. In this section, I wish to give the reader a brief perspective of how the field of high energy physics evolved in a fairly natural way.

It was around 1909-1911 when Rutherford, along with Geiger and Marsden, were performing scattering experiments of $\sim$ 5 MeV α-particles off thin metal foils. In order to explain the amount of large angle scatters (greater than 90 degrees), Rutherford put forth his model of the atom as a small center of positive charge surrounded by an orbiting (cloud of) electrons. Since the atomic mass was about twice as large as the number of units of positive charge, it was believed that the extra mass was supplied by neutral particles, which were formed from a proton-electron bound state. For example, an oxygen atom was thought to have 16 protons + 8 electrons in the nucleus, with 8 additional atomic electrons. In 1932, Heisenberg argued that the protons and neutrons could be held together by the exchange of these "nuclear electrons".

It was during the 1930's that Chadwick and others began to understand that the neutron was fundamental in itself. If Heisenberg's model of electron exchange was correct, then one would not expect to see the strong forces between 2 protons, but only the weaker Coulomb force, since the proton did not contain any electrons. In 1936, Tuve, Heydenberg, and Hafsted performed a proton-proton scattering experiment[1] and found large deviations from the Mott formula, which indicated

that the force between 2 protons was not simply electromagnetic, but in fact similar to that between a neutron and a proton[1]. From this point onward, it was accepted by most that the neutron was elementary, just as was the proton and electron.

In the 1930-1940's, several new particles had been discovered in cosmic rays, including pions, kaons, positrons, and muons. The former two were observed to interact strongly with protons and neutrons, whereas the latter two interacted much more weakly. The kaons seemed to act differently than pions in that they always seemed to be produced in pairs, either with another kaon, or another strange particle. For this reason, they were coined as "strange", a name which would eventually become the name of the quark which gave the kaon this property.

Beginning in the 1950's, accelerators began to make a major impact on the ability to produce well defined beams of particles in order to investigate nuclear scattering in the 30-700 MeV range. In the next 10-15 years, many new baryon and meson resonances were identified via scattering experiments. Each particle had its own "good" quantum numbers such as spin, parity, isospin, strangeness, etc. All of these new particles decayed with short lifetimes, and hence were not observed until they were produced artificially in high energy collisions. As far as physicists could tell, these new particles seemed elementary, just as the proton, neutron, electron, or pion.

It was in 1964 that Gell-Mann[2] and Zweig[3] suggested that the observed particle spectrum could be accounted for by constructing composites of SU(3) triplets(3) and anti-triplets($\overline{3}$), provided that the so called "quarks" had non-integral charges. Fractionally charged objects were not widely accepted as being physical entities, but rather they were viewed as mathematical constructs. This quark "formalism" restored the *economy of particles* to but a few basic units, as was

[1] The incident proton energy was $\sim$ 600-900 keV as obtained by a van de Graaf accelerator.

the case before the plethora of particles arrived on the scene in the previous two decades. These 3 quarks were referred to as the *up(u), down(d)* and *strange(s)* quarks. With these quarks assignments, one could build the observed baryons as bound states of 3 quarks. Similarly, the observed mesons could be accounted for by constructing quark anti-quark states. .

In 1969, using the quark model current algebra, Bjorken[4] showed that if the proton was composed of structureless point-like constituents, then the following scaling relations should hold for deep inelastic lepton-quark scattering. For,

$$Q^2 \to \infty$$

and,

$$\nu \to \infty$$

with $x = Q^2/2M\nu$ fixed, the nucleon structure functions scale as,

$$MW_1(Q^2,\nu) \to F_1(x)$$

$$\nu W_2(Q^2,\nu) \to F_2(x).$$

Here, Q^2 is the square of the four momentum transfer, and ν is the energy exchanged.

Bjorken showed that if lepton-quark scattering was pointlike, then F_1 and F_2 should not depend on Q^2, and are only functions of x^2. Consequently, F_1 and F_2 remained finite even as Q^2 and ν tended toward infinity. This feature of the theory is known as ***Bjorken scaling***[4].

Around 1967, a SLAC-MIT collaboration began performing experiments involving scattering of $\sim$ 20 GeV electrons off nucleons. The group showed that

---

[2] This x is commonly referred to as Bjorken x, or x_{BJ}.

the nucleon structure function νW_2 was essentially independent of ν and Q^2, and only a function of $x = x_{BJ}$[5, 6]. This result was remarkable, since the experiment supported the conjecture that the electrons appeared to be scattering off spin 1/2 pointlike quarks inside the nucleon. The interpretation that quarks were not only mathematical objects, but physical constituents, began to prevail. Later, it was found that exact scaling is violated, where terms such as $\ln(Q^2/\mu^2)$ (μ^2 is the quark mass) enter as radiative corrections to the distribution functions. Such logarithmic violations to scaling are a characteristic feature of corrections to the free (scaling) parton model[7].

It was later that year that Feynman gave his interpretation of scaling as the scattering of the leptons off pointlike constituents called *partons*[8]. Feynman showed that the x_{BJ} was in fact the fraction of the hadrons momentum which the partons carried. Therefore, the measurement of the cross section, or similarly $F_2(x)$, is a measure of the momentum distribution of the partons inside the nucleon. In simple scattering theory, $F_2(x)$ is simply the fourier transform of the spacial distribution of the scattering center(s).

Further experimental results supported the parton model of Feynman, that hadrons were composed of pointlike constituents of spin 1/2, and normal Dirac magnetic moments. The results include, verifying the Callan-Gross relation[9], the linear rise of neutrino-nucleon cross sections with energy, the famous ratio $R = \sigma(e^+e^- \rightarrow \text{hadrons})/\sigma(e^+e^- \rightarrow \mu^+\mu^-)$, Drell-Yan production of lepton pairs, and many other results. The outcome of numerous experimental tests over the past 2 decades have lent strong support for the parton model. The experiments support the conjecture that hadrons appear to be composed of spin 1/2 quarks and anti-quarks, bound together by the strong force.

Our current understanding of the fundamental constituents of matter has obviously grown dramatically over the past century. By increasing the energy of the collisions between particles, experimentalists have been able to probe physics

at the scales of $\sim 10^{-14} - 10^{-15}$ cm. Furthermore, the large center of mass energies produced have allowed for the production of massive particles (such as W and Z) which cannot otherwise be created. The discovery of the sixth and heaviest quark ("top"), having an equivalent mass of ~180 protons, was just recently reported in $p\bar{p}$ collisions at a center of mass energy of 1.8 TeV[10, 11][3]. We have learned that with each new generation of increased energy, a new frontier of physics has opened. In the current energy regime, experiments are performing rigorous tests of the predictions of the Standard model, in both QCD and the Electroweak sectors. In addition, many scientists are looking beyond the Standard model in order to address questions which need to be answered. For example, many physicists find it unsatisfactory that the Standard Model does not predict some of the theory's most fundamental parameters, such as the quark masses, coupling constants, mixing angles, the CKM CP violation phase, the "Higgs potential" parameters, and the θ parameter for invoking *strong* CP violation. It would be more aesthetic to uncover a picture where all the forces (see Table 1.3) were in fact low energy residuals of a single force[4], and that the underlying theory could predict the (fewer) fundamental constants. Ambitiously, scientists are working hard to uncover any hints of supersymmetric (SUSY) particles, which would uncover yet an even more fundamental substructure of matter.

1.2 The Standard Model

It is the current understanding that all matter is composed of two classes of particles, *quarks* and *leptons*. Table 1.1 and Table 1.2 summarize the basic properties of the quarks and leptons respectively. The theory which describes the interactions among the quarks and leptons is known as *The Standard Model*. The interactions are believed to take place via exchange of mediating bosons, which

---

[3] 1 TeV = 10^{12} eV.

[4] The energy scale at which this might occur would be of order $\sim 10^{15}$ GeV.

are the carriers of their respective forces. According to Yukawa theory[12], the range of a force is inversely related to the mass of its mediating particle. The electromagnetic quantum, which is the massless photon, has infinite range, whereas the weak quantum, having masses $\sim 80 - 90$ GeV/c^2, are confined to within about 10^{-15} meters. The gluons which mediate the strong force are also massless vector bosons, but unlike the photon, they also are confined to very short ranges. The reasoning for this will be made more clear in a later section. Table 1.3 summarizes the properties of the strong, weak and electromagnetic (EM) forces. Gravity has been intentionally ignored in this discussion.

Table 1.1 Properties of the Quarks

Generation	1		2		3	
Quark	u(up)	d(down)	s(strange)	c(charm)	b(bottom)	t(top)
Charge	+2/3	-1/3	-1/3	+2/3	-1/3	+2/3
Mass(MeV/c^2)	~300	~300	~500	~1500	~5000	~170000

Table 1.2 Properties of the Leptons

Generation	1		2		3	
Lepton	e^-	ν_e	μ^-	ν_μ	τ	ν_τ
Charge	-1	0	-1	0	-1	0
Mass(MeV/c^2)	0.511	0	106	0	1870	0

Table 1.3 Properties of the Forces

Force	Electromagnetic	Weak	Strong
Field Quantum	Photon	$W^{\pm}, Z^0$	Gluon
Spin-Parity(J^P)	1^-	1^-,1^+	1^-
Mass(GeV/c^2)	0	80-90	0
Range of Force(m)	∞	10^{-18}	$\leq 10^{-15}$
Source	Electric Charge	Weak charge	Color Charge
Coupling Const.	$\alpha \sim 1/137$	$G \sim 10^{-5}$	$\alpha_s \leq 1$ (high q^2)
Typical lifetimes for decays (s)	10^{-20}	$10^{-8} - 10^{-13}$	10^{-23}
Particles to which it couples to	charged quarks & leptons	quarks & leptons	quarks and gluons

In the standard model, the quarks and leptons are grouped into 3 *generations*, such that the first generation contains the lightest quarks (leptons), and the third contains the heaviest. The interactions between the members of a doublet are generally more dominant than between doublets. In the interaction lagrangian, the CKM matrix gives the relative amplitudes for such transitions[5]. In the case of the leptons, there is no mixing between the doublets. This means that the weak currents cannot transform a lepton from one generation into a lepton of a different generation. For example, the process of muon decay, $\mu^- \rightarrow e^- + \nu_\mu + \nu_e$, can be realized as the product of two charge changing weak currents along with the usual propagator for a massive vector boson.

---

[5] The elements of the CKM matrix are the measured mixing angles which give the relationship between the weak eigenstates and the mass eigenstates, i.e. eigenstates of the Hamiltonian.

1.3 Quantum Chromodynamics (QCD)

The theory which describes the interactions between quarks is called *quantum chromodynamics*. QCD is similar to quantum electrodynamics (QED), in that both are based on being renormalizable gauge theories. By a gauge theory, we mean a theory which exhibits a gauge invariance, and in particular, a *local* gauge invariance with respect to rotations of the fields. Electromagnetism is known as an *Abelian* theory, since the product of any two gauge transformations is independent of which order they are applied[6]. Gauge invariance is a symmetry, and symmetries of the lagrangian lead to conservation laws. The gauge invariance of electromagnetism leads directly to charge conservation.

In the formalism of making a gauge invariant theory, it becomes necessary to introduce *compensating fields*, which transform in a particular way under local gauge transformations. In the case of electromagnetism, these fields can be shown to be simply the familiar vector potential A^{μ}. In quantum theory, these fields become quantized into photons, and are identified as the carriers (quantum) of the electromagnetic force. Electromagnetic interactions are believed to proceed via exchange of these J=1 massless photons[7].

QCD, much like QED, also has spin 1 massless vector bosons which mediate the interactions. However, the symmetry group of QCD is that of SU(3) color. At first, the property of color was introduced in order to antisymmetrize the total wavefunction of the Δ^{++} (In the absence of a color component, the Δ^{++} had a symmetric total wavefunction, which violated the Pauli Exclusion Principle). The quarks were allowed to come in three colors, red (R), green (G), and blue (B), each forming a triplet under SU(3)[8]. In order to account for the observed

---

[6] The phase rotations of electromagnetism belong to the group U(1).

[7] The local gauge invariance requires massless photons.

[8] Antiquarks carry anticolor, i.e. $\overline{\mathrm{R}}, \overline{\mathrm{G}}$, and $\overline{\mathrm{B}}$.

spectrum of quark combinations i.e. qqq or $q\bar{q}$ only, it was asserted that only *colorless* states may be observed in nature[13]. In this case, mesons would be formed from color-anticolor combinations, and baryons (antibaryons) from RGB ($\overline{RGB}$) pairings. In order to have quarks interact with one another i.e. via the strong force, it was proposed that the property which was responsible for these interactions was their *color charge*. In analogy with QED where the photon couples to electromagnetically charged objects, the quarks possess color charge, to which its gauge bosons can couple. These mediators of the strong force are known as the *gluons*. In constructing the lagrangian for the strong interactions, the requirement of local gauge invariance under the color phase transformations of 3 quark color fields necessitates the introduction of 8 independent massless vector fields. These vector fields are precisely the aforementioned gluons. Furthermore, since QCD is *non-abelian*, gauge invariance implies that these gluon fields can interact with one another i.e. gluon-gluon interactions. Consequently, the gluons themselves carry net color charge. This is significantly different from QED where the photons cannot interact directly with one another, since the photons do not carry EM charge. Finally, the color force of QCD needs to have a mechanism by which quarks and gluons are confined within hadrons, since we do not observe them as free particles. In high energy collisions, we only observe color singlets, so there must be a mechanism by which the quarks are confined inside hadrons. This differs from QED in that photons and charged objects are obviously not confined. The issue of *color confinement* is addressed in the next section.

1.3.1 Asymptotic Freedom

As discussed in the previous section, quarks and gluons, or simply *partons*, are confined within hadrons. The confinement mechanism which occurs in QCD, and not in QED, becomes more transparent after looking more closely at the coupling constants of each. In QED, the EM coupling constant may be expressed to leading log as,

$$\alpha(Q^2) = \frac{\alpha(Q^2 = 0)}{[1 - (\alpha/3\pi)\ln(Q^2/m^2)]} \qquad 1.1$$

for $Q^2 >> m^2$. This form comes about as a result of the vacuum polarizations which occur in the vicinity of a charge i.e. electron. In QED, this electron can emit photons which subsequently form e^+e^- pairs. This cloud of e^+e^- pairs will configure themselves so to screen the *bare* charge on the electron, i.e. the virtual electron pairs become polarized. The result is that the *measured charge* will depend on the distance, or more appropriately, the Q^2 of the probe. For large distances, or equivalently, low Q^2, one observes $\alpha \simeq 1/137$. At high Q^2, the probe "sees" more of the bare charge, and the measured charge, or equivalently, the coupling constant, increases.

In much a similar way, the color charge of quarks can be screened by vacuum polarization. However, a very crucial difference occurs as a result of the additional $g \rightarrow gg$ coupling. It turns out that when calculating these vacuum polarization effects to screening the color charge, the $g \rightarrow q\bar{q}$ and $g \rightarrow gg$ contributions enter with opposite signs. Upon summing all the appropriate terms, one can express the *strong coupling constants*[9] as,

$$\alpha_s(Q^2) = \alpha_s(\mu^2)[1 + (\frac{\alpha_s(\mu^2)}{12\pi})(33 - 2n_f)\ln(Q^2/\mu^2] \qquad 1.2$$

This may be expressed more conveniently as,

$$\alpha_s(Q^2) = \frac{12\pi}{(33 - 2n_f)\ln(Q^2/\Lambda^2)} \qquad 1.3$$

where n_f is the number of quark flavors, μ is an arbitrary scale, and Λ is defined by,

$$\ln \Lambda^2 = \ln \mu^2 - \frac{12\pi}{[(33 - 2n_f)\alpha_s(\mu^2)]} \qquad 1.4.9$$

One observes that, $\alpha_s(Q^2) \rightarrow 0$ as $Q^2 \rightarrow \infty$ i.e. when probing short distances. This property is commonly known as *asymptotic freedom*. This feature of the theory

[9] Politzer 1973, Gross and Wilczek 1973

behaves oppositely to its QED analog, where the coupling constant increases with Q^2. It is precisely this feature that allows one to make predictions using perturbative QCD (PQCD), provided $Q^2 >> \Lambda^2$. On the other hand, for $Q^2 \simeq \Lambda^2$, α_s becomes large, and PQCD can no longer make reliable predictions. One may regard Λ as the scale at which the "strong interactions become strong". If one considers that the partons are confined within a region of $\sim$ 1 fm, this suggests a value of Λ of about 200 MeV[7]. One may interpret this increase in the strong coupling constant as $Q^2 \rightarrow \Lambda^2$, as the mechanism for confinement. As two partons separate, one can imagine that the *color field lines* are squeezed into a tube-like region as a result of the strong interactions between the gluons. If the energy density per unit length is constant across the tube, then the potential energy between the $q - \bar{q}$ pair will increase proportionally to their separation, much like a stretched spring[13]. Consequently, as partons separate, one can imagine that the increase in the potential between the two partons provides the mechanism for confinement. If the partons are energetic enough, the *spring* between the partons may break, with the stored energy being converted into a $q\bar{q}$ pair. Experimental results showing the linear dependence of the total spin J, of the Δ and Λ resonances versus the square of the resonance's mass (J vs M^2), lends support for such a linear potential[14]. Hence in this model, it is essentially the gg interactions which provide the mechanism for confinement.

1.4 Phenomenology of High p_T Interactions

As mentioned in the previous section, the applicability of PQCD becomes realized only for large momentum transfers, $Q^2 >> \Lambda^2$. In such cases, the partons inside the hadrons can be considered to be quasi-free, and the hard scattering subprocess can be described in terms of the pointlike scattering of the partons inside the hadrons. Figure 1.1 depicts such a hard scatter. In this diagram, parton *a* inside hadron *A* collides with parton *b* residing inside hadron *B*. The parton distribution functions $G_{a/A}(x_a)$ ($G_{b/B}(x_b)$) give the probabilities of finding partons *a(b)* with

the fraction $x_a(x_b)$ of hadron *A(B)*'s momentum i.e. the momentum distribution of the partons inside the hadrons. Partons *a* and *b* undergo a hard scatter, described by the pointlike cross section $d\sigma/d\hat{t}$, yielding partons *c* and *d*, which emerge at high transverse momentum with respect to the direction of the incoming partons. This pointlike cross section $d\sigma/d\hat{t}$, is in principle calculable from PQCD. In the final stage of the interaction, the colored partons hadronize into color singlet hadrons. The fragmentation functions $D_{C/c}(z_C)(D_{D/d}(z_D))$ give the probability of finding hadron *C(D)* with a fraction $z_C(z_D)$ of the outgoing partons' momentum. Both the parton distribution functions and the fragmentation functions need to be determined experimentally at some value of Q^2, and then evolved to the scale of interest.

One can express the lowest order $(2 \rightarrow 2)$ invariant cross section for observing particle C at high p_T as[10],

$$E_C \frac{d\sigma}{d^3p_C}(A + B \rightarrow C + X) = \sum_{abcd} \int dx_a dx_b dz_c G_{a/A}(x_a, Q^2) G_{b/B}(x_b, Q^2) \times D_{C/c}(z_c, Q^2) \frac{\hat{s}}{z_c^2 \pi} \frac{d\sigma}{d\hat{t}}(ab \rightarrow cd) \delta(\hat{s} + \hat{t} + \hat{u}) \quad 1.5$$

The Mandelstam variables $\hat{s}$, $\hat{t}$, and $\hat{u}$ define the kinematics of the interacting partons, and are given by

$$\hat{s} = (p_a + p_b)^2 \quad 1.6$$

$$\hat{t} = (p_a - p_c)^2 \quad 1.7$$

$$\hat{u} = (p_a - p_d)^2 \quad 1.8.$$

In these equations, p_i refers to the momentum of parton i.

---

[10] This equation assumes that the partons are collinear with their corresponding hadrons.

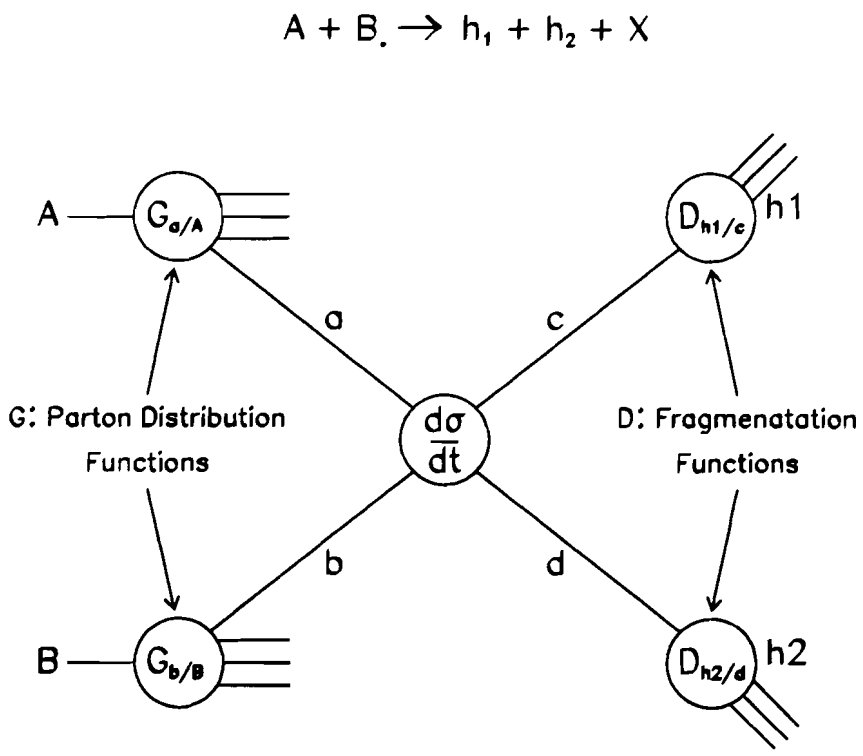

Figure 1.1 Schematic representation of a high p_T hadronic interaction.

One immediately observes in 1.5 the explicit dependence of the distribution and fragmentation functions on Q^2, the momentum transfer of the process. These scaling violations enter logarithmically when including the effects of $q \rightarrow qg$ and $g \rightarrow q\bar{q}$ splittings in the structure functions. The origin of the Q^2 dependence becomes apparent upon increasing the momentum transfer as in the case of deep inelastic (electron) scattering (DIS). As the wavelength of the virtual photon decreases (Q^2 increases), the photon penetrates deeper into the partonic structure, and begins to resolve a cloud of low x partons, which surround a given (valence) quark. Hence, DIS experiments show that as one increases the Q^2 of the virtual photon probe, one begins to resolves more low x partons, and fewer high x partons[15]. Although PQCD does not predict the parton distribution functions, it does describe their evolution with Q^2. The well-known *Altarelli-Parisi equations* describe mathematically how a quark with some observed value of x, could have "evolved" from a parton with momentum fraction y, where $y > x$. As mentioned previously, the distribution functions cannot be calculated via PQCD, and one must resort to fitting the experimental data at some value of Q^2 i.e. $Q^2 = M_W^2$. One can then use the Altarelli-Parisi equations to evolve the distribution functions to the scale of interest.

The last stage of the hard scatter, whereby the colored partons hadronize into color singlets is not described by PQCD. The fragmentation of a parton is inherently a low Q^2 process (as evidenced by the color confinement which occurs during the hadronization), and one must resort to models of how this process occurs. In the String Fragmentation Model[16], the color lines between partons form color strings of uniform energy density as a result of the self-interactions of the gluons. As the partons separate, the energy stored in the string increases, and eventually it becomes energetically favorable for the color string to break, with subsequent formation of $q - \bar{q}$ pairs. This is believed to proceed until one reaches a minimal "mass", at which point the partons are combined to form hadrons. There are several free parameters which are tuned based on experimental data. Another widely used

model of fragmentation is the *cluster fragmentation* as used in the Herwig monte carlo program[17]. Regardless of the fragmentation scheme, one must try to tune the various parameters of the model to match experimental results.

1.5 Direct Photon Production

Direct photons are those photons which couple directly to the constituent quarks of the hard subprocess and emerge as final state particles. At leading order, they carry off the full Q^2 of the hard scatter, and hence probe the short range dynamics. Since photons only couple to electrically charged objects, only two subprocesses enter into the leading order calculation for direct photon production. These subprocesses are the familiar Compton and Annihilation diagrams, which are shown in Figure 1.3. In contrast, since quarks (colour triplet) and gluons (colour octet) are both colour charged, there are a large number of diagrams which enter into QCD jet production. In particular, for 3 quark flavours, there are 127 diagrams for inclusive single particle hadroproduction, whereas there are 18 such diagrams for direct photon production. Theoretical and experimental overviews of direct photon production can be found in the references [18, 19, 20].

There are several factors which make the study of direct photons rather aesthetic to experimentalists. Here we mention a few of those reasons.

- Unlike quarks and gluons, the momentum components of a photon can be measured in a fairly straightforward way. Since quarks and gluons fragment into jets, one must employ an algorithm in which to experimentally define *a jet*. Therefore, it is not only more difficult to measure a jet, but the kinematics will in general depend on the jet algorithm employed.
- Since production of direct photons involves gluons in the initial state for the Compton graph, and in the final state for the Annihilation graph, one has a well-defined environment in which to study gluons.

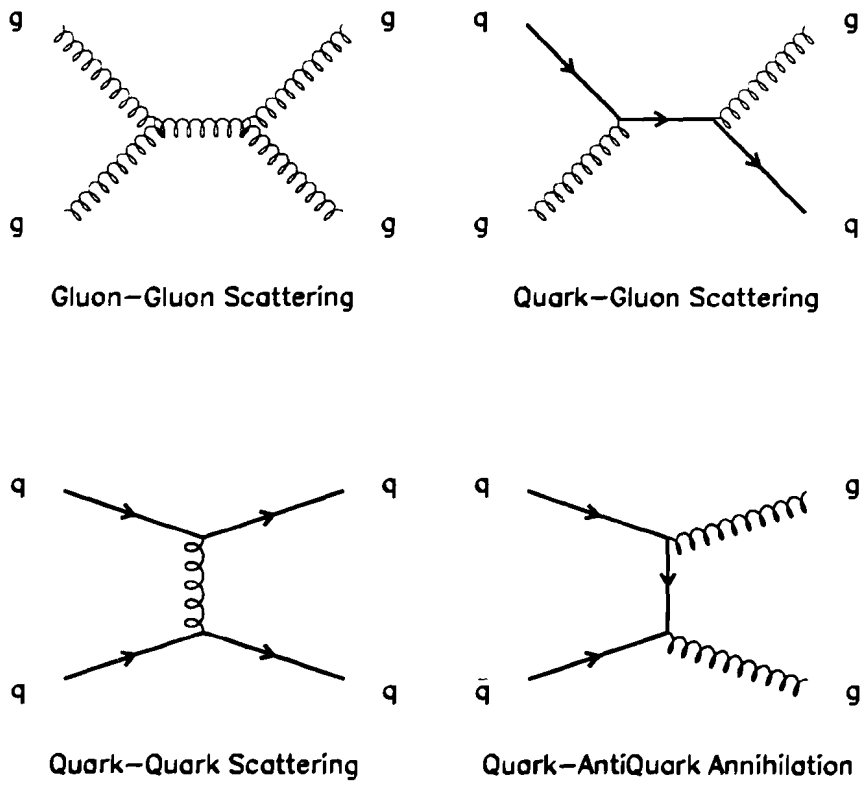

Figure 1.2 Examples of order α_s^2 parton-parton interactions.

By isolating the contribution from the Compton graph, one has the opportunity to measure the gluon structure function of the colliding hadrons[11]. Analogously, if one can isolate the Annihilation graph, one can study gluon fragmentation.

- NLL calculations for direct photon production are available for comparisons with experimental data[21].

To leading order, one can express the inclusive direct photon cross section for the hadronic interaction $A + B \rightarrow \gamma + X$ as,

$$E_\gamma \frac{d\sigma}{d^3p_\gamma}(A + B \rightarrow \gamma X) = \sum_{ab} \int dx_a dx_b dz_c G_{a/A}(x_a, Q^2) G_{b/B}(x_b, Q^2) \frac{\hat{s}}{\pi} \frac{d\sigma}{d\hat{t}}(ab \rightarrow \gamma d)\delta(\hat{s} + \hat{t} + \hat{u}) \quad 1.9$$

At leading order, the partonic cross sections for the production of direct photons via the Compton and Annihilation graphs are given by[22],

$$\frac{d\sigma}{d\hat{t}}(qg \rightarrow q\gamma) = -\frac{\pi\alpha\alpha_s}{3\hat{s}^2} e_q^2 \frac{\hat{u}^2 + \hat{s}^2}{\hat{u}\hat{s}} \quad 1.10$$

$$\frac{d\sigma}{d\hat{t}}(q\bar{q} \rightarrow g\gamma) = \frac{8\pi\alpha\alpha_s}{9\hat{s}^2} e_q^2 \frac{\hat{u}^2 + \hat{t}^2}{\hat{u}\hat{t}} \quad 1.11$$

The next to leading order calculations have been performed[21] and are discussed in the references[23, 24]. The main features of the higher order corrections are diagrams involving gluon emissions off of the quark lines, perturbative gluon splitting, one loop graphs (a gluon is emitted and reabsorbed internally), and photons arising from quark bremstrahhlung. Upon performing the calculations, one encounters various divergences which must be handled within the framework of

---

[11] This statement assumes one has a measurement of the quark structure functions, as from deep inelastic scattering (DIS).

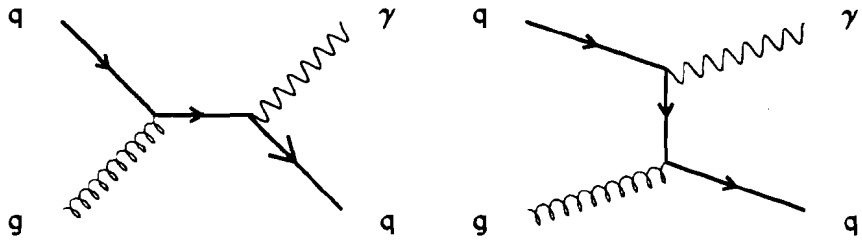

Compton Diagrams

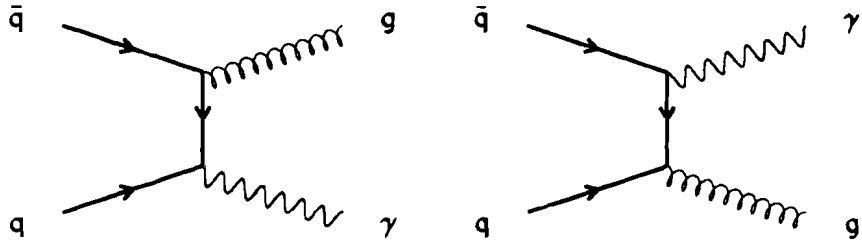

Annihilation Diagrams

Figure 1.3 Leading order diagrams contributing to direct photon production.

PQCD in order to yield a finite result for the physical process. These divergences are:

- Collinear Divergences and Soft Divergences - Collinear or Mass divergences occur in the tree diagrams where a gluon is emitted collinear to the parent quark's direction. This feature is a result of terms such as $(p_1 \cdot p_2)^{-1}$ appearing in the NLO calculations of tree diagrams. In the case of massless quarks and gluons, this term diverges as the two partons become collinear. One can also see that this term will diverge as $p_1 \rightarrow 0$ or $p_2 \rightarrow 0$ (soft divergences).
- Ultraviolet Divergences - These divergences are connected with gluon loops in the feynman diagrams. Since the gluon is emitted and reabsorbed, the gluon momentum can range from 0 to ∞. As a result of integrals over these (unbound) momenta, the integrals are divergent.
- Infrared Divergences - These divergences are also associated with the gluon loops in the NLO diagrams. However, in this case, divergences occur as the gluon momenta approach zero, in much the same manner as the soft divergences mentioned above. Also, one can have gluon loops which exhibit collinearity, as in the case of *real* gluon emission.

These divergences can be handled within the framework of PQCD. Remarkably, it turns out that the soft divergences mentioned above cancel with the infrared divergences due to the loop diagrams. The divergences associated with collinear gluon emission can be summed, and absorbed into the uncalculated portions of the distribution and fragmentation functions (factorization theorem)[25, 26, 27]. Finally, the ultraviolet contributions are regulated by some renormalization scheme, and then subtracted off. The result of all the higher order contributions is to yield a finite theoretical prediction for physical processes within the framework of PQCD.

E706 was specifically designed to study the production of direct photons and their associated jets. A high precision measurement of the direct photon cross section allows one to constrain the gluon structure function over the kinematical range accessible to E706. The primary background to measuring the direct photon signal is the large cross section for jet production. Consequently, E706 doesn't specifically trigger on direct photons, but rather it triggers on all high p_T phenomenon yielding high transverse momentum photons. A more detailed discussion of the direct photon backgrounds are discussed in the next section.

1.5.1 Backgrounds to Direct Photon Detection

The difficulties involved in studying direct photons are primarily associated with separating the direct photon signal from the prompt decays of neutral mesons. Due to the larger number of diagrams in jet production, as well as the fact that direct photons only enter at order $\alpha\alpha_s$ (as opposed to α_s^2 for jets), direct photons are only produced at about $1/1000^{th}$ of the rate of jets. However, since the fragmentation function is steeply falling with increasing z[12], the probability of getting a single particle with a large fraction of the jet momentum is fairly small. When folding this factor in, one finds that direct photons compete fairly well with high p_T neutral meson production. In the p_T range from 5-8 GeV/c the $\gamma : \pi^0$ ratio increases from $\sim$ 1:3 to $\sim$ 5:1. The neutral meson background arises from the inability to distinguish some high p_T photons as coming from neutral meson decays. The main sources of this ambiguity are the following:

- Acceptance losses: For decays which occur with a large energy asymmetry[13] one of the photons can escape the detector's acceptance. In this case, the higher p_T photon looks like a direct photon.

---

[12] Recall, z is the fraction of momentum that the hadron carries with respect to the initial quark.

[13] The energy asymmetry, $\alpha = (E_1 - E_2)/(E_1 + E_2)$ is proportional to the opening angle in the center of mass system (CMS).

- Coalescence: For a high p_T π^0, the 2 photons may overlap within the resolution of the detector. In this case the 2 photons from the π^0 are reconstructed as a single high p_T photon.
- Other various losses: Some other losses, which are highly detector dependent are fiducial losses, trigger biases, photon conversions, and any software cuts applied in the software reconstruction.

In order to measure the direct photon cross section, one must be able to measure the direct photon backgrounds well. In E706, individual photons from π^0 and η meson decays are reconstructed, and the invariant mass calculated. A sophisticated monte carlo is used to measure the losses due to the sources mentioned above. The estimates made of the losses are used to correct the measured neutral meson cross section, as well as to estimate the contribution of these losses to artificially increasing the direct photon cross section. Schematically, the direct photon cross section is calculated as,

$$N_\gamma^{TRUE}(p_T) = N_\gamma^{TOTAL}(p_T) - F_{FAKE}^\gamma(p_T) \times N_{\pi^0}^{DATA}(p_T).$$

where,

$$F_{FAKE}^\gamma(p_T) = \left(\frac{N_\gamma(p_T)}{N_{\pi^0}(p_T)}\right)_{MC}^{BKND}$$

is the fraction of neutral mesons which falsely mimic the direct photon signal at a given p_T, as a result of the losses mentioned above.

This equation simply expresses that the *true* number of direct photons N_γ^{TRUE} at a given p_T is given by the total number of candidate direct photons N_γ^{TOTAL} at a given p_T, minus a fraction F_{FAKE}^γ of the total meson cross section. The fraction $F_{FAKE}^\gamma(p_T)$ is simply the ratio of the fake direct photon cross section to the neutral meson cross section as a function of p_T. This fake contribution is estimated by producing neutral mesons with a MC, and observing how often the reconstruction

yields a (fake) direct photon. Since the main contribution to the fake direct photon signal at any given p_T, (say p_T^0) is due to the acceptance losses, *it is generally the neutral meson cross section at* $p_T \geq p_T^0$ *that contributes to the direct photon cross section at* p_T^0. Therefore, the estimation of the number of fake direct photons at a given $p_T = p_T^0$ is fairly sensitive to the MC input spectrum of the neutral mesons at $p_T \geq p_T^0$. Consequently, one needs to have the MC reproduce the meson cross sections in the relevant kinematic variables (generally p_T and rapidity are sufficient). By using the appropriate admixture of the relevant neutral mesons, and their known branching ratio's to photons or π^0's, one can subtract off each's contribution to the direct photon background. It is primarily the π^0 and η mesons which are responsible for almost all the background to direct photons at high p_T.

1.6 Charm Production

In this thesis, our objective is to measure the cross section for charm production in π^--nucleon collisions. One might wonder how one goes about measuring the charm cross section in an experiment designed to measure direct photons. The answer lies in the fact that E706 triggers on all high p_T phenomenon[14], including high p_T charm quark jets. Therefore, the E706 data affords an opportunity to study charm production in high p_T jets.

The process of charm production is schematically the same as in Figure 1.1, with the final state partons being a charmed and anti-charmed quark. The total cross section for the production of a heavy quark pair at a given center of mass (CM) energy S, may be written as,

$$\sigma_{Q\overline{Q}}(S) = \sum_{ij} \int dx_i dx_j \hat{\sigma}_{ij}(x_i x_j S, m_c^2, \mu^2) F_i^A(x_i, \mu) F_j^B(x_j, \mu). \qquad 1.12$$

In this equation, the total cross section is a convolution of the partonic cross sections, σ_{ij}, with the structure functions F_i^A, F_j^B. The partonic cross sections are functions

[14] That is, all high p_T physics which produce high p_T electromagnetic showers.

of the partonic center of mass energy $x_i x_j S$, the charm quark mass m_c, and the renormalization scale μ, while the structure functions F_i^A and F_j^B are functions of their respective momentum fractions x_i and x_j and the renormalization scale μ[15].

At leading order (LO), the partonic cross sections (σ_{ij}) for producing heavy quark pairs are described by the $q\bar{q}$ annihilation and gluon fusion diagrams. These Feynman diagrams are shown in Figure 1.4. Since these diagrams each have 2 vertices, they enter at $O(\alpha_s^2)$.

From these diagrams, the LO, total and differential charm quark cross sections were calculated[28, 29, 30, 31, 32]. These LO predictions for the total charm cross section were found to be 2-3 times lower than the experimental values. Various mechanisms such as intrinsic charm[33] were put forth to explain this excess by investigating the possibility that there was a non-negligible $uudc\bar{c}$ component in the proton.

In recent years, the NLO $O(\alpha_s^3)$ charm production cross sections have been published[34, 35, 31], and provide an enhancement of 2-3 times over the LO prediction. The NLO distributions are now in general agreement with the available data, but even at NLO, there still remains a factor of 2-3 uncertainty, mainly in the overall normalization. However, the shapes of the x_F and p_T distributions do not change substantially upon inclusion of the NLO terms. Still some questions lie unanswered, particularly with respect to hadroproduction. This will be discussed later in this chapter.

At next to leading order (NLO), various $2 \rightarrow 3$ diagrams enter the calculation. Generally, this involves 2 heavy quarks and 1 light parton in the final state, i.e. $g + g \rightarrow c + \bar{c} + g$. This final state may be produced in a variety of ways, including, (a) perturbative gluon emission from a quark line, (b) gluon splitting of a final state

---

[15] The structure functions are also have a Q^2 dependence introduced through scaling violations.

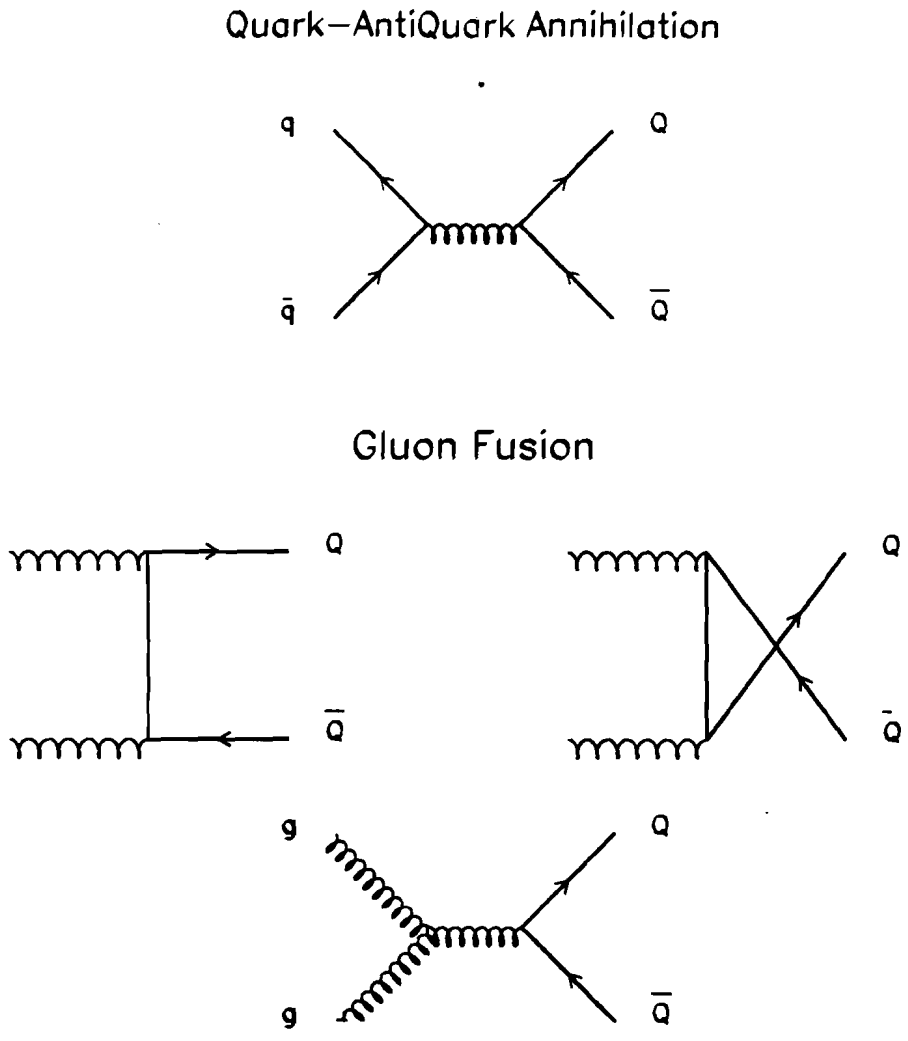

Figure 1.4 Leading order diagrams for the production of charm. Shown are the gluon fusion and quark anti-quark annihilation diagrams.

gluon into a pair of charm quarks, and (c) charm excitation i.e. via evolution of the gluon structure function to the Q^2 of the hard scatter. These processes involve *real* partons in the final state. Depending on the energy regime and accessible x_F range, different subprocesses dominate. In the energy regime of E706, the gluon fusion graph dominates the production at LO, and the NLO contributions are expected to be mainly from (a) above. At collider energies, (b) and (c) generally dominate the production rate.

In order to obtain the appropriate cancellations at NLO $O(\alpha_s^3)$, the perturbative calculation must include the interference of the $O(\alpha_s^4)$ virtual gluon loop diagrams with the LO diagrams at $O(\alpha_s^2)$. The cross terms from the interference provide for cancellations of various divergences appearing at $O(\alpha_s^3)$. When all appropriate diagrams are included in the perturbative expansion, one can obtain a theoretical prediction for the charm cross section at NLO. Figure 1.5 shows some of the various diagrams which enter the calculation at NLO. Shown are the real and virtual gluon emission diagrams, as well as the gluon splitting graphs.

Programs are available[36], which allow one to calculate the total and differential cross sections at LO and NLO. Also provided is the capability to vary such parameters such as the charm quark mass m_c, the renormalization and factorization scales, μ_r and μ_f, as well as allowing the usage of a variety of input structure functions. Figure 1.6 shows the theoretical prediction for the total charm production cross section as a function of the beam energy in π^-N interactions. Shown in the figure is the prediction with various choices of the renormalization scale. The calculations use $m_c = 1.5$ GeV/c^2, $\mu_f = m_c$, and $\Lambda = 190$ MeV. The SMRS2[37] structure functions were used for the pion and HMRSB[38] for the nucleon. Shown in Figure 1.7 is the ratio of the total NLO cross section to the LO cross section as a function of beam energy for the same input parameters as in Figure 1.6. One observes the large increase upon inclusion of the NLO terms.

The necessity of the NLO calculations was expected based on some simple arguments. Within the framework of PQCD, an expansion in α_s should converge

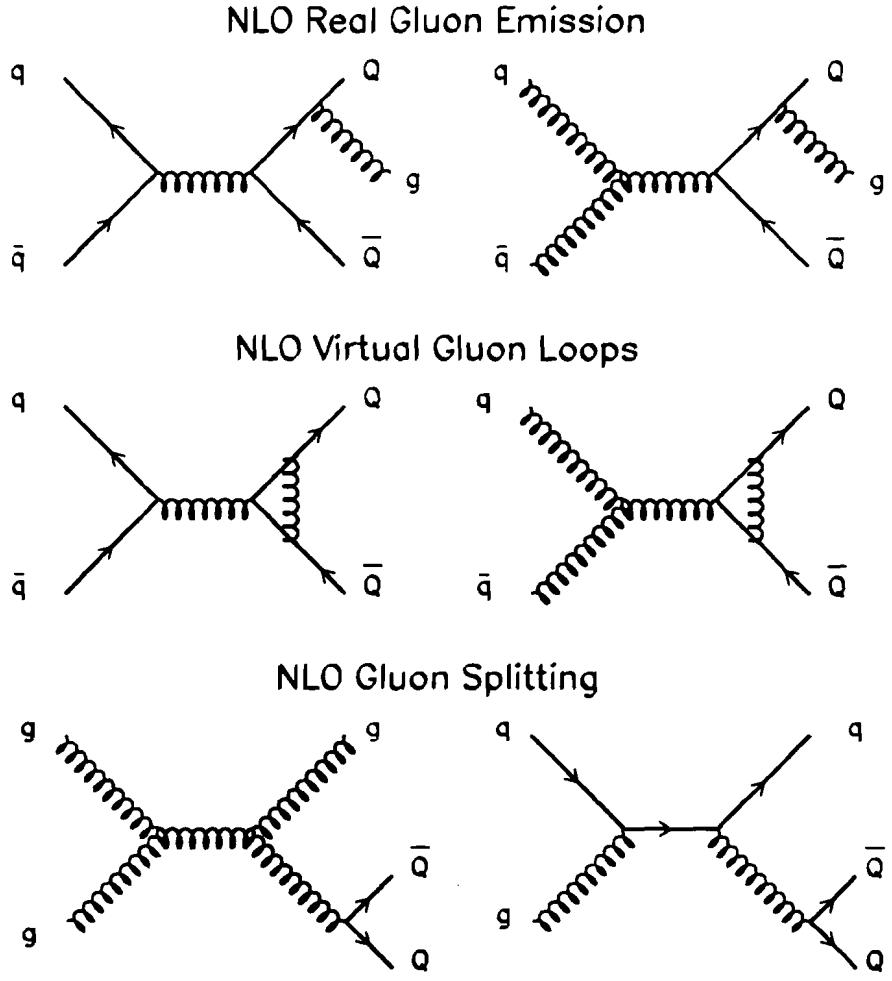

Figure 1.5 (a) Real gluon emission diagrams $O(\alpha_s^3)$, (b) Virtual gluon loops at $O(\alpha_s^4)$, and (c) Gluon splitting diagram at $O(\alpha_s^3)$.

provided α_s is small. However, since the charm quark mass is not large[16] compared to the renormalization scale, α_s is not quite as *small* as one would like. Consequently, one must include higher orders in perturbation theory in order for the result to converge. One can get a lower limit on the theoretical uncertainty at a given order in perturbation theory by examining the sensitivity of the result to changes in the renormalization scale. The sensitivity to the renormalization scale should decrease with increasing orders in PQCD, and the cross sections should be independent of μ_r when the calculations are carried out to all orders. It has been shown[39] that the sensitivity of the theoretical prediction to μ_r does not improve substantially when going from LO to NLO. This suggests that for charm production, one probably needs to go beyond NLO. In contrast, the variation in the bottom(B) quark cross section improves significantly upon the inclusion of the NLO corrections. This is expected since the b quark mass is $\sim$ 5 GeV/c^2 and so α_s is smaller, which improves the reliability of the calculations.

In addition to the uncertainty introduced as a result of the truncation of the perturbative expansion at NLO, there are other uncertainties. These are described below.

- Choice of parton structure function and Λ_{QCD};
- The value of the charm quark mass;
- Choice of scales (renormalization and factorization scales);
- Non-perturbative effects such as intrinsic k_T of the incoming partons.

Various sets of modern parton densities exist which are tuned based on a variety of experiments, including deep inelastic lepton-nucleon scattering, Drell-Yan cross sections, J/Ψ production and direct photon production[40, 41, 42, 43, 44]. Generally, one has some flexibility to choose a set of structure functions for

[16] The charm quark mass is usually used as a measure of the momentum transfers involved in charm production.

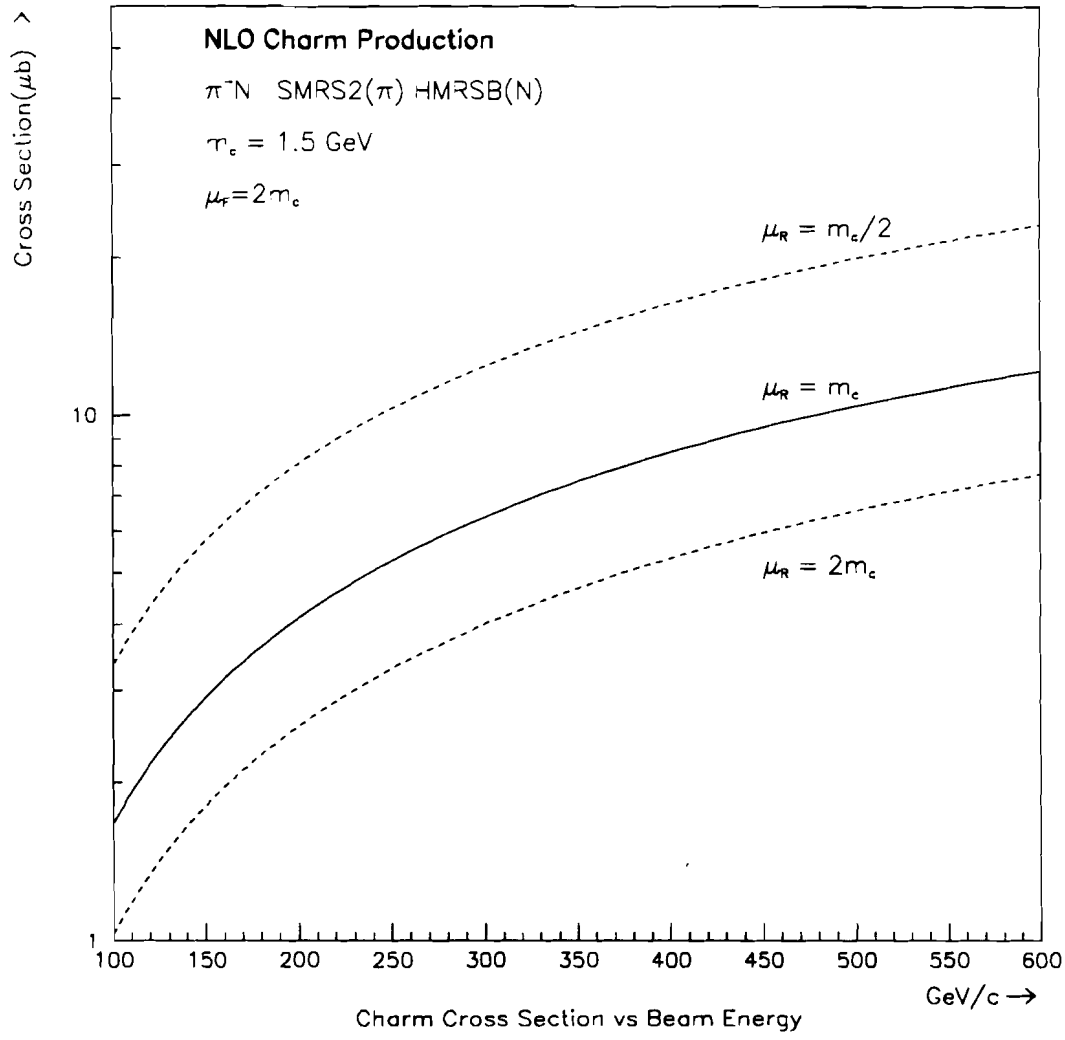

Figure 1.6 Theoretical prediction for total cross section ($O(\alpha_s^3)$) for the process $\pi^- N \rightarrow c\bar{c}$ as a function of the beam energy.

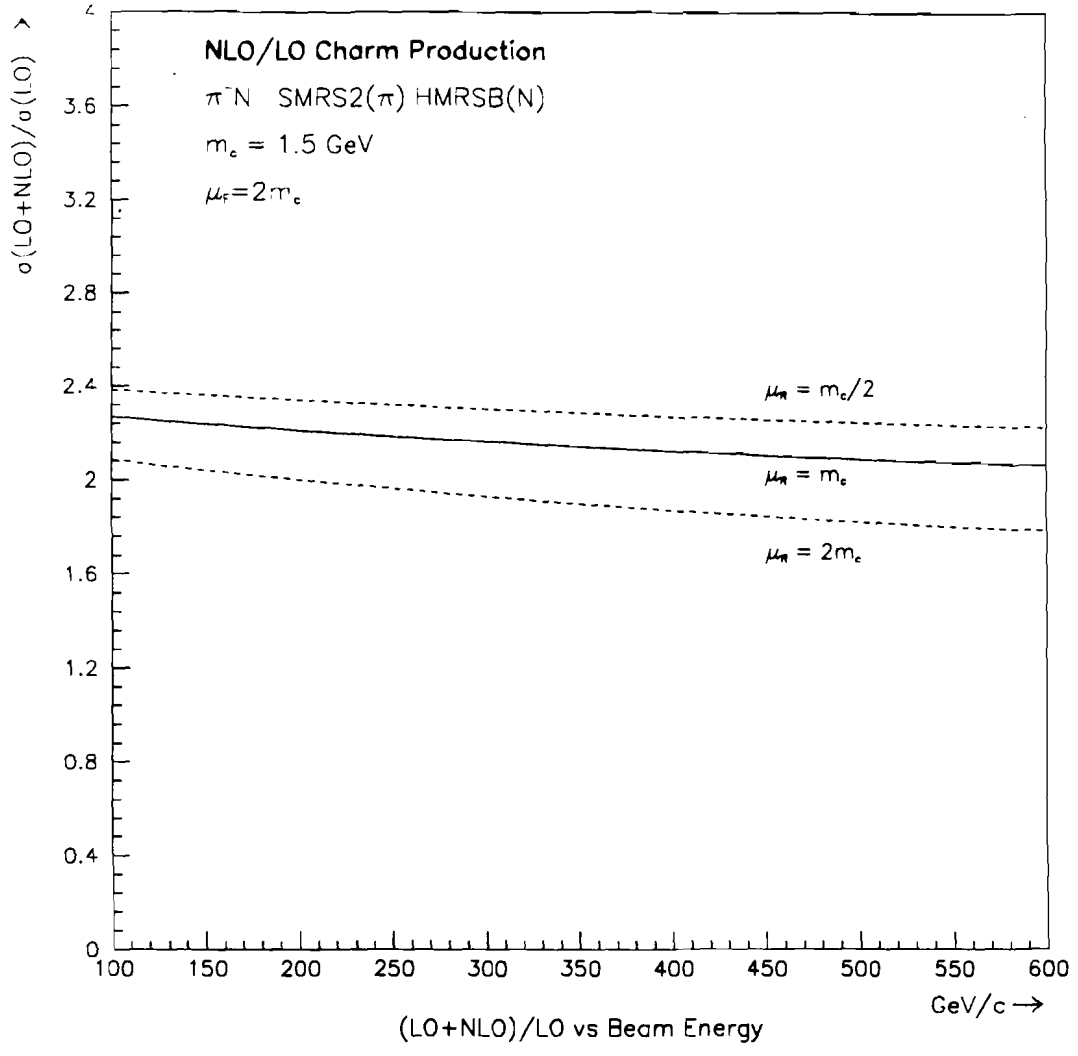

Figure 1.7 Ratio of the LO+NLO cross section to the LO result as a function of beam energy for π^-N collisions.

input into the calculations. For a given structure function is an associated value of Λ_{QCD}, which typically ranges from 100-300 MeV. Uncertainties in the cross section as large as a factor of 2-3 may be introduced, depending on which structure function is used and the choice of Λ.

The theoretical cross section is particularly sensitive to the choice of the charm quark mass. In fact, varying the charm quark mass by $\pm$ 300 MeV/c^2 with respect to the value $m_c = 1.5$ GeV/c^2, can yield an increase or reduction of the cross section by a factor of 3.

As mentioned previously, one can use the variations of the cross section with respect to the renormalization and factorization scales to obtain a lower limit on the theoretical uncertainty involved in the calculation. In [39], the authors varied only the renormalization scale from $\mu_r = m_c/2$ to $\mu_r = 2m_c$, holding the factorization scale at $\mu_f = 2m_c$, and found variations by a factor of 3-4 times the central value. Varying the factorization scale is expected to yield similar size uncertainties. Therefore, the theoretical uncertainties are fairly large, even at NLO.

In order to compare differential distributions, such as the transverse momentum, with experiments, one must account for the hadronization of the charm quark into a charm hadron. One generally expects that a universal, process independent, fragmentation function can be used to describe the softening of the p_T distribution of the heavy quarks as they fragment into hadrons. A commonly used fragmentation model for heavy quarks is that of Peterson[45]. Comparisons have been made between the NLO predictions and the available data[39, 46, 47]. One finds that the pure unfragmented charm quark p_T distributions agree fairly well with the available measurements. However, upon application of the Peterson fragmentation to the NLO prediction, one is left with a p_T distribution which is somewhat softer than the data. This discrepancy can be partially accounted for by the intrinsic k_T present inside hadrons, which is expected to be several hundred MeV. This primordial k_T tends to harden the p_T distribution. In references [46, 47], the authors verified that

an artificially large $< k_T^2 > \sim 2$ GeV^2 could bring the NLO predictions in agreement with the data of E769 and WA82. This amount of k_T is uncomfortably large, and more data will be needed to get a clearer understanding.

Another difference between the pure NLO result and the data from charm hadroproduction is in the x_F distribution. In reference [39], the authors compared the predictions of the NLO calculations with the LO results from the Herwig[17] monte carlo, with and without fragmentation effects[17]. The authors found that the LO unfragmented result from Herwig agreed fairly well with the NLO calculation. (Recall that LO and NLO x_F distributions are similar.) However, upon inclusion of the fragmentation model of Herwig, i.e. cluster fragmentation, the x_F distribution becomes harder than the NLO prediction. This non-perturbative effect is understood in terms of the dragging of charm quarks produced at large rapidities in the color field of the beam fragments. In this case, the charm quark can form a color singlet cluster with either of these fragments, or with other partons produced at small angles. Consequently, a large fraction of the momentum of these fragments may be transferred to the charm hadron, which will boost its longitudinal momentum with respect to the charm quark. The authors also showed that the fragmented Herwig result is softer in p_T than the unfragmented result, both of which are harder than the pure NLO prediction. The authors traced this result back to an infrared cutoff inside Herwig of 1 GeV for initial state space-like gluon radiation. This results in the initial state gluons having an average p_T of about 1.7 GeV. Since gluon fusion is a large component of the charm production, this initial state gluon p_T manifests itself in a stiffer charm p_T distribution. This cutoff is an adjustable parameter of Herwig, which provides a mechanism for intrinsic k_T of gluons, and should not be taken as a theoretical prediction. The authors verified

---

[17] Herwig produces charm pairs at LO, but higher order effects such as gluon radiation in the initial and final states produce decorrelations from the pure LO result.

that by invoking a $< k_T^2 > \sim 2 - 3$ GeV^2, into the NLO calculations, they could reproduce the results of Herwig.

In summary, the pure NLO p_T distribution agrees fairly well with the data of E769 and WA82. However, upon inclusion of a fragmentation model such as Peterson to the NLO calculation, one is left with a softer distribution than is the case with the data. The distribution can be brought back into agreement by supplementing the fragmented NLO result with an intrinsic $< k_T^2 > \sim 2$ GeV^2. This amount of k_T is uncomfortably large, and more data will be needed to get a clearer understanding. The x_F distribution agrees fairly well with the unfragmented NLO result. From the fragmentation of the charm quarks at large rapidities, it is expected that the data x_F spectrum will be somewhat harder than the NLO prediction. After including the softening in x_F due to the strong decays, the data is in fairly good agreement with the NLO predictions. Alternately, in [48], it was shown that the measured x_F distribution for $D^{\pm}$ agrees fairly well with the pure NLO prediction when a delta function was used for the fragmentation. It appears at this time that the largest discrepancy is in the transverse plane. With higher statistics, experiments will be able to make stronger comparisons not only in single differential distributions, but also in double differential distributions, such as the azimuthal opening angle between the charmed hadrons, and the x_F and p_T^2 of the $c\bar{c}$ pair. Such comparisons will give more insight into the dynamics of charm hadroproduction, and test the applicability of PQCD to fixed target hadroproduction of charm.

1.7 Experimental Overview of Pion Induced Charm Production

In this thesis, we attempt to make a measurement of the pion induced charmed meson cross section at a beam energy of 515 GeV/c. This measurement, along with measurements at other beam energies, yields the energy dependence of the production cross section. In the experiment we observe the charmed hadrons, and not the charmed quarks themselves. Assuming a constant fragmentation rate of charm quarks into a given species of charmed hadrons, we can extract the total

charm cross section. A comparison of this energy dependence of the production cross section with the theoretical predictions provides a valid test of PQCD.

Table 1.4 gives a list of some of the recently published measurements of pion induced open charm cross section. The measurements show an increase in the cross section which is consistent with the NLO theoretical prediction. An experimental review of charm hadroproduction at fixed targets can be found in the references[49, 50].

Table 1.4 Recent experimental results on $D^{\pm}$ production cross sections

Collaboration(Ref)	Beam Energy	$\sigma(D^{\pm})$ μb/nucleon
NA32[51]	230 GeV/c	$3.2 \pm 0.3 \pm 0.7$
E769[52]	250 GeV/c	$3.84 \pm 0.70 \pm 0.45$
NA27[53]	360 GeV/c	5.7 ± 1.5
E653[54]	600 GeV/c	$8.66 \pm 0.46 \pm 1.96$

1.8 E706 and Charm Physics

E706 was designed primarily for the study of high p_T direct photons and their associated jets. To select these events, E706 triggers on high p_T electromagnetic depositions in the EMLAC (see Chapter 2). The majority of these events arise from triggering on leading neutrals in high p_T jets. Although these events constitute background to direct photon physics, they are interesting in their own right. These events allow for E706 to make direct measurements of the π^0[24], η[55], and ω[56] cross sections at high transverse momentum.

In addition to the neutral meson and direct photon physics, E706 affords an opportunity to do charm physics. Similar to (light) quark or gluon jets, charm quark jets also will trigger the apparatus, provided the jet contains a leading neutral

(or electron) of sufficient transverse momentum. Since the electromagnetic trigger selects events containing high p_T leading neutrals, the charmed hadrons generally have a transverse momentum typically of the order of the trigger threshold. The argument for this hypothesis assumes that the charmed hadron is the parent of the triggering particle.

Previous experiments had minimal trigger thresholds, and were therefore highly enriched with low p_T events, but lacked statistics at higher transverse momentum. E706 is sensitive to the production at relatively high transverse momentum, and therefore, it complements the low p_T measurements.

In this thesis, we are only attempting to fully reconstruct the charged modes, in particular $D \rightarrow K\pi\pi$. Since this is a fully hadronic mode, it has very little chance of triggering the electromagnetic calorimeter itself. In order to trigger on events containing charm, and to observe the above decay mode, we expect that the partner charm particle decay contains an electromagnetic particle, **and** it carries a large fraction of the charm hadron's transverse momentum. This is the bias introduced by the E706 trigger. The corrections to the cross section for this trigger bias are discussed in chapter 5, where we discuss the software simulation of the on-line trigger.

1.9 Direct Photon plus Charm Production

The topic of production of charm in association with direct photons is another capability of E706. As mentioned in the preceding sections, E706 was designed primarily for the study of direct photons and their associated jets. Observation of charm in such events is interesting in that there are very few diagrams which can produce such an event. At lowest order, one expects this final state to be produced via perturbative gluon splitting in the direct photon annihilation graph, and charm excitation in the Compton graph. These diagrams are represented in Figure 1.8. In the Compton graph, the charm particles are produced via the evolution of the

gluon structure function to the Q^2 scale of the hard scatter. In the annihilation graph, the charm quarks are produced in the fragmentation of the awayside gluon jet.

Since it is the direct photon in these processes which triggers the apparatus, the cross section measurement is unbiased by the trigger provided the direct photon is above the trigger threshold. This differs from LO charm production, as discussed above, in that (for LO charm) the charmed hadron does not directly trigger the apparatus. Therefore, the direct photon + charm measurement is less model dependent than the measurement of the total charm cross section. While this measurement can be made in E706, the emphasis of this thesis is on the production cross section for charm. This section is intended to introduce another possible area of exploration in the E706 data.

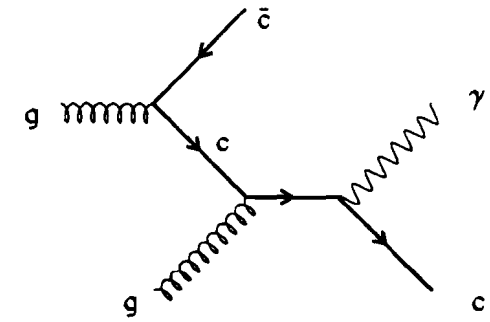

Compton Diagram

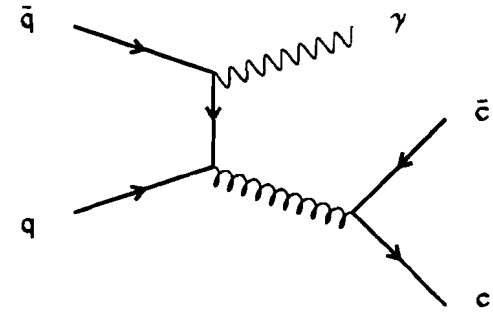

Annihilation Diagram

Figure 1.8 Lowest order Feynman diagrams contributing to the production of charm in association with direct photons

Chapter 2 Experimental Apparatus

The MWEST spectrometer was designed to study direct photons and their associated jets. In order to meet these physics goals, the E706 collaborating institutions designed and developed the detectors deemed necessary to carry out those measurements. The elements of the MWEST spectrometer include both the E706 and E672 apparatus. The E672 apparatus has been described elsewhere [57, 58]. The main elements of the E706 spectrometer were,

- MWEST Beamline and Cerenkov
- Trigger and Data Acquisition (DA) Systems
- Silicon Strip Detector System (SSD)
- Dipole analysis magnet
- Proportional Wire Chamber System (PWC)
- Straw Tube Drift Chamber System (STDC)
- Liquid Argon Calorimeter (LAC) having both electromagnetic (EM-LAC) and hadronic (HALAC) sections
- Forward Calorimeter (FCAL).

Figure 2.1 shows the physical relationship of the various detectors to one another. A discussion of these various systems is discussed in the remainder of this chapter.

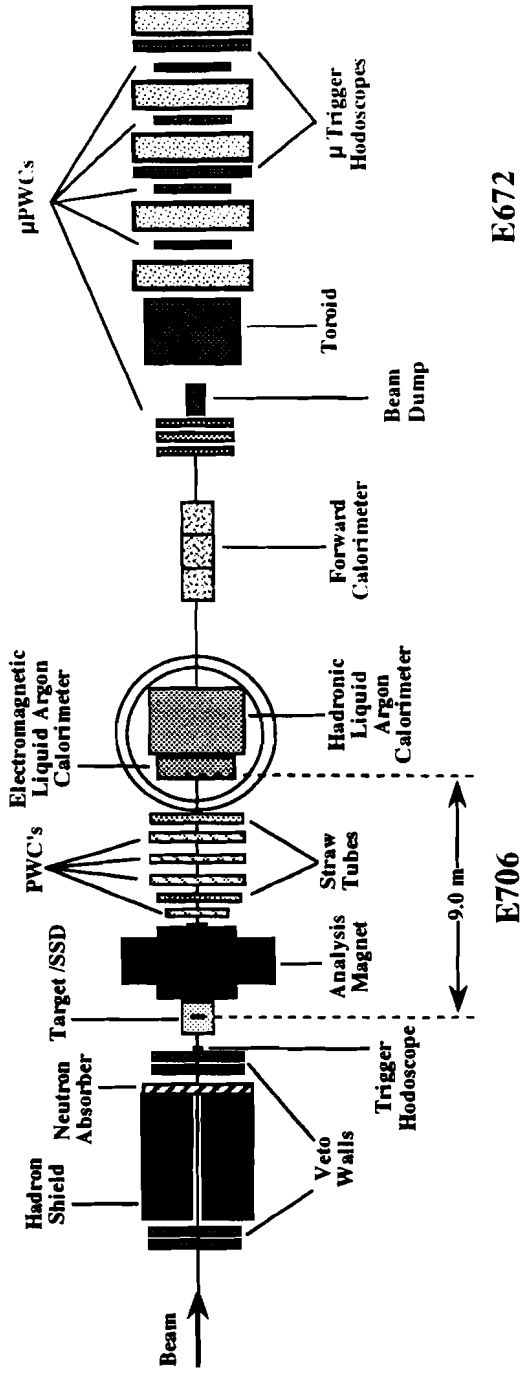

Figure 2.1 Schematic of MWEST spectrometer.

2.1 MWEST Beamline and Cerenkov

2.1.1 Beamline

The Tevatron at Fermilab accelerates protons (and anti-protons) to an energy of $\sim$ 1 TeV. The deliverance of the beam from the Tevatron to the MWEST beamline took place in 2 steps. First, during a 35 second period, the beam was accelerated to its nominal peak energy. In the second step, the beam was extracted from the Tevatron and delivered to the experimental areas. The second phase spanned a 23 second period, typically referred to as a *spill.* The primary protons delivered by the Tevatron were localized into *time buckets* which were $\sim$ 1 ns wide and $\sim$ 19 ns apart. This 19 ns (53 MHz) RF structure was important in establishing a reference for much of the timing circuitry in E706.

The MWEST beamline was designed to transport both positive and negative high intensity beams into the MW9 experimental hall. The beamline was capable of delivering either (a) primary protons from the Tevatron at 800 GeV/c, or (b) secondary beams of lower energy. In the latter case, secondary particles were produced by interactions of the 800 GeV/c primary protons on a 1.14 interaction length Beryllium target (primary target) which resided $\sim$300 meters upstream of the E706 target. The secondaries produced within the given momentum bite were transported to the MW9 experimental hall via a series of dipole (bending) and quadrupole (focusing) magnets. For the 1990 run, E706 utilized a secondary beam of particles of mean momentum 515 GeV/c which had a momentum bite of $\sim$20 GeV/c. In the 1991 configuration, both positive and negative secondary beams were utilized, as well as the 800 GeV/c primary protons. The -515 GeV/c secondary beam was predominantly pions, with smaller contributions of kaons and anti-protons, while the +520 GeV/c beam was primarily protons. Typically, it was desirable to have $\sim$ 2 x 10^8 particles per spill incident upon the E706 target. For +515 GeV/c secondaries, this corresponded to a primary proton beam intensity of $\sim$ 2 x 10^{12} per spill, while -515 GeV/c secondaries required about 3 times that amount to achieve

the same intensity. This is primarily due to the extra unit of positive charge in the proton. A more detailed description of the MWEST beamline can be found in the references[59].

2.1.2 Cerenkov

In order to make measurements of the relative contributions of pions, kaons and protons (anti-protons) in the secondary beam, a differential Cerenkov detector was installed. A detailed description of the detector and its performance can be found in the references [59, 55]. The Cerenkov detector was located in the MWEST beamline ~98 meters upstream of the E706 target. The counter was 42.1 meters long with a radius of 24.4 cm. Cerenkov light was reflected from the mirror located at the downstream end of the detector to the phototubes located at the upstream end of the counter. Helium gas, operated at pressures from 4-8 psia, acted as the radiator. Due to the momentum bite of the beam and its angular and spacial dispersion, resulting spectra from the counter have some level of mixing of the Cerenkov light from different particles. During the course of the data run, *pressure curves* were periodically taken to determine the pressure at which optimal particle tagging occurred. Offline analysis of the Cerenkov data should allow for the determination of optimal definitions for various particle tags. In practice, one generally can use the Cerenkov to isolate a sample of events with a higher concentration of a minority beam particle i.e. such as a $K^{\pm}$ beam tag. The determination of the relative contribution of particle types for the 1990 and 1991 runs is still in progress. Since the numbers are not expected to change very much, we cite the fractions determined for the 1988 data (see Table 2.1).

2.2 Veto Walls and Hadron Shield

In order to protect the apparatus from triggering on *beam halo*, E706 installed a large hadron shield and 3 muon walls. Beam halo was those particles which were produced at the primary target (~ 300 meters upstream), that travelled along, but

Table 2.1 1988 Beam Composition

Positive Beam			Negative Beam		
$\pi^+(\%)$	$K^+(\%)$	p(%)	$\pi^-(\%)$	$K^-(\%)$	$\bar{p}(\%)$
7.2±0.1	1.7 ±0.1	91.2±0.1	96.9±0.2	1.9 ±0.2	0.2 ±.01

outside of the beampipe. Much of the beam halo particles were deflected away by spoiler magnets (located in the beamline), and then absorbed by appropriately placed shielding. The remaining halo particles, which were primarily stable hadrons and muons, were mostly eliminated by the hadron shield, neutron shield, and the veto walls. All 3 elements had a hole in the center where the beam particles passed. The large hadron shield consisted of a stack of steel plates with dimension 4.3 m high × 4.7 m long × 3.7 m high. The hadron shield absorbed most of the hadron component of the beam halo. The neutron shield, located just downstream of the hadron shield, was used to absorb any remaining neutrons passing through the hadron shield. The 3 veto walls were used to detect and veto events containing a halo muon. Halo muons can become a large source of background for the direct photon analysis, unless they were rejected. One veto wall was place just upstream of the hadron shield, and the other two were placed just downstream of the neutron absorber. Each veto wall was made of large paddles of scintillators which connected to phototubes at their ends. For the 1990 LAC triggers, an event was vetoed if it satisfied the following logic:

$$\mathrm{VW} = (\mathrm{VW1} \oplus \mathrm{VW2}) \otimes \mathrm{VW3}.$$

In other words, an event was vetoed if veto wall 3 and either veto wall 1 or 2 registered a hit in a given time bucket.

2.3 Trigger and Data Acquisition (DA) Systems

E706 was designed to study high p_T inclusive particle production arising from direct photons and jets. It was known that such high p_T processes were expected to be fairly rare. Hence, it was necessary to operate at high interaction rates of ~1 MHz (~20 million interactions per spill). Consequently, it was necessary to design on-line systems which could handle these high interaction rates, as well as select out the events of interest. The DA and Trigger systems were designed to address these demands. In particular, they were designed to perform the following tasks:

- Trigger - Select out the desired rare events from the multitude of other events. E706 typically selected ~ 1000 events from the ~ 20 x 10^6 interactions during a single spill.
- DA - The DA system was responsible for collecting and concatenating the data received from the various subsystems. It served as the "middleman" between the data stored in the hardware (trigger and detectors) and the output of the raw data onto some storage media (8 mm exabyte).

In the upcoming sections, a brief description of these components is given. For more details regarding the design and operation of the trigger, consult the references [60]. A more lengthy discussion of the DA system can also be found in the references [55, 24, 61].

2.3.1 Trigger

An event which was to be written to tape was required to satisfy at least one of the E706 trigger types. The essential criteria for forming a trigger were the following:

- Beam Definition
- Interaction Definition

- Pre-Trigger Definition
- Trigger Definition

Beam Definition

In order to satisfy any of the standard triggers, it was required that a *triggerable beam particle* be present. In this section, we describe the basic elements needed to identify a triggerable beam particle (BEAM1).

The first criteria for generating a BEAM1 signal was the detection of a beam particle. Beam particles were detected by way of a beam hodoscope (BHODO) located upstream of the SSD system and just downstream of the third veto wall. The hodoscope consisted of 12 overlapping scintillators arranged in three 3 views (X, Y, and U). The scintillators varied from 1 mm in width at the center to 5 mm on the peripheries. Each element provided a time history of 15 buckets. When any two of the three hodoscope planes registered a hit cluster[1], a BEAM signal was generated. If multiple clusters were registered in the beam hodoscope in a given time bucket, any subsequent interactions within that bucket were eventually vetoed by the trigger system.

In addition to the beam hodoscope, a beam hole counter (BH) was installed $\sim$2 cm downstream of the hodoscope. BH was composed of 2 scintillating paddles each having a semicircular hole cut out at the end. The two paddles were placed so to form a hole $\sim$.48 cm in radius. BH was aligned to the SSD system so that particles passing through the hole were also passing through the central portion of the silicon detectors. It was required that the beam particle pass through the hole of BH. This anti-coincidence ($\overline{\text{BH}}$) was applied later in the logic to veto such beam particles which were off center of the target/SSD system.

---

[1] A hit cluster was either a single element or a pair of adjacent elements which registered a hit.

The remaining requirements for generating a triggerable beam particle logic pulse were BM_GATE and RF_CLOCK. The former of these was a pulse generated by the DA system which designated the time interval during the spill which incoming beam particles were to be considered as triggerable. The RF_CLOCK signal was a 1 ns pulse ($\sim$ 53 MHz) generated to be in phase with the RF structure of the beam. The detected beam particle was required to be in phase with this logic pulse.

Combining all of these criteria, one obtains the working definition of *triggerable beam* (BEAM1), as,

$$\text{BEAM1} = \text{BHODO} \otimes \text{BM\_GATE} \otimes \text{RF\_CLOCK} \qquad 2.1$$

Interaction Definition

E706 used 4 interaction counters with which to define an interaction. Two of the counters were located just upstream of the analysis magnet (SE1 and SW1), and the other two counters just downstream of the analysis magnet (SE2 and SW2). Each pair of scintillating counters were placed side by side to one another. A hole was formed in a manner similar to BH, which allowed non-interacting beam particles to pass through, without hitting the counters. An interaction (INT) was defined when any 2 of the 4 counters registered a hit in the same time bucket, in coincidence with BEAM1. If an INT logic pulse was generated, the signal was passed through an EARLY-LATE cleaning filter. The details of the filter can be found in the references [60]. The heart of the filter was to require that there be no other interaction occurring within $\pm$ 3 (time) buckets of the given interaction. If these criteria were satisfied, CLEAN_EARLY and CLEAN_LATE logic pulses were generated. This early-late clean filter was implemented to avoid pile-up[2] in the detectors. In order to generate a *live triggerable interaction* (LINT1) logic pulse, it was additionally required that a COMP_RDY signal be present which signified that

[2] Pileup was the effect of several interactions occurring very close in time.

the computers were ready to accept a trigger. Summarizing, the live triggerable interaction logic pulse was generated from the following logic:

$$\text{LINT1} = \text{BEAM1} \otimes \overline{\text{BH}} \otimes \text{INT} \otimes \text{COMP\_RDY} \otimes \text{CLEAN} \qquad 2.2$$

where,

$$\text{CLEAN} = \text{CLEAN\_EARLY} \otimes \text{CLEAN\_LATE}$$

Pre-Trigger Definition

One might consider the pre-trigger as a first level trigger in which a large fraction of low p_T interactions were rejected. The decision is based upon the amount of electromagnetic p_T deposited within the innermost or outermost 128 r-strips of the EMLAC. Each LAC amplifier had a "fast-out" whereby the electromagnetic p_T could be measured quickly. The p_T for the i^{th} strip was given by,

$$p_T^i = E_i \sin(\theta_i) \approx E_i \times R_i / Z_{LAC}. \qquad 2.3$$

where R_i is the radius (cm) of the i^{th} strip, E_i is the energy measured in the i^{th} strip, $Z_{LAC} = 900$ cm, is the distance from the target to the front face of the LAC, and θ_i is the angle that the i^{th} strip subtends with the z-axis (direction of beam). A pretrigger decision was based upon the p_T sum of the R strips in each octant [3]. The requirements for generating a pretrigger were the following:

- LINT1 logic satisfied
- A minimum of 1 octant having significant p_T of at least $\sim$ 1.7 GeV/c in the inner or outermost 128 strips;
- No more than $\sim$ 1.5 GeV/c p_T in the octant in the preceding 100-200 ns (early p_T);
- No VW Veto (defined above);
- No SCRKILL - This was to reject the 400 Hz noise spikes coming from the LAC power supplies.

[3] A factor of 2 was included in order to account for the ϕ strip energies.

Each octant had the opportunity to satisfy the pretrigger definition. A pretrigger was generated if any of the LAC octants satisfied the pre-trigger. In the case that a pretrigger was satisfied, a LOAD signal was sent to the various subsystems, which latched the data associated with that interaction until a final trigger decision could be made.

Trigger Definition

The final trigger decision was based upon at least one of the available trigger's requirements being satisfied. The LAC triggers were all defined in terms of a summed p_T, of which there were 3 varieties; LOCAL, GLOBAL, and 1/2-GLOBAL. For the LOCAL definition, the 256 R view strips in each octant were organized into 32 groups, each having 8 strips. Each of the adjacent pairs of groups (1+2, 2+3, 3+4, ..., 31+32) defined a *group of 16*, for the LOCAL trigger. The LOCAL trigger discriminated on the p_T sum of each of these adjacent groups (31 adjacent group pairs per octant). The GLOBAL trigger discriminated on the p_T sum of all the r-strips in the entire octant. The 1/2-GLOBAL performed independent sums of the innermost and outermost 128 r-strips for each octant. Each type of p_T sum (LOCAL, GLOBAL, and 1/2 GLOBAL) discriminated at two different thresholds, HI and LO. The HI threshold was typically around 3.5 GeV/c, and the LO around 1.6 GeV/c. The various triggers discriminated on the sum of the p_T contained in the front and back sections of the EMLAC. From these categories, several LAC triggers were employed. A list of these various LAC triggers is given below.

- LOCAL GLOBAL HI (GLHI) = (LOCAL LO) $\otimes$ (GLOBAL HI).
- LOCAL 1/2 GLOBAL HI (1/2 GLHI) = (LOCAL LO) $\otimes$ (1/2 GLOBAL HI).
- LOCAL GLOBAL LO (GLLO) = (LOCAL LO) $\otimes$ (GLOBAL LO).
- SINGLE LOCAL HI (SLHI) = LOCAL HI
- SINGLE LOCAL LO (SLLO) = LOCAL LO

- TWO GAMMA = $(\text{LOCAL LO})_I \otimes (\text{LOCAL\_LO})_J$, where I and J refer to any 2 octants which have are on opposite side of the LAC[4].

The LOCAL triggers simply required a localized, high p_T deposition in the electromagnetic calorimeter above the given threshold. By localized, we simply mean that a large fraction of the shower's energy should be contained within a given *group of 16*. The LOCAL trigger fired in a given octant if any of these *groups of 16* were above the threshold. The SINGLE LOCAL HI trigger threshold was adjusted during the course of the run to maintain an acceptable live time fraction ($\sim$ 50 %). The SLLO triggers were prescaled down by a factor of 40, so not to dominate the trigger rate. The TWO GAMMA required that the SLLO trigger be satisfied in any 2 octants which were at least 90 degrees apart. This higher level coincidence yielded an acceptable rate so that this trigger did not need to be prescaled.

The GLHI and 1/2 GLHI trigger required that the LOCAL LO threshold was satisfied, as well as the GLHI logic. Hence, the GLHI trigger still required that a large fraction (typically, at least 50 %) of the total octant p_T be contained within a group of 16 strips. Similarly, the GLLO triggers also had the requirement that the SLLO trigger fire in that octant, in addition to the GLOBAL LO threshold being satisfied. A prescale factor of 40 was applied to the GLLO triggers, as was the case for the SLLO.

An important feature of the global triggers were the applied cutoffs. In the p_T sum over the octant, only *groups of 8* above the *group cutoff*, (typically about 250-300 MeV/c p_T), were considered in the sum. For those groups above the cutoff, the cutoff was subtracted from the measured trigger p_T to arrive at the Global p_T. This cutoff/subtraction was applied to each of the groups in the front and back sections of the EMLAC. The motivation for this subtraction was to protect against image

[4] An opposite octant is any octant which is at least 3 or more octants away.

charge effects in the EMLAC[62]. This strongly suppressed triggering on events where the total p_T in an octant was a result of multiple low p_T showers. This has the strongest bias against triggering on events where the jet p_T was distributed among many particles. In particular, jets whose leading particle(s) are hadrons are strongly suppressed since hadrons deposit only a fraction of their energy ($\sim$ 35 %, on average) in the EMLAC. In addition, since hadron showers are usually spread over more *groups of 8* than a photon shower at the same physics p_T, the reduction from the cutoffs is more severe for hadronic showers. As a result of the SLLO requirement, the global cutoffs and the thresholds, there was a strong coincidence between the GLHI and the SLHI triggers. The overlap was typically 50%.

In addition to these triggers, there existed a set of minimum bias triggers which were integrated into the trigger logic. The intent of these low bias triggers was to provide the capability to study the biases introduced by the various triggers at a later stage in the analysis. It also allowed for independent cross-checks on the normalizations of the measured cross-sections. These three additional triggers were:

- Beam Trigger - Only BEAM1 was required.
- Interaction Trigger - Only LINT1 was required
- Prescaled Pretrigger - Only a pretrigger was required.

These triggers were also prescaled so not to dominate the trigger rate. They typically accounted for $\sim$ 5-10 % of the recorded triggers. Table 2.2 summarizes the properties of the various triggers. Since any given event may fire several triggers, one does not expect the trigger fractions in the table to add up to 100%.

If any of the above triggers were satisfied, it was written to tape. After all the various subsystems were read out, a clear signal was broadcasted to the various detectors, readying the apparatus for another trigger.

Table 2.2 Summary of 1990 Triggers

Trigger	Fraction(%)	Threshold (GeV/c)	Prescale Factor
Local Global Hi	35	3.0	1
Local Half Global Hi	30	3.0	1
Local Global Lo	17	2.5	40
Single Local Hi	35	3.5	1
Single Local Lo	18	2.0	40
Two Gamma	20	1.6	1
Prescaled Beam	2	none	15^6
Prescaled INT	2	none	15^5
Prescaled Pret	5	1.7	2925
Di Muon	20	Hi Mass Muon Pair	1

In Chapter 5, we will present more details of the trigger. In that chapter, we discuss the simulation of the online triggers in order to estimate the trigger biases against selecting charm events.

2.3.2 Data Acquisition System (DA)

The role of the DA was to provide a means of collecting and concatenating the raw data from the various subsystems, once an event had triggered. A DEC 3200 Vaxstation (host node) communicated with 3 DEC PDP-11 mini-computer's and the FASTBUS system, which in turn were responsible for reading out the event information from the various detectors. Figure 2.2 shows the relationship between the various components of the DA system. The data from the FCAL, SSD, PWC, Trigger and Cerenkov and the E672 experiment, were all stored in CAMAC modules, while the LAC and Straw information were stored in FASTBUS modules[55]. When a trigger was satisfied, the READ signal initiated a readout of the CAMAC and FASTBUS systems, and the event was subsequently written out to 8 mm tape.

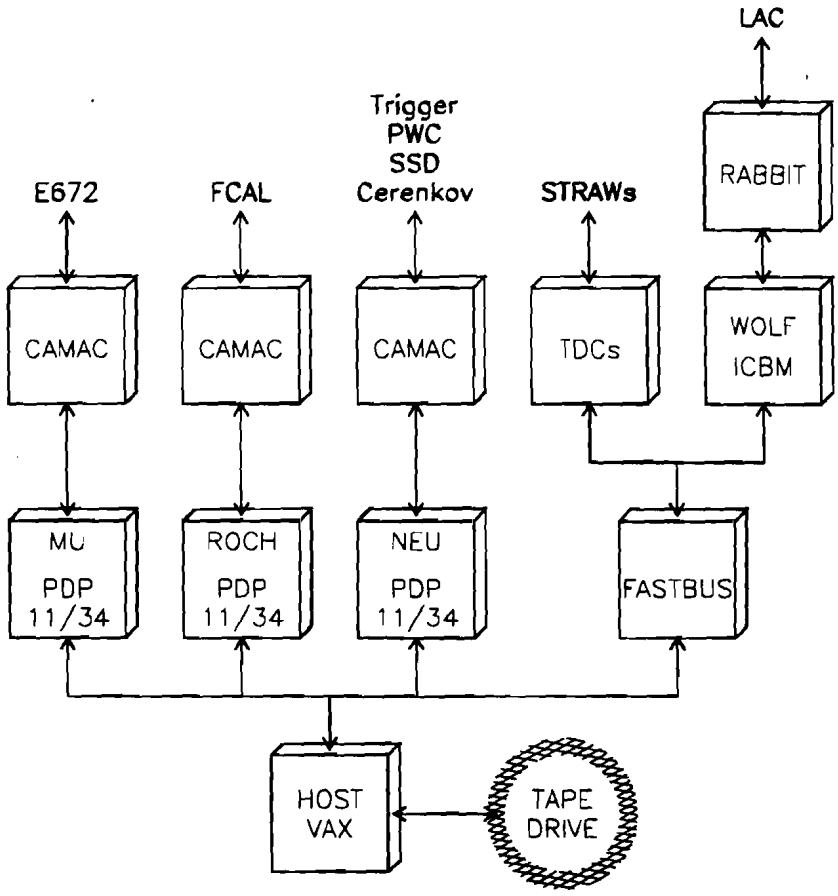

Figure 2.2 Schematic representation of the online data acquisition system.

The software package, VAXONLINE[63], which ran on the host VAX node, was used to control the operations of the DA system. Vaxonline offered five main programs which controlled the data readout. These programs performed the following operations:

- GLOBAL_MENU provided an interface to the other four programs.
- RUN_CONTROL performed all the necessary tasks to begin the run, i.e. calibration tasks, downloading trigger information, and hardware initialization. From this program the user designated the begin and end of run. Each run was limited to a maximum of $2^{16} - 1$ events.
- EVENT_BUILDER was responsible for combining the sub-events from the various sub-systems into a single event. Each sub-system provided a common event number which allowed the EVENT_BUILDER to match up the sub-events with one another.
- OUTPUT wrote the concatenated data events to various media. These media include 8 mm tapes, 9 track tapes, or disk. For the 1990 data run, OUTPUT was configured to write data to two 8 mm tapes. Hence for each run, the data was subdivided onto 2 tapes (FSA and FSB), each containing about half the events. This 2 tape mode decreased the dead time due to start-up procedures involved when mounting and dismounting tapes. Each pair of tapes could accommodate $\sim$ 150,000 raw data events.
- BUFFER_MANAGER took a fraction of the events and shipped them off to an on-line event pool where monitoring programs could be run to scrutinize the quality of the data. In particular, hit profiles in the planes were useful for finding malfunctioning camac modules, such as latches or crate controllers. Also, on-line event displays allowed one to survey events individually for overall quality.

A detailed description of the hardware components for the readout of the LAC (FASTBUS system) can be found in the references[24, 55].

2.4 Silicon Strip Detector System (SSD)

The E706 silicon strip detector[64], was developed for E706 in order to accurately measure the location of the primary vertex[5]. This was essential to making measurements of the nuclear dependence of various cross-sections on the number of nucleons. Furthermore, the system was designed with the hope that E706 would have a unique opportunity to observe (short-lived) heavy quark decays. The SSD system consisted of 16 5 cm × 5 cm microstrip detectors, assembled into 8 XY modules. Each XY module consisted of 2 detectors which were separated by a 1/4" aluminum plate. On the front face, the microstrips were oriented vertically, while on the back, the strips were aligned horizontally. In this configuration, a charged particle passing through an XY module will yield an (X,Z) and a (Y,Z) measurement of the particle's trajectory. In order to reconstruct the charged tracks upstream and downstream of the target, 3 XY modules were placed upstream of the target, and 5 XY modules downstream. All of the detectors were ~300μ thick and featured microstrips having 50μ pitch[6], with the exception of the first module downstream of the target. This *hybrid* module featured a high resolution central region, having 25μ pitch, with the peripheries having 50μ pitch. Each strip yields a theoretical hit resolution of P/$\sqrt{12}$, where P is the pitch. Since the SSD spanned ~20 cm along the beam axis, the angular resolution was ~0.06 mrad. For the 1990 run, a total of 8192 strips were instrumented, which gave an angular acceptance of ~ ±150 mrad in each view. Further technical details regarding the design of the SSD system can be found in the references[65, 66]. Figure 2.3 shows a scaled drawing of the SSD/Target region. Not shown in the figure are two beam modules which reside upstream of the third beam module. See Table 2.3 and Table 2.4 for the geometrical parameters of the SSD system.

---

[5] The primary vertex was the interaction point of the beam particle.

[6] The pitch is synonymous with "wire spacing".

Table 2.3 Beam Chamber Geometrical Parameters

Module - View	Number of Strips	Active Region (cm)	Z Position (cm)
1 - X	256	1.28	-130.23
1 - Y	256	1.28	-129.33
2 - X	256	1.28	-34.15
2 - Y	256	1.28	-33.26
3 - X	256	1.28	-19.23
3 - Y	256	1.28	-18.34

Table 2.4 Vertex Chamber Geometrical Parameters

Module - View	Number of Strips	Active Region (cm)	Z Position (cm)
1 - X	640	2.08	-6.3170
1 - Y	640	2.08	-5.2840
2 - X	512	2.56	-3.6890
2 - Y	512	2.56	-2.7756
3 - X	704	3.52	1.7827
3 - Y	704	3.52	2.7061
4 - X	832	4.16	7.3063
4 - Y	832	4.16	8.2247
5 - X	1000	5.00	12.7959
5 - Y	1000	5.00	13.7094

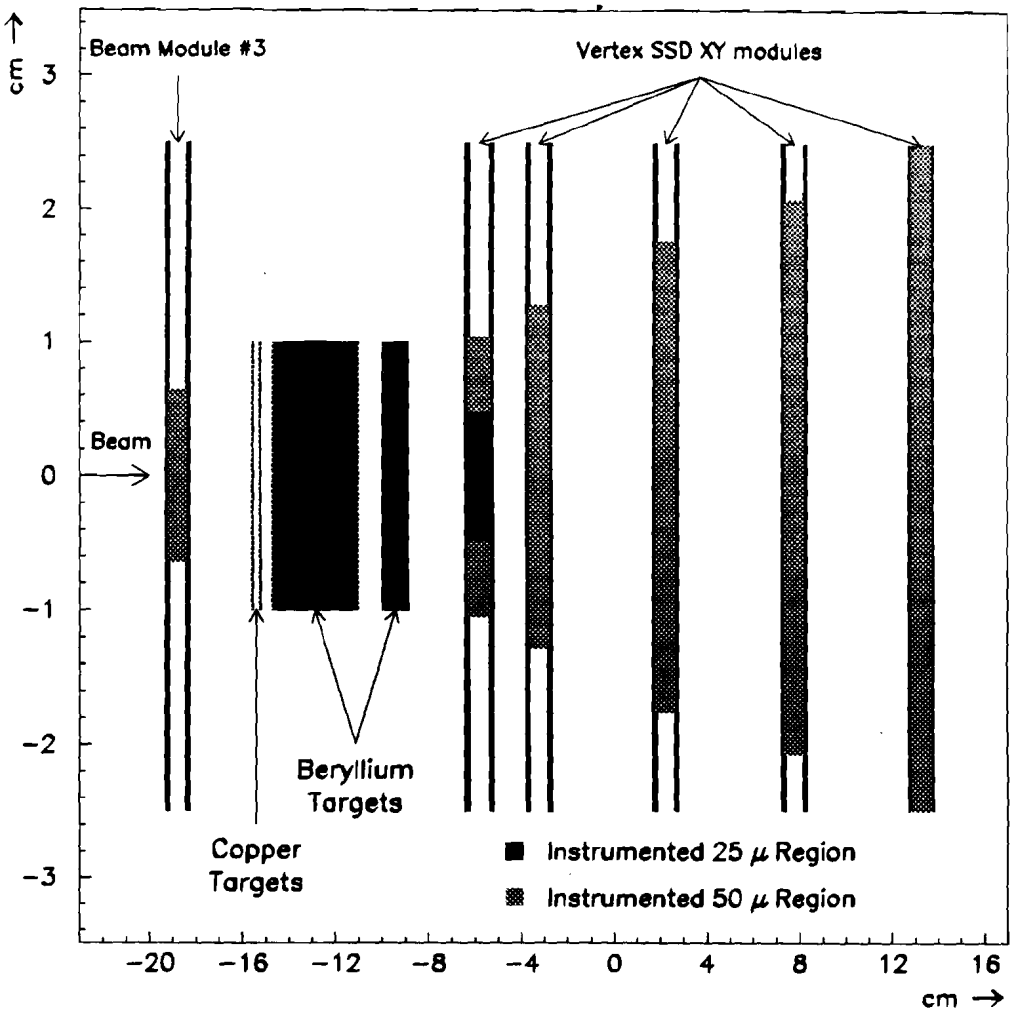

Figure 2.3 Scaled diagram of SSD/Target region for the 1990 run.

The SSD readout took place in 3 stages. These stages were:

- Pre-Amplification: Signals generated from a MIP[7] were first amplified by a Rel-Lab IO 323-C charge sensitive pre-amplifier. These amplifiers were optimal because of their relatively small size, low noise, and high speed.
- Second Stage Amplification: Amplified pulses from the Pre-Amplifiers are transported ~20 ft along a twisted pair cable to N-277 amplifier cards[67]. These cards[8] provided a second level of amplification and pulse shaping. This amplifier produces a "time over threshold" ECL output pulse, with a maximum width of 45 ns. The threshold was tunable from an external ADC, and was tuned for optimal signal/noise discrimination.
- Latching and Readout: Signals from the N-277 cards were driven through a ~50 ft twisted pair cable into N-278 latches[67]. The latches[9] provided a pre-programmed delay of ~600 ns, during which time the pretrigger decisions were being made. If the leading edge of the delayed pulse fell within the 100 ns load pulse generated by the pretrigger, the data was latched, and subsequently loaded into a 32 bit register. The latched data was held until a final trigger decision was made. If the event satisfied the trigger, a READ pulse was sent to the N-280 crate controller, and the data was read out serially from the CAMAC system to an N-281 interface unit[10]. The N-281 transferred the data to the PDP-11, where it was stored until it was concatenated with the data from the other subsystems. The final step was that the

---

[7] MIP is short for a *minimum ionizing particle.*

[8] Each card contained 16 channels.

[9] Each latch contained 32 channels.

[10] Transmission occurred along a RS-422 data bus.

trigger sent a RESET signal to the CAMAC system, which readied the system for the next event.

2.5 Dipole Analysis Magnet

The dipole analysis magnet was used in conjunction with the upstream and downstream tracking chambers to measure the momentum of charged tracks. The analysis magnet was ~241 cm in length, and was centered ~210 cm downstream from the target center. The PWCs and STDCs were located just downstream of the analysis magnet, and the SSD system just upstream. Charged tracks which passed through the magnetic field bent along the arc of a circle whose magnitude and direction yield the momentum and charge of the particle respectively. The magnet current was set to ~1050 Amps, which corresponded to a field strength of ~6.24 kG. Given this operating current, charged tracks received an impulse[11] (or p_T kick) of ~450 MeV/c. The dipole field within the magnet was oriented along the Y direction, but small fringe fields at the upstream and downstream ends resulted in a small B_z component to the magnetic field. Thus, bending occurred primarily in the XZ plane, while in the YZ plane, the trajectory was almost unchanged[12].

2.6 Proportional Wire Chambers (PWC)

The PWC system was the first component of the downstream charged particle tracking system located just downstream of the analysis magnet. It was used to provide a spacial measurement of the charged tracks' parameters downstream of the dipole magnet. In order to achieve 3D space tracks, the PWC featured 4 independent views, with 4 PWC planes in each view. The 16 planes were arranged in 4 modules, with each module housing one plane of each view. The planes within

[11] By Impulse (I), we mean the integral of the magnetic field (B) over its length (l), i.e. $I \sim \int B \cdot dl$.

[12] See Chapter 3 for more details.

the module had the wires oriented at the angles $-90°$ (X view), $0°$ (Y view), $37°$ (U view), and $-53°$ (V view). Thus, the X and Y views were orthogonal to one another, as were the U and V views. An exploded view of a single module is shown in Figure 2.4. The modules were spaced by $\sim$1 m from one another, so that the PWC system spanned about 3 meters along the beam axis. Each plane consisted of an array of .8 mil gold plated tungsten wires, sandwiched between 2 graphite coated[13] cathode planes. The spacing between adjacent anode wires was 0.1 in, while the anode to cathode spacing was .226 in. The cathode planes were placed at a high negative voltage $\sim$2800 V, while the anodes were kept at ground, establishing the intense electric field needed for operating the chamber for charged particle detection. The cathodes were segmented into 3 electrically independent regions; the beam region, the diffractive region, and the main region. The small, high intensity beam region was desensitized by dropping the voltage to the cathode by an amount proportional to the current draw at that point. For high intensity running, the beam region efficiency was $\sim$20 %, while the remainder of the chamber provided an efficiency of $\sim$90-100%.

The PWC chambers were operated with a gas mixture of 79.7% argon, 18% isobutane, 1.1% isopropyl alcohol, and .1% alcohol. The ionized argon atoms provided the bulk of the free electrons, while the other components were added to absorb secondary photons and electrons emitted as the positive argon ions were neutralized[68].

The 16 planes had a total of 13,440 fully instrumented wires. Each wire provided a measurement resolution of $\sim$750 μ, so that the angular resolution of the PWC system was $\sim$.30 mrad. As with the SSD system, the instrumented region increases in size as we move downstream in order to maintain uniform acceptance. Table 2.5 gives the geometrical parameters of the PWC system. The readout of the chamber was provided by the Nanometric system as described previously in

[13] 1 mil in thickness.

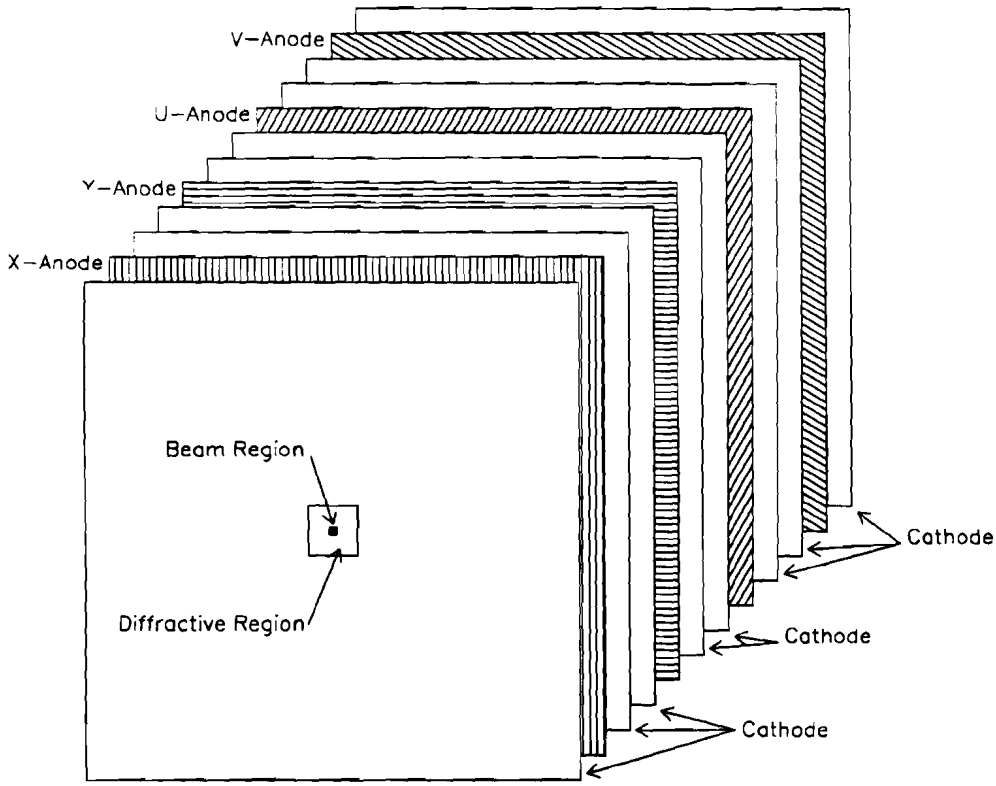

Figure 2.4 Schematic representation of a single PWC module.

conjunction with the SSD readout. For technical details regarding the design and operation of the PWC system, the reader may consult the references[68, 69].

2.7 Straw Tube Drift Chamber System (STDC)

The straw tube drift chamber system was installed prior to the 1990 data run[70]. The primary reasons for this addition was to improve the linking accuracy between the downstream and upstream (SSD) systems, as well as improve the momentum determination of the charged tracks. In order to have the downstream and upstream systems achieve comparable resolution, 2 straw drift chamber stations were added to the downstream system. The first station was located between PWC's 1 and 2, and the second station was situated just downstream of PWC 4. Each station consisted of 1 X module and 1 Y module, and each of these modules was comprised of 4 planes of drift tubes. A straw plane was composed of an array of drift tubes, aligned either vertically (X planes) or horizontally (Y planes). The individual drift tubes were made of 150μ thick mylar cylindrical tubes, with the inner surface being coated with 8μ of aluminum. The anode wire, which ran along the axis of the cylindrical tube, was made of 20μ gold-plated tungsten. Each anode was operated at $\sim$1800 V, while the aluminum inner wall was maintained at ground. The chamber was operated with a gas mixture of 50% Argon + 50% Ethane (bubbled through isopropyl alcohol at 0° C) at atmospheric pressure. As a charged particle passed through the straw tube, the ionization electrons produced in the field *drift* toward the anode, so that a current is generated. Signals were amplified and discriminated by nanometric N-277 cards, and subsequently driven through $\sim$23 ft of twisted pair cable to associated TDC's[14]. The time yielded by the TDC's was mapped into a distance via a *drift time to distance* relationship, which established the radial distance of the hit from the wire as a function of the measured time (see Figure 2.5). Due to the nature of this device, each time measurement yielded 2 legitimate solutions (hits),

[14] TDC is short for time-to-digital converter.

Table 2.5 PWC Geometrical Parameters

Module - View	Number of Wires	Angle (degrees)	Z Position (cm)
1 - X	640	-90.0	379.04
1 - Y	480	0.0	380.76
1 - U	704	-53.1	382.48
1 - V	672	36.9	384.20
2 - X	800	-90.0	472.30
2 - Y	800	0.0	474.02
2 - U	896	-53.1	475.80
2 - V	896	36.9	477.47
3 - X	800	-90.0	567.39
3 - Y	800	0.0	569.13
3 - U	896	-53.1	570.87
3 - V	896	36.9	572.61
4 - X	960	-90.0	660.13
4 - Y	960	0.0	661.90
4 - U	1120	-53.1	663.66
4 - V	1120	36.9	665.43

$$WP - R$$

$$WP + R$$

where WP is the wire's transverse position and R is the radius associated with the measured time. In other words, we only know the magnitude of the drift distance, but not the direction. This is frequently referred to as the *left/right ambiguity.* The staggering between planes was chosen to minimize the effects of the left/right ambiguity on track reconstruction, as well as maximizing the possible number of hits on a pair of tracks separated by less than 1 tube diameter. The measurement error on each hit was primarily a function of its TDC time. Figure 2.6 shows the hit resolution as a function of the measured TDC time. Since the spacing between the upstream and downstream stations was ~300 cm, the resulting angular resolution for a track reconstructed in the straw system was ~.06 mrad, which equilibrated the upstream (SSD) and downstream systems' contributions to the linking uncertainty. Table 2.6 gives the relevant geometrical parameters for the 16 straw planes.

2.8 Liquid Argon Calorimeter (LAC)

The LAC consisted of two sections, an electromagnetic section (EMLAC) and a hadronic section (HALAC). The EMLAC was used to measure photons' energies and positions, as well as forming the basis for the trigger system as described earlier. The HALAC, located just behind the EMLAC, was used to measure the energy and position of high energy hadrons. Both the EMLAC and HALAC resided in a large stainless steel cylindrical cryostat[15], which contained the ~17,000 gallons of liquid argon (see Figure 2.7). The argon served as the active material in both the electromagnetic and hadronic sections. A large, low density filler vessel[16] was placed at the upstream end of the calorimeter (*front filler vessel*) in order to reduce

[15] The cryostat had a diameter of 17 feet and was 21 feet deep.

[16] This vessel was made of Rohacell encased in 1.6 mm stainless steel.

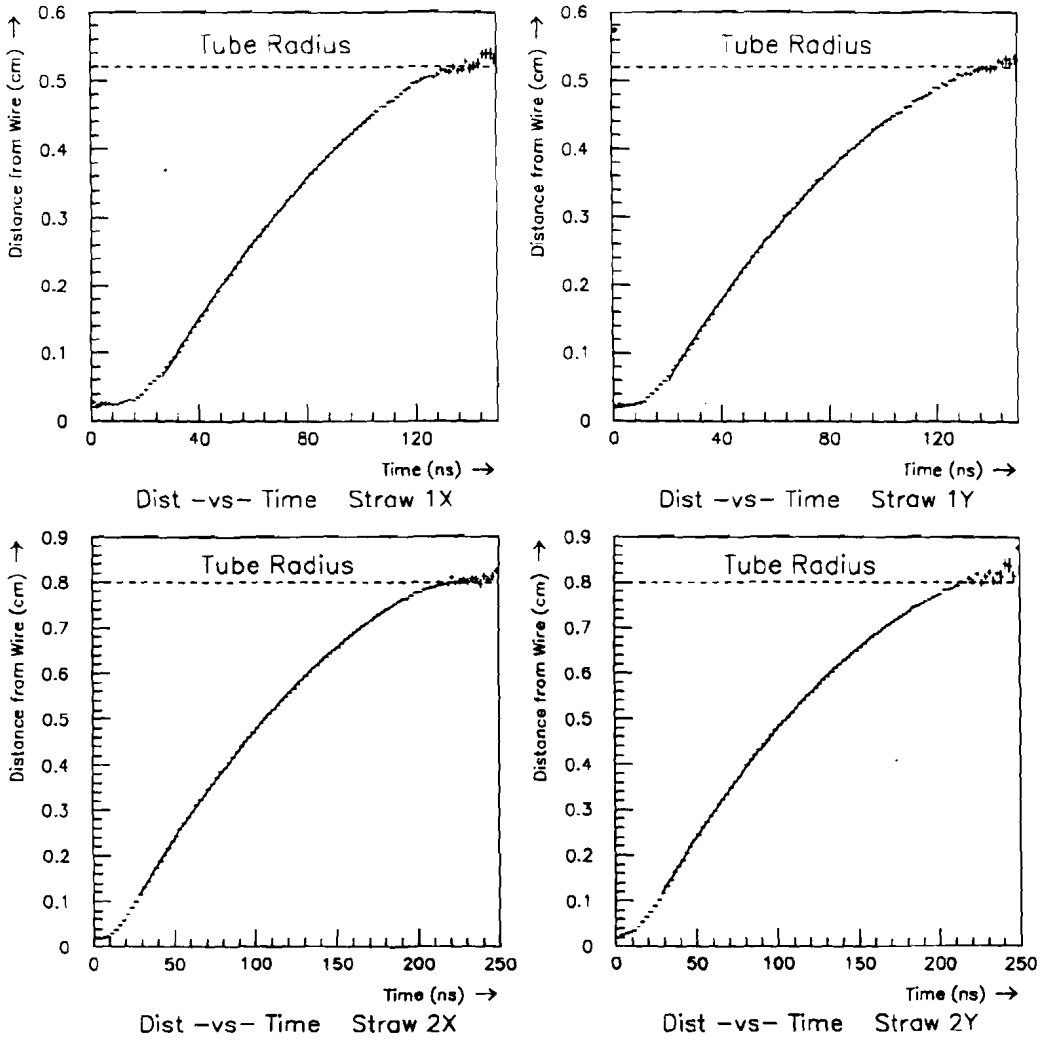

Figure 2.5 Time to Distance relations for each of the 4 straw modules.

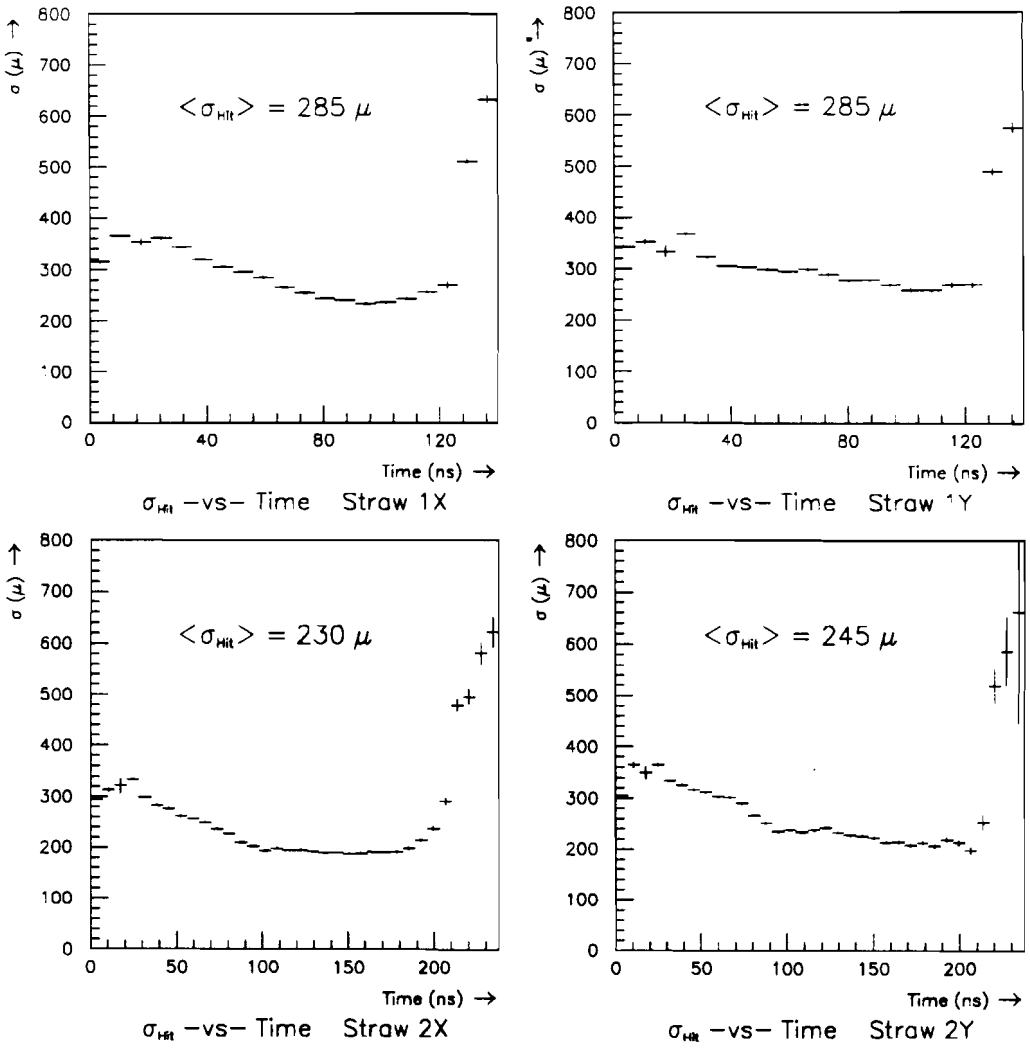

Figure 2.6 Single straw hit resolution as a function of the TDC time for the 4 straw modules.

Table 2.6 Straw Geometrical Parameters

Module - View	Number of Wires	Tube Diam. (cm)	Z Position (cm)
1 - X	160	1.039	426.18
1 - X	160	1.039	427.08
1 - X	160	1.039	428.08
1 - X	160	1.039	428.97
1 - Y	128	1.039	433.97
1 - Y	128	1.039	434.86
1 - Y	128	1.039	435.86
1 - Y	128	1.039	436.76
2 - X	160	1.590	743.92
2 - X	160	1.590	745.33
2 - X	160	1.590	746.98
2 - X	160	1.590	748.39
2 - Y	160	1.590	750.34
2 - Y	160	1.590	751.76
2 - Y	160	1.590	753.41
2 - Y	160	1.590	754.82

the amount of showering of electromagnetic particles prior to reaching the active region of the EMLAC. A second filler vessel (*beam filler vessel*) [17] was inserted through the 20 cm radius hole in the central area through which the beam passed, in order to reduce the effects of beam particles interacting within the beam hole and splattering the LAC. The signals from the calorimeter's strips/cells were read out through through the top (cap) of the cryostat, where a Faraday room was constructed which shielded all the electronics from external noise. The entire LAC was supported by a system of I-beams (called the Gantry), which had the flexibility to move transversely to the beam as deemed necessary. Figure 2.7 shows a cutaway view of the gantry.

2.8.1 ElectroMagnetic Liquid Argon Calorimeter (EMLAC)

The EMLAC resided ~900 cm downstream of the MWEST target and had an inner radius of ~20 cm and an outer radius of ~1.6 meters, thus providing angular coverage from ~22 mrad to ~178 mrad. The calorimeter utilized a polar geometry with respect to the beam axis, making r-ϕ the natural coordinates of the EMLAC. The ϕ-coverage was sectioned into 4 independent, but similar quadrants, with each quadrant having 33 cells (~30 radiation lengths) along the beam axis. Each cell consisted of an R layer and immediately after, a ϕ layer. The R layer consisted of a 2 mm thick lead absorber sheet, a 2.5 mm liquid argon gap, a 1.6 mm double-sided G-10 readout board (R strips), followed by a second 2.5 mm argon gap. The ϕ layer was similar, except that it employed ϕ strips on the G-10 readout board instead of the R strips. See Figure 2.8 for an exploded view of the EMLAC. The choice of lead was made because of it's small radiation length, but large interaction length. This means that electromagnetic showers should develop early, while hadronic showers

[17] This vessel was composed of a 3.2 mm thick stainless steel pressurized with helium gas.

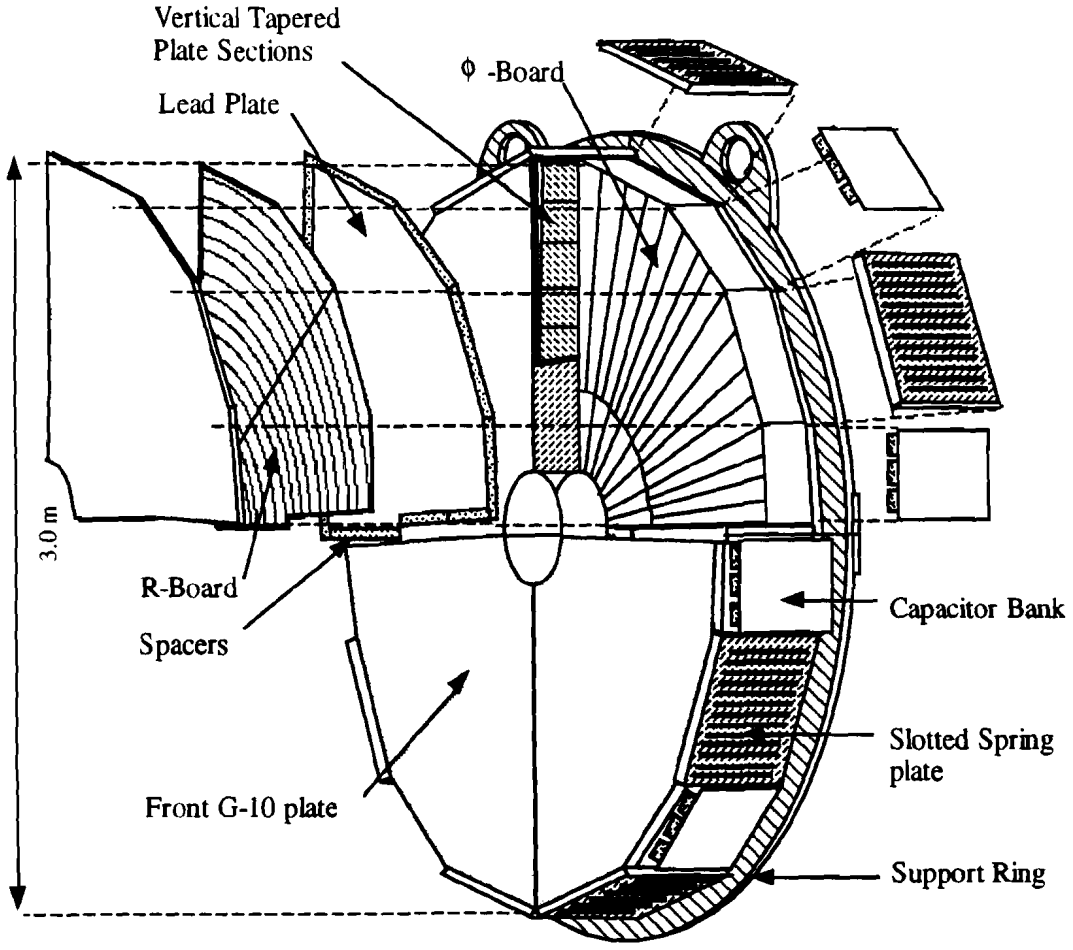

Figure 2.8 Exploded view of the EMLAC.

measurements provided the ability to measure the incident direction (*directionality*) of a particle. This was particularly useful for identifying muons off-line which leaked through the on-line muon veto wall system. The resolution (σ_E/E) of the EMLAC was $\sim 15\%/\sqrt{E}$, with E being the energy in GeV/c.

As alluded to earlier, the EMLAC formed the basis for the trigger system. The signals from the front and back sections were added together to form the trigger p_T sum. The ϕ strips were not used in the trigger, and the R strip energies were doubled to account for the p_T contained in the ϕ strips. It is quite important to note here that the trigger used only the EM depositions which occurred in the EMLAC, and **not** the HALAC. The second half of the LAC, the HALAC, is the subject of the next section.

2.8.2 Hadronic Liquid Argon Calorimeter (HALAC)

The HALAC was used in E706 to make a calorimetric measurement of the energy and position of charged and neutral hadrons. The latter of the two could not be measured in the charged particle tracking system, so this could add additional information for doing the E706 jet analysis.

Hadrons incident upon the LAC encountered ~2 interaction lengths from the EMLAC and 8 interaction lengths from the HALAC. The HALAC was composed of 53 layers, with each layer made of 2 similar cells arranged back-to-back to one another. Figure 2.9 shows an exploded view of a HALAC cell. On each side of the cell, there was a single-sided copper clad G-10 anode plane oriented with the copper siding facing outward. On these anode planes were scribed horizontal rows of 11 cm high triangular ***pads***, with each row separated by a space which the readout lines and edge connectors occupied. The horizontal spaces left by the front plane were covered by the readout pads of the plane in the back half of the cell. Outside of the anode planes on each side were 3 mm argon gaps followed by high voltage (HV) planes. Finally, in front of each cell was a 1 inch steel plate which acted as the absorber for the HALAC. A front view of the hadronic calorimeter is show in Figure 2.10.

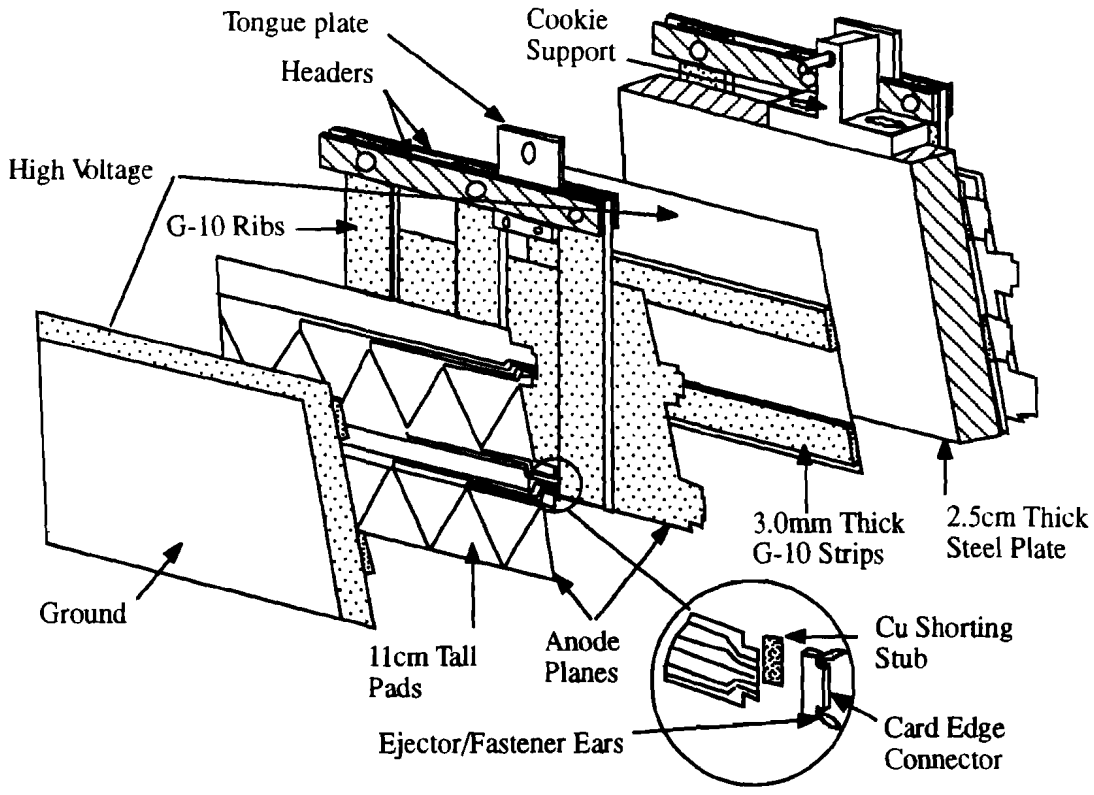

Figure 2.9 Exploded view of a HALAC cell.

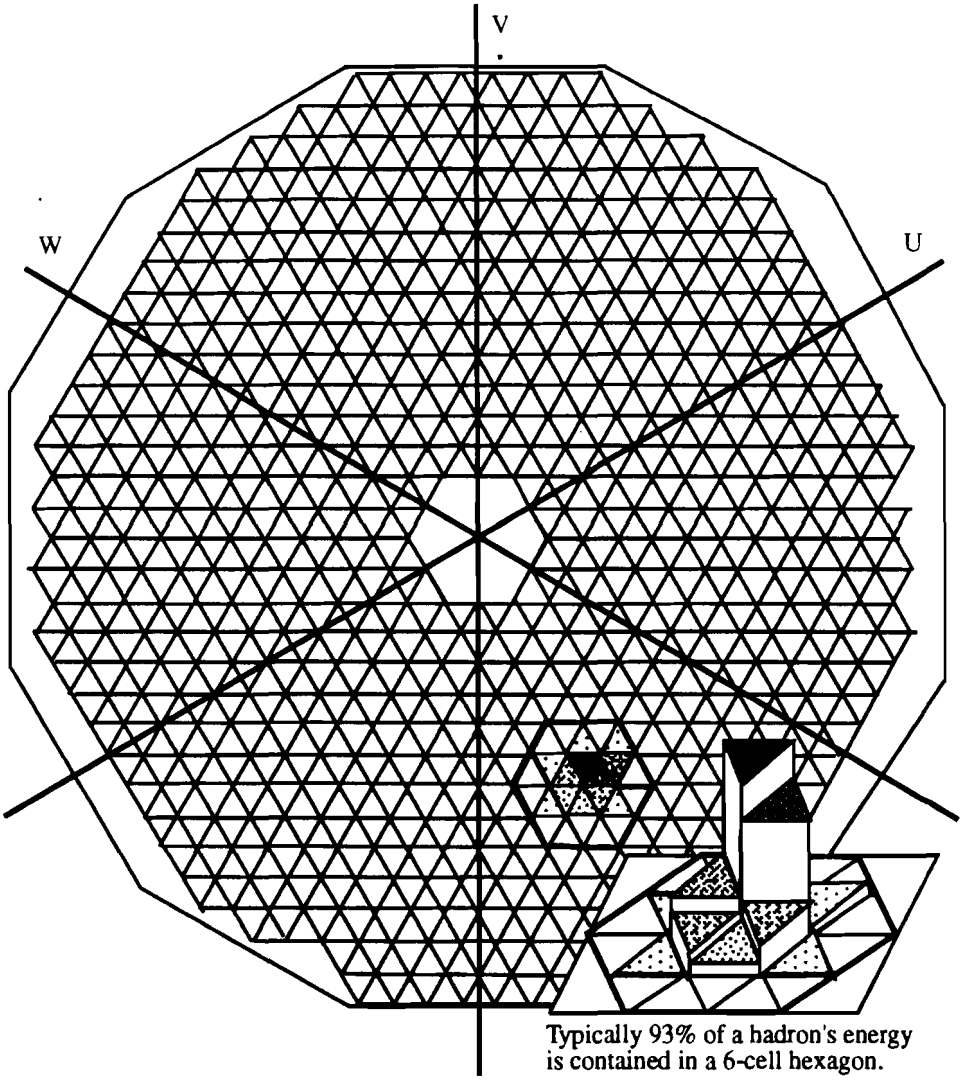

Figure 2.10 Face view of the hadron calorimeter.

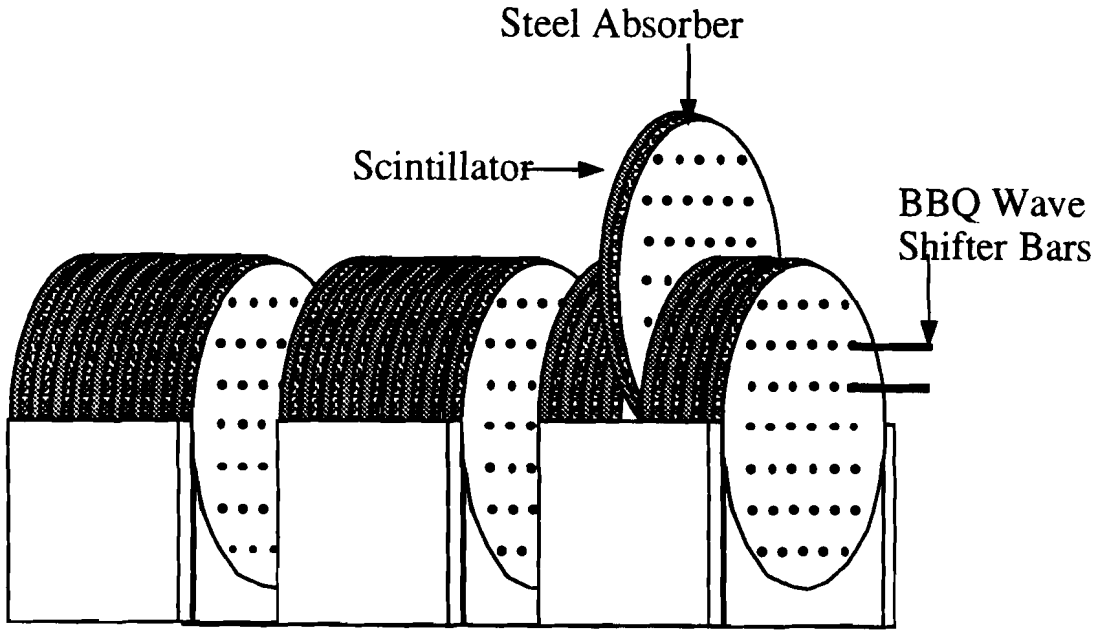

Figure 2.11 Schematic view of the forward calorimeter.

Chapter 3 Event Reconstruction

3.1 Overview

The master program used for the reconstruction of the data and Monte Carlo events, was called MAGIC [75]. MAGIC was written in FORTRAN-77 and utilized the dynamic memory data structures provided by ZEBRA [76]. The dynamic memory management of ZEBRA allowed the user to construct variable size data structures which could be easily manipulated, providing for efficient usage of the computer's memory. Futhermore, ZEBRA allowed the data banks to be written out in a machine independent format, i.e. zebra exchange.

MAGIC fully controlled the flow of the data, from input to output. In particular, MAGIC (a) read in events, (b) called the reconstruction packages as instructed by the user, and (c) wrote out selected events. MAGIC was flexible enough to read in data that was written in several formats, including binary (as from the raw data tapes), and zebra exchange (as in the case of MC data or unpacked raw data previously written out by MAGIC). MAGIC interfaced to all six reconstructors, each of which could be run independently of one another. The user instructed MAGIC as to which reconstructors were to be run via input control switches. The event reconstruction packages involved unpacking the raw data as well as reconstructing the physical parameters of the particles. If only unpacked data was required, the user had the option to turn off any of the reconstructors, while still running the corresponding unpacker. This provided an essential time savings when the full reconstruction was not necessary. Finally, one had the choice to write out any particular event in a machine independent format, such as zebra exchange. Run dependent variables were input into MAGIC via control cards, which designated the run dependent conditions i.e. number of events to process,

which unpacker/reconstruction packages to execute, etc., as well as event level cuts used in the reconstruction packages. The program provided several entry points ("hooks") where the user could interface with MAGIC in order to perform various operations, i.e. histogramming, skipping events based on available information, setting counters, etc. For example, one of the most useful of these hooks was USREV, which was called by MAGIC after all the designated reconstructors had been called. This allowed for initial studies of the hardware (detector) and software performance prior to the SGI reconstruction pass (see below).

The six reconstruction packages called from MAGIC were,

- PLREC - Reconstruction of charged tracks and associated vertices;
- EMREC - Reconstruction of showers' energy and position as detected in the EMLAC (A more detailed description is given in references [77, 55, 78]);
- DLREC - Reconstruction of trigger and Cerenkov logic (A more detailed description is given in reference [60]);
- HCREC - Reconstruction of the showers' energy and position as detected in the HALAC (See reference [73]);
- FCREC - Reconstruction of the forward energy in the event (See reference [74]);
- MUREC - Reconstruction of charged tracks (muons) in the E672 muon spectrometer (see [57],[58]).

For the main line reconstruction, all of the E706 raw data events[1] were processed with all the unpackers and reconstructors turned on. The processing was performed on the SGI farms developed at Fermilab. The SGI farm utilized 1 I/O node and $\sim$ 10 worker nodes (CPU's). The I/O node was responsible

[1] E672 data, residing on the same raw data tapes as the E706 data, were skipped over during the SGI farm processing.

for shipping the data events to the worker nodes where the event would be reconstructed. After the worker node was finished with the reconstruction ($\sim$ 1 sec/event), the reconstructed event was passed back to the I/O node, and was subsequently written out. For the processing of the 1990 data, E706 usually had 2-3 SGI farms at its disposal. The results of the processed data events were written in the form of compressed Data Summary Tapes (DST's). The DST's contained all of the information deemed necessary to carry out the desired physics goals of the experiment. Much of the unneeded raw information was dropped prior to writing the DST, so that reading and analyzing of the DST would be very fast.

The remainder of this chapter is devoted to a description of the reconstruction packages used in this thesis. Since PLREC was used extensively for this thesis, a detailed description will be given. The reader may refer to the references for more details on the other reconstruction packages.

3.2 PLanes REConstruction (PLREC)

PLREC was the software package used to reconstruct the charged tracks and their associated vertices. All of the relevant physics parameters were then calculated and loaded into appropriate ZEBRA banks. In this section, a detailed description of the key elements of PLREC are presented. These main elements are, the beam tracking, PWC tracking, straw (STDC) tracking, SSD tracking & linking, vertex finding, relinking, and secondary vertex finding. Each shall be presented in the order in which the reconstruction was performed.

3.2.1 Beam Tracking

The beam tracks provided a measurement of the slope and intercept of the incident beam particles. The beam tracks were used in several ways. Since the beam track was a high momentum particle of mean momentum $\sim$ 515 GeV/c, the multiple scattering in the beam chambers was small, and hence it enhanced the transverse resolution of the primary vertex. In addition, the beam tracks were used

to identify extraneous beam particles in the event, not participating in the hard collision. Furthermore, the beam track associated with the primary vertex was used in later stages of the analysis to improve the p_T measurement of the particles emerging from the interaction.

The beam tracking was carried out in two stages. In the first stage, only three hit tracks were considered. There were three passes made to get all of the possible three hit tracks[2]. In each pass, a different pair of chambers were chosen as "seed planes"[3]. A line was constructed between all pairs of hits in each of the two seed planes, and projected to the third ("search") plane. The closest hit was found, and if it resided within $\pm$ 75 μ (1.5 wire spacings) of the projected line, a least squares fit was performed. If the χ^2/DOF $\leq$ 3.0, then this track was accepted, and written out. All of the hits used on any 3 hit tracks were marked accordingly. In the second stage, two hit beam tracks were formed from the hits not used by 3 hit tracks. In order to reduce the number of combinations, the 2 hit tracks were required to have a slope of less than 2.0 mr[4]. This procedure was performed for each view independently. The two hit tracks were $\sim$ 20-25 % of the total reconstructed beam tracks. Figure 3.1 shows the transverse miss distance (impact parameter) of the primary vertex beam track to the reconstructed primary vertex. The closest beam track within 100μ was designated as the interacting beam particle which produced the event.

---

[2] One only really needs 1 set of seed planes to get all 3 hit tracks. Redundant tracks were removed from the 3 hit track list.

[3] Seed planes were a chosen set of planes with which to begin the view track finding.

[4] 1 mr = 1 milliradian.

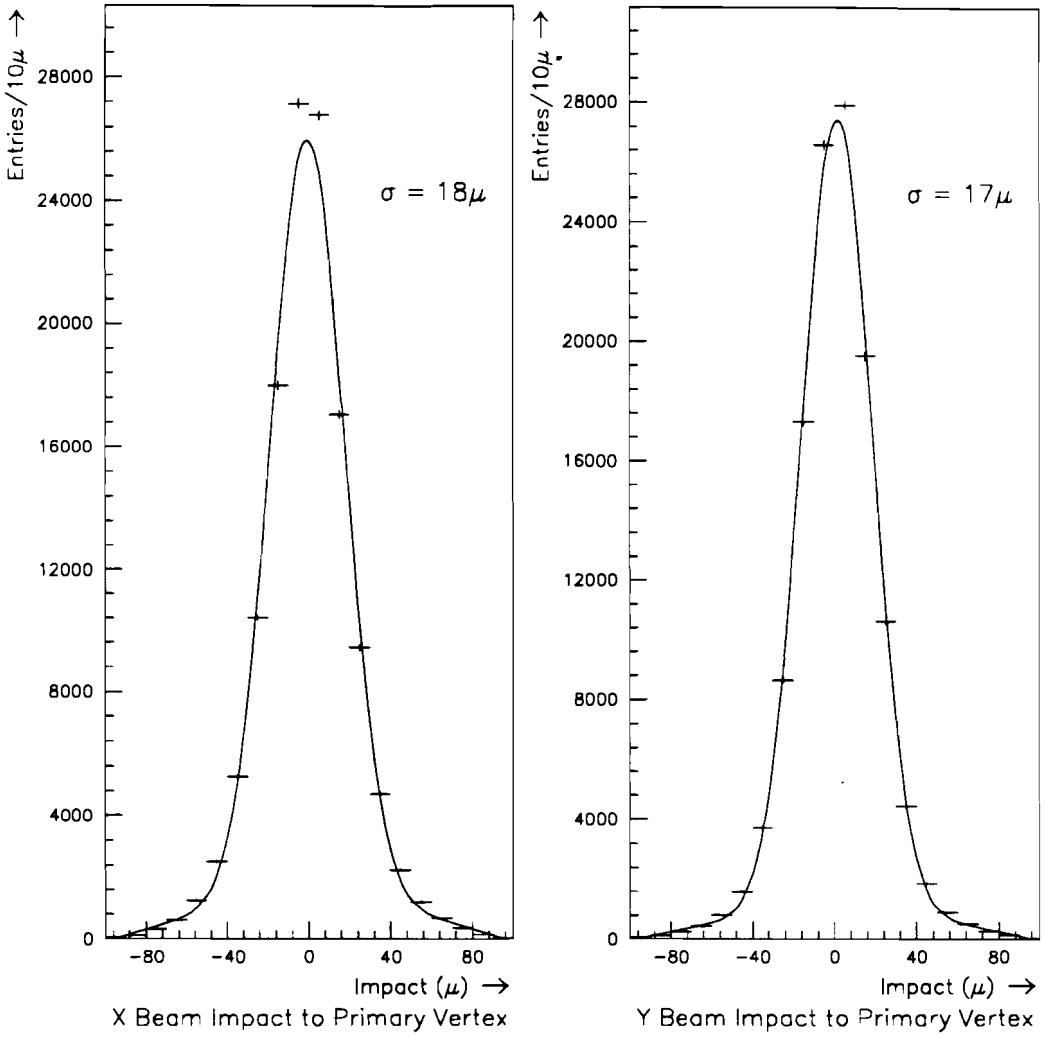

Figure 3.1 Impact Parameter of X and Y view Beam Tracks to Primary Vertex.

3.2.2 PWC Tracking

The PWC tracking made use of the 16 PWC's to produce 3-D space tracks downstream of the analysis magnet. This spacial feature of the PWC tracks was necessary for several reasons. Firstly, it was necessary to have all three direction cosines in order to measure the momenta (PX, PY, and PZ) of the charged tracks. Furthermore, this 3-D capability was necessary for correlating charged tracks with showers in the LAC (See Section 3). In particular, the identification of Zero Mass Pairs (ZMPs) from photon conversions played a key role in tuning the energy scale of the EMLAC. Finally, since the SSD and STDC systems consisted of only X and Y views, they relied on the PWC system to correlate the segments in one view with the other.

The reconstruction of the space tracks was fairly simple in spirit. The reconstruction followed an iterative procedure, with each successive iteration being fairly similar in sequence. In each iteration, the common features were, (a) the view tracking, and (b) the space tracking. View tracking was performed first, and the space tracking was done afterwards. The motivation for using this iterative approach was to improve the reconstruction efficiency, particularly for the complicated events. In the final iteration, the reconstructor searched for very wide angle tracks which just passed through the first two PWC stations. We now describe the main facets of the PWC tracking program.

4 Hit View Tracking

The 4 hit view tracking required only 1 set of seed planes since all 4 planes in the view were required to have a hit. The outermost pair of planes in each view were assigned to be the seed planes, while the innermost pair was designated to be the search planes. A line was formed between all pairs of hits in the seed planes, and projected to the search planes. If each of the search planes registered a hit within 1.0 wire spacing of the projection, a least squares fit was performed. If the χ^2/DOF was below the accepted cut, the track was accepted. During the view tracking, each

accepted candidate was compared to all the previous 4 hit view tracks, to determine if it was part of a "track cluster". If any tracks shared 3 or more hits with this new track, it was deemed part of this track cluster. If the number of tracks in the cluster was 2, then only the lower χ^2 solution was kept. If the number of tracks in the cluster was 3 or more, then two tracks were kept. The two tracks kept were, (a) the one with the lowest χ^2, and, (b) the next best χ^2 solution which shared less than 3 hits with the first choice. The remainder of the tracks in the cluster were removed from the ZEBRA banks. The view tracking procedure was performed for each of the 4 views independently. The maximum number of view tracks in any view was restricted to 130. If this limit was reached, the tracking in that view was stopped and appropriate bits were set. This limit was reached during the 4 hit tracking in $\sim$ 2 % of all events.

3 Hit View Tracking

The 3 hit view tracking followed the 4 hit tracking, and proceeded in much the same way. The main difference was that in order to reconstruct all 3 hit possibilities among 4 planes, one is required to have 2 sets of seed planes. The sets were chosen to be planes 1 & 3 and 2 & 4. The search planes were the 2 planes that were not the seed planes. As a result of having only 1 constraint on 3 hit tracks, i.e. #DOF = 1, it was possible to construct a large number of 3 hit tracks in most events. For this reason, 3 hit tracks were allowed to share only 1 hit with the previously made 4 hit tracks. Just as with 4 hit tracks, a χ^2 cut was imposed on the 3 hit track candidates. The same clustering algorithm was applied to 3 hit view tracks as was to 4 hit tracks, the only difference being that a cluster was defined here as any 3 hit track which shares at least 2 hits with the new 3 hit track candidate. As before, three hit tracking was performed in each of the 4 views independently. If the limit of 130 view tracks (4 hit + 3 hit) was reached during the 3 hit tracking phase, a cleaning algorithm was employed to remove some of the larger χ^2 3 hit solutions which also shared hits with the 4 hit view tracks. After the cleaning phase, the 3 hit tracking picked up where it had left off. The 3 hit tracking concluded when all

possible solutions were tried, or when the 130 track limit was reached and all the 3 hit tracks passed the cleaning cuts. The view track limit was reached during the 3 hit tracking in ~5% of all events.

2 Hit View Tracking

The 2 hit tracking was a very special case as employed in the overall PWC tracking scheme. Only the first 2 planes in each view were used for making the 2 hit tracks. Since any 2 hits would make a satisfactory line, only a small subset of all 2 hit tracks were of interest. In particular, the algorithm was only looking for charged tracks which may have escaped the acceptance of the 2 most downstream PWC modules. In order to be able to apply tight constraints on the 2 hit tracks, the 2 hit tracking was done only in the X and Y views. In the X view, the 2 hit tracks were forced to miss PWC's 3 & 4, while in the Y view, the segment was required to point back to the target region. The intention here was to reduce the losses of lower momentum tracks which were bent outside the full acceptance of the PWC system.

Space Tracking

The task of the space tracking was to combine the view track segments to form 3-D space tracks, i.e. correlate the X and Y segments with one another. Each of the X and Y view segments were paired together to define a hypothetical space track. By using the appropriate rotation matrix, a projection was formed in the U & V (search) views for this XY combination. If this XY combination was the true 3-D matchup, then one should find hits along those projections in the U & V views. Due to the resolution of the X & Y view tracks, a window of 1.5 wire spacings around this projection was required in order to pick up all of the hits in the search views associated with that track. Since the U & V views were also orthogonal to one another, correlation of the U & V segments also sufficed for defining a 3-D space track. In light of this, a second pass was made in which the roles of the XY and UV views were interchanged. Most of the space tracks made in this pass were duplicates

of space tracks made in the XY matching phase. However, a fraction of the space tracks may be missed in the XY phase due to inefficiencies. Hence, one has the opportunity to improve the space track finding efficiency by also trying to correlate UV pairs as well. During the space tracking stage, each additional candidate is compared to all the previous space tracks. If any track shares 9 or more hits with the new candidate, the lower quality track was removed, i.e. the track with lower number of hits, or, in case of equal number of hits, the one with the larger χ^2.

In each iteration, view tracking was performed, and then it was followed by space tracking. We now describe the cuts used in each iteration with respect to the view and space tracking.

Iteration #1

The view tracking was performed as described above. In this iteration, χ^2/DOF cuts of 3.0 and 2.0 were imposed upon 4 hit and 3 hit view tracks respectively. The space tracks candidates were required to have at least 2 hits in each of the search views, and a minimum of 13 hits in total. The χ^2/DOF cut was 2.0 for the 13 hit tracks, and 3.0 for space tracks with more than 13 hits. If a space track failed the χ^2 cut and there was more than the minimum number of required hits, the worst hit was removed and the track was refit. This procedure was repeated until the track passed the χ^2 cut and was accepted, or until the number of hits dropped below 13, in which case it was dropped.

Iteration #2

The second iteration was developed for two reasons. First, there were some loss of space tracks primarily due to inefficiencies in the 3 hit tracking of the first stage. Secondly, it was desirable to expand the charged particle tracking acceptance by reconstructing the space tracks passing only through 3 out of the 4 PWC modules. The outcome of the second stage was to increase the space tracking efficiency by $\sim$ 3-8 %, depending on the efficiencies of the chamber/readout system at that time.

Prior to beginning with this second iteration, all of the hits used on the "good" space tracks from the first iteration were removed from the pool of hits available for making new space tracks. The hits on suspicious tracks were not removed, so that those hits still had the opportunity to contribute to making other space tracks in the second iteration. Upon removing all of the aforementioned hits, one was presented with a fairly low multiplicity situation. Thus, most of the ambiguities present in the first iteration were not present in the second iteration. In light of this, several of the tracking cuts were made less stringent, in order to maximize the track finding efficiency in this iteration. The view tracking was performed with these remaining unused hits in much the same way as the first iteration, except that the χ^2/DOF cut for both 3 and 4 hit view tracks was increased to 4.0. The space tracking also proceeded in a similar manner to iteration #1. Again, the cuts were loosened to improve the track reconstruction efficiency. First, the minimum number of hits required was lowered to 11 for a track passing through all 4 PWC modules. However, for a track passing through only 3 PWC modules, the multiplicity requirement was reduced to 10 out of a possible 12 hits. Furthermore, the number of hits required in a search view was lowered to 1, but the total number of hits found in both search views had to be at least 3. The χ^2/DOF was required to be less than 2.0 for space tracks with 12 or more hits, otherwise it was set to 1.5. Just as before, any duplicates were removed as the space tracking proceeded.

If at any point[5] the number of space tracks exceeded a limit of 130, a cleaning routine was called to reduce the number of space tracks so that the remaining XY (UV) pairs could be tried. The decisions were based upon a **combination** of the following three characteristics: total number of hits, track χ^2, and Y impact parameter at the target center. The first two criteria should be fairly transparent. The last one perhaps requires some explanation. Since the magnetic field was almost completely in the Y direction, (small B_z fringe field), the change in the Y slope of

[5] This applies to both iteration #1 and #2.

a charged track from the Y view production angle was small[6]. As a result, the Y view projection of space tracks to the target center should usually point back to the production point within errors. Hence, space tracks with large Y view impact parameter at the target center provided another handle on track quality. However, since weak decays of some long-lived particles i.e. K^0, Λ, can occur substantially downstream of the production point, the reconstructed daughter products need not point back to the target. Consequently, the Y view impact parameter criteria was only used in conjunction with low number of hits and larger χ^2, in the cleaning routine. Figure 3.2 shows the Y view impact parameter at the primary vertex for all downstream tracks. The tails of the distribution are predominantly a result of low momentum tracks and weak decays of strange particles. There is also a contribution from fake combinatorial PWC tracks.

Iteration #3

The final iteration was tailored for the sole purpose of increasing the reconstruction efficiency for wide angle (and usually lower momentum) tracks. The class of tracks to be reconstructed in this last iteration consisted of tracks which were only in the acceptance of the first 2 PWC modules. Once again, prior to beginning the view tracking, all of the used hits from previously reconstructed space tracks were removed from the pool of hits to be used in this iteration. Since there was only 2 planes used in each view for the view tracking, further constraints were imposed on the 2 hit tracks. In the X view, if the 2 hit segment projected within the active volume of the straw chambers, a minimum of 2 straw hits were required to lie within 6.5 mm from the projection. Furthermore, the line was required to project outside the acceptance of the two most downstream PWC modules. In the Y view, the projection of the 2 hit track segment to the target center was required to fall within

[6] The small change in Y slope resulting from B_z effects was dependent upon the track momentum. For $p \geq\sim 10$ GeV/c, it was negligible on the scale of the angular resolution.

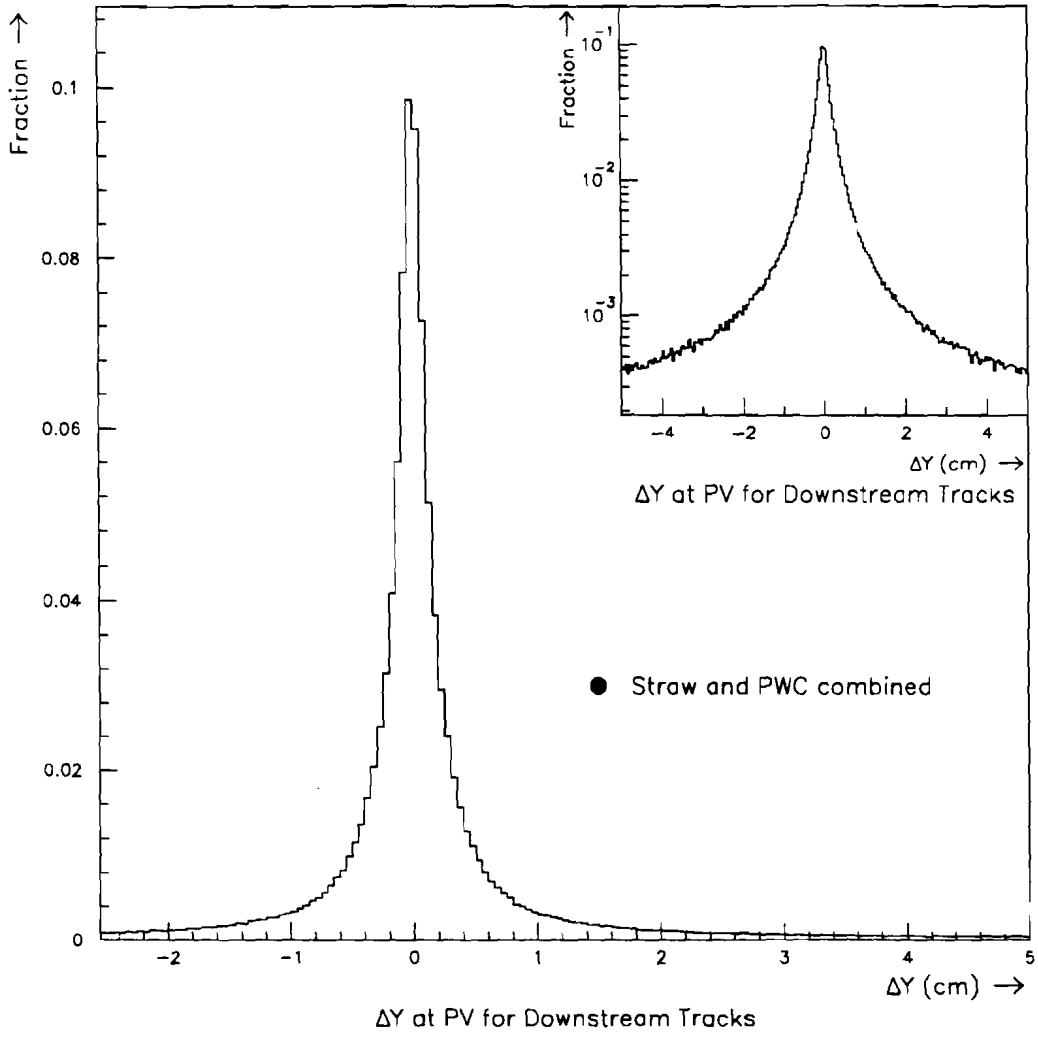

Figure 3.2 Y view impact parameter distribution of downstream space tracks at the primary vertex (PV).

a window of ± 4.5 cm. The X and Y view tracking reconstructed all 2 hit view tracks satisfying these cuts. No attempt was made to do similar 2 hit tracking in the rotated (U & V) views. Space tracks were formed as described previously. In finding these space tracks, it was required that there be at least 1 hit in each of the search views. If this was satisfied, a least squares fit was performed. For tracks having a total of 7 or 8 hits, the χ^2/DOF was required to be less than 1.2, whereas for 6 hit tracks, the cut was 1.0.

Figure 3.3 shows the number of reconstructed space tracks per event prior to the cleaning which occurred at the DST level (See Chapter 4). There is a long tail beyond 40 tracks per event, which is usually a result of having several spurious track solutions. At the DST analysis level, a cleaning routine was invoked to weed out these highly questionable tracks. Figure 3.4 gives the distribution of the number of hits on PWC tracks integrated over the course of the 1990 run. Given this hit distribution, one can show that the average PWC plane efficiency is $\sim$ 93-94 %. Figure 3.5 shows the χ^2 distributions for PWC tracks with various hit requirements.

3.2.3 Straw Tracking

The straw tracking provided an opportunity to improve the resolution of the space tracks downstream of the analysis magnet. The enhanced resolution of the straw chambers improved the quality of the charged tracking in two ways. As mentioned previously, the downstream tracks were used to correlate the X & Y view tracks in the SSD system[7]. Ideally, one would like that each downstream track match up with **one and only one** SSD track in each view so that correlation was trivial. However, since the number of possible PWC-SSD matchups was limited by the combined projection uncertainty of the SSD & PWC tracks, one was often presented with several choices, which yielded some level of ambiguity. This "window of uncertainty" was dominated by the intrinsic resolution of the

[7] Refer to the later section on SSD tracking and linking.

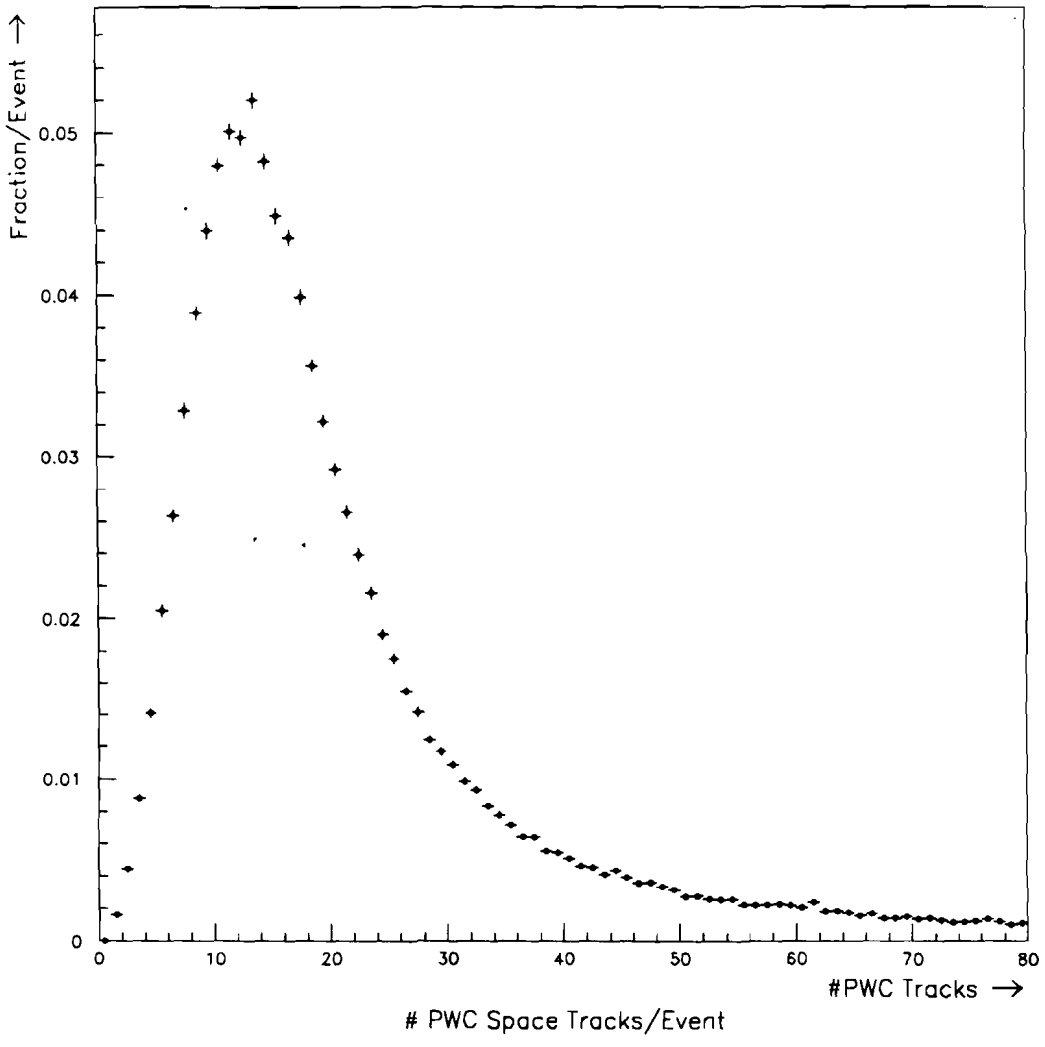

Figure 3.3 Distribution of the number of reconstructed PWC tracks per event.

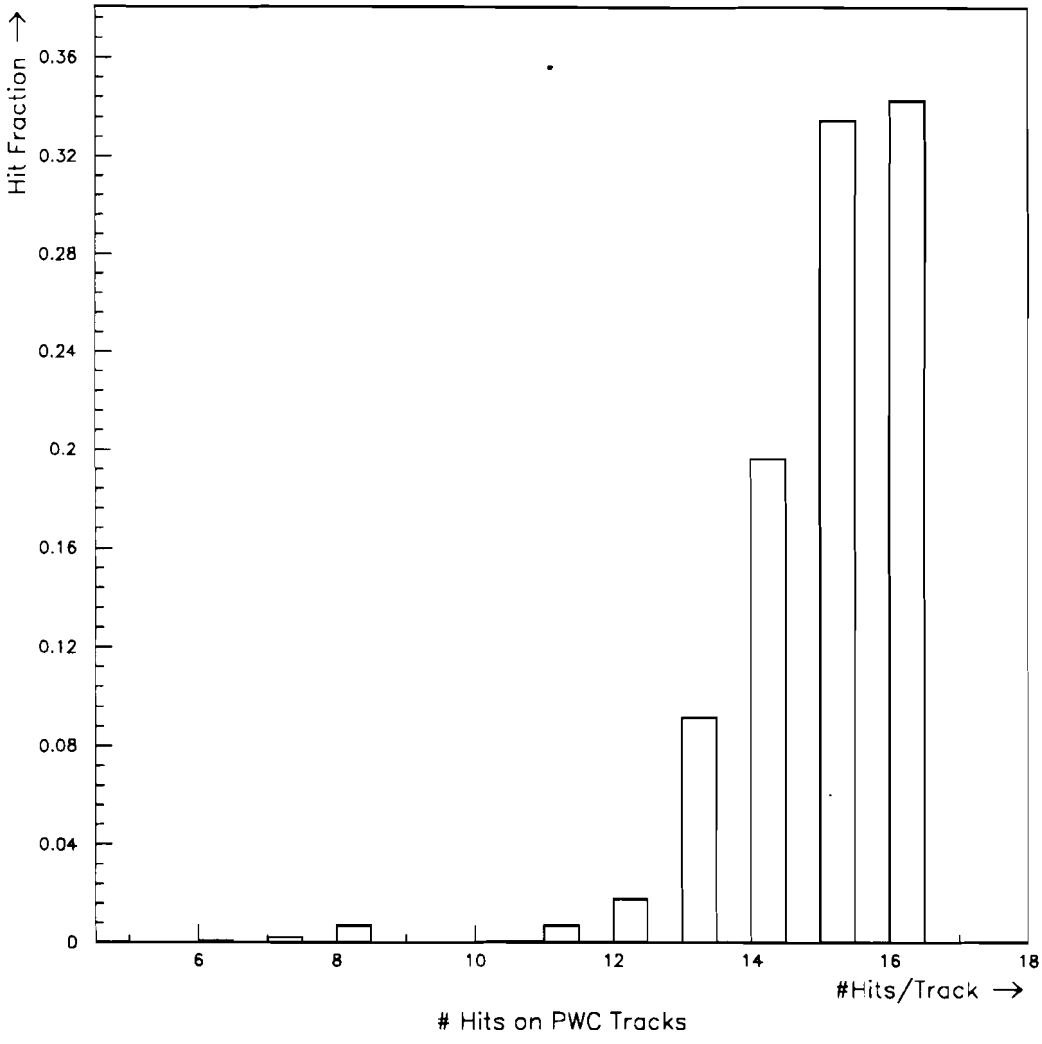

Figure 3.4 Number of hits on PWC physics tracks.

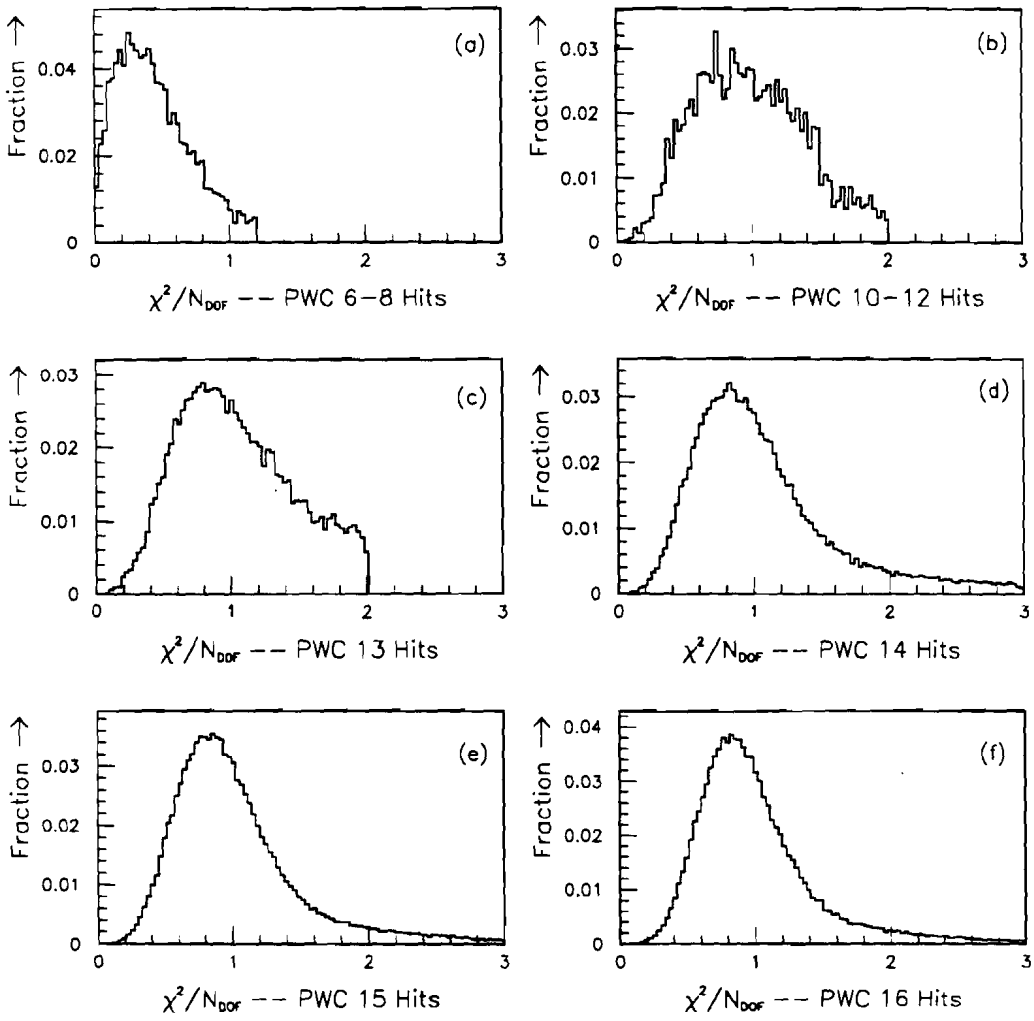

Figure 3.5 χ^2 distributions for PWC tracks with various numbers of hits.

PWC's. Implementation of the straw chambers allowed one to shrink this projection uncertainty by about a factor of 3X, making the upstream and downstream uncertainties comparable. Furthermore, the STDC/SSD momentum resolution was improved by about the same order of magnitude with respect to the PWC/SSD measurement. (See linking & momentum comparison plots.)

The straw tracking relied on there existing a predefined set of space tracks as found from the PWC system. As mentioned previously, the straw chambers were designed with XY geometry, and so it was necessary to use the PWC tracks to correlate the X and Y straw track segments. An iterative procedure to finding the straw tracks was adopted. In each successive iteration, the minimum number of hits required on a straw track was reduced in order to increase the overall straw track finding efficiency.

Each iteration was similar in structure. Within each iteration, there were 3 PASSES made in order to guide the reconstruction of the straw tracking. With each successive pass, the search window for straw hits from the estimated position was reduced, as the precision of the track segment improved[8].

In the first pass, the PWC tracks were used to assign the straw hits (and their mirror partners) in each plane to a particular space track. A search window of 3.5 mm was used to account for the PWC projection error to the straw planes. If any single hit was selected by two tracks, the hit was assigned to the track passing closest to the *straw tube wire*. This convention was adopted since only the earliest TDC time was kept. Consequently, the track passing closest to the wire was expected to be the proper choice. If the same hit was picked by 3 or more tracks, the hit was not assigned to any of the tracks. After the hits were assigned to the space tracks, each track was refit using only the straw hits, provided the number of hits

---

[8] The improvement was due to refitting the track segment using the straw hits during each iteration.

was above the set criteria for that iteration. The error associated with each hit was primarily a function of its TDC time[9]. After refitting the track, the ambiguous hits in each plane were also tried. The solution yielding the minimum χ^2 was deemed the correct choice.

This newly fitted track was used as input to the second pass. Since the straw hits improved the measurement of the track's parameters, the search window for straw hits was decreased to 1.3 mm. With this new search window, the straw hits were assigned to tracks in the same way as in the first pass. Because of the smaller search window, some of the hit ambiguities were resolved. Furthermore, by narrowing the search window, one imposes convergence of the forthcoming fit. As before, the track is refit with the set of straw hits chosen in this pass to determine a new track definition.

In the final pass, the search window was reduced to .8 mm with respect to the track made in pass 2. The hits were assigned as previously described. The tracks were refit for a final time to obtain the final set of straw track parameters for each initial PWC space track.

Depending on which iteration of the straw tracking one was in, different criteria was applied with respect to the number of hits required on the straw track. For each of the 4 iterations below, the aforementioned *3 pass procedure* was performed, so that each new iteration potentially added more straw tracks. In all cases, the resultant χ^2/DOF was required to be less than 3.0. The hit requirements are described below.

Iteration #1

In the first iteration, only the highest quality straw tracks were made. Each straw track candidate was required to have a minimum of 8 out of a possible 16 hits. Each view was required to have at least 4 hits, with at least 2 hits in both

[9] The mean straw hit resolution was $\sim 250\mu$.

the upstream and downstream modules. If the straw track satisfied these criteria, it was written out. Afterwards, the hits used on these straw tracks were marked, so not to be used in later iterations.

Iteration #2

In this iteration, the requirement that there be at least 2 out of 4 hits in a module was relaxed. The requirement was reduced to 1, but the criteria of 4 hits/view was still imposed. As before, the hits used in this iteration were marked, and were not used at later times in the straw tracking.

Iteration #3

Here, we begin to accept cases where we were not able to make both X and Y view straw track segments for a given PWC track. This may occur as a result of acceptance, chamber efficiency or hit ambiguities from overlapping tracks[10]. In this iteration, we try to make straw segments in the X view only. A total of 4 hits were required with at least 2 in both the upstream and the downstream modules.

Iteration #4

In the final iteration, we search only for Y view segments. The same hit requirements were imposed here as in the third iteration.

Upon completion of the straw tracking, one had available both the original PWC tracking results, as well as the STDC tracking results for each track. The overall success rate for finding straw tracks was dependent mostly upon the track density, i.e. the level at which several tracks are passing through a single tube. For most events, typically $\sim$ 75-80 % of PWC tracks had an associated straw track.

[10] Y view overlapping was more common than X view because the X view was the bend plane of the magnetic field.

For the final result, each downstream track was refit using both the STDC and PWC information. Since straw hits provided much better resolution, the results of the fit were dominated by the straw tube information. Figure 3.6(a) shows the χ^2/DOF distribution for all straw tracks. Figure 3.6(b)-(d) show the total numbers of hits for X and Y views added together, as well as individually. From Figure 3.6(b), one sees that $\sim$ 75% of straw tracks have both X and Y view segments. The lower mean number of number of hits in the Y view is attributed to the larger fraction of overlapping tracks. Recall that the Y view was the non-bend view. Figure 3.7 shows the difference in angle in the X and Y views as reconstructed in the PWC and STDC systems. The width of these distributions is dominated by the PWC angular resolution, and so that one observes that the PWC angular resolution is $\sim$ .35 mrad.

3.2.4 SSD Tracking and Linking

The SSD tracking system was used in several ways. First and foremost, the SSD tracks were used as input into the vertex finding algorithm to locate the interaction point (primary vertex). This was necessary since E706 used several types of nuclear targets in order to measure the dependence of the measured cross sections on the number of nucleons in the nucleus ("A dependence"). Furthermore, the SSD tracks improved the momentum measurement of charged tracks, since the bend angle was then measured on both sides of the analysis magnet. Finally, the SSD tracks were used for reconstructing secondary vertices in the events. Secondary vertices were a result of secondary interactions as well as from decays of unstable particles. The latter was used to study properties of strange, as well as charmed particles.

The SSD tracking and linking were merged together so that the SSD tracking could benefit from the external constraints provided by the downstream system. In particular, this was useful in rejecting spurious solutions arising from the combinatorial background. This background suppression was provided by the "linking" at the center of the magnet. Recall that the analysis magnet was a dipole

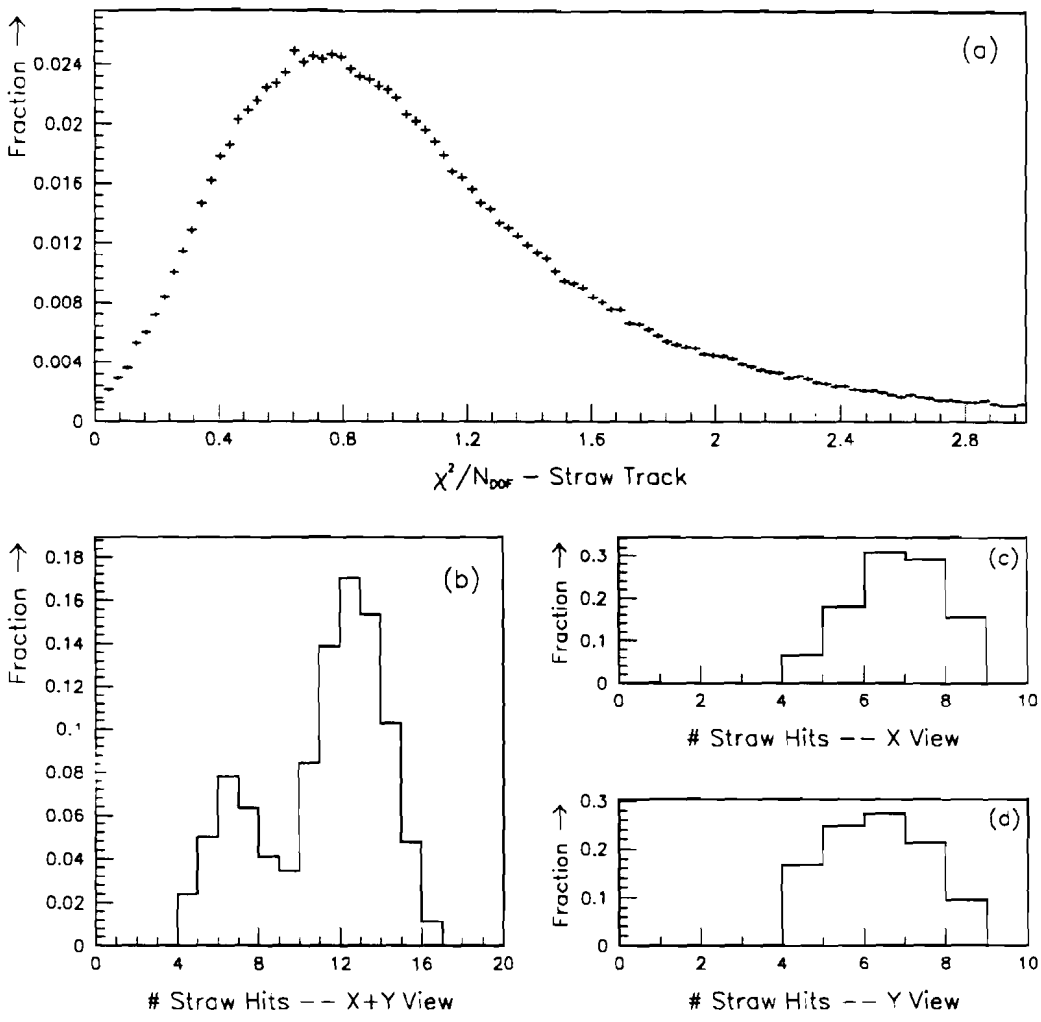

Figure 3.6 (a) Straw Track χ^2/N_{DOF}, (b) Total number of hits on straw tracks, (c) Number of X view hits, and (d) Number of Y view hits.

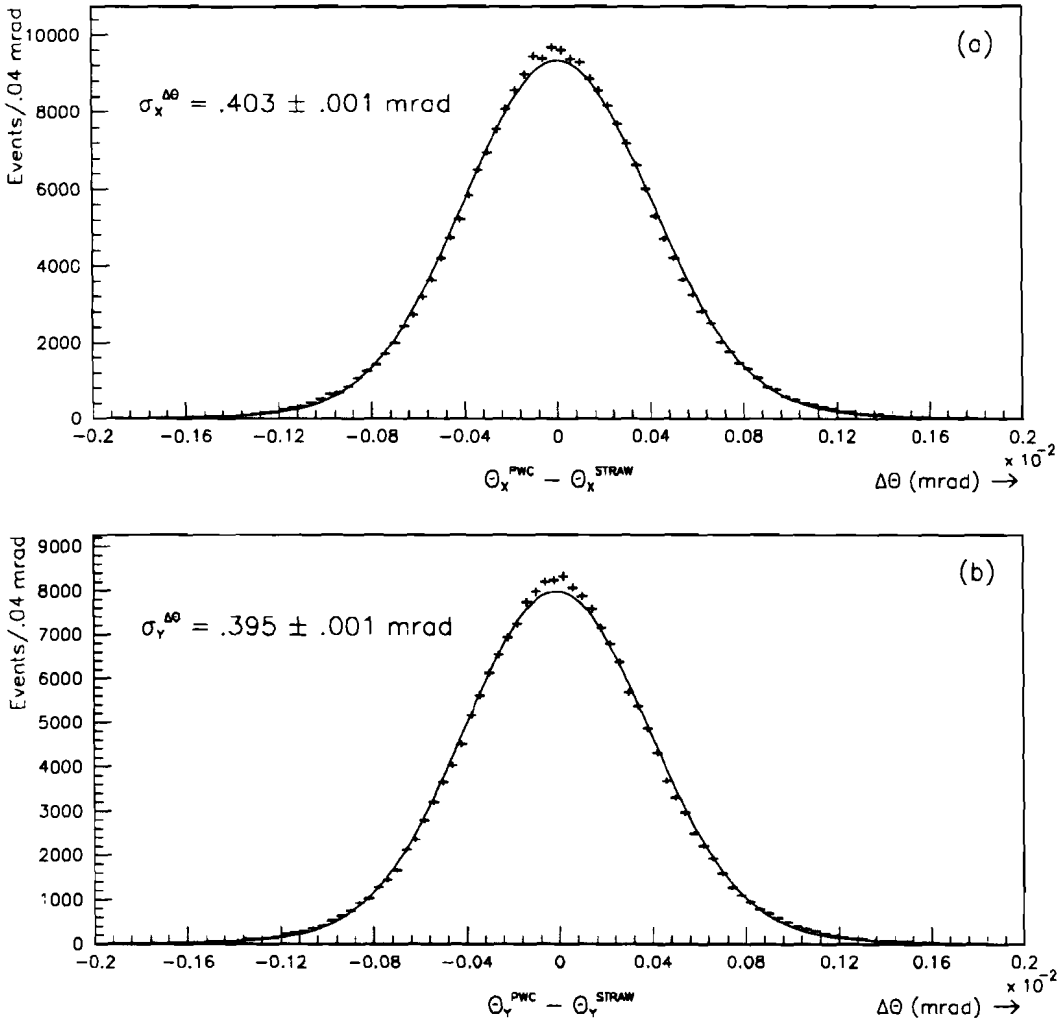

Figure 3.7 Difference in the angle as reconstructed in the PWC and STDC systems in the X and Y views.

magnet with its field oriented along the Y direction. Charged tracks traversing the magnetic field will receive an impulse proportional to the product of the field and its length, i.e. $I \sim B \cdot L$. To first order, one could apply the dipole approximation, and assume that the charged tracks underwent a single momentum kick at the effective center of the magnetic field. Consequently, it is expected that the projections of the upstream and downstream tracks should intersect near the effective center of the magnetic field[11]. Furthermore, since the field was oriented along the Y direction, there was only a very small change in the Y slope upon traversing the magnetic field[12] In addition, there is further broadening due to effects of the fringe fields at the upstream and downstream ends of the magnet. Corrections for both geometry and the fringe field were applied on a track by track basis to account for these effects[79]. The measured differences between upstream and downstream tracks at the center of the magnet were commonly referred to as ΔX, ΔY, and ΔYS distributions. ΔX and ΔY give the difference in projections at the center of the magnet while ΔYS gives the slope difference in the Y view between the upstream and downstream segments. As the momentum increased, the dipole approximation becomes better, and all three distributions narrow. Since prior to linking, the track momentum was not known, an estimate was made by assuming that the particles were produced at the center of the target, and then calculating the bend angle with respect to that point. For low momentum, the momentum estimate was quite good, but degraded as the momentum increased. However, for $p \geq \sim 20$ GeV/c, the linking resolution was fairly flat with momentum, so that the degraded momentum estimate did not change the linking window significantly. Gaussian fits were made to the ΔX, ΔY, and ΔYS distributions, and their widths plotted as a function

[11] Higher order corrections produce an intersection not exactly at the magnet mid-plane.

[12] Upon traversing the magnetic field, p_X changes, and therefore, so must p_Z (in order to conserve momentum). While p_Y is unaffected, the change in p_Z results in a change in the Y angle, since $\Theta_Y = p_Y/p_Z$.

of the track momenta. Figure 3.8, Figure 3.9, and Figure 3.10 show the widths of each of these distributions as a function of the estimated momentum for the PWC and STDC tracks. One observes the clear rise at low momenta which was a result of the multiple scattering and the departure of the field from being a perfect dipole. Furthermore, the plots show that the STDC-SSD linking resolution was significantly improved from the PWC-SSD measurement. These distributions were used to determine a "linking window" in which a SSD track must reside in order to declare that this SSD track was a legitimate link to a given downstream track.

The SSD tracking was carried out in two stages. In the first stage, the algorithm searched only for 4 and 5 hit tracks. In the second stage, a search for 3 hit tracks was performed with the unused hits from the first stage. The view tracking proceeded quite similarly to that described in the PWC view tracking. In the first stage, two sets of seed planes were required to reconstruct all of the 4 and 5 hit tracks. In the second stage, 4 sets of seed planes were required to get all of the possible 3 hit combinations.

In the first stage, all 5 and 4 hit track combinations satisfying χ^2/DOF cuts of 5.0 and 4.0 respectively were written out. Four and five hit tracks were allowed to share a maximum of 3 hits with each other. If any pair shared 4 or more hits, only the track with more hits was kept. In the case of equal numbers of hits, only the lower χ^2 solution was saved.

After reconstructing all of the 4 and 5 hit view tracks in both the X and Y views, a cleaning routine was implemented. The cleaning was based on the premise that a given track should not share many of its hits with *several* other tracks. For example, one does not expect a real 5 hit track to share all of its hits with 4 different 5 hit tracks. This is simply because most of the tracks emerge from a common point, and hence there should be minimal overlapping of tracks. Of course secondary interactions compromise this approximation somewhat, but the

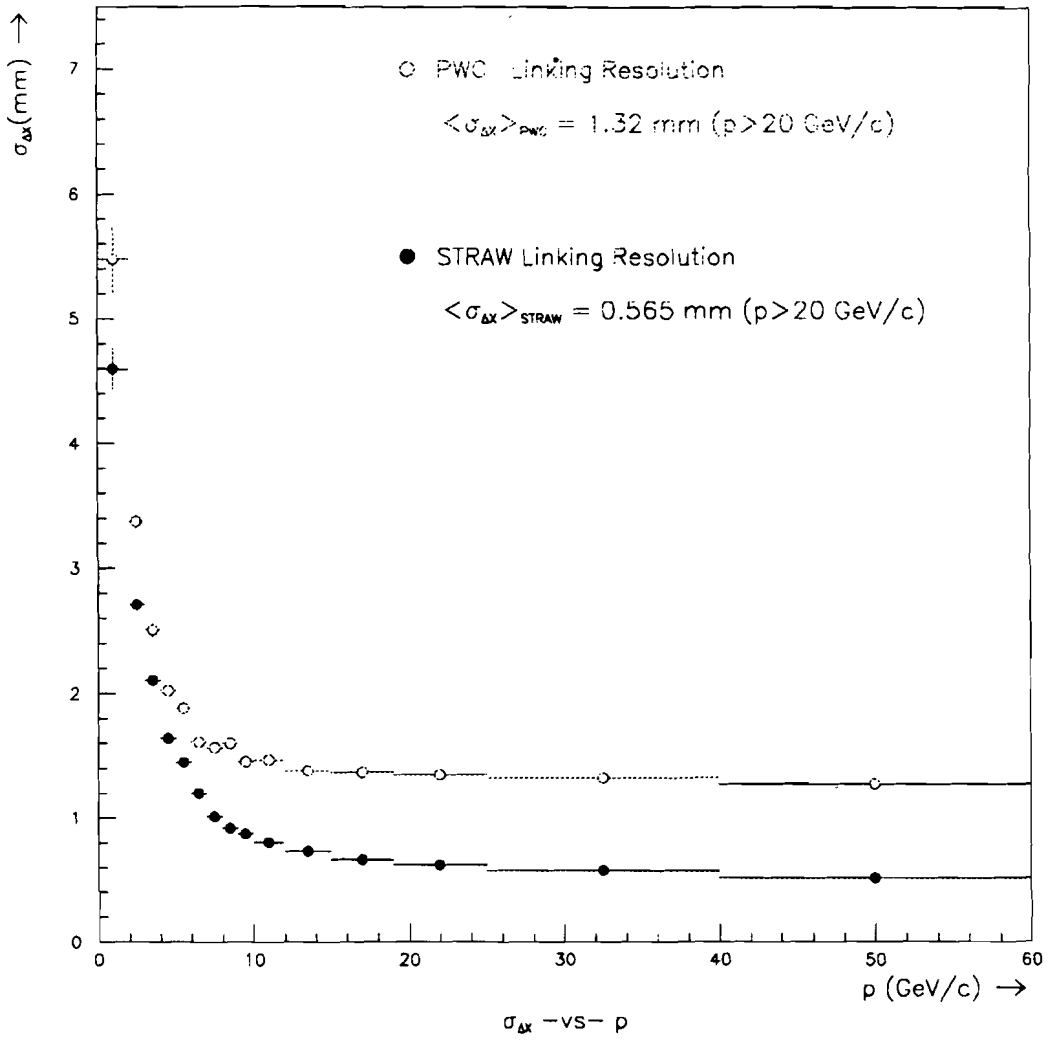

Figure 3.8 ΔX linking resolution as a function of the track momentum.

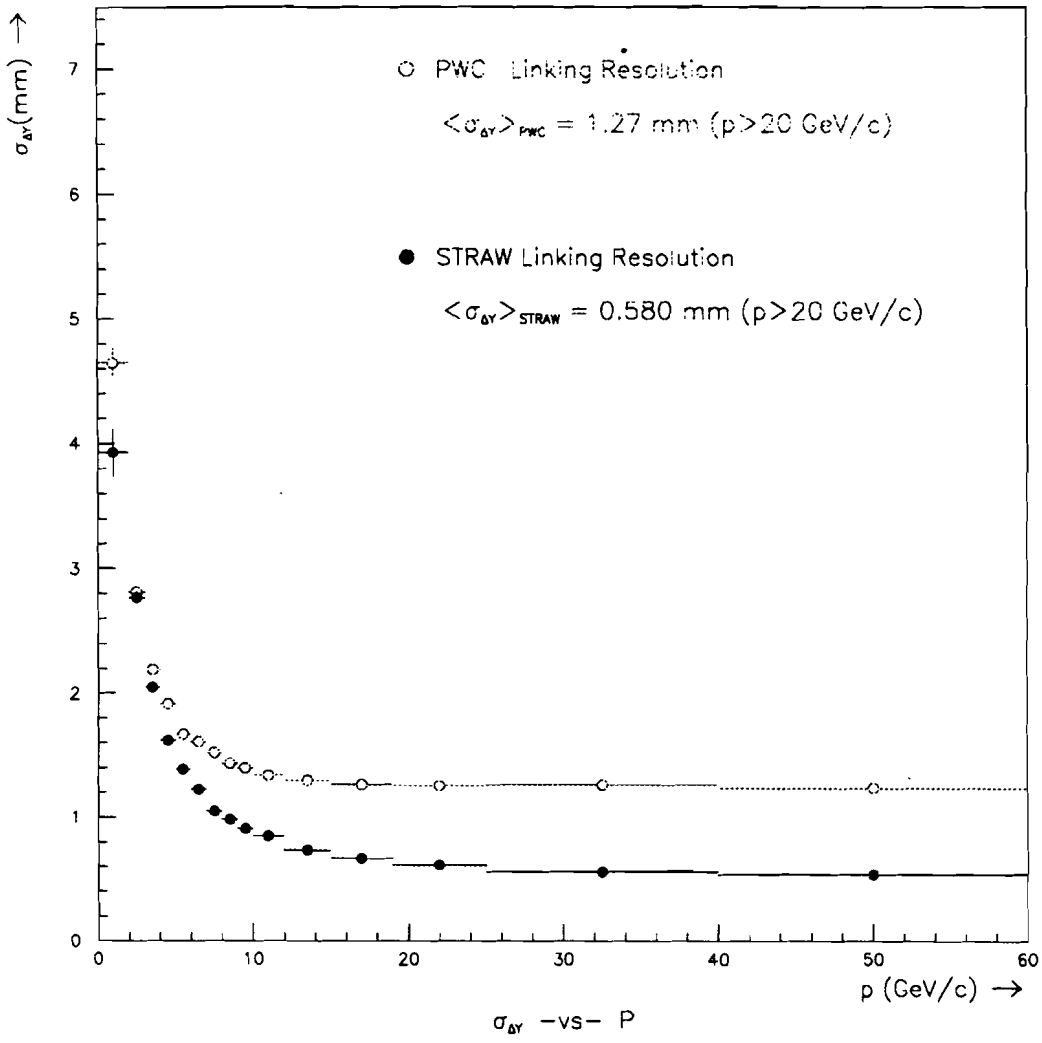

Figure 3.9 ΔY linking resolution as a function of the track momentum.

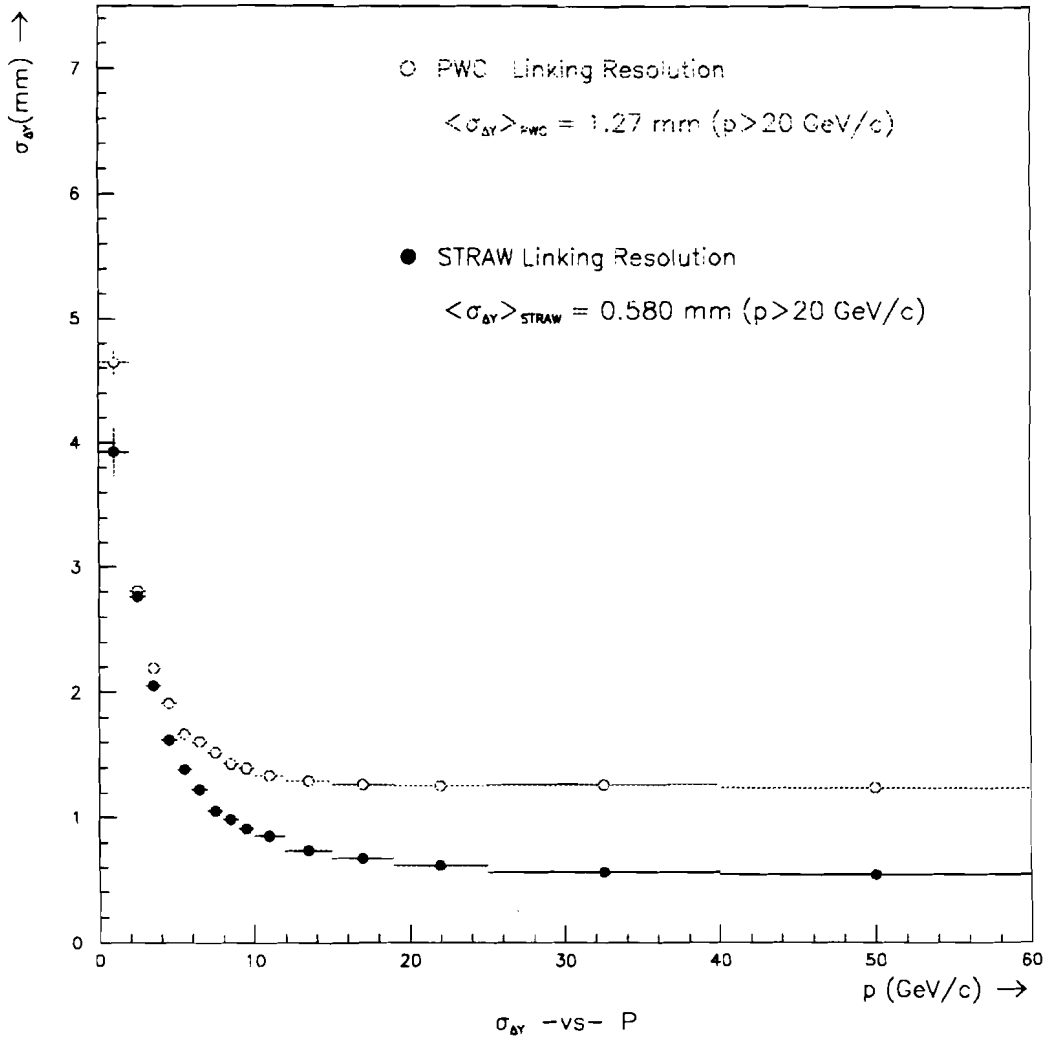

Figure 3.10 $\Delta\Theta_Y$ linking resolution as a function of the track momentum.

hit sharing should still be minimal[13]. Tracks sharing many hits were usually the result of the hit combinatorics in the event. This method of cleaning tracks (based on hit sharing) proved to be quite effective in eliminating the SSD tracks produced from the combinatorial background, with very little loss in real tracks.

The next step was to link the downstream tracks to the 4 and 5 hit SSD tracks. For each downstream track, a linking window was assigned based on (a) whether the downstream track had an associated straw track or not, and (b) the estimated momentum of the track. These resolution functions were shown in Figure 3.8, Figure 3.9, and Figure 3.10. In the X view, the SSD link was required to fall within $3.3*\sigma_{\Delta X}$ from the downstream projection. Similarly, in the Y view, a $3.3*\sigma_{\Delta Y}$ cutoff was applied, as well as a $3.3*\sigma_{\Delta YS}$ cutoff on the slope matching between the upstream and downstream tracks. For each downstream track, the SSD links were ordered in terms of their "linking χ^2". The linking χ^2 was defined by,

X View:

$$\chi^2_X = (\Delta X/\sigma_{\Delta X})^2 \qquad 3.1$$

Y View:

$$\chi^2_Y = (\Delta Y/\sigma_{\Delta Y})^2 + (\Delta YS/\sigma_{\Delta YS})^2 \qquad 3.2$$

with,

$\sigma_{\Delta X}$ = Expected error in ΔX (Figure 3.8)

$\sigma_{\Delta Y}$ = Expected error in ΔY (Figure 3.9)

$\sigma_{\Delta YS}$ = Expected error in ΔYS (Figure 3.10)

---

[13] The amount of hit sharing is primarily dependent upon the track density.

Each downstream track was permitted to have a maximum of 5 possible SSD links in each view. The SSD link with the smallest linking χ^2 was labelled the **best link**. The remaining tracks in the list were referred to as **extra links**. For cases when there was more than 5 SSD links, only the 5 best linking χ^2 solutions were kept. The linking was done on a track by track basis, so that any given SSD track could be a best link to one or more downstream tracks[14].

After assigning all possible SSD links to the downstream tracks, all SSD tracks which were neither (a) linked to a downstream track, or (b) isolated from the other tracks in the event[15] were deleted from the ZEBRA banks. The isolated tracks were generally low momentum tracks which were swept out of the acceptance of the downstream system by the analysis magnet. However, they were kept since they could possibly aid in the vertex finding when there was a relatively small number of linked charged tracks. All of the hits used by these remaining tracks were removed from the list of hits which could be used in the next stage.

The next stage was to reconstruct the 3 hit tracks from the unused hits of the first stage. A χ^2/DOF cut of 2.0 was imposed on all 3 hit SSD track candidates. Furthermore, the only 3 hit tracks considered were those which linked to a downstream track which did not have a SSD link from the first stage. Only the best 3 hit SSD link was saved in these cases.

Figure 3.11 shows the number of reconstructed SSD tracks in each view. One observes an average multiplicity around 19 tracks per event. The Y view is seen to have slightly less. This is a consequence of the tighter linking requirement in the Y view which additionally demands slope matching as compared to the X view.

---

[14] The two downstream tracks' projections tot he center of the magnet would obviously have to be in close proximity to one another for this to occur.

[15] By isolated, we mean that it doesn't share any hits with other tracks in the event.

Figure 3.12 shows the fractional distribution of the number of hits found on the reconstructed SSD tracks.

3.2.5 Vertex Finding

As mentioned previously, the primary vertex was essential to doing any physics associated with the nuclear dependence of various cross sections. It was absolutely essential for the scope of this thesis. The main difficulty that occurred in finding the primary vertex was when there were two or more vertices in the event. The vertex algorithm reconstructed a maximum of 2 vertices. In the case of 3 or more vertices, generally the algorithm converged to the vertices with the higher track multiplicity. In the case that 2 vertices were reconstructed, the most upstream vertex was chosen as the primary vertex under the presumption that the more downstream vertex was a result of a secondary interaction of one of the primary vertex particles. The five basic steps in the vertex finding procedure is described below.

(A) Choose the Tracks

The selection of tracks was done on a hierarchal basis. First, only the SSD tracks which were **best links** to downstream tracks were used in the vertex finding. If this was not satisfactory to find a vertex, then the **extra links** and unlinked tracks were added to the track list for vertex finding.

(B) Vertex Finding

The vertex finding procedure was applied to the X and Y views independently. The set of tracks to be used in the vertex fitting were input from external routines, i.e. as in (A). To initiate the vertex finding, only the best links were used as the input set of tracks. The vertex finding was first performed using an impact parameter minimization (IPM) scheme as described in the references [66]. This algorithm provided a good estimate of the vertex position. However, a second refit was done using this vertex position as a seed for two reasons. First, the IPM yielded an error matrix which underestimated the errors in the fitted parameters. This was

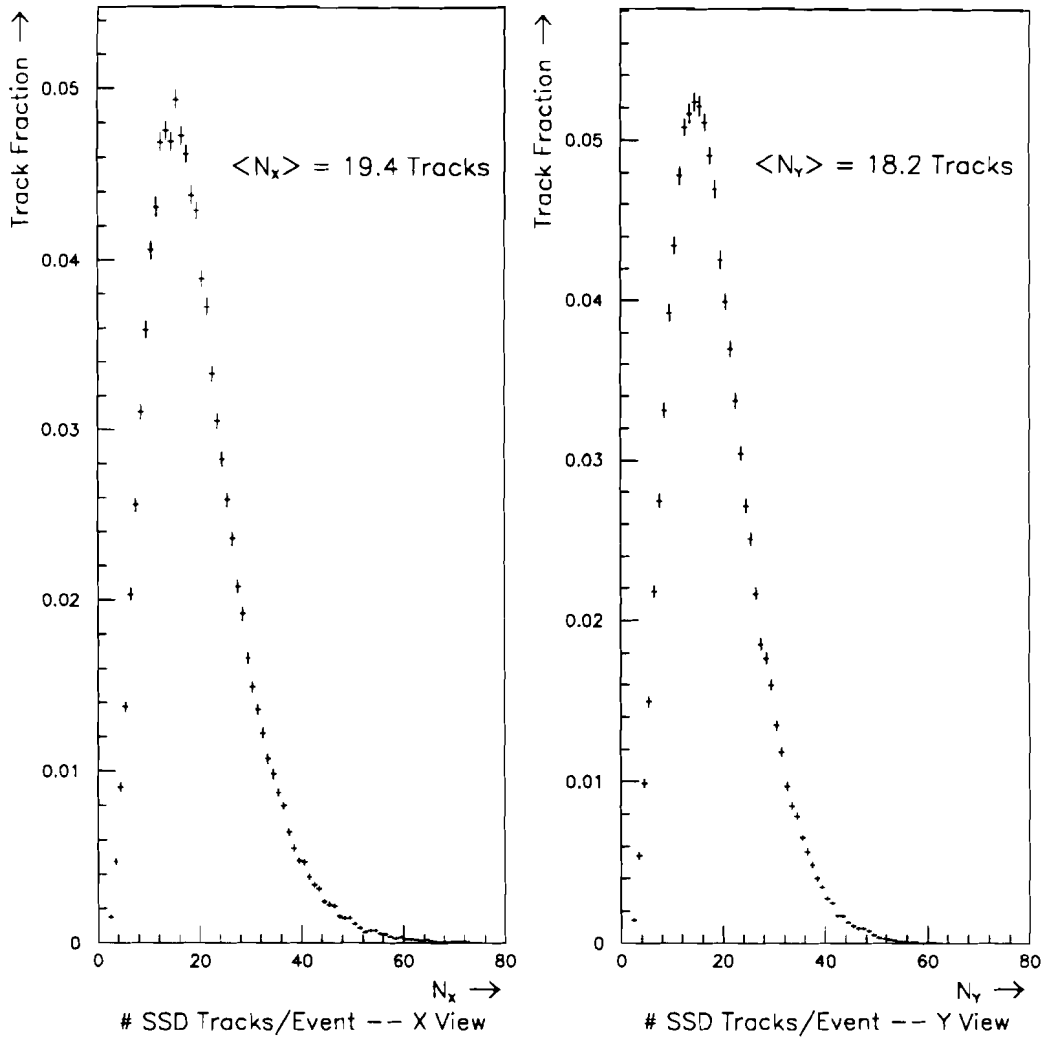

Figure 3.11 Distribution of the number of reconstructed SSD tracks per event in the X and Y views.

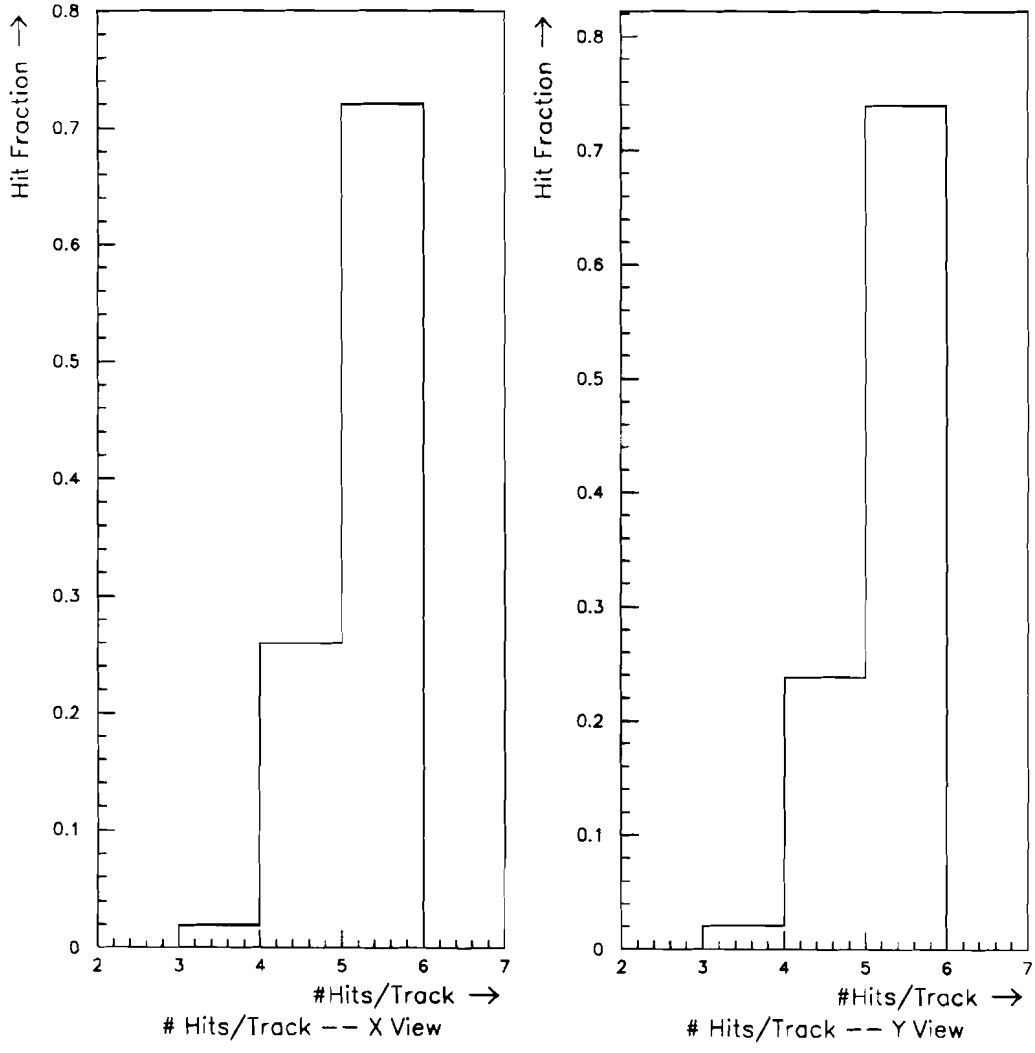

Figure 3.12 Distribution of the number of hits on SSD tracks in the X and Y views.

a result of approximations made in the algorithm. Secondly, and more important, was that the intial fit measured vertex quality in terms of an "average impact parameter" (AIP) of the tracks used in the fit. This method will be dependent on the extrapolated distance of the tracks i.e. the vertex location. As a result, a vertex located more upstream in the target will generally have a larger AIP than one located further downstream. To remove this bias, each track needed to be weighted by its projection error to the position of interest. Hence, subsequent to the IPM, a chisquare minimization (CQM) was performed, using the vertex seed from the IPM. After the CQM fit, the vertex was tested for *convergence*. Convergence required that either (a) the vertex $\chi^2/\mathrm{DOF} \leq 5.0$, or (b) the worst track in the fit had $\chi^2_i \leq 9$ [16]. If either of these conditions was met, the vertex was accepted. If neither of these conditions were met, the worst track in the vertex was removed. The worst track was determined by removing each track from the fit, one at a time, and redoing the CQM for each case. The worst track was defined as the one which yielded the lowest vertex χ^2 upon its removal from the fit. This method of track removal was fairly important for excluding tracks which were from nearby secondary vertices (decays). This procedure of removing tracks and refitting was performed until either of the aforementioned criteria was met, or the number of remaining tracks was equal to 2. In the latter case, it was required that a beam track be pointing at that 2 track vertex, in order to provide a further constraint. If no beam track pointed at the vertex, the *extra link* and *isolated* SSD tracks were added into the track list, and the entire vertex finding procedure was repeated. Usually this was not necessary, since most events had a fair number of charged tracks within the acceptance of the spectrometer. The view verticizing yielded independent measurements of the vertex location in the X and Y views.

Once the view vertices were found, a refitting procedure was performed. Any pair of Y view SSD tracks whose Z intersection was within 6 standard deviations of

[16] χ^2_i was the contribution for a single track to the vertex χ^2.

the Z location of the X vertex, were loaded into a track list. This set of tracks, and only this set, were put through the vertex finding procedure as described above. This was commonly referred to as *refitting the Y view around the X view vertex.* This provided another estimate of the Y view vertex position, which was "seeded" by the X view. Similarly, the X view was refit around the Y view vertex. This procedure was useful when, because of multiple vertices, the X and Y view converged to different vertices in the event. The refitting procedure increased the probability for the vertices in the two orthogonal view to be *correlated* with one another. The correlation of the view vertices is discussed in the next section.

(C) Vertex correlation

The vertex matching relied on the notion that the Z locations in the two views should match within a given measurement error. There were generally 2 vertex candidates in each view after the refitting procedure. This provided a maximum of 4 possible XY matched vertices. To form a matched vertex candidate among the 4 choices, it was required that the X and Y view vertices have a separation along Z of less than 5 mm, or, the significance of separation[17] be less than 8.0 Generally, one was faced with 2 scenarios. The first of these is that there is one and only one vertex in the event. The second possibility is that there really were 2 or more distinctly separated matched vertices present in the event. In the former case, one generally finds 4 possible choices for a matched vertex, all of which were very close in space. The choice made was that which had the smallest value of ΔZ[18]. In the latter case, when there were 2 choices for the matched vertex, the most upstream vertex was designated as the primary vertex. After making the choice, one had the first matched vertex candidate.

---

[17] Significance of separation was defined as the separation divide by the expected error in that separation.

[18] ΔZ was defined as the difference in the Z coordinates between the X and Y views.

(D) Second Vertex Pass

Since $\sim$ 15 % of events had secondary interactions in the target, it was necessary to ensure that one really had found the most upstream vertex in the event. Recall that this was imposed under the assumption that any secondary vertices were a result of particles produced from a more upstream vertex. Since the SSD angular acceptance increased as the production point along Z increased, the vertices occurring further downstream in the target would tend to have more reconstructed SSD tracks associated with them. Consequently, for an event with 2 vertices, it was more likely for the vertex fitting algorithm to converge to the more downstream vertex. Furthermore, the wide angle tracks tend to dominate the fit, which gives preference to a downstream vertex over an upstream one. Since it was desired to define the most upstream vertex as the primary, a second vertex pass was performed. First, all of the tracks used in the first matched vertex were removed from the list of SSD tracks eligible for vertex finding. All other tracks were fed into the identical algorithm as defined in (A)-(C). For the majority of cases where there was only one vertex in the event, this stage did not yield another vertex. In the remaining fraction of the events, a second vertex will be identified, provided that there are enough charged tracks associated with it. Consequently, some fraction of the events had more than one choice for the primary vertex. The next step was to decide which vertex was to be designated as the primary vertex.

(E) Primary Vertex Identification

In the case that there was only 1 matched vertex candidate from steps (A)-(D), the choice for primary vertex was trivial. If a second matched vertex was found *downstream* of the first, then we choose the first matched vertex as the primary. The more difficult case was when a second matched vertex lay *upstream* of the first matched vertex. In this case, it had to be decided whether or not this more upstream vertex should be defined as the primary vertex for the event. The main concern was to reject the cases where the upstream vertex was formed from the combinatorial

background of SSD tracks not used in the first vertex. For this reason, the following cuts were applied to the more upstream vertex, when it was found in (D) above.

$$NX + NY > 6$$

$$NBX + NBY \geq 3$$

$$NLX + NLY \geq 5$$

where,

- NX(NY) = # of SSD tracks in X(Y) view vertex
- NBX(NBY) = # of SSD tracks in X(Y) view vertex which were BEST links of downstream tracks.
- NLX(NLY) = # of SSD tracks in X(Y) view vertex with impact parameter to the DOWNSTREAM matched vertex greater than 100 μ.

If the upstream vertex passed all three of these criteria, then this vertex was assigned as the primary vertex.

If the upstream vertex failed one or more of these criteria, another refit was performed. In this case, all tracks passing within 100 μ of the upstream matched vertex were input into the vertex fitting algorithm as described in (B). This differs from (D) in that tracks passing close to the first matched vertex were not excluded from this track selection. This procedure was performed on both the X and Y views. The refitted vertex was then put through the same constraints as above, to see if it would have passed the above criteria, had it not been biased by the initial track removal as described in (D). If these 3 conditions were met, the final check was to make sure that after the refit, the X and Y views still satisfied the definition for a matched vertex as described in (C). If so, the upstream vertex was declared as the primary vertex. If either of these conditions were not met, this second vertex was rejected, and the first matched vertex (more downstream vertex) was declared as the Primary Vertex.

3.2.6 Relinking

The motivation behind the relinking code was to benefit from the information gained as a result of the vertex finding. Since most of the particles produced in the high energy collisions were produced at the primary vertex, it was decided to reassign the choice of best link based upon a "relinking χ^2". The relinking χ^2 contained terms involving the linking quality, as well as terms proportional to the impact parameter of the SSD track to the primary vertex. Since the accuracy in identifying the correct SSD link was limited by the linking resolution, it could happen that a best link, as determined from the linking code, was actually a spurious (combinatorial) track. Hence, by using the extra constraint of knowing where the primary vertex was located, one could significantly reduce the background from mislinking. The relinking χ^2 was defined as follows:

X View:

$$\chi^2 = (\Delta X/\sigma'_{\Delta X})^2 + (\Delta V_X/\sigma_{\Delta V_X})^2 \qquad 3.3$$

Y View:

$$\chi^2 = (\Delta Y/\sigma'_{\Delta Y})^2 + (\Delta YS/\sigma'_{\Delta YS})^2 + (\Delta V_Y/\sigma_{\Delta V_Y})^2 \qquad 3.4$$

with the errors given by,

$$\sigma'_{\Delta X} = \sigma'_{\Delta Y} = 1 \text{ mm}$$

$$\sigma'_{\Delta YS} = 1.8 \text{ mrad}$$

$$\sigma_{\Delta V_X} = \sigma_{\Delta V_Y} = 50\ \mu$$

These expressions are quite similar to those in the linking, with a couple of exceptions. First, the relinking weights were assigned a fixed value. The relinking was not very sensitive to the actual value of the weights, but rather it was more

sensitive to the relative magnitude of the weights among the terms in the χ^2. Secondly, the last term was introduced in order to give preference to links coming closer to the primary vertex. Since the magnitude of the linking terms were bounded by the linking code i.e. since all links must have been in the momentum dependent linking window, their contribution to the χ^2 was capped off from above. On the other hand, the impact parameter term could become quite large compared to the 50 micron error which it was assigned. The result of this is to put a strong bias against SSD tracks which have a large impact parameter on the scale of 50 μ.

The first step was to calculate the relinking χ^2 for the best link and the extra links of a give downstream track. If any of the extra links of that downstream track was also a best link of a different downstream track, it was excluded. This was done so not to force the correlation of 2 downstream tracks to have the same SSD link. The SSD link which yielded the minimum relinking χ^2 was deemed the "physics link". Once the physics link was assigned, the fundamental physical parameters of the track i.e. momentum, charge, and direction cosines, were calculated with respect to the *physics link*, **not** the *best link*[19]. Once the physics links were assigned, one may consider that the X and Y SSD links define a space track in the SSD system. It is worth noting at this point that this SSD space track definition is unambiguous only if there is a single link in both the X and Y views. If multiple links exist, in either or both views, still some level of ambiguity exists, as to whether or not one has identified the correct SSD space track.

Momentum Resolution

Based on the upstream and downstream reconstruction, we proceed to measure the momentum resolution of the tracking system. A sample of MC data was used which included a full detector simulation. One dimensional plots of (P_{REC} –

[19] In most cases, the physics link and the best link were the same.

$P_{GEN})/P_{GEN}$ were generated for several bins in P_{GEN}[20]. The RMS or gaussian width of each distribution gives a measure of the resolution in $(P_{REC}-P_{GEN})/P_{GEN}$. The results of the fits are summarized in Figure 3.13, where we plot the relative error $(\Delta P/P_{GEN})$ as a function of P_{GEN}. The best resolution is achieved at a momentum of ~6 GeV, and rises linearly with increasing momentum. The plot begins to turn up slightly below 6 GeV, which may be attributable to multiple scattering and/or the effects of the fringe fields. The momentum resolution may be parametrized in the familiar form,

$$\sigma_p/p \sim 0.0076 + 0.00026 * p \qquad 3.5$$

where p is measured in GeV/c.

3.2.7 Secondary Vertex Finding

The secondary vertex finding used the reconstructed charged tracks to search for secondary vertices resulting from decays and secondary interactions. Secondary vertices were required to have a minimum of 2 associated charged tracks. For such cases when there were only 2 charged tracks, the vertices were referred to as *vees*, otherwise, they were simply called *secondary vertices*. The algorithm implicitly assumed that there existed a set of predefined space tracks, not only in the downstream system, but in the SSD system as well. Recall that the X and Y view segments of the SSD were correlated via the space tracks in the downstream system. When there is only 1 link in both the X and Y views of the SSDs, the correlation is trivial. However, if there were multiple links in either/both views, the choice of which SSD XY pair was correct was not straightforward. In general, a downstream track may have links consistent with multiple vertices, as well as with no vertex at all (as is the case of a fake SSD track). Only with the proper pair of XY links will one define a space track in the SSD which extrapolates back to its

[20] Here, P_{GEN} and P_{REC} are the generated and reconstructed momentum of the MC track.

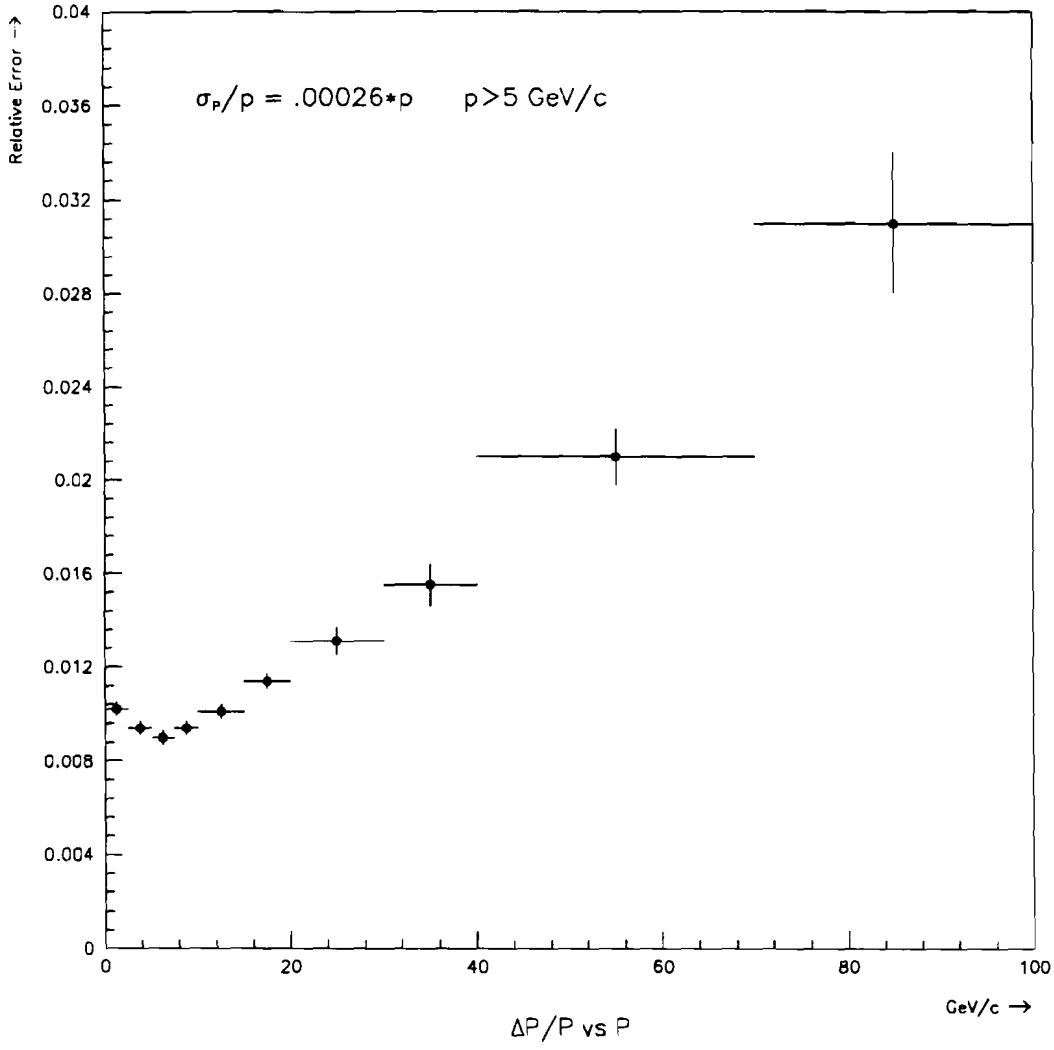

Figure 3.13 Relative momentum resolution ($\Delta p/p$) as a function of the generated momentum.

production point within the expected error. The task at hand is to identify the correct links efficiently enough, so that the true secondary vertices can be located using these SSD space tracks. If there were 2 or more charged particles produced at a given vertex, and the tracks were within the tracking acceptance, we should be able to identify a secondary vertex or vee.

The algorithm proceeded in three main stages. These stages were, (a) vee finding, (b) vertex seeding, and (c) secondary vertex finding. The program relied on the linking and relinking results in order to reconstruct the vees/vertices, along with their associated tracks. Throughout the program, each track had its error matrix calculated using the approximate 1/p (GeV/c) behavior for the multiple scattering.

Vee finding

The first step to identifying secondary vertices was to reconstruct vees. Vees were formed by taking all pairs of downstream tracks, and finding the intersection point in the X and Y views using the *physics' links.* The following criteria were then applied.

$$\frac{(Z_X - Z_Y)}{\sqrt{\sigma^2_{Z_X} + \sigma^2_{Z_Y}}} \leq 5 \qquad 3.6$$

$$\frac{(Z_{SEC} - Z_{PRIM})}{\sqrt{\sigma^2_{Z_{SEC}} + \sigma^2_{Z_{PRIM}}}} \geq 3 \qquad 3.7$$

where Z_X and Z_Y are the Z positions in the X and Y views for the vee, Z_{PRIM} and Z_{SEC} are the Z coordinates of the primary vertex and vee, σ_{Z_X} and σ_{Z_Y} are the errors in the Z position in the X and Y views, and $\sigma_{Z_{PRIM}}$ and $\sigma_{Z_{SEC}}$ are the longitudinal errors of the primary and secondary vertices respectively.

Equation 3.6 requires that the Z positions of intersection in the X and Y view be consistent with coming from the same point. The second equation, (3.7) demands

that the vee is sufficiently displaced from the primary vertex of the event. All vee candidates passing these cuts were loaded into an array. There was one important weakness in the vee finding which propagated throughout the secondary vertex program. Vees were formed using **only** the ***physics' links***. Since the choice of physics link was biased toward the primary vertex (see RELINKING above), this degraded the efficiency of finding displaced vertices. Regardless of the choice of physics links, one was always faced with some level of ambiguity whenever there was more than 1 possible SSD link associated with a downstream track. The alternative of trying all possible SSD link combinations was discounted.

Vertex Seeding

Once all possible vees were found as described above, the next task was to combine the vees to produce "vertex seeds". In the case of a multi-track secondary vertex ie, 3 or more tracks, there may be several vees reconstructed in close proximity to one another. In this case, vees were combined to form seeds provided their transverse and longitudinal significance of separation[21] was less than 3.0. After seeds were formed by appropriately combining vees, the remainder of the vees not already used in seeds were individually loaded into the list of seeds. The seeds provided a list of 3 dimensional coordinates with which the secondary vertex finding was seeded.

Secondary Vertex Finding

The vertex finding used the seeds determined previously to reconstruct vertices. In addition, the primary vertex as found in the primary vertex program was also input as a seed, so that the secondary vertex program could refit this vertex with the inclusion of multiple scattering. For each seed, one tried to attach all possible downstream tracks, making use of their associated links. First, only the best links

[21] Significance of separation is used throughout the text, and it refers to the measured separation divided by the expected error in that separation.

of each downstream track were tried. After attaching all possible PWC-SSD space tracks using only best links, the extra links were tried as well. This hierarchy was invoked since SSD tracks could be used only once for a given vertex. Therefore, preference was given to using the best links before trying the extra links. Once all possible space tracks had been attached, the resulting set of tracks were put through a χ^2 minimization to determine the fitted coordinates, error matrix, and the χ^2/DOF. If the χ^2/DOF > 5.0, the worst track in the fit was removed, and the remaining set of tracks refit again. This procedure continued until the χ^2 cut was satisfied or until 3 tracks remained. In the latter case, the vertex fitting was stopped, and this vertex was saved. The downstream tracks associated with the refit primary vertex were not allowed to appear in any of the other vertices in the event. For the other (secondary) vertices in the event, the space tracks were initially allowed to appear in more than 1 vertex.

After making all the possible secondary vertices, a second iteration was to be performed. Prior to beginning, the list of vertices were reordered, with the lowest χ^2 vertices appearing first in the list. Each of these vertices now acted as a seed and the secondary vertex finding was repeated. In this final pass, the PWC tracks could be used in one and only one vertex. On the other hand, the SSD tracks were allowed to appear in more than 1 vertex, but could not be used more than once in any single vertex. This two step method was applied in order to remove the bias of the order dependence of the initial seeds.

All secondary vertices were required to have a significance of separation from the primary vertex greater than 3.0. All vertices satisfying this criteria were written out. Finally, once all vertices were established, any vees which did not result in a secondary vertex were also saved, provided neither of their space tracks were used in any secondary vertices.

3.3 ElectroMagnetic Shower REConstruction (EMREC)

The task of the software package EMREC was to determine the energy and position of all particles producing electromagnetic showers. Any particle producing an electromagnetic shower will yield some amount of energy on the strips in the EMLAC. To convert the strip ADC counts into energy E_i, the following formula was used,

$$E_i = A_{em} G_i B(t)(N_i - N_{0_i}) \qquad 3.8$$

where,

- N_i was the ADC pulse height in channel i .
- N_{0_i} was the pedestal (in ADC counts) for channel i .
- A_{em} was a normalization factor to convert from ADC counts to energy (determined from electron data to be $\sim$ 3.1 MeV/count).
- G_i was the relative gain of the amplifier channel i.
- B(t) was the (beam) time dependent energy scale correction [24].

The EMLAC strips were oriented in the radial (r) and azimuthal (ϕ) directions, and were focused on the target as mentioned in Chapter 2. Each of the 4 quadrants were organized into 4 views; left R, right R, inner ϕ, and outer ϕ. The left and right R referred to the R strips in the left and right octants of each quadrant, while the inner and outer ϕ strips referred to the ϕ strips on the inside and outside of the detector respectively. Furthermore, within a view, one can identify 3 sections; front, back and sum sections. Electromagnetic showers were identified in each of the views independently, and subsequently the R and ϕ GAMMAS were correlated to make PHOTONS[22].

[22] GAMMAS were showers reconstructed in a single view, while PHOTONS were R-ϕ correlated GAMMAS.

3.3.1 Photon Reconstruction

The reconstruction of photons in the EMLAC was performed in the following manner:

- Group and Peak Finding;
- Reconstruction of GAMMAS in the R and ϕ views;
- Correlation of the R and ϕ view GAMMAS to form PHOTONS.

Group and Peak Finding

First EMREC was to find *groups* in each of the 4 views (sum section). Groups were defined as any cluster of consecutive strips satisfying the following criteria:

Inner ϕ:

- 3 or more consecutive strips each with $E_i \geq 80$ MeV;
- Total group energy $E_{TOT} \geq 600$ MeV;
- Strip with the largest energy $E_i^{max} \geq 300$ MeV.

Outer ϕ:

- 2 or more consecutive strips each with $E_i \geq 95$ MeV;
- Total group energy $E_{TOT} \geq 600$ MeV;
- Strip with the largest energy $E_i^{max} \geq 350$ MeV.

The difference in the cuts between the inner and outer ϕ was due to the widening of the strips with increasing radius. These groups should not be confused with the *groups of 8* used in the trigger logic.

Once all the groups satisfying these criteria were found (in the sum section), a *peak* was identified in each of the groups. The peak was defined as the point at which the derivative of the energy distribution within the group flips its sign. In

addition, for each group, 2 *valleys* were defined on either side of the peak. A valley was defined as the lowest energy point between 2 adjacent peaks, or, in the case of an isolated peak[23], the end strips in the group. In order to recover some of the low energy peaks which may have coalesced with nearby higher energy peaks in the sum section, the peak finding algorithm was reapplied to the front and back section separately, looking for low energy peaks between the pre-existing valleys determined from the sum section. The final step was to identify/match the corresponding peaks in the front and back sections, so that the *directionality* could be measured. The directionality was a measure of the direction of the particle as it entered the EMLAC. For particles emanating from the target region, the directionality is centered on 0, with a width of $\sim .10$. The directionality measurement was useful in the off-line analysis to reject halo muon induced events[24] since muons generally had large directionality.

Reconstruction of GAMMAS in the R and ϕ views;

Once all the peaks were identified within the groups, the next step was to fit the associated energy distributions in order to determine the energy and position of the GAMMA's. A parametrized shower shape[55] was developed using the GEANT full shower simulation in order to describe the transverse and longitudinal shower development. The simulation was shown to agree quite well with the isolated photons present in the data. For isolated peaks, one simply fit the energy distribution to the functional form of the shower shape to determine the energy and position of the photon. For cases where there were multiple peaks within a group, the situation was more complicated. In such cases, a χ^2 minimization technique was used to extract the energies and positions of the GAMMA's within the group[24, 55, 77].

---

[23] By isolated, we mean the only peak in the group.

[24] See Chapter 1.

Correlation of the R and ϕ views to form PHOTONS.

The final step in reconstructing the showers was to correlate the R and ϕ view GAMMAS to form PHOTONS. The correlations ranged from trivial to quite complicated. The basic assumption in correlating showers in the two views was that (a) the GAMMA energies in the R and ϕ views should be close, and (b) the longitudinal development of the shower in the 2 orthogonal views should also be quite similar. For GAMMAS where there is only 1 R GAMMA and 1 ϕ GAMMA with similar energies and longitudinal deposition (E_{front}/E_{total}), the correlation was trivial (1-1 correlation). However, more difficult situations may arise. For example, there may be 2 photons which overlap in 1 view, but not the other (2-1 or 1-2 correlations). Likewise, even higher order correlations may be necessary. Furthermore, there may be 2 similar energy photons striking an octant, in which case there is some level of ambiguity in determining the correct r-ϕ positions for the 2 photons. It should be clear that more complicated situations can and do arise in the correlation phase. The reader is encouraged to consult the above mentioned references for more details regarding the correlation of GAMMAS.

After the correlation phase, the ϕ view GAMMAS were refit using the radial information. Since the shower shape was dependent on the strip width[25], the energy of the ϕ view GAMMA could be more accurately determined after determining the radial position of the PHOTON. Afterwards, the correlation phase was redone with the newly determined ϕ energies. The final photon energies were simply the sum of the correlated R and ϕ view GAMMA energies.

3.3.2 Photon Timing

The TVC[26] was used to provide a time of arrival of the photon with respect to the interaction time. Since each TVC was sensitive to 4 strips on an amplifier,

---

[25] Recall that the ϕ strips increased in width with increasing radius.

[26] The Time to Voltage Converter is a timing circuitry inside the LAC amplifier modules.

a GAMMA could produce several TVC times, depending on the lateral width of the shower. The TVCs were grouped into sets which yielded timing values which were within 21 ns of each other. The time chosen for the GAMMA was the one with the most TVCs participating within one of those sets. If there were 2 sets with the same number of participating TVCs, the set with the larger energy was selected. The final GAMMA time was calculated as the energy weighted average of the chosen set of TVCs.

3.4 Discrete Logic REConstruction

The DLREC program was used to unpack the bit information pertaining to the trigger logic as well as the Cerenkov detector. The discrete logic unpacked the bit information provided by the camac system in order to provide the following information for each event:

- The beam and interaction related logic (including Cerenkov);
- Identification of which veto wall elements registered a hit;
- Determination of which of the trigger octants fired the trigger, as well as the trigger status of all other octants.

The beam and interaction related logic provided the status of the beam and interaction counter elements. In particular, each element provided a time history of $\pm$ 7 buckets (19 ns/bucket) with respect to the trigger. An on-line filter rejected events based on the beam/interaction counters' information. For example, the EARLY/LATE CLEAN FILTER required that the in-time interaction not be accompanied by any other interaction within $\pm$ 3 buckets. In addition, the timing information was particularly useful for studying local intensity dependent effects in various detectors. Further information was provided about the beam by the Cerenkov counter. The logic provided the status of the counter's phototube's for the in-time interaction. Coincidences and anti-coincidences of certain tubes were used

to provide information on the beam particle type. At this time, the performance of the Cerenkov detector is still being studied.

The status of the veto walls was used to provide a second level of off-line rejection against muon induced events. Events registering a sufficient number of veto wall hits in the same quadrant[27] as the trigger, as well as within $\pm$ 5 buckets of the in-time bucket, were rejected. Most of the muon induced events were rejected on-line, so that this cut was implemented to address any events which leaked through the on-line filter.

The final task of DLREC was to relay the information regarding which of the octants fired which of the triggers. Each octant had the opportunity to satisfy any of the triggers. Any event which had any octant(s) satisfying a trigger would be written out. Having the trigger bit information allowed for the performance of the trigger to be studied off-line at a later time.

---

[27] The veto walls were divided into 4 quadrants. Each quadrant could be associated with a quadrant of the EMLAC.

Chapter 4 DST Analysis

4.1 Overview

This chapter serves to introduce the reader to the higher level of analysis which was carried out at the DST level. These analyses include, fiducial cuts, tracking cuts, momentum and energy scale corrections, and a more sophisticated secondary vertex finding algorithm. In this chapter we discuss these aspects of the DST analysis.

4.2 Vertex Cut

For each event it was demanded that the primary vertex be reconstructed in the target region. The target region included 2 pieces of 0.08 cm thick copper targets and 2 pieces of beryllium of thicknesses 3.74 and 1.12 cm. Figure 4.1(a) shows the distribution of reconstructed primary vertices for events containing a high p_T π^0. The events are not corrected for losses such as beam attenuation and photon conversions, and hence shows a net slope. Also clearly seen are the interactions occurring in the silicon tracking chambers which are $\sim$ 300 μ thick[1]. For this analysis, the primary vertex was required to be within the beryllium or copper target pieces, with some allowance for resolutions smearing along Z.

Figure 4.1(b)-(c) shows the transverse profile of the interaction vertices. A cut is made on VZ[2] to determine which target the vertex was located in. The scatter plot shows the enhancement in the region R $\leq$ 1.0 cm for the Be target,

[1] For some analyses, the silicon chambers were used as targets as well.

[2] VZ is the Z position of the primary vertex.

and a truncated circle of larger radius for the copper target. The circles indicate the physical positions of the targets, and the box depicts the position of the beam hodoscope. The excess of vertices outside of the physical boundaries of the Be and Cu target are a result of interactions occurring in the rohacell target holder on which the targets are mounted. In order to avoid edge effects, a fiducial cut was made on the radial position of the vertex with respect to the center of the target. The transverse coordinates of the primary vertex were required to lie within the circle,

$$R = \sqrt{(V_X - X_0)^2 + (V_Y - Y_0)^2} \leq 0.98 \text{ cm.} \qquad 4.1$$

where X_0 and Y_0 are the measured centers of the targets. This definition was used for both the beryllium and copper vertices, so that the fiducial corrections were nearly the same for both materials.

4.3 Track Selection

The physics tracks which were written to the DST from PLREC were all possible solutions which passed various cuts (see Chapter 3). In order to remove the occurrence of combinatorial background tracks, another level of track filtering was performed at the analysis level. This was commonly referred to as *track marking*, and it refers only to the tracks reconstructed downstream of the analysis magnet. The convention is that marked tracks were usually spurious solutions, and unmarked tracks were generally true physics tracks. Track marking was based on the premise that charged tracks bend in the magnetic field, and therefore should be somewhat separated in the PWC system. Consequently, for events of moderate multiplicity[3], any given charged track should not share a large number of hits with the other charged tracks in the event. Reconstruction of spurious tracks usually occurs via the combinatorials of all the hits generated by true tracks. For example, a fake 13

[3] By moderated multiplicity, we mean of order 20 or less charged tracks.

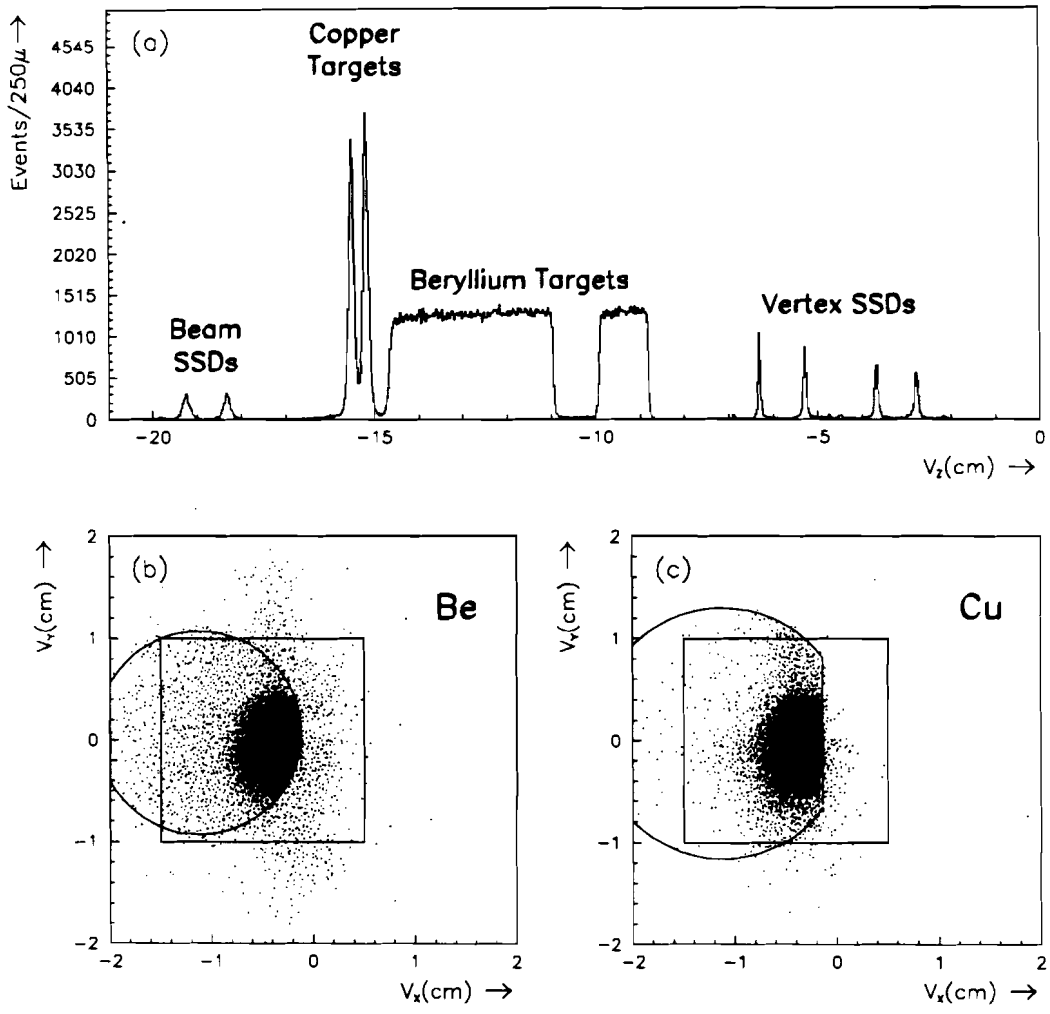

Figure 4.1 Primary vertex position for events having a reconstructed high p_T π^0. In (a) is shown the Z coordinate, with (b) and (c) showing the transverse profile in the beryllium and copper targets respectively.

hit track may be reconstructed by sharing 4 hits with 1 track, and the remaining 9 hits with 8 different tracks from the event. Clearly, this situation occurs rather infrequently for real tracks.

Since the Y view was non-bending, any track sharing 2 or more of its hits in that view with other good physics tracks, usually resulted in that track having a poor impact parameter at the primary vertex. In fact, the majority of large impact parameter tracks were combinatorial background. For this reason, the track marking program distinguished between tracks having small and large Y view significance[4] to the primary vertex. The cuts used to weed out the suspicious tracks in the events were the following:

- No associated straw track. PWC tracks which had an associated straw were never marked (rejected). Approximately 70% of the true tracks had corresponding straw tracks.
- The PWC track must share several hits with other tracks in the event. This maximum hit sharing criteria was based on the Y view significance of the DS track to the primary vertex, as well its χ^2. The maximum number of shared hits was bounded by the number of hits on the track.

The count of shared hits is the number of hits a given PWC track shares with a subset of all the tracks in the event. An iterative procedure was used to determine this subset. In particular, the hit sharing was first calculated for the large impact parameter PWC tracks, and afterwards for the good impact parameter tracks. The hit sharing calculation for the good impact parameter tracks ignored any of the large impact parameter tracks in the event which shared more than 60% of its hits,

[4] Here, significance refers to the Y view impact parameter divided by the expected error.

as determined in the previous iteration. Table 4.1 and Table 4.2 show the various sharing cuts used to identify the suspicious tracks. The tracks were marked if they did not pass either a direct hit sharing cut or a looser hit sharing cut in conjunction with a χ^2 cut. The cuts were dependent on the track's Y view significance as well as its number of hits. For example, from Table 4.2, one sees that a 13 hit PWC track, with **no** associated straw track, having $\sigma_Y > 5$, may share a maximum of 2 hits with other PWC tracks in the event, unless its $\chi^2/DOF \leq 1.75$, in which case it can share a maximum of 4 hits.

Table 4.1 Summary of Track Marking Cuts for $\sigma_Y \leq 5$

# Hits	$\sigma_Y \leq 5$	
	NSHAR1 $\leq$ P1 and $\chi^2 \leq$ P2	NSHAR2 $\leq$ P3
13	P1 = 5 P2 = 1.75	P3 = 3
14	P1 = 7 P2 = 2.00	P3 = 4
15	P1 = 8 P2 = 2.00	P3 = 7
16	P1 = 14 P2 = 2.00	P3 = 12

Table 4.2 Summary of Track Marking Cuts for $\sigma_Y > 5$

# Hits	$\sigma_Y > 5$	
	NSHAR1 $\leq$ P1 and $\chi^2 \leq$ P2	NSHAR2 $\leq$ P3
13	P1 = 4 P2 = 1.75	P3 = 2
14	P1 = 5 P2 = 2.00	P3 = 3
15	P1 = 7 P2 = 2.00	P3 = 5
16	P1 = 11 P2 = 2.00	P3 = 9

A second iteration was made afterward which used the information obtained about the marking from the first iteration. In particular, the algorithm tried to save tracks which had a good significance to the primary vertex. The criteria for saving a previously marked track was the following:

- The track has a significance S $<\cdot 5$, and matched with a reconstructed shower in the EMLAC, or
- The track has a significance S < 5, and the hit sharing is primarily with a single track, where the 2 tracks overlap in one of the 4 PWC views[5].

Studies of the track marking routine on MC events showed that the rate of accidental marking of real tracks was less than 2%. Figure 4.2 shows the fraction of unmarked tracks to total tracks for various hit requirements versus the average hit multiplicity in the PWC system. One observes that the occurrence of spurious tracks is a strong function of the event multiplicity, as one might expect. The average PWC multiplicity is peaked around 22 hits, so one expects about 40%, 60%, 85%, and 90% unmarked 13, 14, 15, and 16 hit tracks respectively in the average event. The χ^2/DOF distributions for various hit multiplicities of unmarked tracks was shown previously in Figure 3.5.

---

[5] Track overlapping occurred predominantly in the Y view because it was the non-bend view.

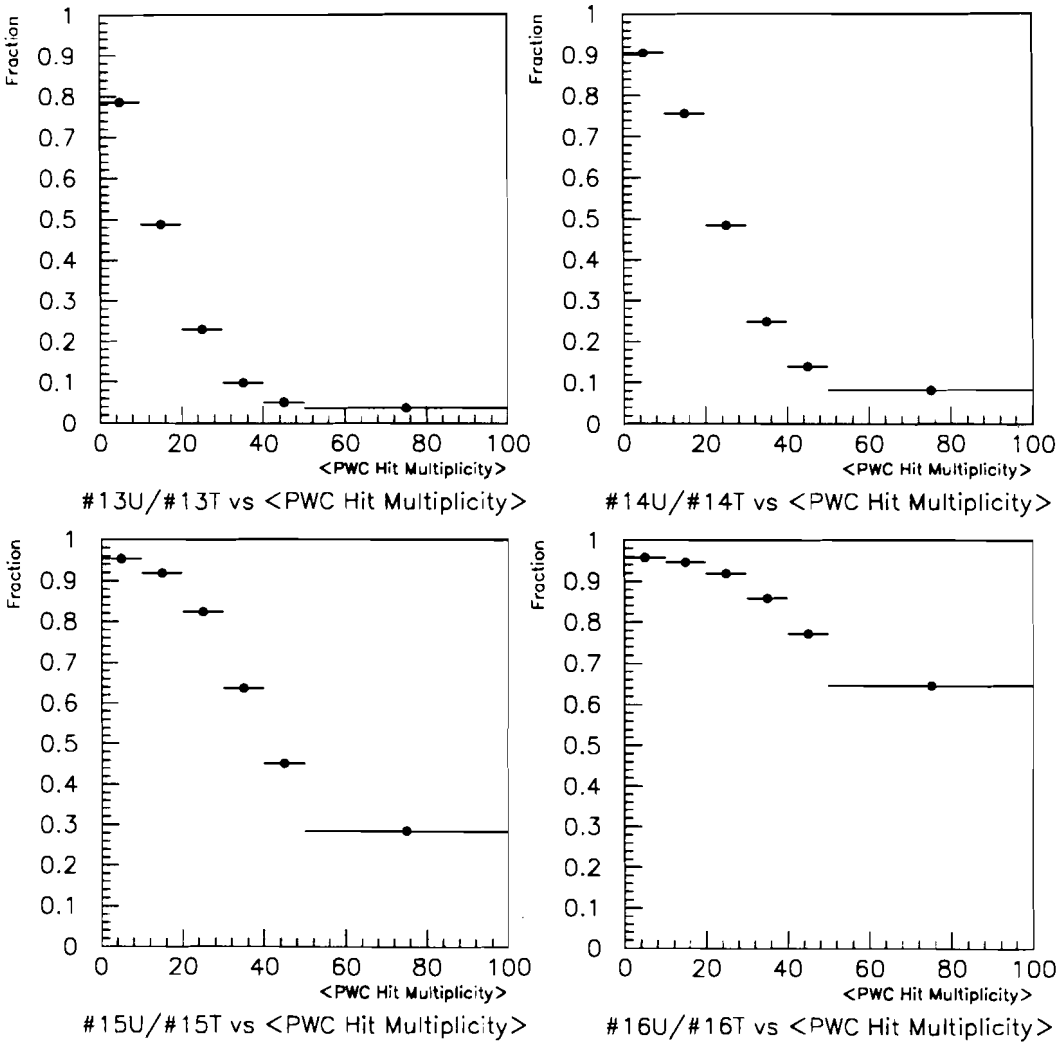

Figure 4.2 Fraction of unmarked tracks to total tracks for various numbers of hits versus the average PWC hit multiplicity.

In order to measure the effect of track marking on the data, three distinct samples were identified. These samples were (a) the dipions produced via decays of K^0_S mesons, (b) the electron pairs created from photon conversions in the target and detector[6], and (c) dimuons produced from the J/ψ resonance. Since each sample involves a measurable mass peak, the effect of the track marking can be seen by observing the effect on the signal with and without the track marking.

From the K^0_S sample, we can identify 2 subsamples. The samples are differentiated by the position of the reconstructed decay point. These samples are,

- The decays which were located using the SSD tracks, and hence the decay point is within a few centimeters of the primary vertex ($Z_{PRIM} < Z_{DECAY} < 0.0$ cm).
- Decays which occur beyond the SSD tracking acceptance, ($0.0 < Z_{DECAY} < 200$ cm).

The latter of the two only makes use of the downstream tracks to reconstruct the decay point, whereas the first uses the SSD tracks to locate the decay point. The features which differentiate these samples are (a) the average momentum of the pions in the decays, and the Y view impact parameter distribution at the primary vertex. As the decay distance increases, so will the average momentum of the decay products, and hence the charged tracks from these subsamples populate different regions of phase space. Secondly, since the *downstream Y view impact parameter* distribution varies between the samples (it broadens as the decay distance increases), one can see the difference in track marking as the impact parameter of the charged tracks varies from small to large. Recall that the cuts are substantially tighter for tracks with large Y view significance.

---

[6] Electron pairs from photon conversions were referred to as zero mass pairs or ZMPs.

Figure 4.3(a) shows the $\pi^+\pi^-$ mass distribution for all pairs of oppositely charged tracks in the first of the above mentioned samples. Figure 4.3(b) shows the same distribution, except that the marked tracks are removed. Figure Figure 4.3(c) shows the difference between Figure 4.3(a) and Figure 4.3(b). One observes little or no loss of K^0_S signal events, indicating that the track marking works reasonably well for this class of tracks (low momentum, small Y view impact parameter).

Figure 4.4(a)-(c) shows the same distributions for the second class of tracks mentioned above. Here the impact parameter distribution of the charged tracks is somewhat broader, and the momenta somewhat higher. For this class of tracks, there is a huge reduction in background with only a minimal loss of signal.

From these plots it is clear that the track marking has the largest effect on tracks which have large Y view impact parameter (significance), where the combinatorial solutions are most abundant. The large Y view impact parameter is generated by the high degree of hit sharing which occurs among spurious tracks. The large impact parameter tracks generated via downstream decays are not expected to have a high degree of hit sharing, and therefore the track marking does not degrade the signal significantly.

The Zero Mass Pair (ZMP) sample is also quite sensitive to the track marking since the electrons from the conversion have an opening angle which cannot be resolved until the electrons are split by the magnetic field. Therefore, the signature of a ZMP is 2 downstream tracks which overlap in the Y view, and intersect at the middle of the magnet in the X view (within errors). Furthermore, the invariant mass of the two tracks should be nearly zero. Due to the overlap in the Y view, the tracks usually share all of the hits in that view, making ZMP's another sensitive sample to the hit sharing cuts. Figure 4.5(a) shows the invariant mass distribution of all pairs of oppositely charged tracks which intersect within ± 15 cm of the center of the magnet and have a slope difference in the Y view less than 4 mrad. The peak at ~ 1 MeV i.e. 2 m_e, is a result of the photon conversions in the target and detector

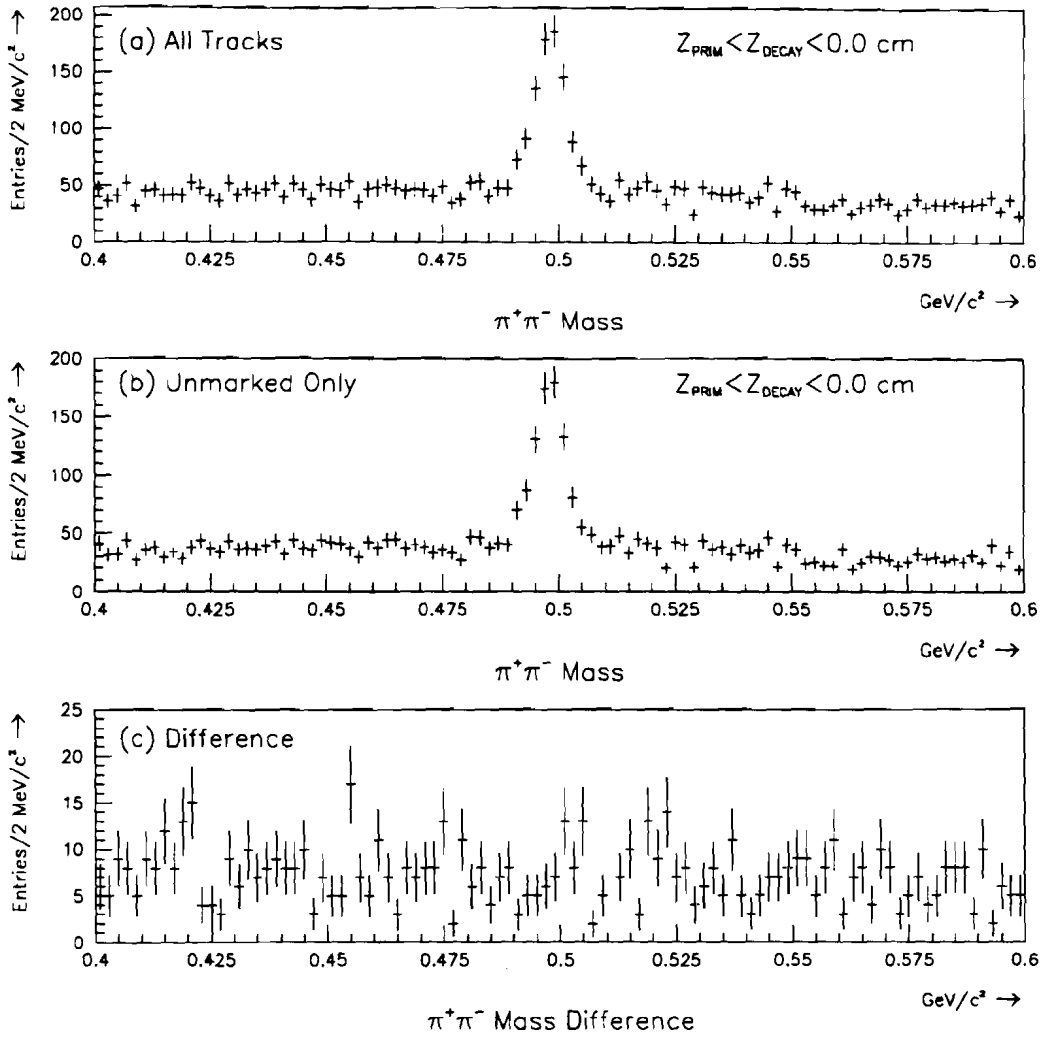

Figure 4.3 $\pi^+\pi^-$ mass distributions for (a) all tracks, (b) unmarked tracks only, and (c) the difference between (a) and (b). The decays are restricted to the region $Z_{PRIM} < Z_{DECAY} < 0.0$ cm.

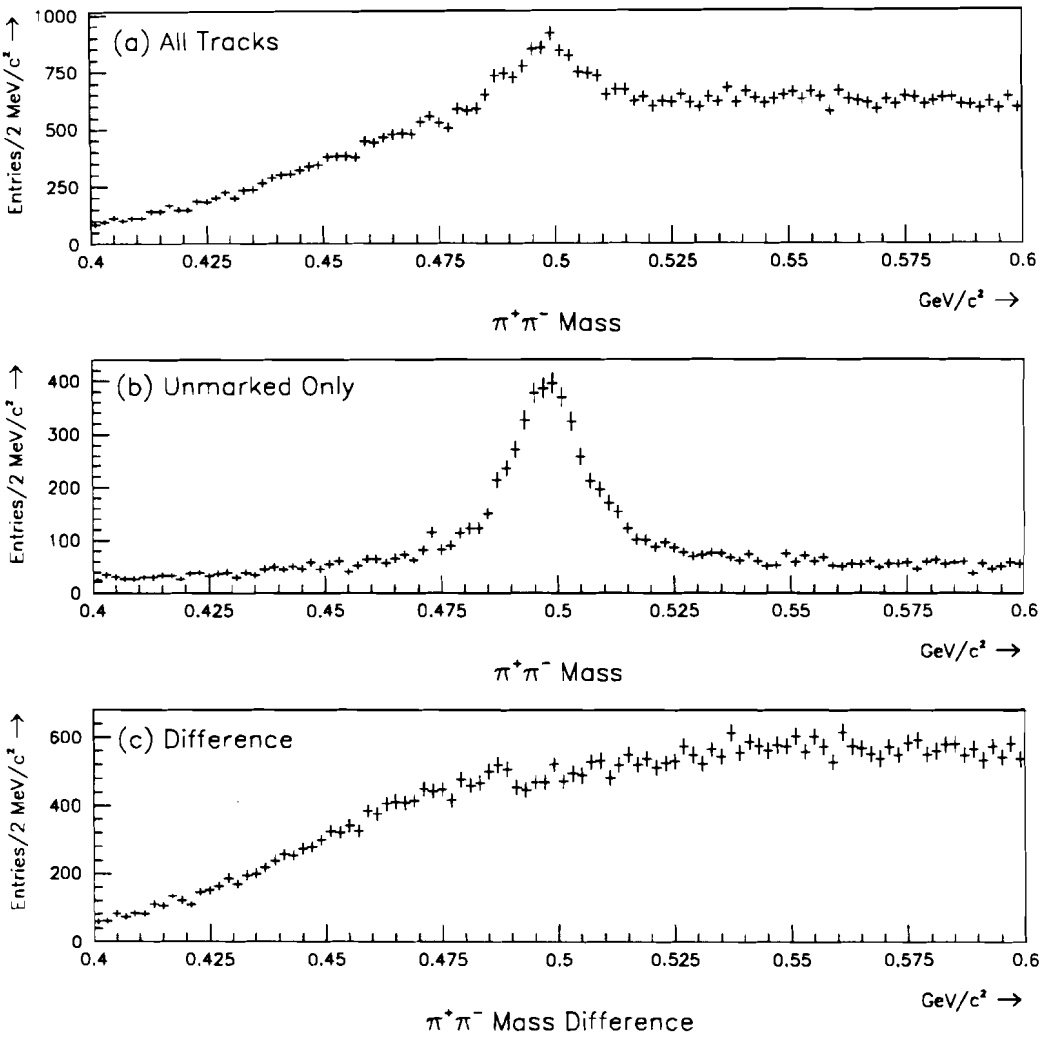

Figure 4.4 $\pi^+\pi^-$ mass distributions for (a) all tracks, (b) unmarked tracks only, and (c) the difference between (a) and (b). The decays are restricted to the region $0 < Z_{DECAY} < 200$ cm.

(ZMPs). Figure 4.5(b) shows the fraction of the tracks which have an invariant mass less than 2.0 MeV which are unmarked. The fraction is plotted in two bins of the *average PWC hit multiplicity*. One observes that more ZMP electrons are mistakenly marked as the event multiplicity increases. This is a special class of tracks, and certainly the most sensitive to the track marking cuts.

The third sample comes from data taken using the E672 dimuon spectrometer, which triggers on high mass dimuons. Since E672 used the E706 tracking detectors, and similarly, the corresponding tracking software, the effects of the track marking could be tested on the J/ψ signal. The muon tracks emerging from these triggered J/ψ decays cover a wide range of momentum, with a minimum momentum of about 15 GeV/c[7]. Furthermore, these muons are expected to have a good Y view impact parameter to the primary vertex ($\sigma_Y < 5$). Figure 4.6(a) shows the J/ψ signal with no track marking criteria used. Figure 4.6(b) shows the same plot, except it is required that both muon tracks are not marked. Figure 4.6(c) is the difference between (a) and (b). From this set of plots, one can conclude that the track marking does not remove a significant number of high momentum tracks from the data.

The downstream track multiplicity before marking was shown in Figure 3.3. One observes the tail of events extending much beyond 40 tracks/event. A plot of the number of *unmarked* physics tracks/event is shown in Figure 4.7. From this plot, and the preceding discussion, one observes that the track marking has cleaned the sample substantially, with only a minimal loss of real tracks. From this point onward, unless stated otherwise, physics tracks refers to the unmarked tracks only.

[7] The momentum cutoff at 15 GeV/c is a result of the full E706 spectrometer in front of the E672 dimuon spectrometer.

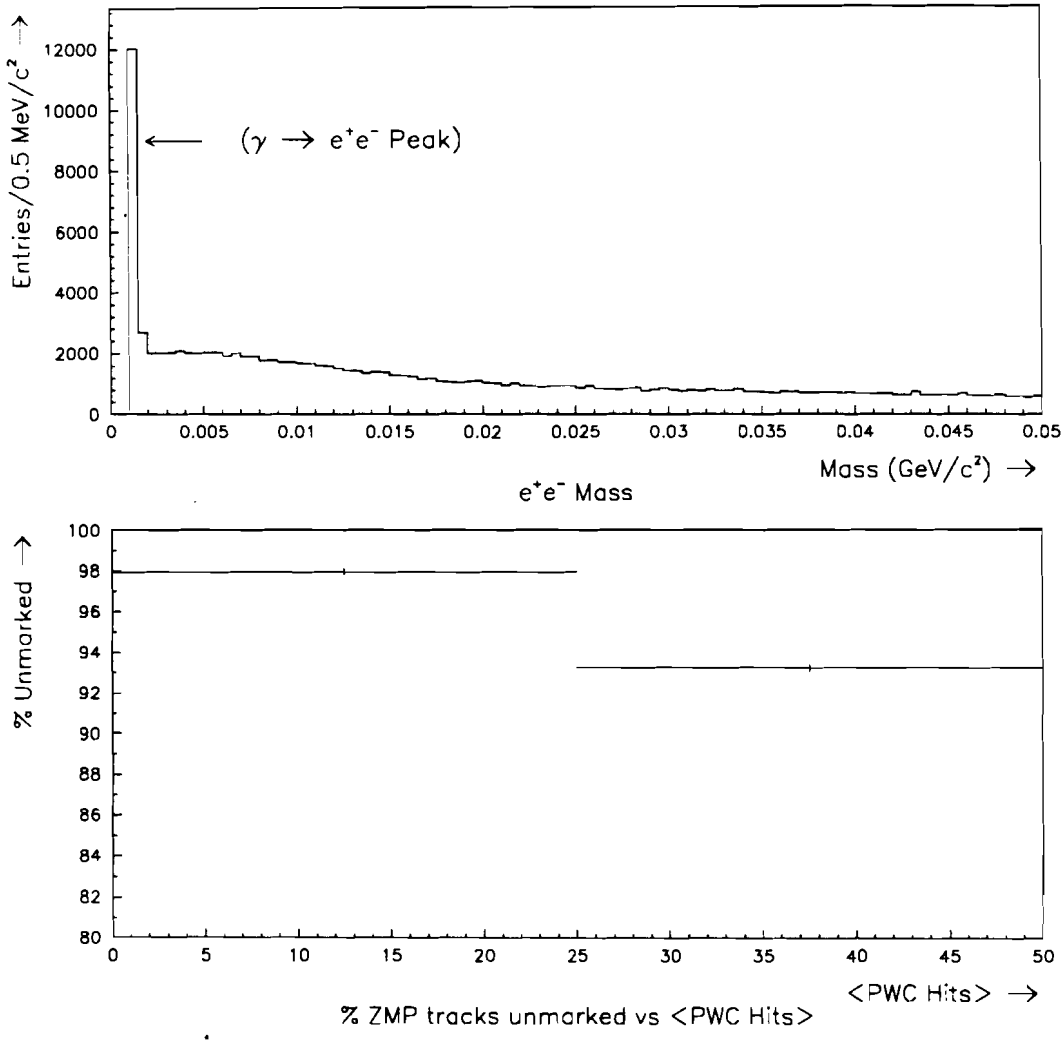

Figure 4.5 (a) e^+e^- invariant mass distribution, and (b) Fraction of electrons from ZMP's marked as a function of the average PWC hit multiplicity.

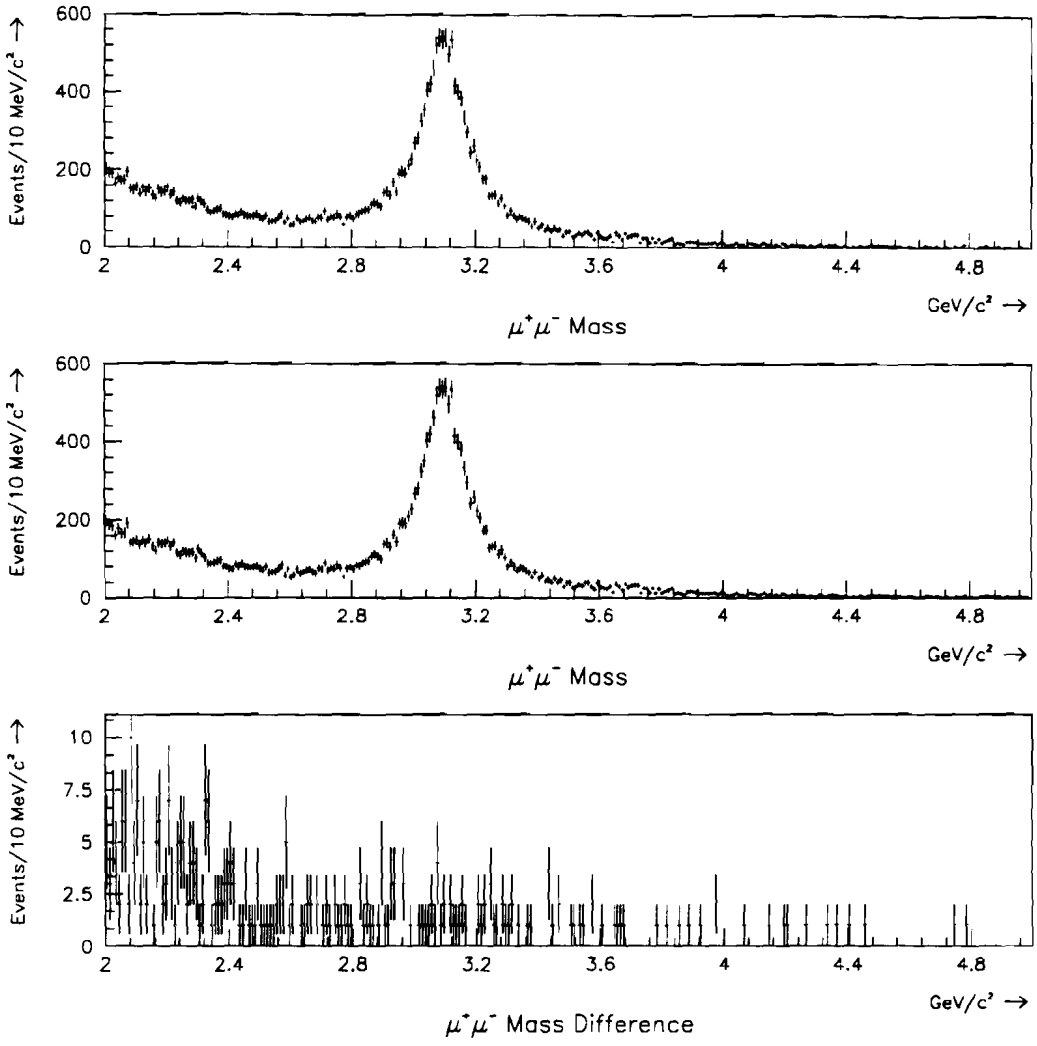

Figure 4.6 Dimuon invariant mass distribution for (a) All opposite sign muons, (b) Unmarked tracks only, and (c) the difference between (a) and (b). Compliments of H. Mendez (E672).

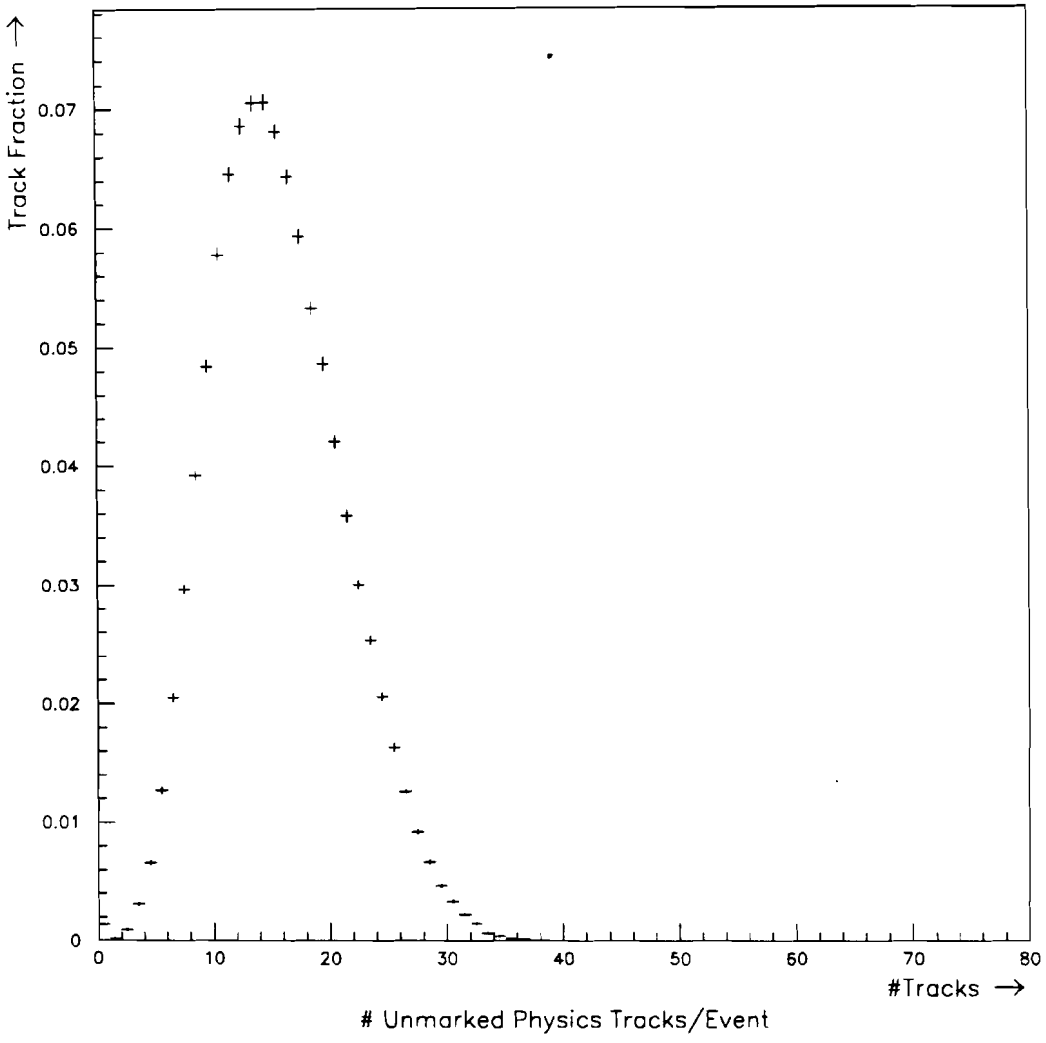

Figure 4.7 Number of unmarked physics tracks per event for events containing a high p_T π^0.

4.4 Tuning of the Momentum Scale

In order to perform the physics analysis using the tracking information, it was necessary to make sure that the momentum scale was correct. The best estimates of the magnetic field strength and magnetic length were used to measure the momentum of charged tracks. The data taken with the MWEST apparatus included an abundant sample of K^0_S, Λ^0 (E706), and J/ψ (E672), which were used to tune the impulse of the magnet. All three particles mass distributions were simultaneously brought into agreement with average world values. Since the charged tracks from these decays cover a wide range of momenta, the momentum measurement of charged tracks is quite linear over the full momentum range. Figure 4.8 shows the $\pi^+\pi^-$ mass distribution for (a) secondary vertices reconstructed using SSD and PWC/STRAW tracks, and (b) secondary vertices located downstream of the SSD system where only PWC/STRAW tracks were used in locating the secondary vertex. Figure 4.9 shows the corresponding pπ mass plots in the Λ mass region. The background is higher in the combined SSD+PWC/STRAW mass plots due to very loose reconstruction cuts. Nearly all of the background can be removed by requiring that the parent momentum vector of the 2 track vertex points back to the primary vertex in the event. Also shown in Figure 4.10 is the $\mu^+\mu^-$ invariant mass distribution in the region of the J/ψ. All three signals are seen to agree well with the world averages.

4.5 Tuning of the EMLAC Energy Scale

The tuning of the EMLAC energy scale involved linearizing the reconstructed energy as a function of the input energy. Since this work has been presented elsewhere in great detail [24], only a brief description is given here.

The overall EMLAC energy scale was set using the electrons whose momenta was measured in the tracking system. Since electrons shower similarly to photons, the overall EMLAC scale could be set to within a few percent using electrons. The

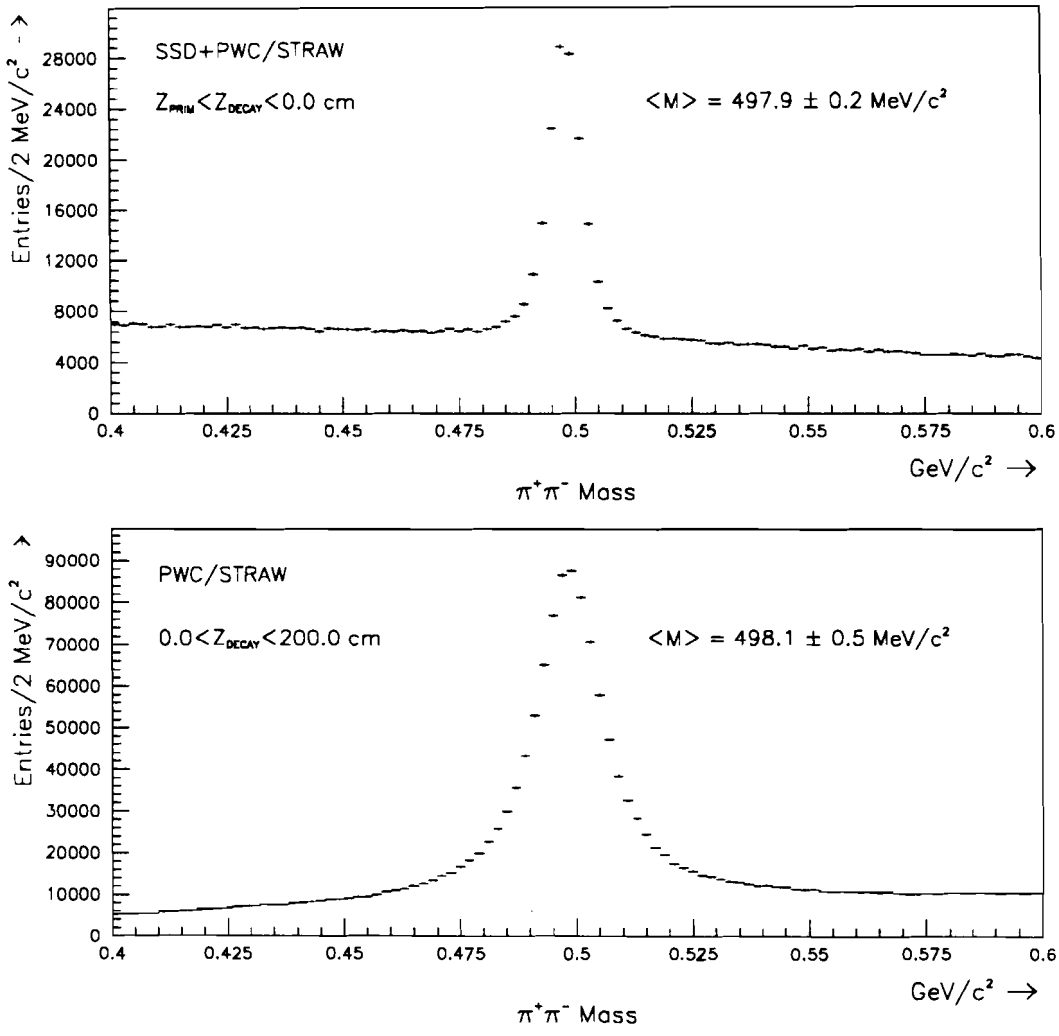

Figure 4.8 (a)Dipion invariant mass distribution for secondary vertices located using the SSD tracks, and (b) dipion mass distribution for decays beyond the SSD acceptance, using only the PWC/STRAW chambers.

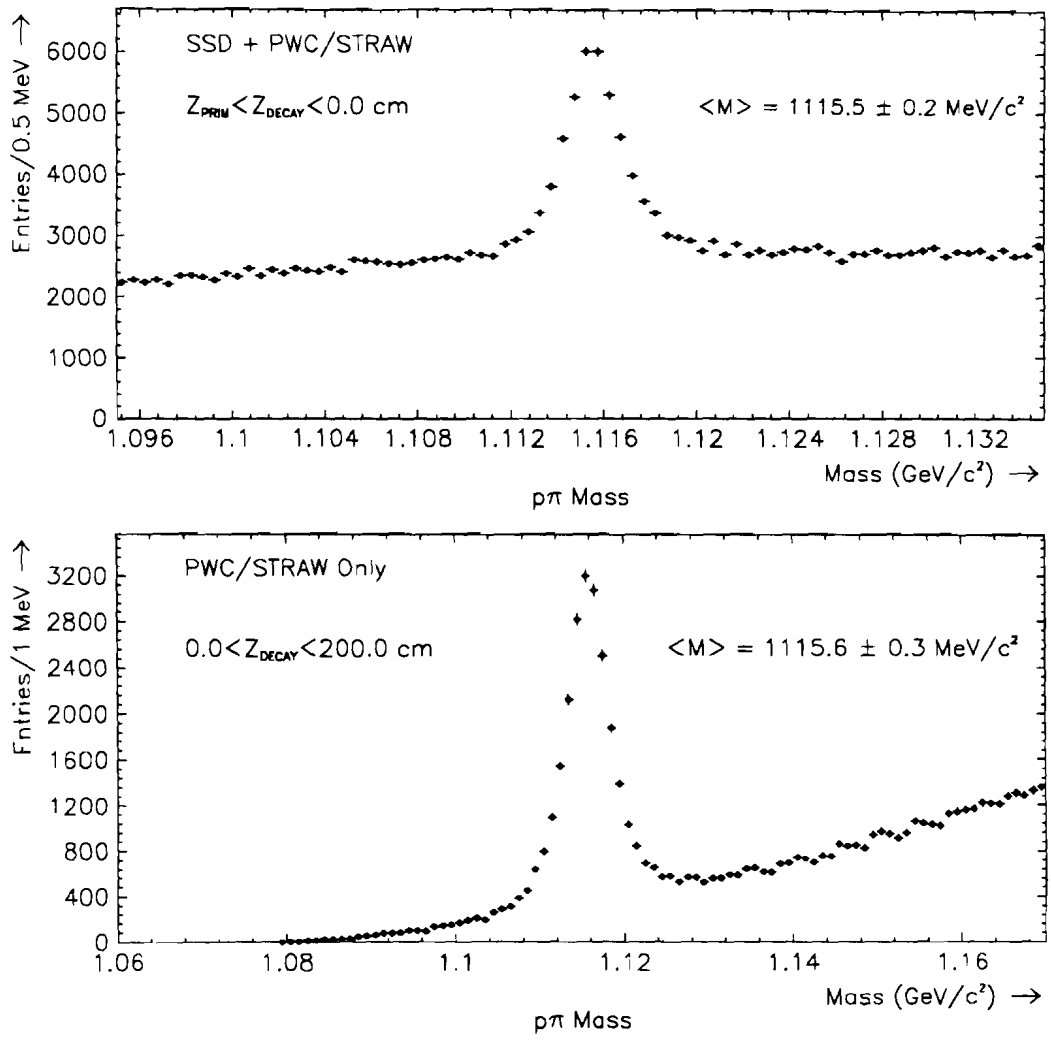

Figure 4.9 (a) pπ invariant mass distribution for secondary vertices located using the SSD tracks, and (b) pπ mass distribution for decays beyond the SSD acceptance, using only the PWC/STRAW chambers.

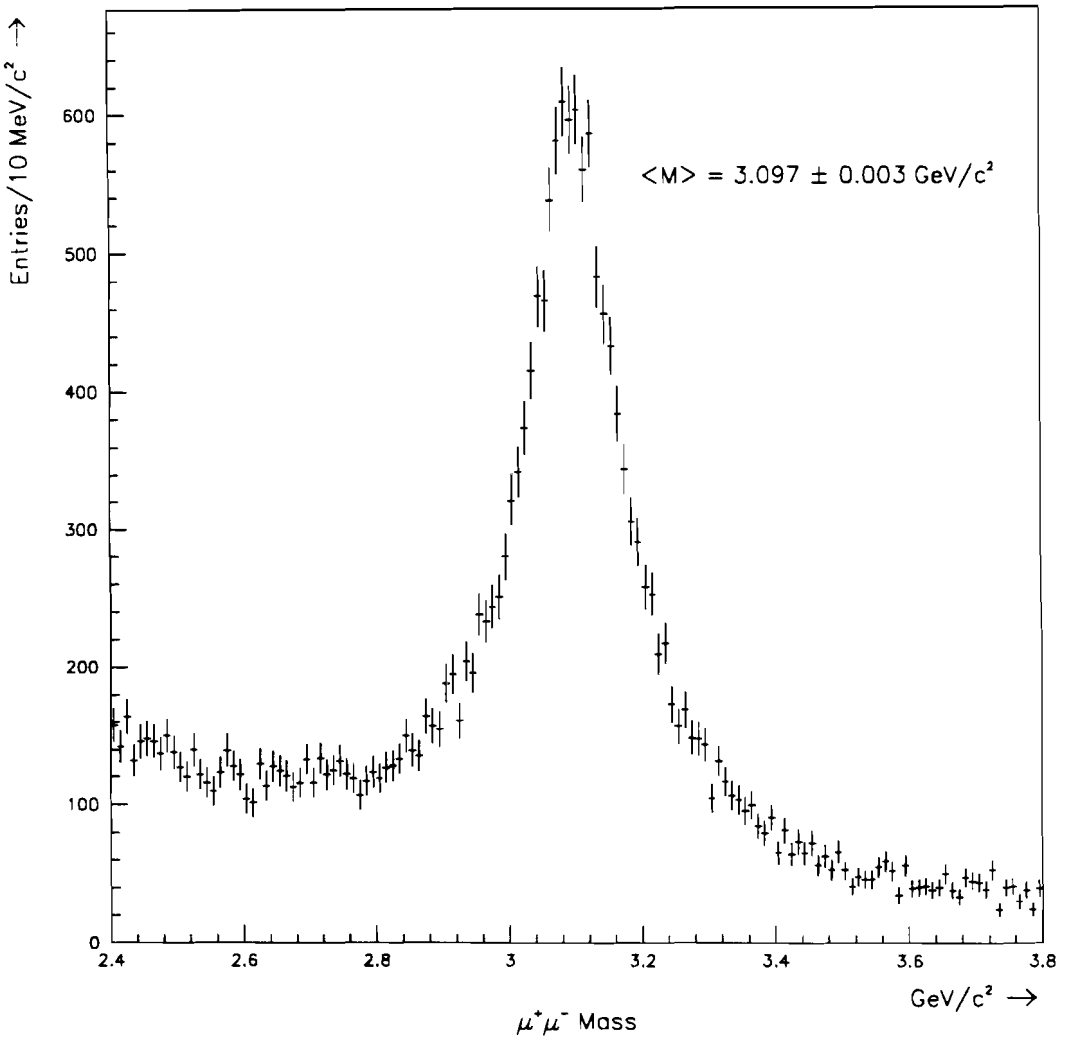

Figure 4.10 Dimuon invariant mass distribution in the region of the J/ψ resonance, compliments of H. Mendez (E672).

residual corrections in the 1990 data were performed using the π^0 and η signals, as well as electrons.

The most striking feature of the energy scale of the EMLAC was the observed increase in the energy read out as a function of the number of beam exposure days. This same feature was seen in both the π^0 and η mass signals. The same effect was also observed in the HALAC, when comparing the momentum of charged tracks to the associated energies measured by the hadron calorimeter. Figure 5.1 shows the observed increase in the EMLAC energy scale as a function of beam days. A correction to the reconstructed energies was introduced which accounted for this dependence of the energy scale on beam days. While this effect has been corrected for, at this time there is no definitive understanding of its cause[24].

Further tuning of the EMLAC energy scale included a correction for the energy lost by photons and electrons in the material in the front of the EMLAC. The remainder of the energy corrections were typically less than 5% as an extreme. These corrections included octant to octant variations, radial dependence of the energy scale, and fine tuning of the energy scale as a function of beam days. Upon completion, the energy scale was observed to be flat in all the relevant variables i.e. p_T, Rapidity, Energy, etc. Figure 4.12 shows the 2 photon invariant mass distribution in the π^0 and η mass regions, which are both in good agreement with the world averages.

4.6 Charm Event Selection Algorithm

The events of interest for this analysis are those events which have secondary vertices. It was found that the reconstruction efficiency could be substantially improved with an alternate algorithm which could run directly from the information available from the DST. This algorithm, developed by the author of this thesis, was shown to increase the K^0_S signal by about a factor of 2 over that provided by PLREC. It was likely that the improvement to the charm signal would be more

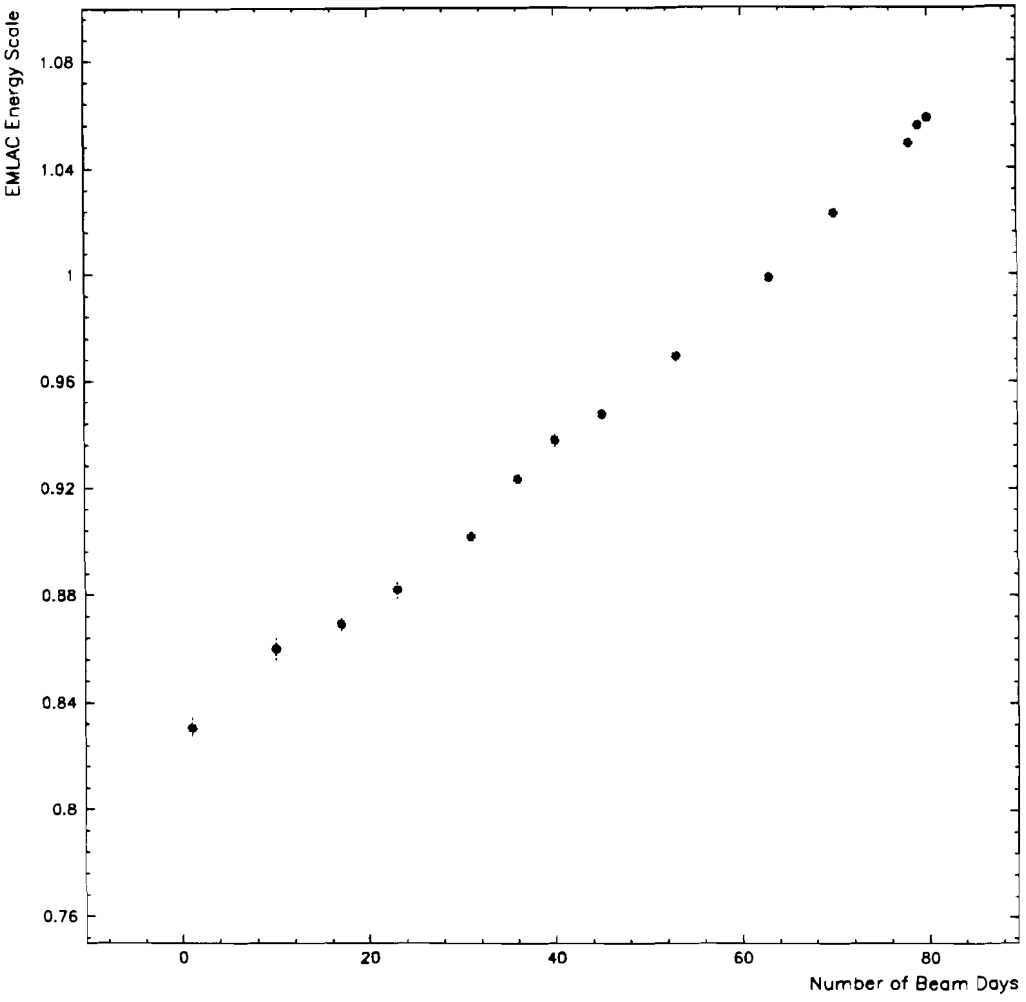

Figure 4.11 Ratio of the reconstructed π^0 mass to its nominal value as a function of the beam days for the 1990 running period.

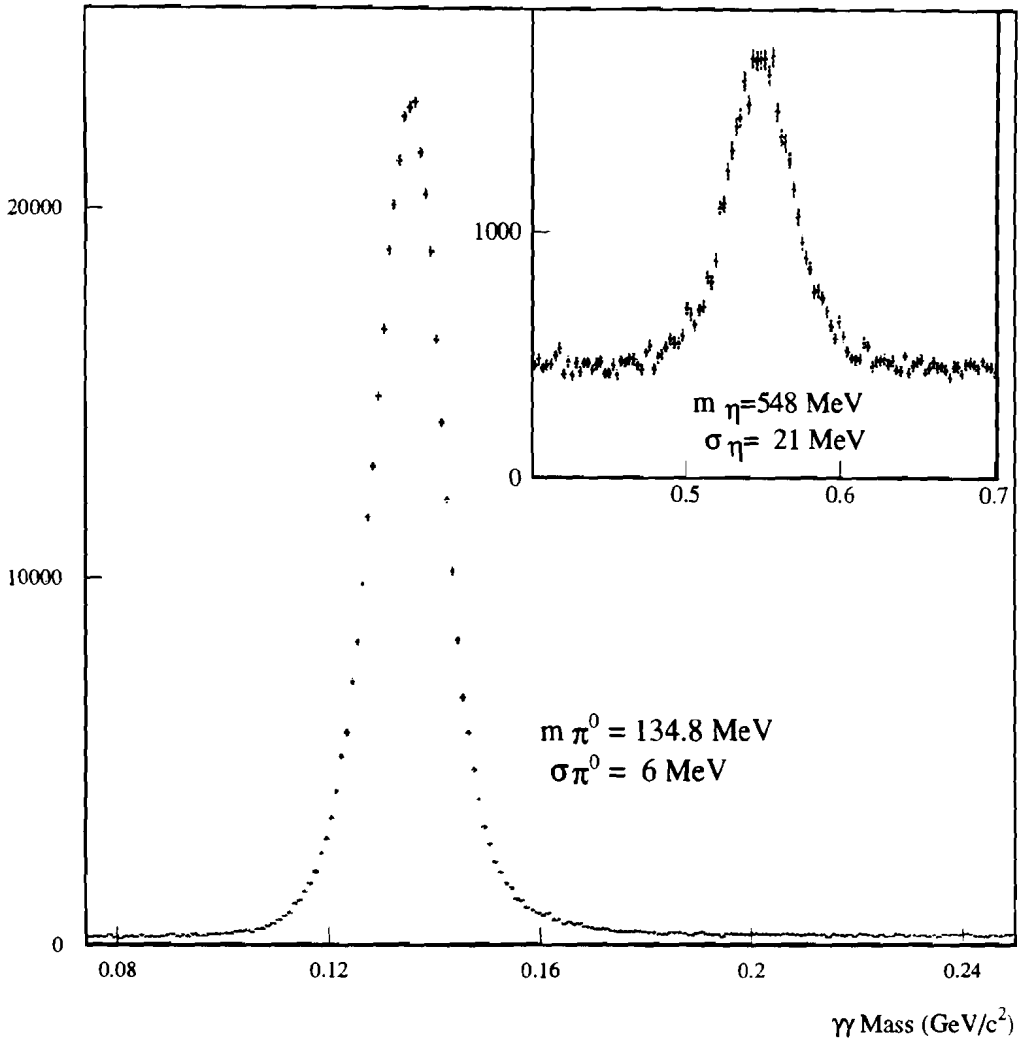

Figure 4.12 Di-photon invariant mass distribution in the region of the π^0 and η mesons for the 1990 data.

substantial than to the K^0_S signal. This was suspected due to the biases invoked in the relinking stage of PLREC (see Chapter 3). In the following sections is a discussion of the reconstruction program used to locate secondary vertices using the information available on the DST. The main features of the algorithm include,

- DST linking;
- Determination of SSD space tracks and identifying primary and secondary tracks;
- Vee and vertex finding.

The efficiency of the algorithm was estimated using a MC full detector simulation. The details of the detector simulation and various comparisons will be presented in the next chapter.

4.6.1 Preliminary Issues

Before diving into the details of the reconstruction algorithm, we shall discuss a few of the more important preliminary issues which were addressed in the early stages of this analysis. These issues were,

- SSD X and Y view scales; and
- Estimation of the SSD track resolution.

SSD X and Y View Scales

Upon completion of the alignment of the SSD chambers, it was observed that the Z position of the primary vertex as reconstructed in the X and Y views independently (ΔZ), had an offset of $\sim$150 μ. In order to understand the effect more clearly, the (ΔZ) was plotted as a function of the Z position of the primary vertex. A flat offset would indicate a simple shift in the overall intercept, whereas a slope would indicate a scale difference between the X and Y views. A scale problem implies that the slopes of SSD tracks are being systematically mismeasured by a small amount. Figure 4.13(a) shows the difference in the Z location as found in the

X and Y views independently. Figure 4.13(b) plots the same difference as a function of the vertex position. One observes a 0.05% slope, indicating that there is a scale difference in the 2 views.

A correction was introduced to correct the tracks' parameters to account for the scale difference. Using magnet off data, and projecting SSD X and Y view tracks to the PWC's, it was concluded that the X view scale was slightly contracted. Consequently, the correction was applied to the X view only. Figure 4.14 shows the same plots as in Figure 4.13 after the correction was applied. The X view scale in the monte carlo was also contracted as seen in the data, so that the same correction could be applied to both the data and the monte carlo.

Estimation of SSD track errors

In order to decide whether or not a SSD track belongs to the primary vertex, one needs to know the expected error in the impact parameter. Generally, one expects that most of the tracks emanating from the primary vertex should have an impact parameter δ to the primary vertex which is of the same order as its associated error (σ). Since tracks produced at the primary vertex tend to have a significance s $= \delta/\sigma < 3$, one can assign a large fraction of tracks to the primary vertex based on a significance cut.

The projection uncertainty is primarily a function of the momentum, the intrinsic hit errors, the number of hits on the track, and the hit configuration[8]. In a more complicated way, it also depends on the local hit density around the track as well. To incorporate all the experimental effects, the errors were determined directly from the data. By measuring the distribution of impact parameter's of SSD tracks to the primary vertex in various momentum and Z bins, we obtained an experimental measurement of the projection resolution in these variables. Figure 4.15 shows the

[8] By hit configuration, it is meant which of the SSD planes registered a hit for a given track.

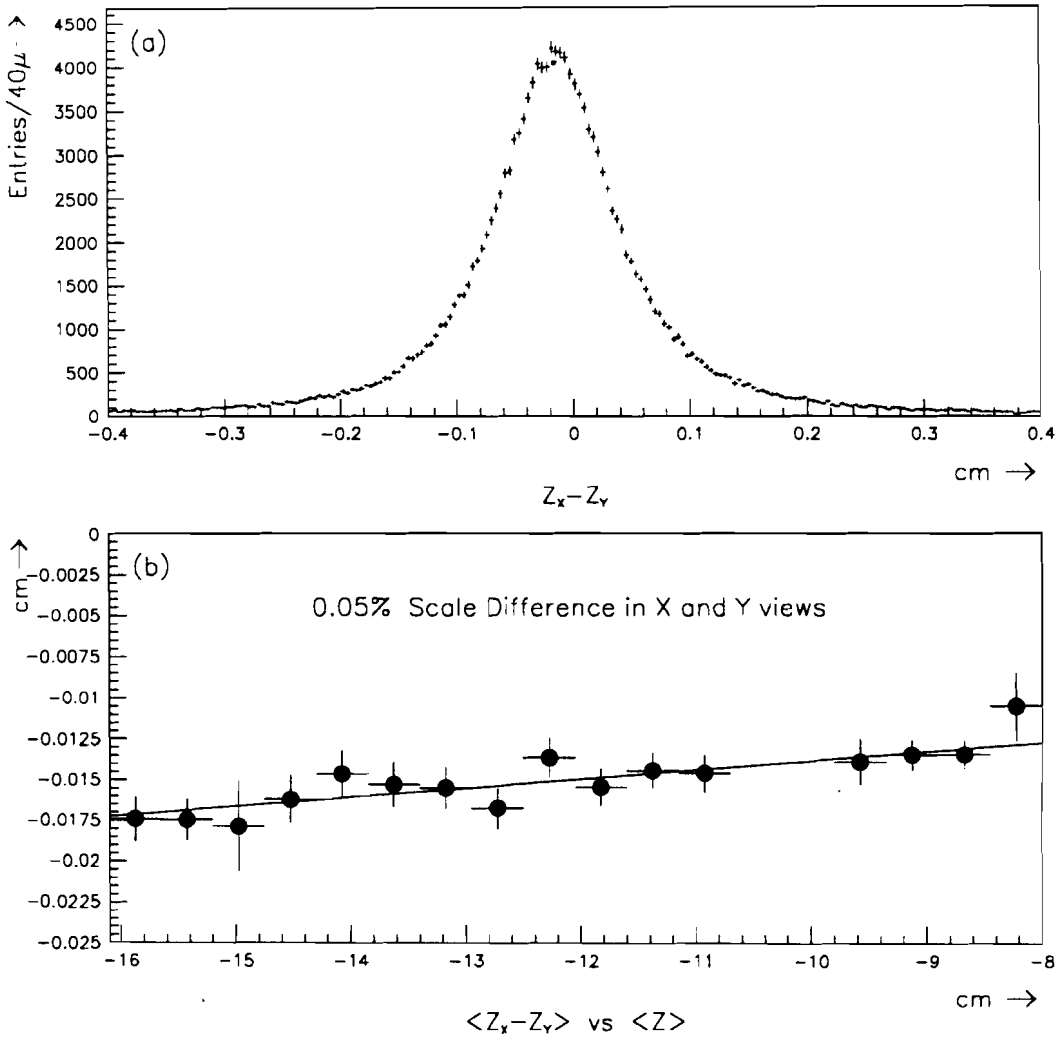

Figure 4.13 (a) Difference between the X and Y locations of the primary vertex, and (b) ΔZ plotted as a function of the primary vertex location, before correction.

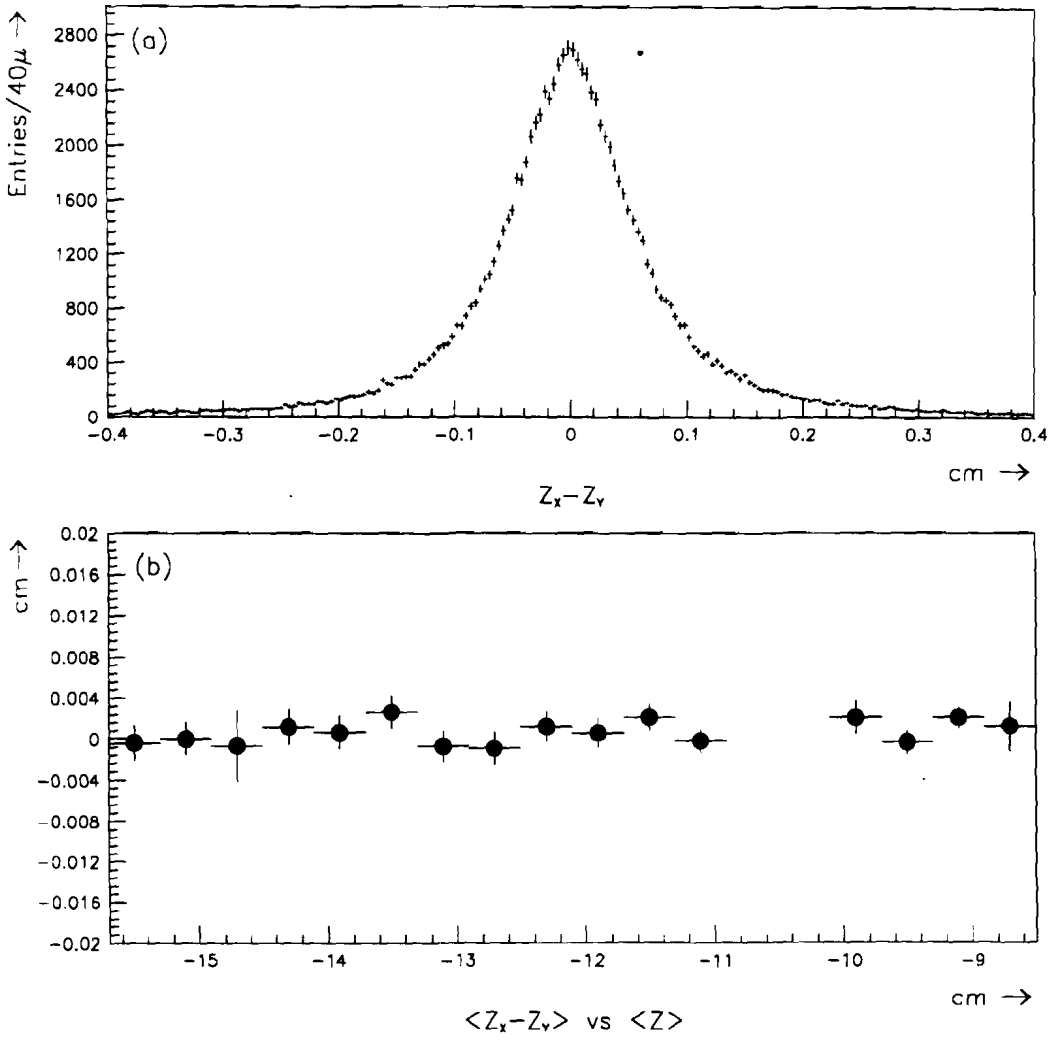

Figure 4.14 (a) Difference between the X and Y locations of the primary vertex, and (b) ΔZ plotted as a function of the primary vertex location, after correction.

measured projection error (uncertainty) of 3, 4, and 5 hit tracks in the X and Y views of the SSD's as a function of the track momentum and production point. All of the surfaces were fit to the form,

$$\sigma_{\mathrm{PROJ}} = (\mathrm{K}_1 + \mathrm{K}_2 * \mathrm{Z}) * \exp(-\mathrm{K}_3 * \mathrm{p}) + (\mathrm{K}_4 + \mathrm{K}_5 * \mathrm{Z}) \qquad 4.2$$

where the constants $\mathrm{K_I}$ depend on the number of SSD hits and the view (X or Y), while p and Z are the momentum and production point respectively. For a fixed Z, the function gives an exponential form for the projection error, while for a fixed momentum, the function exhibits a linear increase as the projection distance increases. Each sample averages over all hit configurations[9]. From this functional form, the momentum dependent piece was isolated. To get the projection error for a given track, this momentum dependent piece was added in quadrature with the projection error calculated from each track's error matrix. The error matrix reflects the hits used in the SSD track fit and their associated errors. It was determined that the theoretical hit errors needed to be scaled up by ~20 % in order to agree with the experimental error. This effect is primarily due to effects of hit clusters which tend to confuse the pattern recognition program and small alignment defects. The resulting experimental resolution was still fine enough to distinguish tracks from secondary decays with some reasonable efficiency.

---

[9] For example a 4 hit track has 5 hit configurations for the 5 plane SSD system.

vertex calculated in the *absence of multiple scattering*[11]. Tracks which had a significance to the primary vertex of less than 3.0 were assigned to the primary vertex. Figure 4.17 shows the X and Y view SSD track significance to the primary vertex **without the inclusion of multiple scattering.**

Based on the initial significance information, tracks fell into the following two categories:

Category 1: Downstream tracks which had both the X and Y view best link having a significance less than 3.0 (as in Figure 4.17) were automatically assigned to the primary vertex. Recall that the best links were chosen based only upon the linking, with no bias toward the primary vertex. If both best links were consistent with the primary vertex, this supported the contention that these tracks belonged to the primary vertex, or were indistinguishable from those which did.

Category 2: The second class consists of the cases where the X and/or Y best link had a significance greater than 3.0. The best link's large significance may be a result of either (a) multiple scattering, (b) combinatorial background, or (c) the track is from a secondary vertex. In addressing these issues, only the view(s) which failed the significance cut were tested.

In order to address the issue of multiple scattering, we recalculated the significance after inclusion of multiple scattering. Figure 4.18 shows the spacial significance to the primary vertex, as well as the individual contributions from the X and Y views **after the inclusion of the momentum dependent errors.** If both the X and Y view links had a significance of less than 2.5, or the spacial significance was less than 2.5, the space track was attached to the primary vertex.

---

[11] The significance without the inclusion of multiple scattering only required the error matrix of the SSD track. Since we initially ignored the multiple scattering, we did not need to worry about the track momentum.

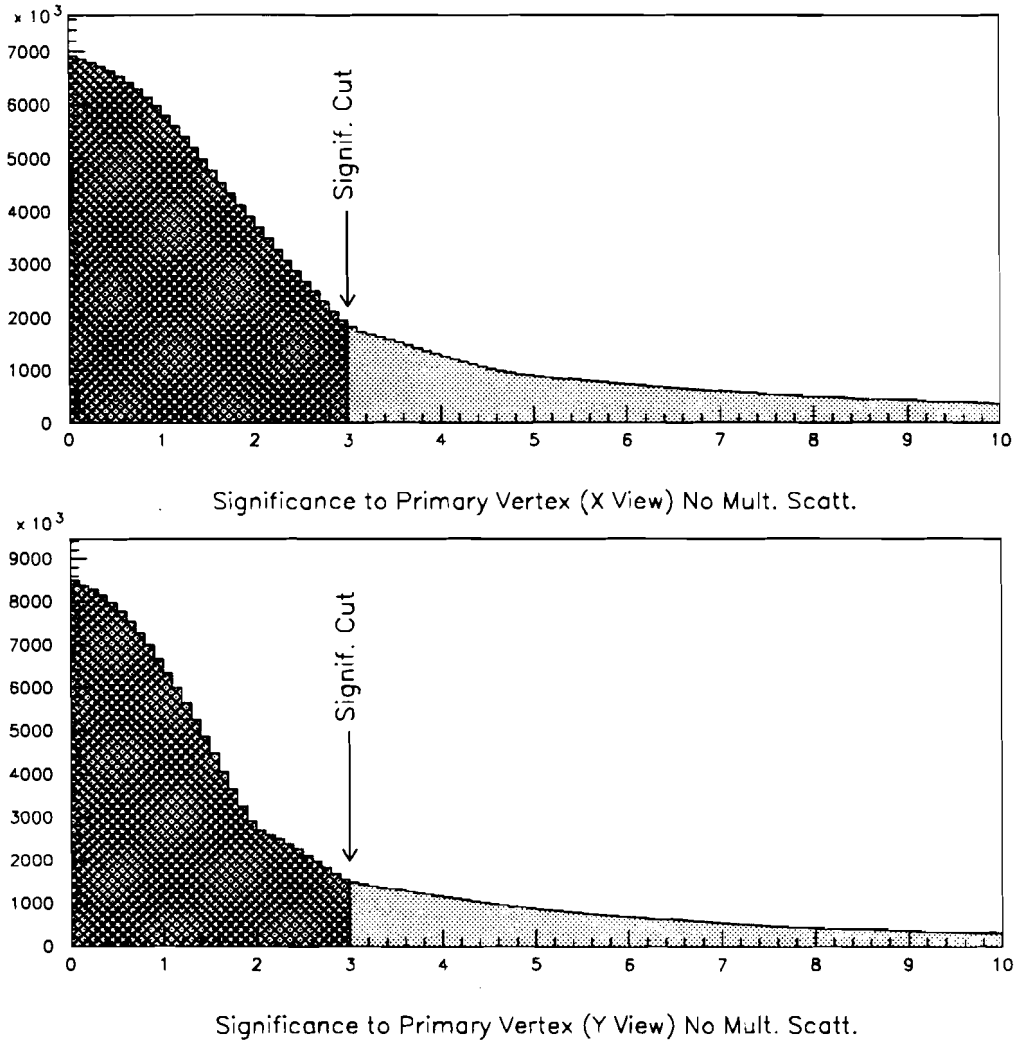

Figure 4.17 Significance of SSD tracks to the primary vertex without the inclusion of multiple scattering in the error calculation for the X and Y views.

In many cases, the best SSD link still failed the significance cut. In this case, we wish to address the possibility that the best SSD link(s) are from the combinatorial background. By combinatorial background, it is meant any SSD track which is mistakenly chosen as the best link. This *mislinking* is usually a consequence of the high track density, where there are several real and possibly fake SSD tracks in close proximity to one another[12]. As the linking resolution improves, the combinatorial background is reduced (see Figure 5.42). Nevertheless, for the case of multiple links, one does not know apriori, on a track by track basis, which link is the correct one. We therefore adopted a set of rules by which extra links could be considered as possible **replacements** for the original best link. The conditions only made use of the linking information, and did not utilize the information about the primary vertex. The rules for overriding the best link with an extra link were the following:

- The SSD extra link in question was **prohibited from being a best link of any other downstream track in the event**. This requirement was implemented so that one does not produce SSD link reassignments which cause two (or more) downstream tracks to have the **same** SSD link. In most cases, each downstream track should have its own SSD track to which it links.
- The second criterion applied to the quality of the linking for the best and extra link. Since the true best link has a high probability of having a small linking χ^2 (see Chapter 3), we allow an extra link to override the best link if either, (a) the extra link has a relatively small linking χ^2, or, (b) it's linking χ^2 is not too much larger than that of the best link.

---

[12] In the E706 tracking detector, there were typically 20 charged tracks contained within an angle of about 6-8 degrees. This contrasts with colliders which have a much larger fraction of the solid angle over which the tracks are distributed.

If any of the extra links passed both of these cuts, and it satisfied the impact parameter significance cut, it was allowed to override the best link. If no extra link passed these these criteria, then the space track in question was tagged as a secondary track candidate.

Figure 4.19(a) shows the fraction of space tracks which have their best links pointing back to the primary vertex. This plot gives the status prior to the inclusion of multiple scattering, or any link reassignments. The last bin represents the fraction which were initially attached to the primary vertex. Therefore, prior to including multiple scattering and the link reassignments, one has ~50% of tracks tagged as secondary particles.

After including the effects of multiple scattering and performing the relinking as described above, the fractions shift as shown in Figure 4.19(b). From the figure, one can see that the fraction of tracks which were candidates for secondaries was reduced from ~ 50% to about 30%. It was this 30% of space tracks which were used in the secondary vertex finding algorithm. The last bin shows that ~70% of the tracks were attached to the primary vertex.

4.6.4 Primary Vertex Refit

In PLREC, the primary vertex was fit without the inclusion of multiple scattering. Therefore, low momentum tracks carried just as much weight as high momentum tracks. In order to improve the resolution of the primary vertex, the primary vertex was refit using the same procedure as secondary vertices, which by default used momentum dependent errors. The tracks used in the refit were those assigned to the primary vertex as discussed in the previous section. The remaining tracks were used to find secondary vertices. (In Chapter 5, we shall present comparisons between MC and data regarding the quality of the vertex finding.)

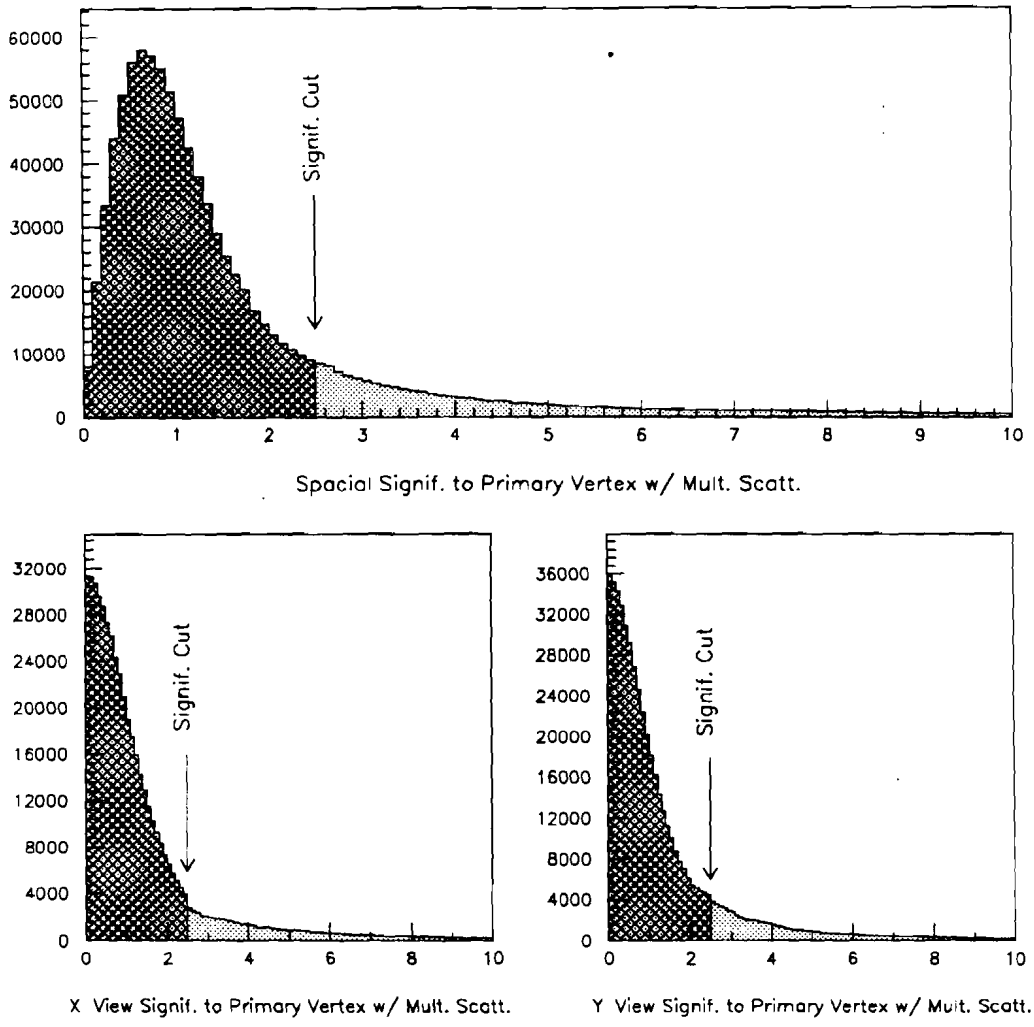

Figure 4.18 Spacial significance of SSD-space tracks to the primary vertex, and significance in the X and Y views, with the inclusion of multiple scattering in the error calculation.

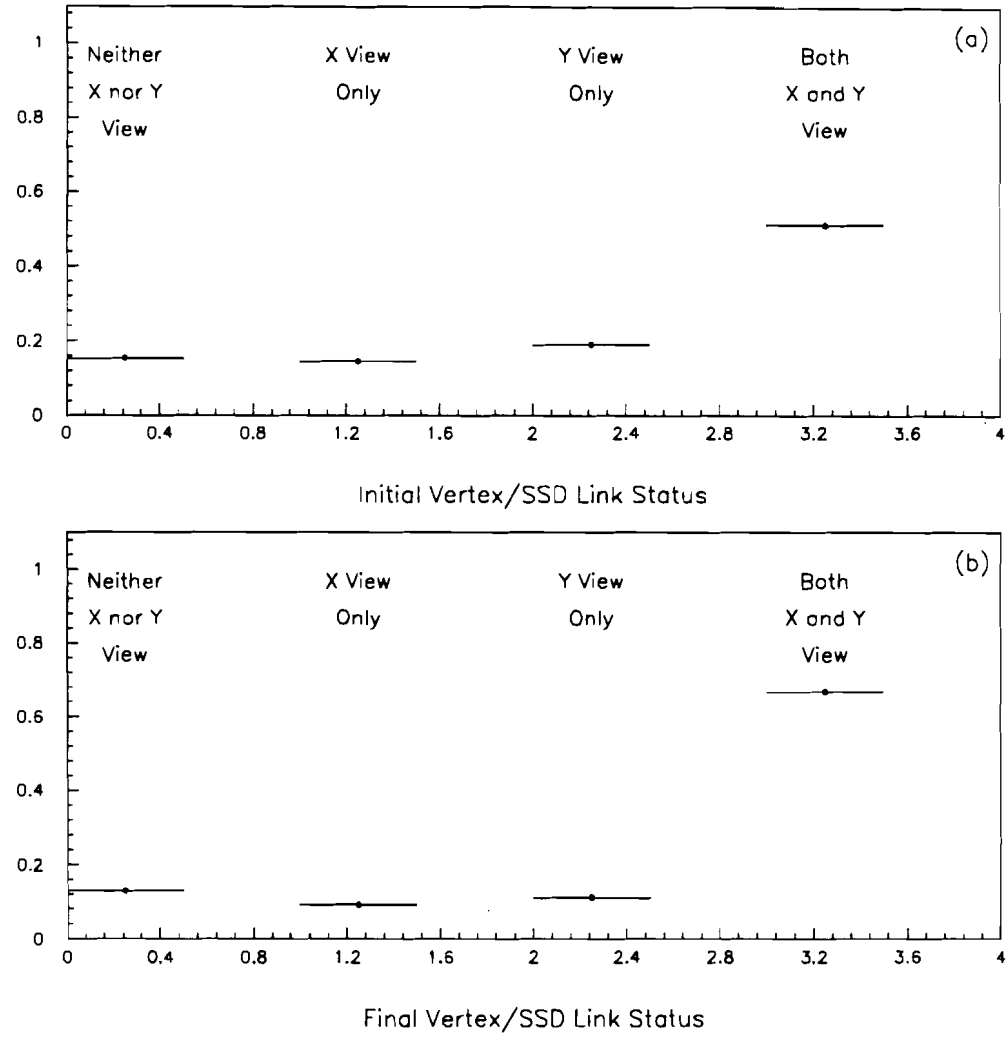

Figure 4.19 Fraction of space tracks whose links point back to the primary vertex based on (a) significance without the inclusion of multiple scattering, and (b) significance with the inclusion of multiple scattering, as well as after the relinking procedure.

Vertex fitting procedure

In this section we briefly describe the procedure used to fit the vertices. Prior to performing the vertex fit, it is assumed that a list of X and Y view SSD tracks has been provided. The set of X view tracks are used to obtain an estimate of the vertex coordinates in the X view, X and Z_X, and their associated errors, σ_X, and σ_{Z_X}. Analogously, one obtains the estimators, Y, Z_Y, σ_Y, and σ_{Z_Y} from the Y view SSD tracks. It is worthwhile to recognize that the X and Y views provide independent measurements of the Z coordinate of the vertex. We shall return to this point shortly.

Given a set of tracks, the vertex fitting procedure followed the usual chisquared minimization (or least squares) technique. For the sake of brevity, we shall only present the result for the X view; the Y view result is obtained by simply replacing X with Y in all of the following equations. The chisquared, $\chi^2_{\rm VERTEX}$, which we minimize is defined by,

$$\chi^2_{\rm VERTEX} = \sum_{i=1}^{N_X} \frac{(a_i * Z_X + b_i - X)^2}{\sigma_i^2} \qquad 4.3.$$

where the sum runs over all N_X tracks to be used in the vertex fit. The a_i's, b_i's, and σ_i's are the slopes, intercepts and projection uncertainties (see Figure 4.15) for the i^{th} track. The numerator of this equation is simply the square of the impact parameter to the point (X, Z_X)[13], and the denominator gives the expected error in the impact parameter. Minimizing 4.3 with respect to X and Z_X allows one to solve for those coordinates. In particular, we solve the simultaneous equations,

$$\frac{\partial \chi^2}{\partial X} = 0 \qquad \text{and} \qquad \frac{\partial \chi^2}{\partial Z_X} = 0 \qquad 4.4.$$

The minimization yields the solutions,

[13] This neglects the small angles of the SSD tracks.

$$\begin{pmatrix} X \\ Z \end{pmatrix} = \begin{pmatrix} S & -S_a \\ -S_a & S_{aa} \end{pmatrix}^{-1} \begin{pmatrix} S_b \\ -S_{ab} \end{pmatrix},$$

with,

$$S = \sum_{i=1}^{N_X} \frac{1}{\sigma_i^2}, \qquad S_a = \sum_{i=1}^{N_X} \frac{a_i}{\sigma_i^2}, \qquad S_{aa} = \sum_{i=1}^{N_X} \frac{a_i^2}{\sigma_i^2}$$

$$S_b = \sum_{i=1}^{N_X} \frac{b_i}{\sigma_i^2}, \qquad S_{ab} = \sum_{i=1}^{N_X} \frac{a_i * b_i}{\sigma_i^2}$$

The solutions to this matrix equation can easily shown to be,

$$\begin{aligned} X &= \frac{1}{D} * (S_{aa} * S_b - S_a * S_{ab}) \\ Z_X &= \frac{1}{D} * (S_a * S_b - S * S_{ab}) \end{aligned} \tag{4.5}$$

where,

$$D = S * S_{aa} - S_a^2$$

is the determinant of the covariance (error) matrix. From the covariance matrix, once can extract the variances in the X and Z coordinates as,

$$\sigma_X^2 = S_{aa}/D \qquad \text{and} \qquad \sigma_Z^2 = S/D. \tag{4.6}$$

The expectation value for the errors in the X and Z coordinates are then given by the square root of their respective variances. Once the set of tracks has been specified, X, Z, σ_X, and σ_{Z_X} are all calculable from 4.5 and 4.6. The same analysis follows for the Y view, which yields Y, Z_Y, and their errors σ_Y and σ_{Z_Y}.

One can easily verify that for the 2 track case (assuming $\sigma_1 = \sigma_2 \equiv \sigma$), we have,

$$Z_X = \frac{(b_1 - b_2)}{(a_2 - a_1)} \qquad \text{and} \qquad \sigma_{Z_X} = \sqrt{\frac{2}{(a_1 - a_2)^2}} * \sigma. \tag{4.7}$$

As expected, the Z position is simply the intersection point of the two tracks. One also finds that the error in the Z coordinate is inversely related to the magnitude of the opening angle, and directly proportional to the track's projection uncertainty. From this simple example, one can see that the track errors enter directly into the calculation of the vertex errors. Therefore, if the errors on the tracks are underestimated (overestimated), the calculated vertex resolution will also be underestimated (overestimated).

In order to investigate the integrity of the assigned track errors (see Figure 4.15), we can compare the **measured value** of $\Delta Z \equiv Z_X - Z_Y$ for the primary vertex, with the expected error based on the fit. If the track errors properly account for their contribution to the vertex uncertainty, σ_{Z_X} should reflect the uncertainty in Z_X, and σ_{Z_Y} should account for the uncertainty in Z_Y. It therefore follows that $\sigma_{\Delta Z} = \sqrt{\sigma_{Z_X}^2 + \sigma_{Z_Y}^2}$ should reflect the error in the measured value of ΔZ. In Figure 4.20(a), is shown the measured difference in the Z location of the primary vertex between the X and Y views. In Figure 4.20(b), we plot the ratio $\Delta Z/\sigma_{\Delta Z}$, for each event. The distribution has unit width, implying that the **calculated vertex error correctly accounts for the experimentally measured view vertex separation**. Therefore, we conclude that the track errors are properly taken into account by the parametrization of 4.2.

It is also worthwhile to discuss Figure 4.20(a) in more detail. As mentioned previously, this figure is the measured difference between Z_X and Z_Y for the primary vertex. If the SSD detector had perfect resolution, this distribution would be a *delta function* peaked at 0.0. Since this is not the case, we expect the width (or half width at half maximum (HWHM)) to give some indication of the magnitude of the longitudinal vertex error (Z error). It is fairly simple to show that the **view vertex resolution** is approximately equal to $\sigma_{\Delta Z}/\sqrt{2} \sim \mathrm{HWHM}/\sqrt{2}$. This argument follows, provided that the number of SSD tracks and their angular distributions in the X and Y views are similar for most events. This is in fact true, since the number of SSD tracks in each view is simply a projection of the total number of

charged tracks onto the XZ and YZ planes. Furthermore, we do not expect there to be any preference with respect to the azimuthal distribution of tracks[14], so that one expects similar angular distributions in each view. Based on these arguments, it follows that the contribution to the width of the ΔZ distribution is similar for the X and Y views, for a large fraction of the events. Under this presumption, we can use the approximation $\sigma_{Z_X} \sim \sigma_{Z_Y} \equiv \sigma_Z^{VIEW}$. Substituting this into the expression for $\sigma_{\Delta Z}$, one arrives at the result that $\sigma_{\Delta Z} \simeq \sqrt{2}*\sigma_Z^{VIEW}$, or, $\sigma_Z^{VIEW} \simeq 1/\sqrt{2}*\sigma_{\Delta Z}$. Since the HWHM of Figure 4.20(a) is $\sim 600\mu$, one finds that the **average view vertex resolution** σ_Z^{VIEW} is $\sim 425\mu$. The tail of events in Figure 4.20(a) with ΔZ larger than ~ 2 mm is representative of events where at least one of the view vertices had a large measurement error. As evidenced by Figure 4.20(b), the calculated errors do account for the large ΔZ events of Figure 4.20(a) as well.

We can carry this analysis one step further. If we assume that Z_X and Z_Y are independent measurements of the same quantity, then we can form the weighted average of the two as,

$$Z_W = \frac{Z_X/\sigma_{Z_X}^2 + Z_Y/\sigma_{Z_Y}^2}{1/\sigma_{Z_X}^2 + 1/\sigma_{Z_Y}^2}. \qquad 4.8$$

When combining the information from two independent measurements as in 4.8, we expect to improve the vertex resolution beyond which was achieved by either Z_X or Z_Y alone. The error in Z_W can be shown to be given by,

$$\sigma_{Z_W} = \sqrt{\frac{1}{1/\sigma_{Z_X}^2 + 1/\sigma_{Z_Y}^2}}. \qquad 4.9$$

In the simple case that $\sigma_{Z_X} \sim \sigma_{Z_Y} \equiv \sigma_Z^{VIEW}$, we get, $\sigma_{Z_W} = \sigma_Z^{VIEW}/\sqrt{2}$. In light of our previous remarks, it follows that the **average weighted vertex resolution** σ_{Z_W} is $\sim \sigma_{\Delta Z}/2$. Given that the HWHM of Figure 4.20(a) is $\sim 600\mu$, the **average primary vertex resolution** is typically $\sim 300\mu$[15].

---

[14] Here, azimuth(ϕ) refers to the angle in the plane perpendicular to the beam axis, i.e. $\phi = \arctan(P_Y/P_X)$.

[15] The events in Figure 4.20(a) represent the majority of the 1990 data events.

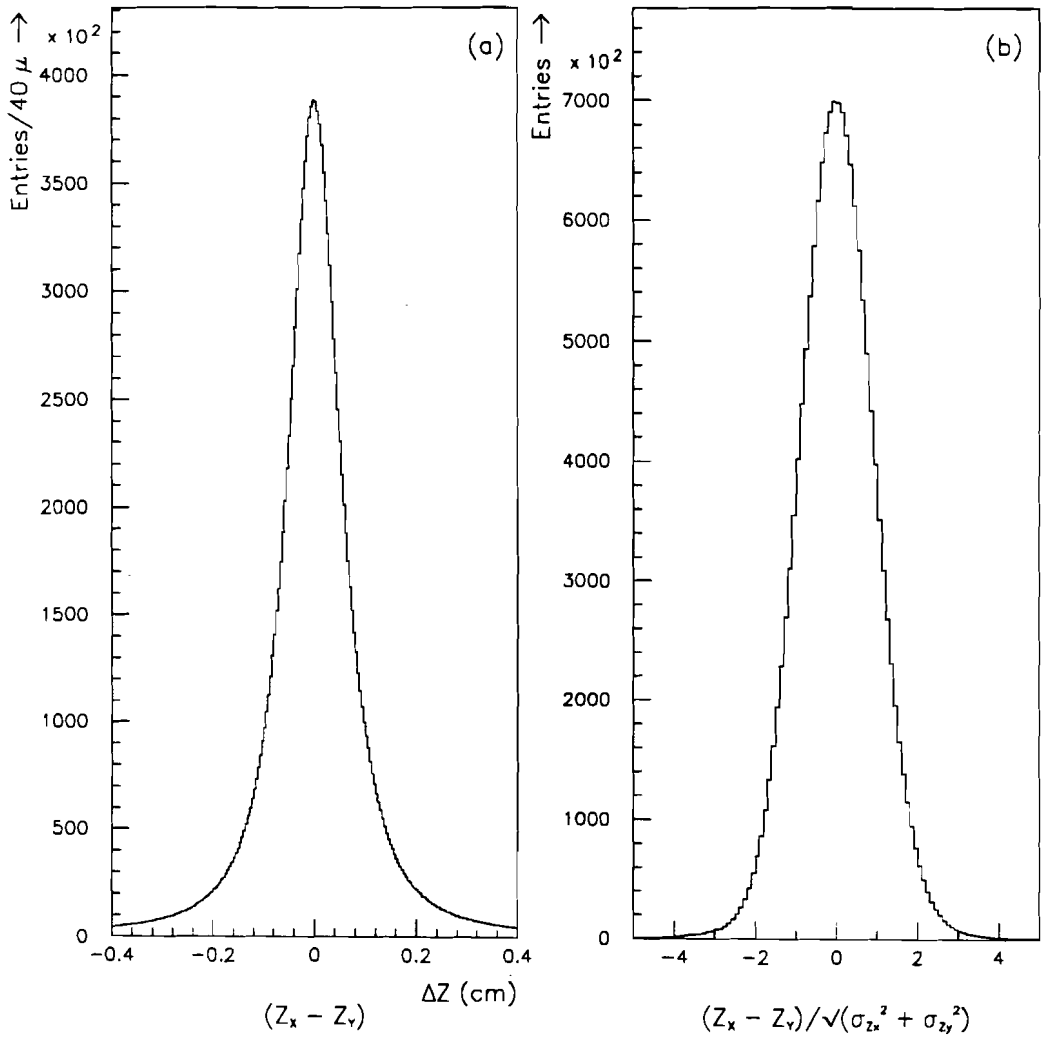

Figure 4.20 (a) Z Separation between the X and Y view vertex, and (b) Significance of separation between the X and Y view vertices.

4.6.5 Secondary Vertex Finding

The tracks tagged as secondary track candidates were used as seeds to find secondary vertices. Each pair of space tracks[16] were combined and a candidate two track vertex was formed in each view (Z_X and Z_Y), with each having its associated errors (σ_{Z_X} and σ_{Z_Y})[17]. The following cuts were applied to the candidate vee:

$$\frac{|(Z_X - Z_Y)|}{\sqrt{\sigma^2_{Z_X} + \sigma^2_{Z_Y}}} \leq 3.0$$

$$\chi^2_{VEE} \leq 1.0$$

$$\frac{|Z_{VEE} - Z_{PRIM}|}{\sqrt{\sigma^2_{Z_{VEE}} + \sigma^2_{Z_{PRIM}}}} > 3.0$$

where,

$$Z_{VEE} = \frac{Z_X/\sigma^2_{Z_X} + Z_Y/\sigma^2_{Z_Y}}{1/\sigma^2_{Z_X} + 1/\sigma^2_{Z_Y}}$$

is the weighted vee position and χ^2_{VEE} is the chisquared of the vee. The first two criteria demand that the 2 space tracks are consistent with emerging from the same X, Y, Z space point. The last equation demands that the vee be separated from the primary vertex by at least three times the expected error in the separation. If the vee failed the last cut, it was dropped, and the next space track pair was tried. If either of the first two criteria was not satisfied, all of the **extra links** for both tracks were scrutinized to find the pair of X and Y links which had the minimum $|(Z_X - Z_Y)|$. This new pair of space tracks were used to define a new vee, which was subjected to the aforementioned criteria. If either of the three was not satisfied,

---

[16] At this stage, each space track was defined by the downstream track along with the X and Y view best links.

[17] Recall that the Z errors are inversely proportional to the opening angle between the tracks.

the vee was dropped, and the next pair of tracks was tried. This procedure was performed for all those pairs of tracks tagged as secondary track candidates.

When a vee candidate passed the three cuts above, the algorithm attempted to attach other secondary tracks to it. For each secondary track, the significance to this vee was calculated using the best links (see Figure 4.18). Based on these results, there were three possibilities.

- Both X and Y best link had a significance of less than 3.0 to the vee in question.
- Neither the X nor Y best link had a significance less than 3.0.
- Either the X or Y had a significance greater than 3.0, but not both.

Only the last case is non-trivial. In the first case, we can try to attach this track to the vee. In the second case, we do not try to attach this track to the vee at all, since it is unlikely that both the X and Y view best links were wrong. In the last case, there is some indication that the secondary track may belong to the vee in question, so further testing was needed. For the view which had the poor significance, we checked the extra links as well. If one of the extra links passes the significance cut, we give the preference to the extra link, and attach the new track to the vee in question. If no extra links passed the significance cut, then we skip over this track, and try the next track.

If a given space track was successfully attached, the vee was refit with the new track included in the fit. The resulting vertex χ^2 in each view was calculated, and at least one view was required to have a $\chi^2_{\rm VERTEX}/{\rm DOF} < 3.0$. If both views failed this cut, this new track was removed from the vertex. If one view failed the cut, the extra links were checked again to see if any of them might have a smaller impact parameter than the chosen link(s). If so, the view vertex was refit using the new SSD link, and the resulting fit was required to pass the aforementioned chisquared cut. If no links were capable of reducing the vertex chisquared below the cut, the

space track in question was removed from the vee. This procedure of attaching tracks was continued until all of the secondary track candidates were tested. Along the way, any time a new track was added, the vertex position was recalculated using the new set of tracks. If any tracks were added, the original *vee* is deemed a *vertex*. If no tracks were added, it remained a *vee*.

Due to this vertex finding scheme, duplicates are likely to occur along the way. We therefore compare each reconstructed vertex with all the previously made vertices, and reject the duplicates. Obviously, the unique vees/vertices were added to the list of vees/vertices for the event.

Since the vertex fitting only used **secondary track candidates**, a second list of tracks was generated which gave a list of all charged tracks which were consistent with each vertex. In this stage, each downstream track could be attached to any vertex provided it had an X and Y link which were consistent with the vee/vertex in question. The only restriction was that either the X or Y link must be unique to that vee/vertex. In other words, it was not allowed that both the X and Y links were already used in the vertex fit for the vertex in question. This **extra list** was useful since it may happen that a secondary track points back to the primary vertex as well as its own production point. In this case it may have been excluded from the secondary vertex search, i.e. accidentally tagged as a primary vertex track. In addition, downstream tracks with only 1 SSD link (X or Y) were not used in the initial secondary vertex finding. These tracks were also eligible to be attached to the vees/vertices in the event, provided that the SSD link was unique to that vee/vertex. The vertices and vees were **not refit** with any of these extra track candidates.

At this stage, one had a list of secondary vertices along with the tracks used in the determination of each vertex. In addition, each vee/vertex had an extra set of tracks which were consistent with emanating from that location. At this stage, one is ready to initiate the search for charmed hadrons among the secondary vertices.

4.6.6 Concluding Remarks

Throughout the algorithm, the extra links were used in order to increase the efficiency of finding vertices. Despite reasonably high linking accuracy, any losses due to having the incorrect best link must be minimized. The reason for this is because any linking inaccuracies enter as **inefficiencies on a per-track basis.** Since each space track has two links (X and Y), if one tried only the best links, an upper limit on the vertex finding would be $\sim \epsilon^{2N}$, where ϵ is the average linking accuracy of the X and Y views, and N is the number of tracks in the vertex. Since in this thesis we will be searching for 3 prong decays, we show in Figure 4.21 the 3 track case. The figure shows that if we were to use only best links, we would need superb linking accuracy in order to have minimal losses due to this choice. This curve does not account for other effects such as acceptance, reconstruction losses, etc, which lowers the vertex finding efficiency even further. Consequently, it was necessary to be fairly aggressive with respect to using the extra links, in order to minimize the sensitivity to this steeply rising (falling) function. On the other hand, being aggressive with the extra links tends to increase the combinatorial background. In this program we have leaned toward being more aggressive with the extra links, with the hope that the combinatorial background could be reduced by other means. The cuts used to extract the charm signal will be discussed in Chapter 6.

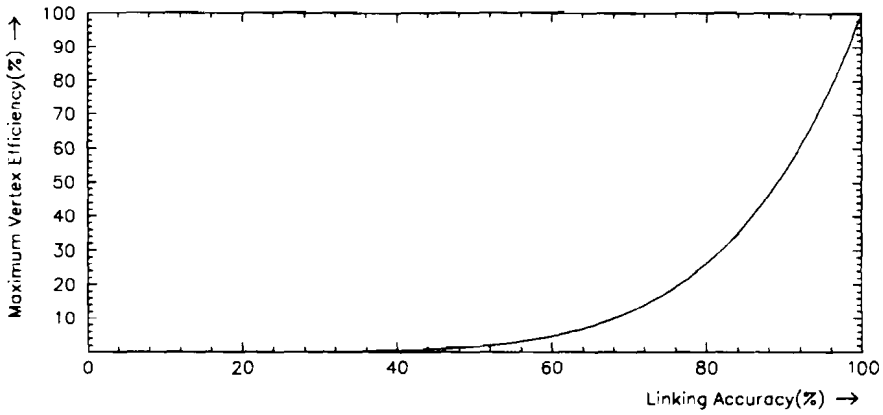

Figure 4.21 Maximum vertex efficiency as a function of the average linking accuracy, if only best links are tried.

Chapter 5 Monte Carlo

5.1 Overview

In this thesis, we are trying to measure the charm production cross section in association with high p_T jets. The focus of this chapter is to discuss the aspects of this analysis which relied on the Monte Carlo (MC). The MC was used in two ways for this analysis. First, it was used to estimate the efficiency for triggering on charm events. The second task of the MC was to evaluate the reconstruction efficiency for locating the displaced vertices associated with charm decays. In this chapter we shall discuss both of these aspects of the monte carlo.

5.2 The E706 Trigger

The E706 trigger was designed specifically to study direct photons and their associated jets. The majority of the events which trigger the E706 apparatus arise from leading EM particles in high p_T jets. This places a bias on the measured jet p_T spectrum, in that the jet is required to have a high p_T, as well as yield a sufficiently high z EM particle from the fragmentation[1]. Therefore, we expect that low p_T jets rarely/never trigger the apparatus. On the other hand, we expect that high p_T jets above the trigger threshold have a monotonicly increasing probability of satisfying the trigger. Clearly this must be true, since it is easier to get a single high p_T EM particle above the threshold from the fragmentation as the jet p_T increases.

[1] We remind the reader that z is the fragmentation variable, defining the fraction of the jet momentum that a single particle carries.

5.2.1 Trigger Probabilities and Turn-On Curves

The probability that an event satisfied the E706 trigger is described by a *trigger turn-on curve.* This function gives an estimate of the probability P that a given event would satisfy the trigger. This probability is primarily a function of the measured *trigger* p_T. Since local triggers discriminated on the *trigger* p_T contained within the *adjacent pairs of groups of 8 (strips)* [2], **each** such group had an associated turn-on curve. On the other hand, global triggers discriminated on the total *trigger* p_T in each octant, so that a single curve described an entire octant's triggering efficiency. In this section, we have intentionally used *trigger* p_T, as opposed to (physics) p_T. The reasoning behind this will be made clear in the later sections. For now, it will suffice to say that the *trigger* p_T is similar, but not the same as the physics p_T.

5.2.2 Trigger Bias

Since the trigger only selects events which deposit a large amount of electromagnetic energy into the EMLAC, it imparts a bias onto the data. Provided one can estimate the probability that a given event fires the trigger, the measured distributions can be corrected for by weighting each event by the inverse of its probability.

The E706 trigger was designed to trigger on events which had the signature of a direct photon. Since high p_T direct photons are **localized**, and trigger the EMLAC with high efficiency, the E706 trigger is a highly local trigger. In other words, it requires a significant amount of localized p_T in order for an event to be accepted. As discussed in Chapter 1, leading mesons (predominantly π^0's and η's)

---

[2] From this point onward, we will use *adjacent pairs of groups of 8 (strips)* and *groups of 16* interchangeably. Both expressions synonymously define the 16 strips formed by combining any 2 adjacent groups of 8 strips in the EMLAC.

in high p_T jets also produce localized, high p_T showers in the EMLAC[3]. Therefore, the EMLAC triggers efficiently on any event which contains either a direct photon or a high p_T meson which decays to $\sim$ 2-3 photons. The high p_T mesons which trigger the apparatus represent a small subsample of the high p_T jets which were produced during the 1990 data run. The majority of the high p_T jet events were not accepted by the E706 trigger, since jets prefer to fragment into many low p_T particles rather than very few high p_T particles. However, occasionally, a jet yields a single high p_T particle (such as a π^0 or η) which triggers the EMLAC. Therefore, the bias against jets is primarily with respect to the way the jet fragments.

As a result of the trigger bias, the EMLAC doesn't trigger on jets with very high efficiency. Although the efficiency increases monotonically with jet p_T, the overall efficiency is still only $\sim$1% for 5 GeV/c p_T jets. However, it important to realize that **the EMLAC was not intended to be a jet trigger, it was intended to trigger on events which had the signature of a direct photon** ! If one plots the **trigger efficiency as a function of the direct photon** p_T, one finds that the trigger turns on around 3.5 GeV/c, and reaches $\sim$100% very rapidly. The same argument holds for π^0's, since the diphotons from π^0 decays are usually within a few centimeters of one another i.e. both photons satisfy the local definition. However, if one plots the **trigger efficiency as a function of jet** p_T, one finds that the trigger turns on slowly as compared to direct photons and π^0's. This is the expected result since only a small fraction of jets above the trigger threshold produce a high p_T EM particle which is also above the trigger threshold. This is the bias which the E706 trigger invokes with respect to triggering on jets.

In the data, we have a sample of charm events which have been tagged by reconstructing one of the charmed hadrons in the event. We wish to know the probability of observing a given number of charmed hadrons within a specified

---

[3] We are primarily referring to those leading mesons which have 2-3 photon decay modes.

kinematic range. This requires an understanding of how the EMLAC trigger responds to high energy particles. It should be clear that charm events were not selected by the trigger because it was designed to select out charm events. In fact, the trigger is fairly insensitive to whether the parent parton of the jet was a light quark or a heavy quark. The trigger can only discriminate particles which reach the EMLAC; clearly, charm particles do not reach the EMLAC! Since in this thesis we are studying charm production, we need to know the probability of triggering on an event which contains charm i.e. a $D^{\pm}$ meson. In other words, we want to know how frequently an event such as,

$$\pi^{-}\text{Nucleon} \rightarrow D^{\pm} + X \qquad 5.1$$

triggers the EMLAC. The $D^{\pm}$ is the *stable* fragment of one charm jet, and X is the remainder of the event, which is primarily the recoiling charm jet. In 5.1, it is not necessarily the decay products of the $D^{\pm}$ which trigger the EMLAC. Therefore, by the **event probability**, we literally mean the probability that the final state in 5.1 fires the trigger. Since we are measuring the inclusive charm production cross section, there is no restriction on X. However, we do know that the charm jets in 5.1 must produce a high p_T localized EM deposition in the EMLAC. However, as with any jet, the probability that there is a single high p_T particle in the final state of 5.1 is fairly small. Therefore, we expect the trigger probability of 5.1 to behave similarly to the trigger probability of any QCD jet[4]. Since in the data, we measure the kinematics of the $D^{\pm}$, the trigger efficiency for the process of 5.1 can be expressed as a function of its p_T (and x_F, if necessary). Clearly one expects as the p_T of the $D^{\pm}$ increases, so must the p_T of the jets in the event. Therefore, we expect that it is reasonable to express the trigger efficiency as a function of the transverse momentum of the observed $D^{\pm}$.

[4] Excluding very heavy quark jets, such as bottom (top is inaccessible at E706, of course).

Ideally, if we had a sample of charm events which were unbiased by the trigger, we could measure the trigger bias directly from the data. Since there are few or no charm events in the minimum bias data, we rely on the MC to estimate the trigger efficiency. In this chapter, we give a detailed description of the method used to measure the trigger bias against charm events.

5.3 MC Trigger

The prescription of using the MC to estimate the losses presumes that the MC simulates the features of the data which are relevant to an event triggering the apparatus. There are three factors which enter into making an estimate of the trigger efficiency. They are,

- The response of the EMLAC to high energy particles must be simulated with reasonable accuracy; and
- The on-line trigger logic must be encoded into software, which includes the various thresholds as well as the associated trigger definitions; and
- A production model for the process of interest must be assumed.

In this chapter we address these three issues in the order in which they appear. The first two clearly address the trigger response, while the last requires us to invoke a model of how charm particles are produced in π^--Nucleon collisions. The final result we wish to arrive at is an estimate of the EMLAC trigger efficiency for charm events which contain a $D^{\pm}$ which decays to $K^{\mp}\pi^{\pm}\pi^{\pm}$.

In order to gain confidence in the MC to reliably estimate the loss of charm events due to the trigger, we must provide an independent cross check that the MC simulation provides reasonable results. Only in this case can we responsibly use the MC to correct the data for the losses incurred as a result of the trigger. In order to make relevant comparisons of the trigger bias between the data and MC simulation, we take the following approach. **From the minimum bias sample**

of data recorded during the 1990 run, we measure the trigger bias against all interactions. This gives us an estimate of how the trigger should bias the events in the MC. We then produce minimum bias events in the MC, and subject them to the software trigger simulation. The resulting bias against the MC events can then be measured and compared to that found for the data events. If the two agree fairly well, this provides us with confidence that the trigger bias is modelled appropriately.

In the next section we discuss the software model of the trigger which was developed for the purpose of extracting the trigger efficiency.

5.3.1 Trigger Simulation Overview

In order to extract the probability for an event to trigger the apparatus, we needed to simulate the response of the trigger to various particles. Since the trigger discriminates upon the strip energies in the EMLAC, it was necessary to model the energy response of the detector. In addition, the trigger logic needed to be encoded in the same way as it was for the online data. For the moment, assume a reasonable event generator has been chosen to simulate the spectrum of particles observed in the data. The output of the generator is a list of stable particles which can be propagated through the detector. In this section, we discuss the software model of the trigger, as well as the logic for the triggers used in this analysis. The goal is to obtain the probability that a given event will fire any of the triggers used in this analysis. The four main steps to arriving at the trigger probability were:

1) Determine the appropriate amount of energy to be deposited into the EMLAC.
2) Distribute the energy longitudinally and transversely across the R strips of the EMLAC.
3) Calculate the *trigger* p_T in the *sums of 8*.
4) Apply the trigger logic, and get the associated event probability.

In the forthcoming sections, we describe these steps in more detail.

5.3.2 Estimation of the Energy Deposition in the EMLAC

In order to simulate the trigger, it was necessary to deposit each particle's energy into the EMLAC, and perform the trigger logic as done in the hardware of the experiment. This can be done by running each particle through GEANT[80], and allowing each particle to shower in the EMLAC according to its allowed physical processes. Due to the length of time it takes to perform the full shower simulation, a parametrization was invoked. The parametrizations used were based on full shower simulations of the EMLAC's response to high energy photons and hadrons. In the this section, we give a detailed description of the parametrizations used to deposit each particle's energy into the EMLAC.

Based on a full shower MC, the following cuts were applied to each stable particle, in order for it to be considered for making a shower in the EMLAC.

- $E_{GEN} > 1$ GeV for all photons.
- $E_{GEN} > 6$ GeV for hadrons.
- $Z_{GEN} < 900$ cm (Particle produced before EMLAC)
- Particle does not hit upstream or downstream magnet mirror plate. (It would be absorbed, or shower into many low energy particles, otherwise.)
- Particle is within the annular $18 < R < 150$ cm at $Z = Z_{LAC}$. (Defines radius at which energy may be deposited in EMLAC)
- Particle doesn't hit steel plates between quadrant boundaries. (Very little energy escapes)

These cuts should be self-explanatory as to why they were used. In short, if a particle did not pass all of these cuts, the particle would not deposit a significant amount of p_T in the EMLAC.

All stable particles passing these cuts were eligible to shower their energy into the EMLAC. The first step was to propagate particles from their production point to

the front face of the EMLAC. Photons were simply projected through the apparatus to the face of the EMLAC. A small fraction of the photons were converted to electron pairs using probabilities obtained from a knowledge of the materials in the apparatus. Typical *photon conversion probabilities* were $\sim$ 6-10%, depending on the production point and direction cosines. Charged particles were bent through the magnetic field using the dipole approximation. The magnet imparts a p_x kick of $\sim$ 450 MeV/c to each charged particle, which either increased or decreased it's p_T with respect to the beam axis. Consequently, the p_T of a charged particle at the face of the LAC may be greater or less than its initial transverse momentum. Obviously photons and other neutral particles are unaffected by the magnetic field.

Once all the particles were propagated to the face of the EMLAC, a parametrized amount of energy was deposited into the R strips. There were several corrections which needed to be applied before depositing each particle's energy. These energy corrections are described below[5]. The energy corrections were based on studies of the mean π^0 and η masses (relative to the world average) projected onto several axes, as well as ZMPs[6] observed in both the tracking system and the EMLAC. With the exception of the **ELOSS** correction (see below), all of the energy corrections were extracted from the data. For each stable particle propagated to the face of the EMLAC, the following energy corrections were applied. Assume the initial energy of each particle is E_1.

- First, we correct for the **time dependent energy scale.** The energy scale of the EMLAC was seen to be increasing as a function of the integrated beam on target. In other words, the EMLAC was providing more ionization for a given input energy as the run progressed. Figure 5.1 shows the ratio of the reconstructed π^0 mass

[5] See reference [24] for a detailed discussion of the determination of these energy scale corrections.

[6] ZMP refers to the zero mass pairs produced from photon conversions.

relative to the world average (mass ratio) as a function of beam days. One observes an increase in the energy response by ~25% over the course of the 1990 run. The data in Figure 5.1 were used to scale the incident energy according to the run number[7]. Let the new energy (after scaling E_1) be referred to as E_2.

- Secondly, we need to **estimate the fraction, f, of the total energy to be deposited for a given particle type.** Clearly, various particles will interact differently, depending on the physical processes available to them in a given medium. The most obvious differences arise between photons and hadrons. To a lesser degree, differences also exist between various hadrons. We relied on the GEANT full shower simulation to describe the development of electromagnetic and hadronic showers in the EMLAC. The GEANT simulation was tuned to match the shower shapes observed in the data[55]. Based upon these studies a parametrization was invoked to reproduce the relevant features of these showers. The total energy deposited in the strips, E_3, was defined by,

$$E_3 = f \times E_2 \qquad 5.2$$

where f is the fractional energy deposition, based upon particle type. Since EM particles deposit all of their energy in the EMLAC, we have, $f = 1$ for photons and electrons. For hadrons, the situation is different. Unlike photons, hadrons interact according to interaction (absorption) lengths, not radiation lengths. The EMLAC consists of $\sim$ 2.0 interaction lengths, so one expects ~80% of hadrons to interact, and the remaining 20% to pass through without interacting. Figure 5.2 shows the fraction of the incident energy deposited in the EMLAC for various particles. One observes that the photons

[7] There was an approximately linear relation between beam day and run number.

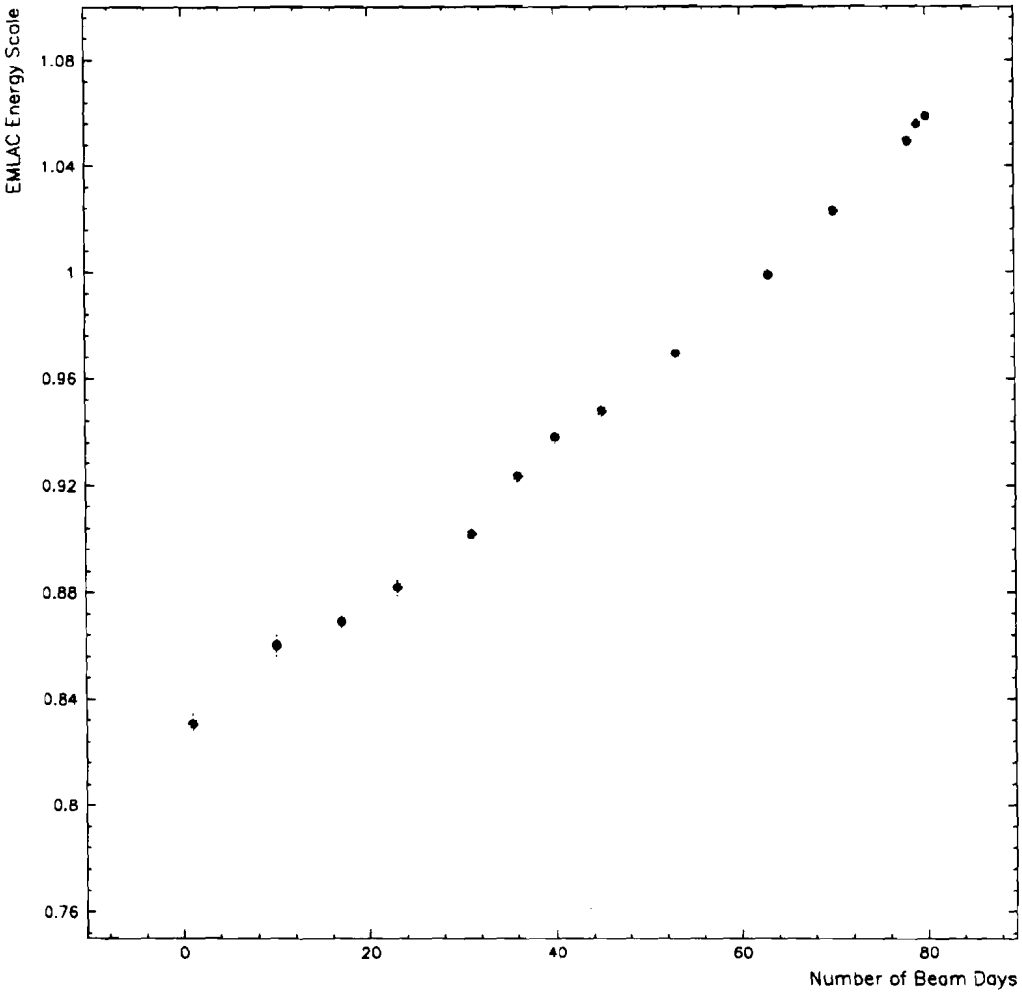

Figure 5.1 Ratio of the reconstructed π^0 mass to its nominal value as a function of the beam days for the 1990 running period.

peak near 1.0, whereas the hadrons do not[8]. There are two clear features observed with respect to hadrons incident upon the EMLAC. First, approximately 20% of the hadrons do not deposit any significant amount of energy in the EMLAC. Secondly, when they do interact, only a fraction of their energy is deposited in the EM section. The figures are normalized to unity, so they show the relative probabilities of depositing a given fraction of energy in the EMLAC. There are subtle differences between mesons and baryons, and smaller differences among the mesons or baryons separately. These distributions were used to parametrize the fractional energy, f, that a given particle deposits in the EMLAC. No strong energy dependence was observed, so that the same parametrization was used for all energies. Other stable hadrons were handled in a similar fashion. To summarize, for hadrons, we have f = 0 for $\sim$ 20% of the hadrons, and for the remaining 80%, f is picked at random from the aforementioned distributions (see Figure 5.2). For photons and electrons, f = 1.

- Energy resolution smearing

For EM showers, we smear the energy by the intrinsic resolution of the detector. For photons and electrons, the resolution is approximately $\sigma_E/E \sim 0.15/\sqrt{E}$. This accounts for the energy smearing due to the nature of this sampling calorimeter. This smearing can easily be seen in the width of the summed strip energies for the 20 GeV photon showers, as shown in Figure 5.2. Define E_4 as the energy after smearing E_3. The parametrizations for f

[8] The photons are not corrected for energy lost in the material in front of the EMLAC (**ELOSS**), so the peak is slightly lower than 1.0

response of the 8 octants. Define E_{DEP} as the energy of the particle after all these corrections were applied to E_4. E_{DEP} is the actual energy which the EMLAC saw from the particle in question.

5.3.3 Longitudinal and Transverse Shower Development

Now that we have the energy, E_{DEP} which will be deposited in the EMLAC, we need to distribute the energy appropriately. This involves distributing the energy, E_{DEP}, appropriately in both the longitudinal and transverse direction. The full shower MC was used to determine the shape of these distributions.

Along the shower direction, the longitudinal development can be described by the ratio of the front energy to the total energy[10]. The variable, E_{FRONT}/E_{TOTAL} gives such a measure of the longitudinal development of showers in the EMLAC. Figure 5.6 shows the E_{FRONT}/E_{TOTAL} distributions for 20 GeV EM and hadronic showers, as determined by the full shower MC. From the figure, it is clear that photon showers develop early (high E_{FRONT}/E_{TOTAL}), and hadrons showers tend to develop later (low E_{FRONT}/E_{TOTAL}). These distributions have some sensitivity to the input energy, but the qualitative feature is representative, and is accurate enough for the purposes at hand. For each shower, a random number is chosen according to these distributions in order to describe the longitudinal development.

In the transverse direction, a radial shower energy profile was generated. The energy in each R strip about the centroid of the shower was divided by the input energy to obtain the fractional energy contained within an R strip, with respect to the total energy. The energy collected in each R strip integrates over the full ϕ coverage of the octant i.e. $\pi/4$ radians. Figure 5.7 shows the fractional energy collected within $\pm$ 11 R strips of the peak strip. Shown in the figure is the integrated radial shower shape for photons, mesons, and baryons. The MC predicts a systematic broadening from photons to mesons to baryons.

---

[10] Recall that the EMLAC is divided into a front section of $\sim$ 10 radiation lengths and a back section of $\sim$ 20 radiation lengths.

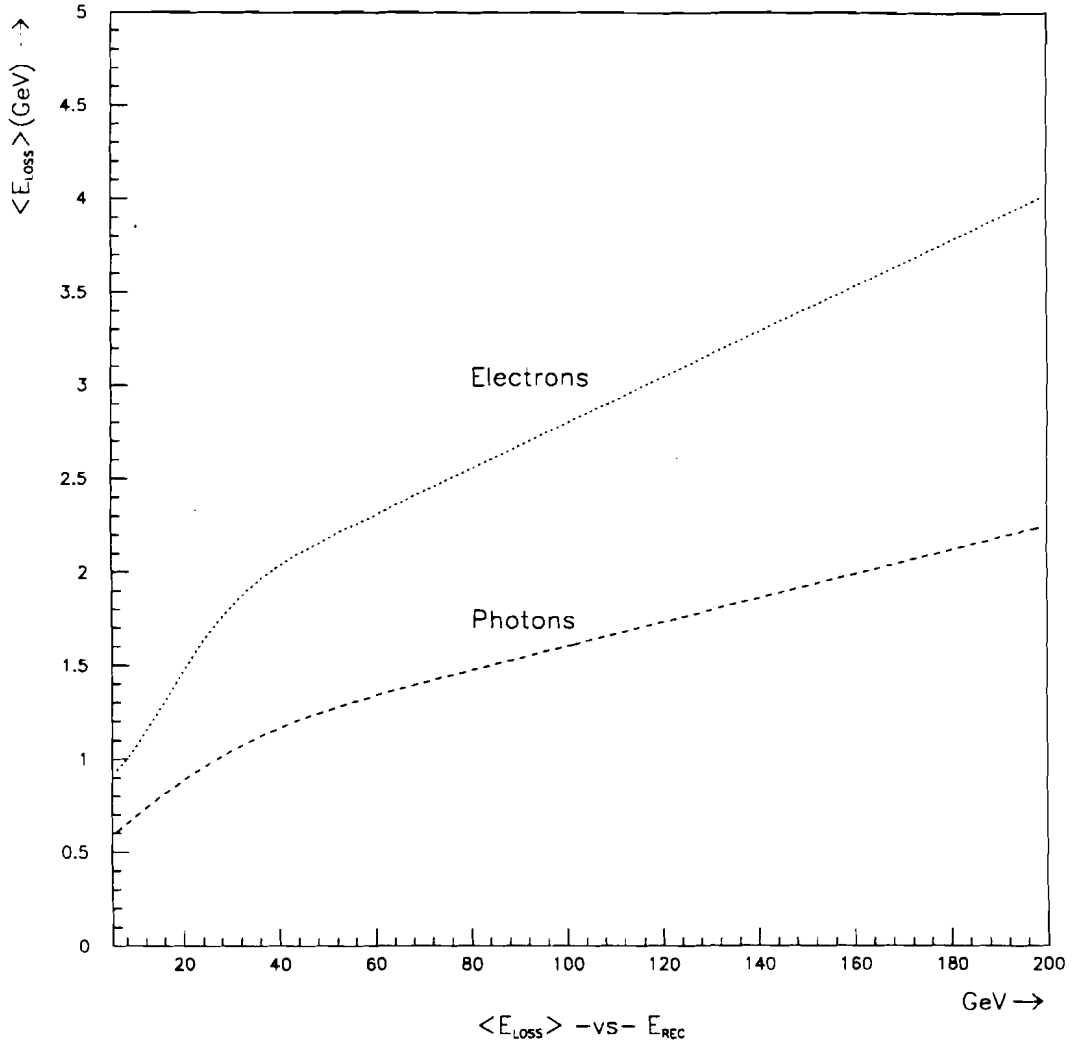

Figure 5.3 Energy.lost in the material in front of the EMLAC as a function of the reconstructed energy.

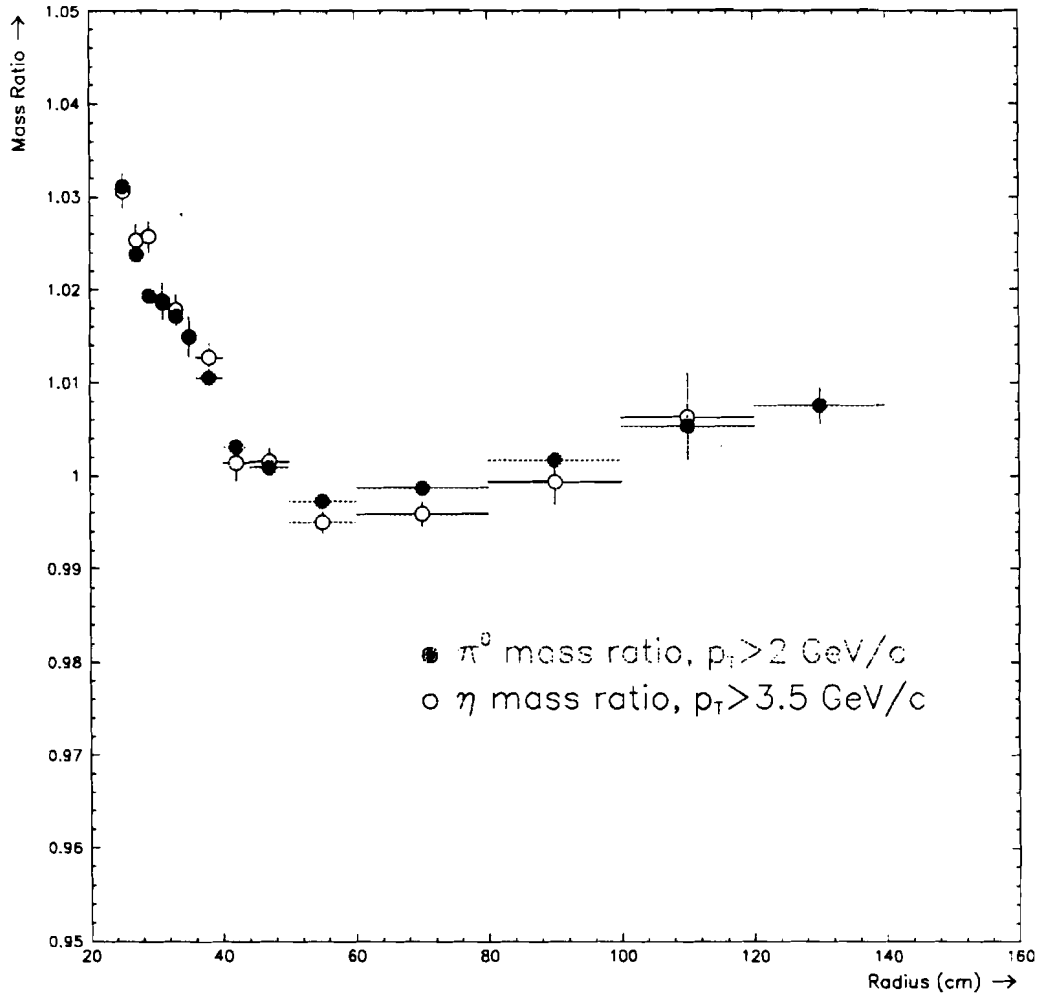

Figure 5.4 Radial dependence of the reconstructed π^0 mass relative to its nominal value.

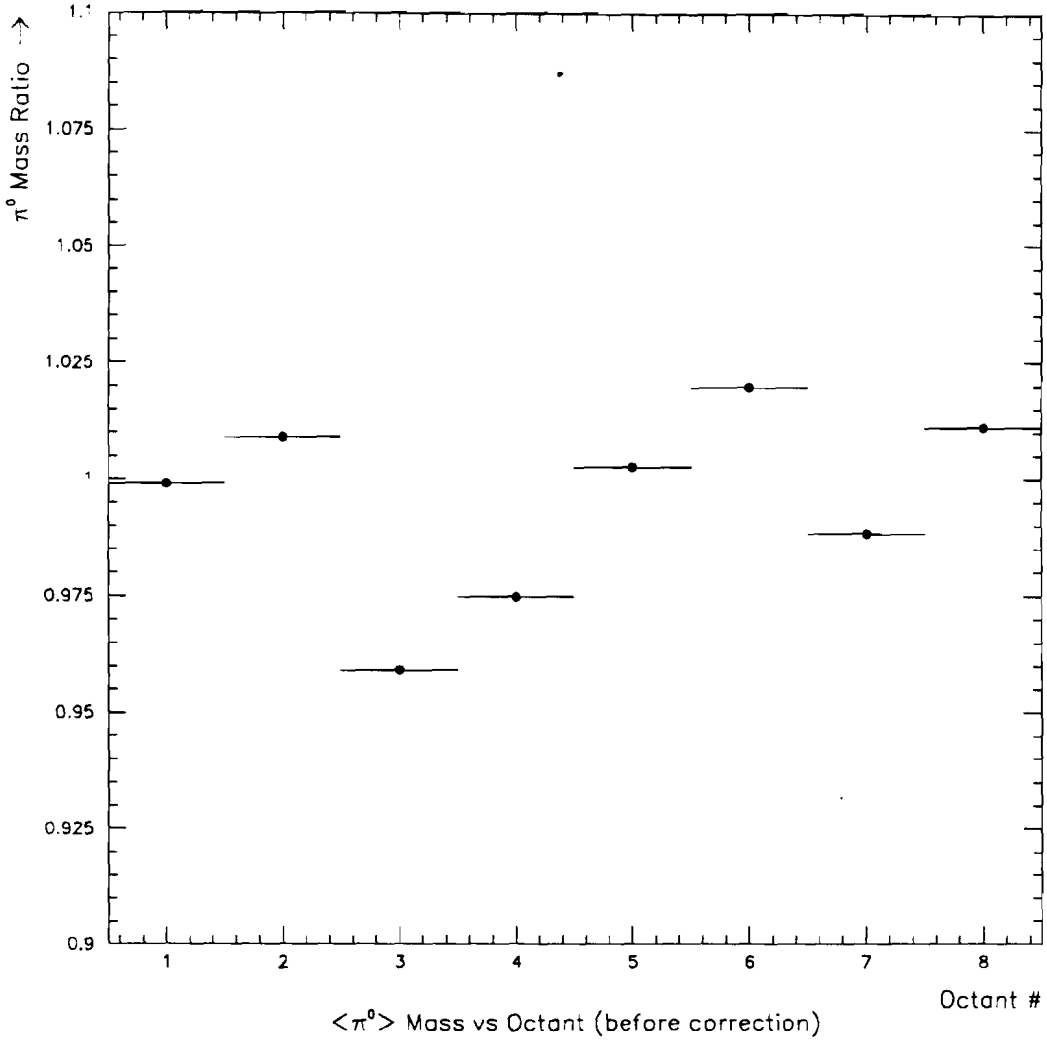

Figure 5.5 Variation of the mean π^0 mass relative to the nominal value as a function of the octant number.

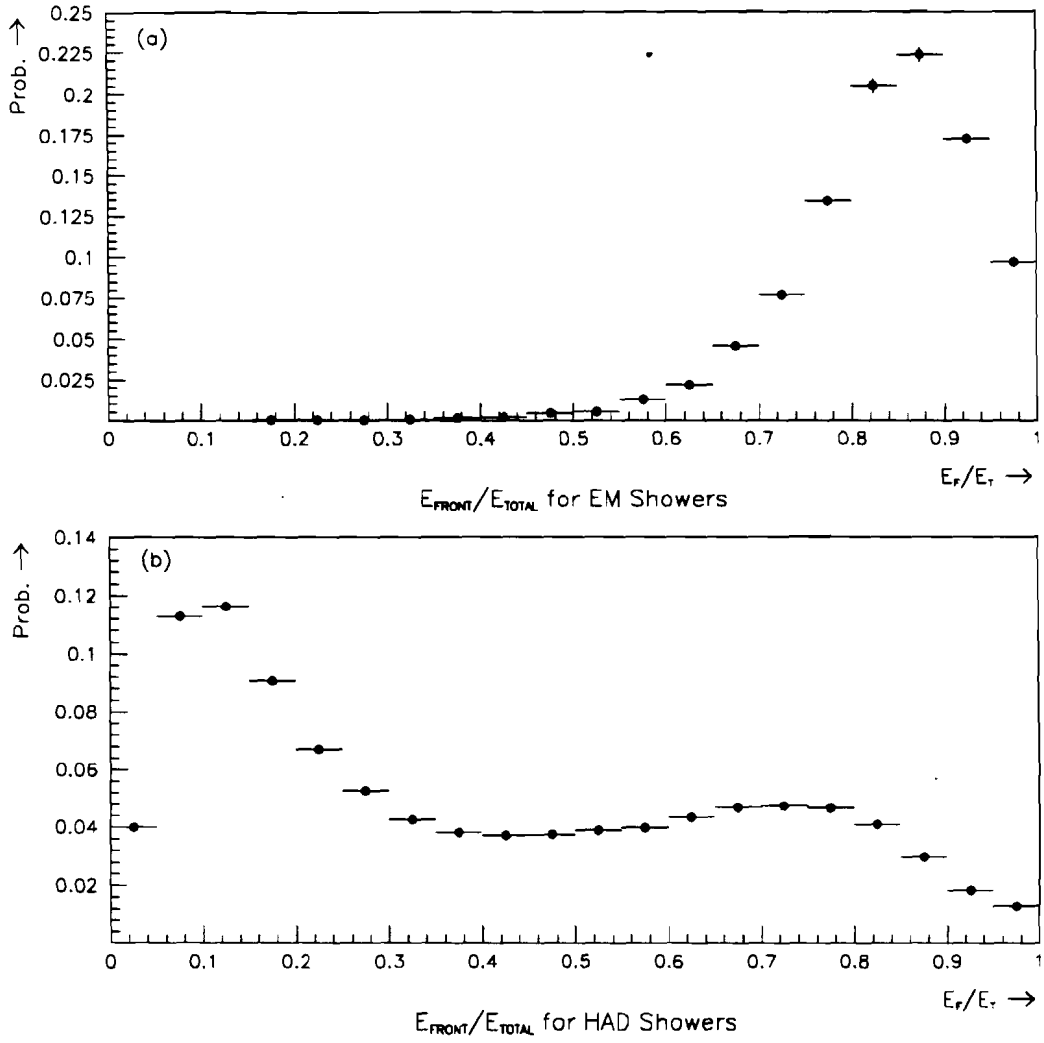

Figure 5.6 The E_{FRONT}/E_{TOTAL} distributions for (a) electromagnetic, and (b) hadronic showers, in the EMLAC.

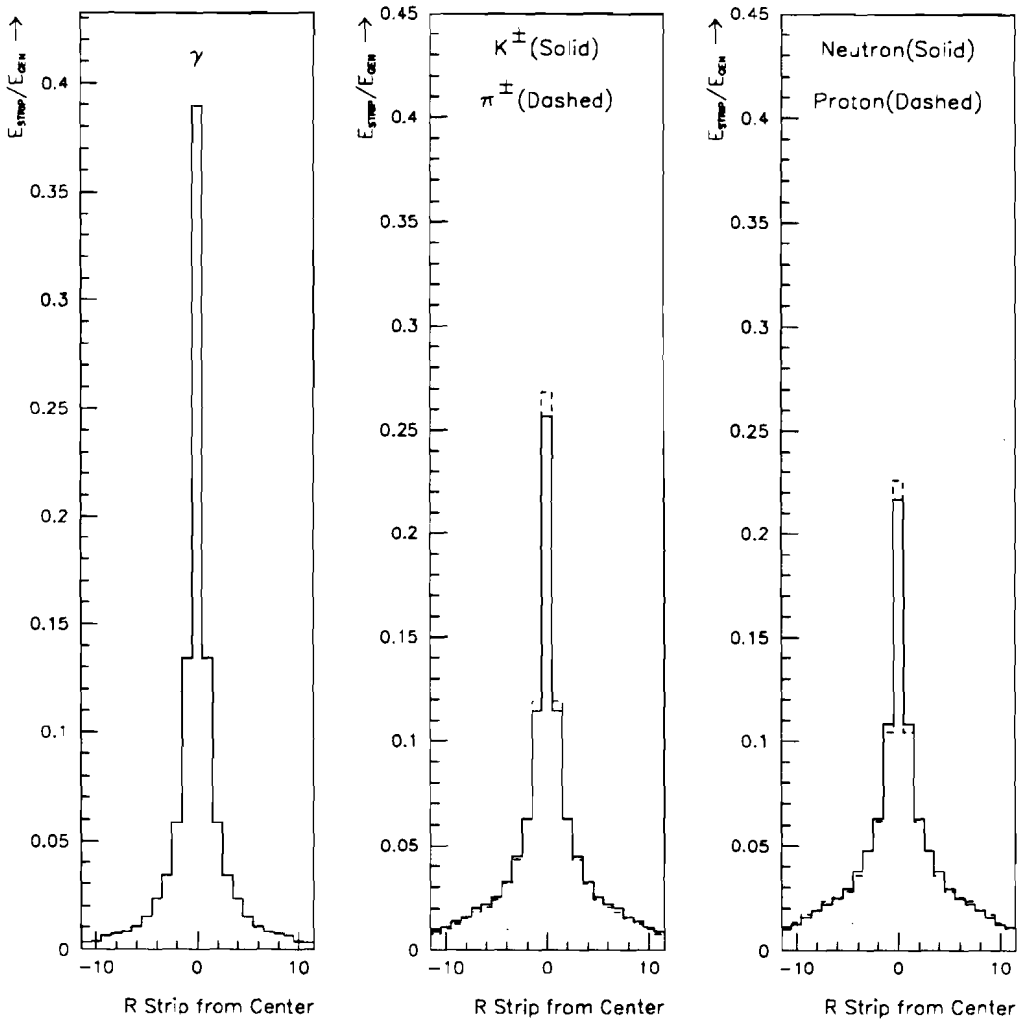

Figure 5.7 Shower shape parametrizations for various particle types. The figures show the fractional energy deposition in the R strips for electromagnetic, and hadronic (mesons and baryons) showers.

Putting all this information together, we obtain the energy collected by the i^{th} radial strip from the center position of a shower, in the front and back sections, as

$$E_i^f = (E_{DEP}/2) \times x_{EFT} \times F_i \qquad 5.3$$

and

$$E_i^b = (E_{DEP}/2) \times (1 - x_{EFT}) \times F_i \qquad 5.4$$

where F_i is the fractional energy in the strip and x_{EFT} is the E_{FRONT}/E_{TOTAL} for that shower. The factor of $1/2$ is inserted since only $\sim 50\%$ of the shower energy is collected by the R strips[11].

After performing this procedure for each final state particle, we can simply sum up the energy deposited in each radial strip by all of the particles. Since the E706 trigger discriminated on p_T, these energies needed to be transformed into corresponding *trigger* p_T. This is the focus of the next section.

5.3.4 Calculation of the Trigger p_T

The energy in each radial R strip corresponds to a certain amount of physics p_T. In particular, the physics p_T in the i^{th} strip at radius R^i_{STRIP} is simply,

$$p_T^i = E^i_{strip} \times \sin\theta_i \qquad 5.5$$

where, $\theta_i = R^i_{STRIP}/(Z_{LAC} - Z_{VERTEX})$ is the polar angle with respect to the Z (beam) axis, and Z_{VERTEX} is the Z position of the primary vertex in the event.

In an attempt to trigger based on p_T, and not energy, *trigger gains* were applied to each R strip in proportion to its radius. The gains were intended to provide $\sin\theta$ weighting to the strip energies. Consequently, the weighted strip energy is simply the p_T measured by that strip. There existed three sets of gains; HI gains,

---

[11] The other half is obviously collected by the ϕ strips.

LO gains, and the GLOBAL gains, for the SLHI, SLLO, and GLOBAL triggers respectively[62]. In addition, there were a distinct set of trigger gains for both the front and back sections. Figure 5.8 shows the HI gains versus strip number for octants 1 and 3. The solid curve is the front gains and the dashed is the back. The superimposed dotted line is the intended $\sin\theta$ weighting. One observes that the trigger gains are $\sim$10% below that of $\sin\theta$ weighting, with typical fluctuations of $\sim$ 10% of $\sin\theta$. Figure 5.9 shows similar plots for the global gains. One observes a systematic flattening of the outer global gains for some of the octants. Consequently, for both the global and local triggers, the *trigger* p_T tends to be less than the corresponding physics p_T. Aside from the aforementioned energy corrections, this is where the main deviation from physics p_T to *trigger* p_T occurred.

We are now in a position to calculate the *trigger* p_T i.e. the p_T which the trigger discriminates upon. The p_T in the i^{th} strip for the trigger type TRIG, is,

$$p_T^i(f,b;TRIG) = E_i(f,b) \times G_i(f,b;TRIG) \times C(f,b,IOCT) \qquad 5.6$$

where,

$G_i(f,b;trig)$ = gain in strip i, in the front(f) or back(b) section for trigger type TRIG,

$C(f,b,IOCT)$ = correction factor to the gain, which depends on the octant, IOCT, and section (front or back), and

$E_i(f,b)$ is the energy observed in the i^{th} strip in the front (back) section.

Consequently, each R strip had an associated HI, LO, and GLOBAL trigger p_T. The choice of which trigger p_T to use depended on which trigger logic was being tested. Since the triggers operated on either *groups of 16*, or the entire octant, it was convenient to sum up the trigger p_T within each *group of 8 (strips)*, and simply provide the *trigger* p_T of the *groups of 8 (strips)*. As a result, each of the 512 groups (32 groups $\times$ 8 octants, both front and back) had a HI, LO, and GLOBAL

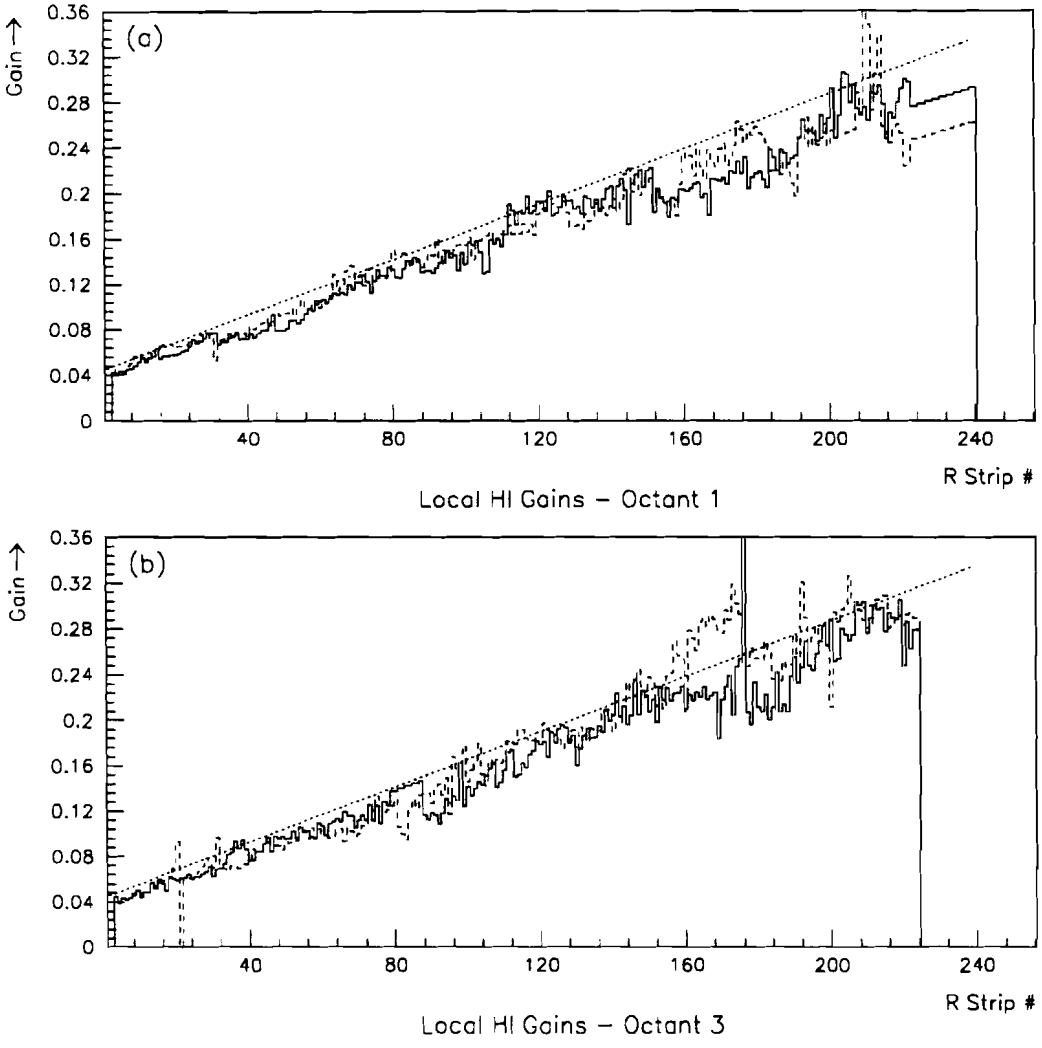

Figure 5.8 The HI gains for 2 of the 8 octants. The solid lines are the front strip gains and the dashed are the back gains. The dotted line is the nominal $\sin\theta$ weighting.

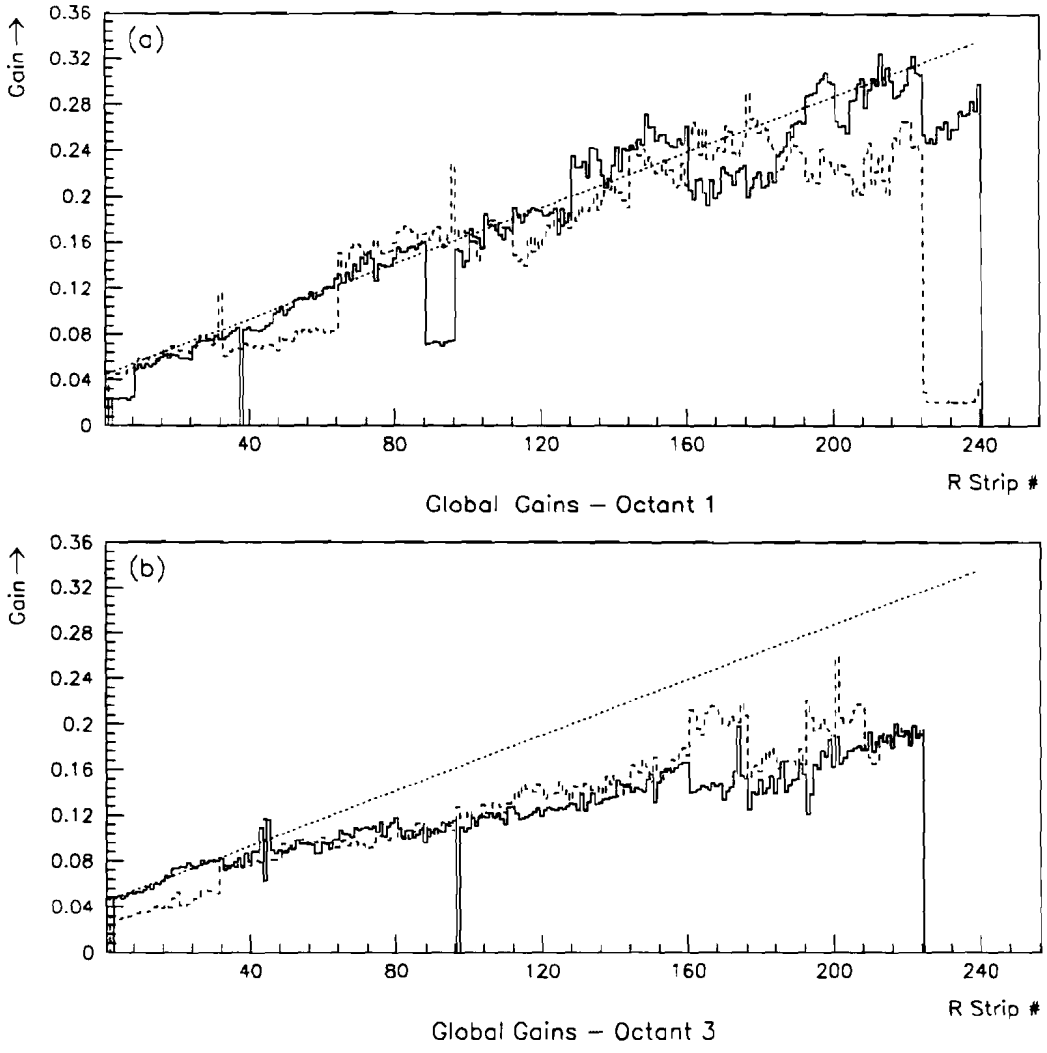

Figure 5.9 The Global gains for 2 of the 8 octants. The solid lines are the front strip gains and the dashed are the back gains. The dotted line is the nominal $\sin\theta$ weighting.

p_T associated with it. For this analysis, we have used the SLHI, 2 GAMMA, and GLHI triggers, which constitutes the majority of the data. The trigger logic for these three triggers is discussed in the next section.

5.3.5 Trigger Definition and Application

The conditions for accepting an event was discussed in detail in Chapter 2. From the standpoint of this MC, only two of those conditions are relevant. They are,

- Interaction definition satisfied (2 or more counters hit); and
- One of the triggers is satisfied.

In the first of these, it is necessary to require that the events of interest, pass the interaction definition. From the data, it was found that less than 1% of interactions failed to satisfy the logic of the interaction counters. Figure 5.10 shows the number of interaction counters struck by charged particles in charm events. The plot is normalized to 100%, so that each bin gives the probability that a certain number of counters register a hit. Since only two interaction counters are required, the losses from the interaction definition are quite small.

The trigger definitions coded into the software were intended to mimic the online definitions. Here, we present the definitions of the various triggers used in this analysis. For a more detailed discussion of the online trigger, one should consult with the references[81].

Single Local Hi

As discussed in Chapter 2, the SLHI discriminated on the *trigger* p_T sum contained in **each** of the *groups of 16* within each octant. From the set of predetermined *trigger turn on curves*[12], one can look up the associated probability

[12] Recall that each such *group of 16* has a characteristic turn-on curve.

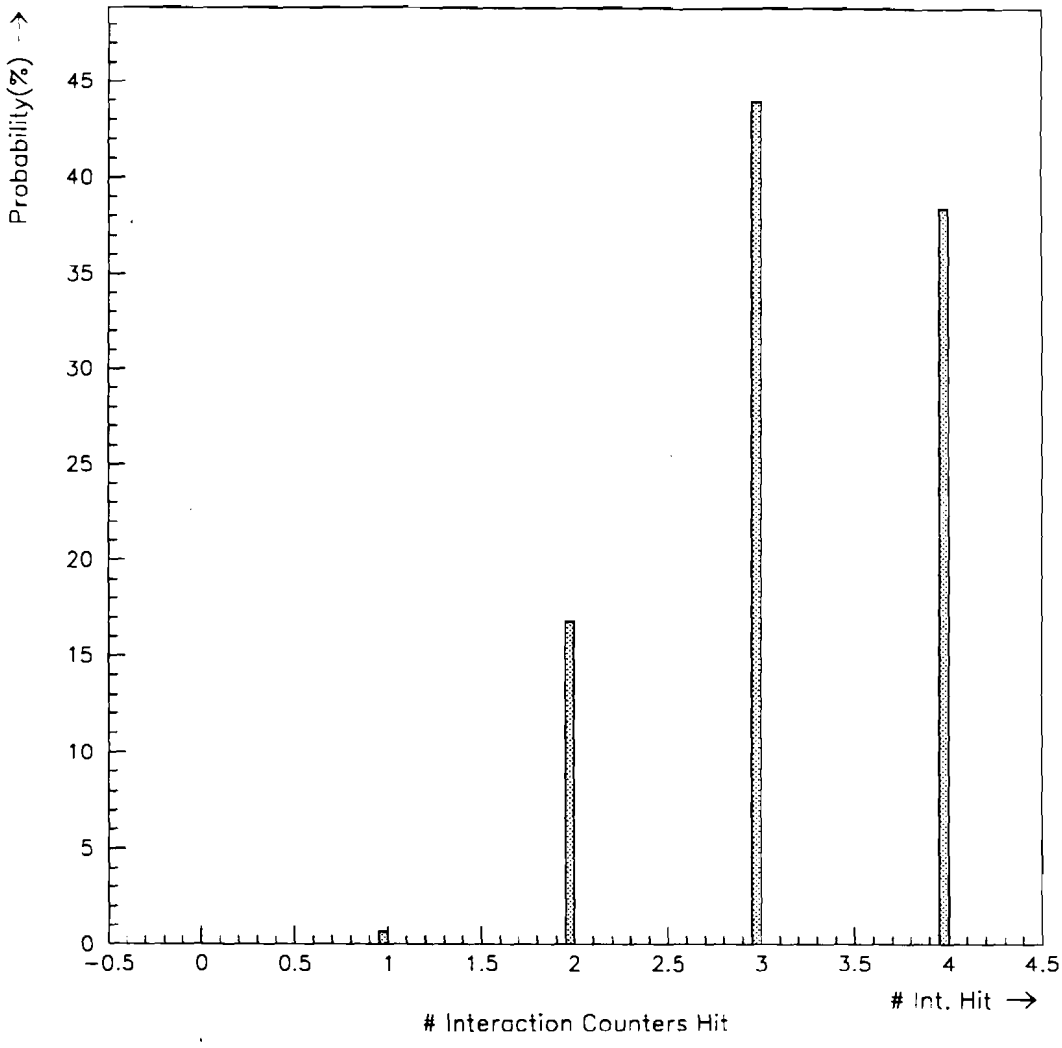

Figure 5.10 The number of interaction counters hit by at least 1 charged track in hadroproduced charm events.

that this amount of trigger p_T would fire that local hi discriminator. In general each of the *groups of 16* yields a probability P^i_{FIRE}, ranging from 0 to 1, that it would fire the SLHI trigger. The probability that an octant fires the trigger is simply $P_{FIRE} = 1 - P_{NOFIRE}$, where P_{NOFIRE} is the probability that **no** *group of 16* in the octant fires the SLHI trigger. This probability may be expanded, and expressed as,

$$P_{FIRE} = 1.0 - \prod_{i=1}^{31}(1.0 - P^i_{FIRE}). \qquad 5.5.11$$

where the sum runs over all *groups of 16*. In this equation, the second term is the expanded form of P_{NOFIRE}. Given P_{FIRE}, we simply generate a uniformly random number from 0 to 1 and generate an octant SLHI trigger if P_{FIRE} is larger than the random number.

Each P^i_{FIRE} above was obtained from the trigger turn on curves for the i^{th} *group of 16*[13]. As alluded to previously, threshold changed during the run demanded that several sets of curves be generated. Figure 5.11 shows the SLHI turn-on curves for a particular *group of 16* in each of the 8 octants. The solid curve is from the first trigger set, and the dashed is the latest. It is these curves which yield P^i_{FIRE} based on the associated trigger p_T. One observes an increase in the *trigger* p_T threshold for the later data. There were two reasons for this higher threshold. The first of these was simply a response to the rising energy scale of the LAC with increasing beam exposure. Since the LAC was generating about $\sim 25\%$ more trigger p_T late in the run than early in the run (see Figure 5.1), the trigger thresholds needed to be increased in order to maintain the same trigger rate. In other words, a fixed amount of physics p_T generates more trigger p_T late in the run than early in the run. Therefore, in order to trigger at approximately the same physics p_T, one needs to raise the trigger thresholds. Of course the time dependence of the energy scale was corrected for at a later stage in the analysis. The second reason for

[13] Recall, that a *group of 16* is synonymous with an adjacent pair of *groups of 8*.

increasing the thresholds was in response to the increased luminosity as the run progressed. With higher luminosity, increasing the thresholds results in more high p_T data being written to tape, while maintaining a similar live time fraction. In this situation, one is intentionally raising the physics p_T threshold in order to provide more suppression to the lower p_T events, and consequently, enhancement of high p_T events. The trigger p_T thresholds used generally equated to the SLHI turning on around 3.5 GeV/c in physics p_T.

In Figure 5.12 we give an illustration of what a SLHI event might look like in terms of the trigger[14]. In this figure, each radial division corresponds to a *group of 8 strips*. The color gradations give an indication of the energy deposition in each group. The trigger octant for an event such as this would be octant 1. Clearly, groups 13 and 14 in this octant contain the highest energy showers. In this event, it is suggested that the trigger arises primarily due to the p_T deposited in groups 12-14 of octant 1. All other groups have zero or nearly zero probability for firing[15]. On the awayside (octants 4-6) is shown some lower energy showers which are the fragments from the recoiling jet. Unlike the **trigger jet**[16], the **recoiling jet**[17] is not biased by the trigger[18]. Therefore, the awayside jet tends to fragment into many low p_T particles, as opposed to very few high p_T particles. Showers induced by high energy hadrons are marked accordingly. Note that the particles can hit anywhere along the length of the strip, and the measured *trigger* p_T would still be the same.

---

[14] The ϕ strips are not used in the trigger, and so they are not drawn.

[15] In Figure 5.12, the first *group of 16* corresponds to the sum of groups 1 and 2, the second *group of 16* to groups 2 and 3, etc.

[16] By trigger jet, we mean the jet which triggers an octant.

[17] By recoiling jet, we mean the jet which is on the awayside to the trigger jet.

[18] The bias we are referring to is with respect to the fragmentation function.

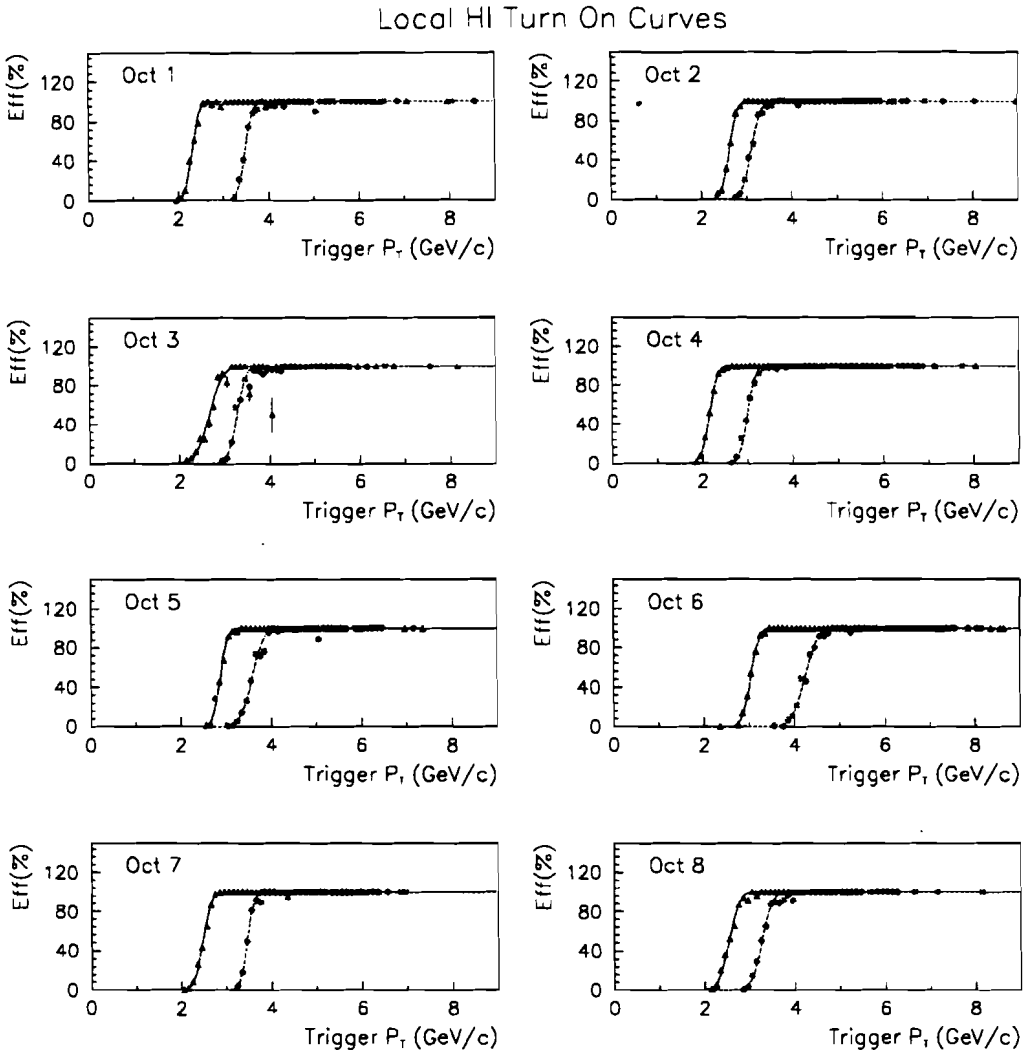

Figure 5.11 The SLHI turn-on curves for a particular group in each of the 8 octants. The fit is superimposed on the data points. The triangles correspond to trigger set 6 (early data), and the circles to trigger set 1 (late data).

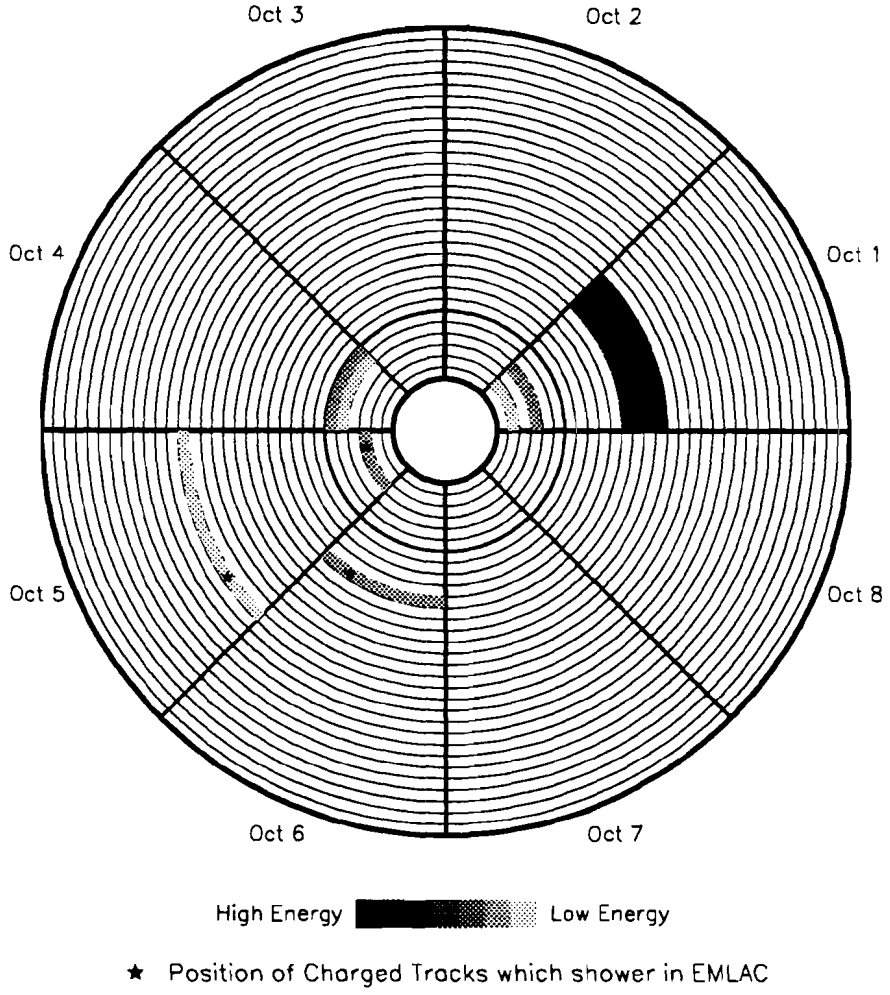

Figure 5.12 Schematic representation of a SLHI event which triggers octant 1.

Two Gamma

The TWO GAMMA trigger required that the SLLO threshold be satisfied in any 2 opposite octants. The turn on curves for the SLLO trigger are shown in Figure 5.13 for the 8 octants. The solid curve corresponds to trigger set 2, and the dashed to trigger set 6. For trigger set 1, the LO thresholds were raised to ~2.5 GeV/c, so that the TWO GAMMA was essentially absent for that trigger set. When mapping the *trigger* p_T into physics p_T, one finds that the SLLO turns on around 1.6 GeV/c (excluding trigger set 1).

The procedure for generating a SLLO trigger for a given octant was analogous to that of the SLHI above. The only difference is that the P^i_{FIRE} is extracted from the SLLO turn-on curves. Due to the lower thresholds, the probability that a **single** octant satisfies the SLLO trigger is much higher than the probability for it to satisfy the SLHI trigger. Since the TWO GAMMA required 2 opposite octants fire the SLLO trigger, the rate was reduced substantially, and was typically about 50-75% of the SLHI rate.

A schematic representation of a TWO GAMMA event is shown in Figure 5.14. Here, one observes that there are two high p_T octants (octants 3 and 8), each which fired the SLLO trigger. Generally, the high p_T objects which trigger an octant, reflect the direction of the jet fairly well. With this in mind, it is apparent from Figure 5.14, that the jets are not back to back in azimuth (ϕ). This may occur as a result of effects such as initial state k_T or having other jets in the event. For reasons such as these, the TWO GAMMA trigger defines **opposite octants** as any two octants which have an azimuthal difference greater then 90 degrees.

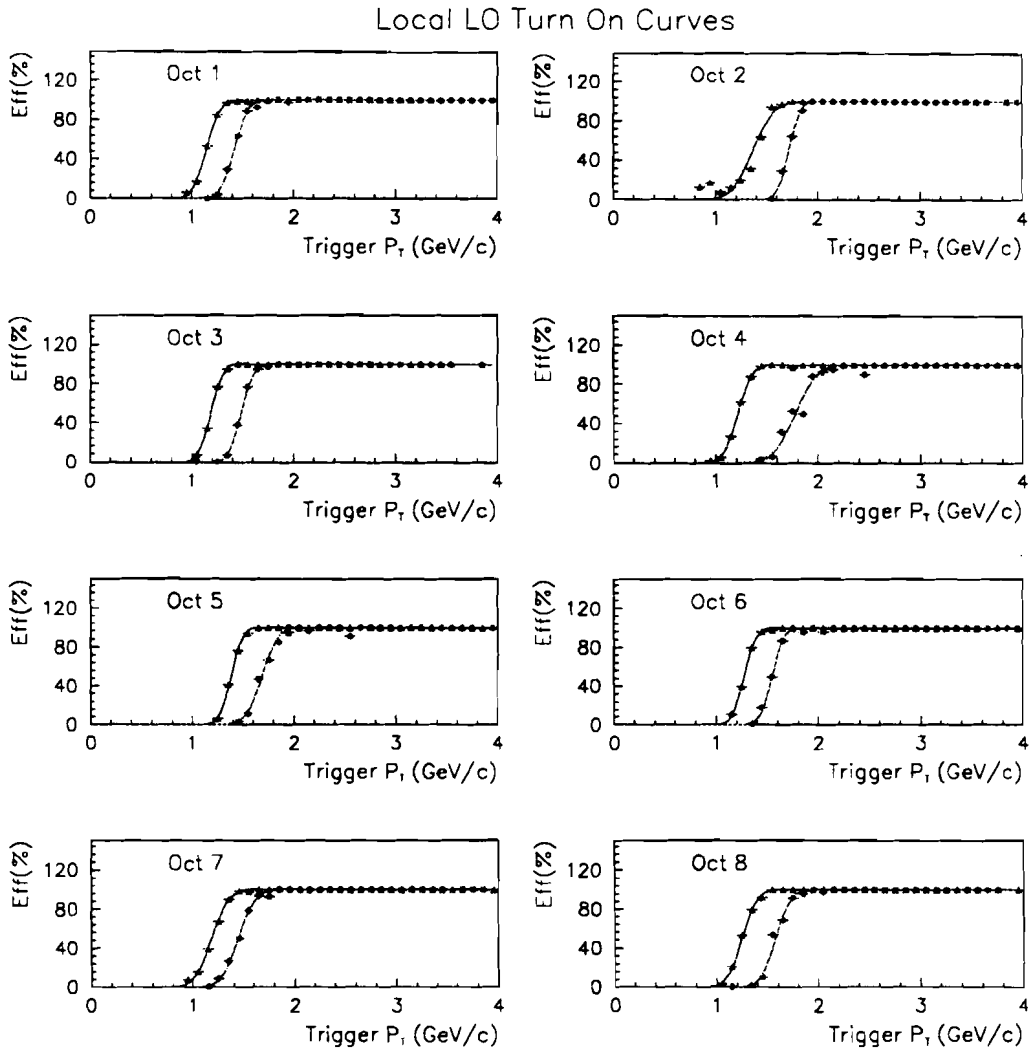

Figure 5.13 The SLLO turn-on curves for a single group in each of the 8 octants. The fit is superimposed on the data points. The triangles correspond to trigger set 6 (early data), and the circles to trigger set 2 (late data).

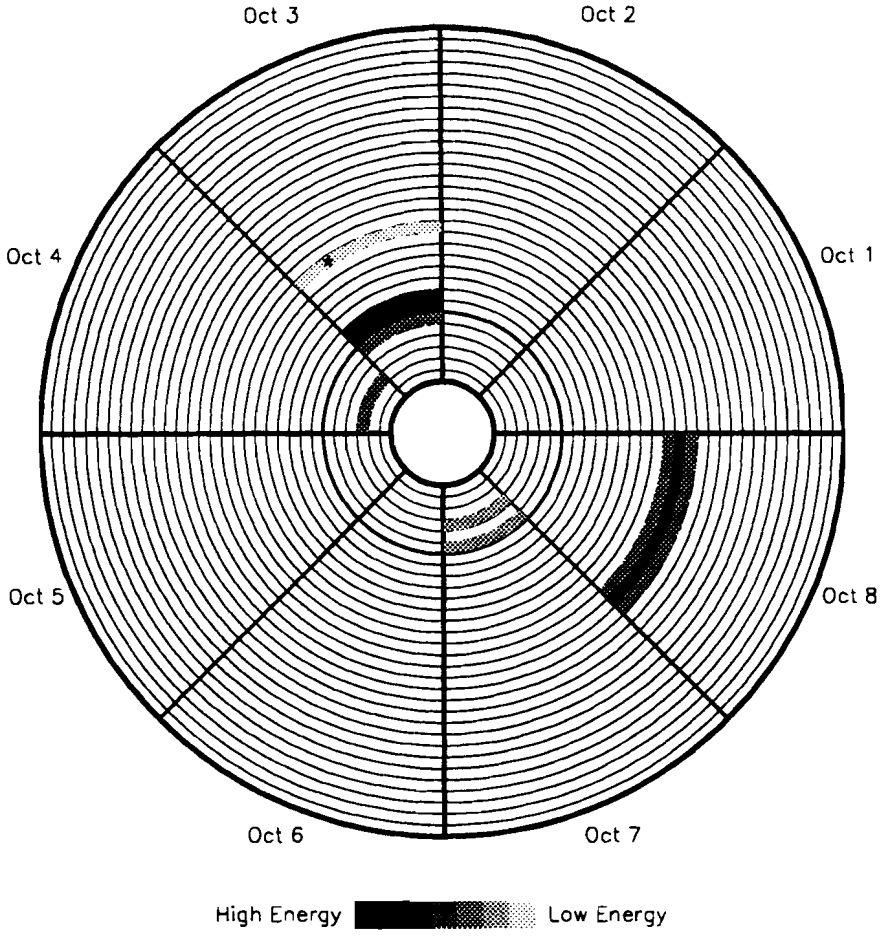

Figure 5.14 Schematic representation of a TWO GAMMA event which triggers octants 3 and 8.

Local Global Hi

The GLOBAL HI trigger is more complicated than the previously described LOCAL triggers. In principle, the GLOBAL trigger should consist of a direct sum of the trigger p_T contained within all the groups of an octant. As alluded to in chapter 2, a *cutoff* was applied to each group, in order to suppress coherent noise effects i.e. image charge. For each group, in both the front and back sections, a p_T cutoff of $\sim$ 250-300 MeV/c was applied to those groups above the threshold. Groups below the threshold were not included in the global p_T sum. In mathematical form the *global trigger* p_T can be written as,

$$p_T^{OCT} = \sum_{i=1}^{32} (p_T^i(f) - p_{CUT}^f) + (p_T^i(b) - P_{CUT}^b) \qquad 5.8$$

where, $P_{CUT}^{f,b}$ is the cutoff, based on group number, octant and section (front or back). The sum is over all groups in the octant. If a group's p_T is below the cutoff, the group was neglected in the above sum. To demonstrate the effects of the cutoffs, we show in Figure 5.15(a)-(d) the ratio of the GLOBAL "subtracted" p_T to the "total" GLOBAL p_T in various bins of "total" GLOBAL p_T. For example, Figure 5.15(a) shows that for events where the "total" GLOBAL p_T was in the range from 1-2 GeV/c, only about 20% of that p_T (on average) remains after the subtractions. In $\sim$10% of these events, the GLOBAL "subtracted" p_T=0.0. In contrast, Figure 5.15(c) shows that $\sim$50% (on average) of the GLOBAL p_T survives the subtractions. The width of each of these distributions is a result of the multitude of possible event topologies which may occur in any given event. For example, consider two events with the same p_T, but different topologies. Assume that one event has 3 particles with 1 GeV/c each, and the second event has a single particle with 3.0 GeV/c. Since each particle's EM shower is distributed over $\sim$3 groups, each EM shower has its GLOBAL p_T reduced by $\sim$750 MeV/c in the above sum (see 5.8). Therefore, the GLOBAL "subtracted" p_T will be $\sim$750 MeV/c and $\sim$2.25 GeV/c for these two events respectively. In the former case, the ratio of "subtracted" to "original" p_T is 0.25, and for the latter case it is 0.75. Due to

the way the p_T is distributed over the particles, we refer to these two examples as representative of *diffuse* and *local* event topologies. One can locate where these cases would lie in Figure 5.15(c), to get a flavor for the topological bias introduced by the GLHI trigger. In this example, the first event would certainly not fire the GLHI trigger, whereas the second case might (see Figure 5.16).

Figure 5.16 shows the GLOBAL HI turn-on curves for the 8 octants. The p_T axis refers to the GLOBAL p_T after the subtractions/cutoffs are applied. As expected, the turn-on's are somewhat broader than the locals', and the threshold is lower (around 2 GeV/c in GLOBAL p_T). The broadness is a result of integrating over the characteristics of many groups in the octant, as opposed to looking at any single group. In addition, event topology, fluctuations in the gains, as well as other global effects, will tend to widen these turn-on curves, as compared to the local turn on's. The GLHI trigger also required that the SLLO be satisfied in that octant. Since the SLLO definition was described previously in conjunction with the TWO GAMMA trigger, we refer the reader to that section for details. This local requirement tends to impose a more local nature to the global trigger. In conclusion, the GLHI trigger will be satisfied if both the GLHI and the SLLO thresholds were both satisfied in any given octant.

Finally, in Figure 5.17 we show a schematic of what a GLHI event might look like. It looks quite similar to the SLHI events shown in Figure 5.12 in that both contain a single high p_T shower in the trigger octant. The difference between the two is that the GLHI event in Figure 5.17 has additional high energy hadron showers in the octant as well. In this GLHI event, both the SLLO and GLOBAL HI must be satisfied. The SLLO was triggered by groups 13-15, while the GLOBAL HI fired based on the octant p_T sum, as defined in 5.8. As with the SLHI, the awayside recoil jet has produced several low p_T showers.

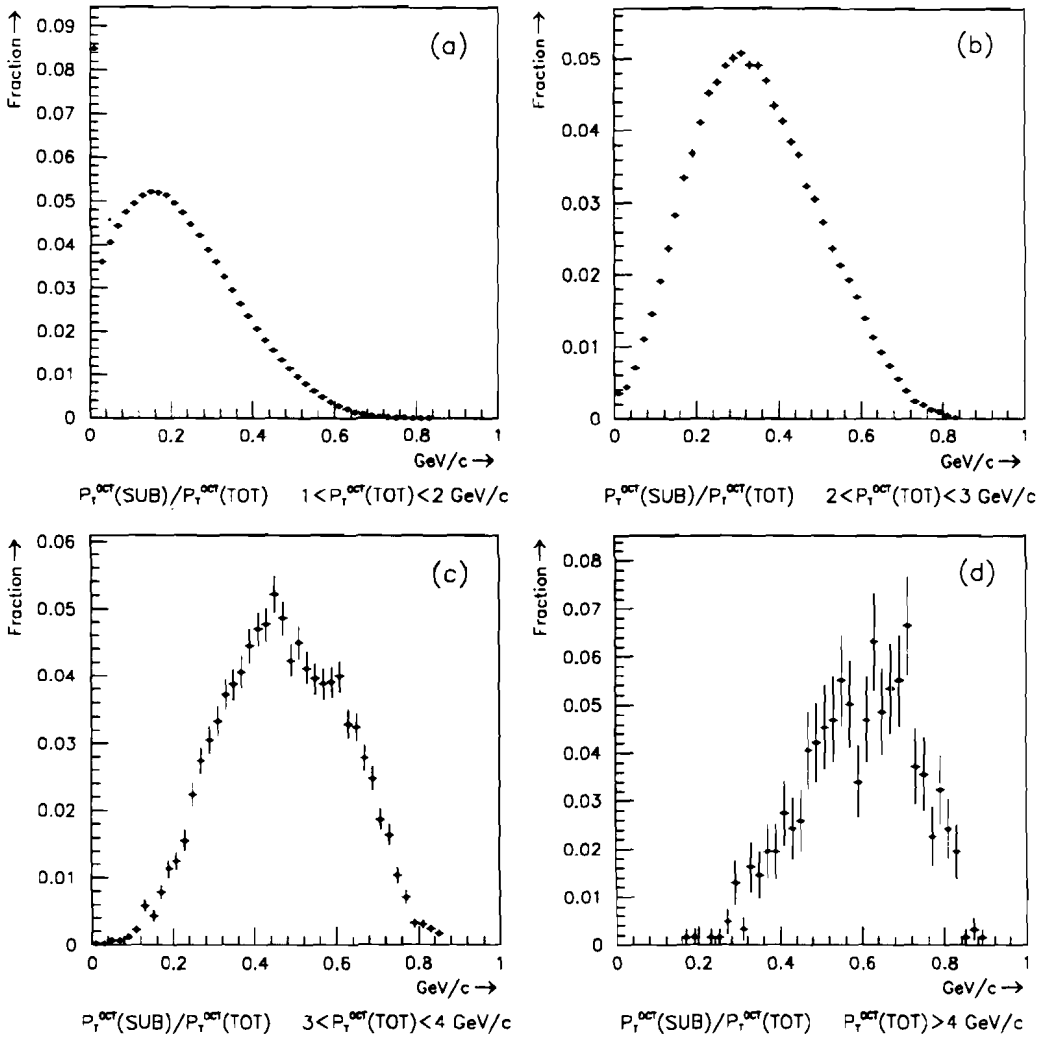

Figure 5.15 The fraction of the total global p_T which remains after applying the cutoffs in various bins of total global p_T (before subtraction).

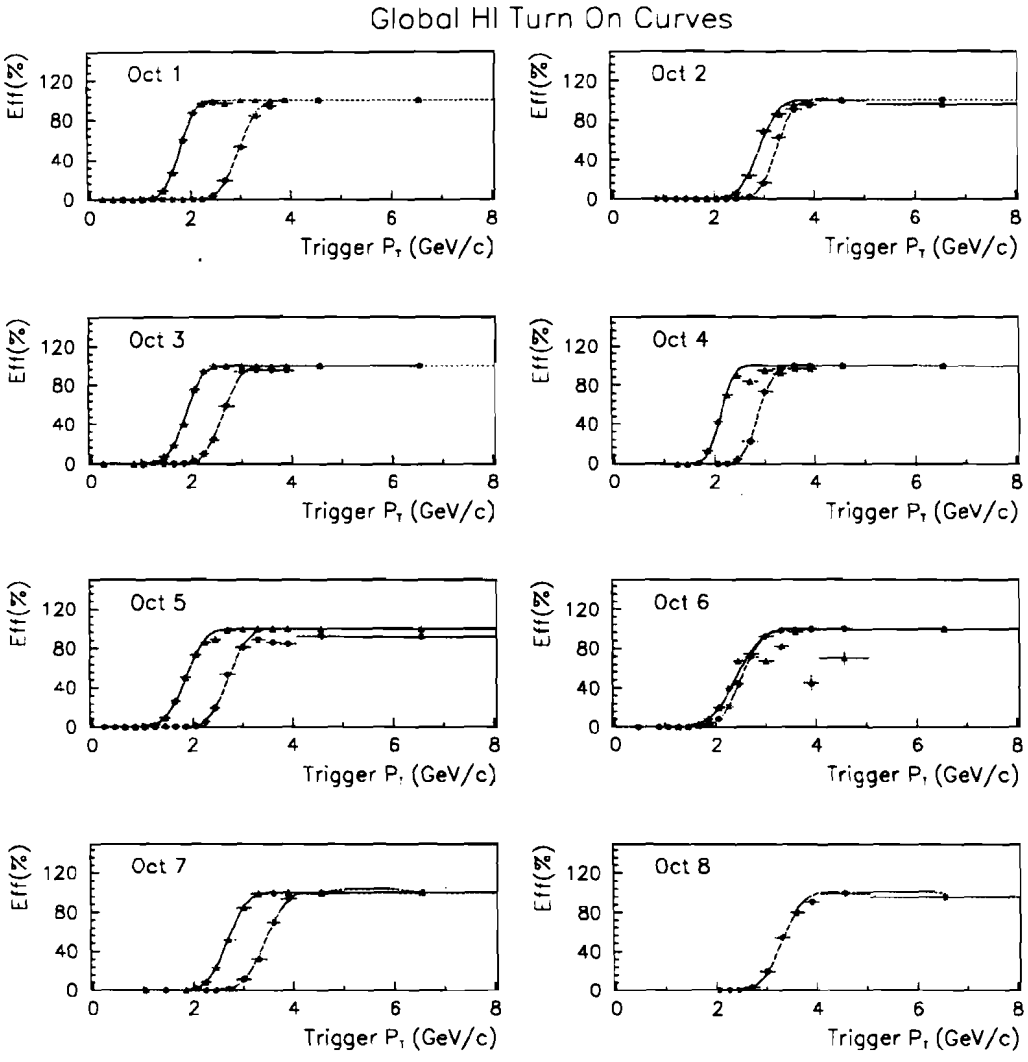

Figure 5.16 The global hi turn-on curves for the 8 octants for the early (triangles) and late (circles) data.

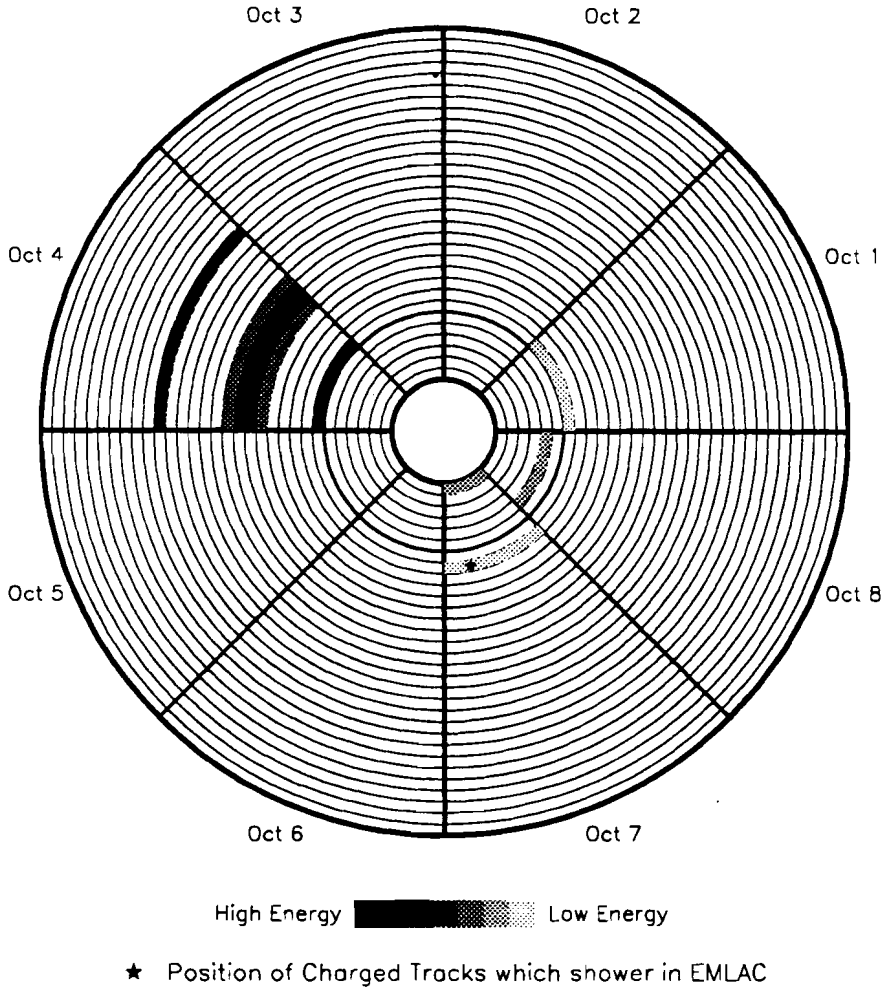

Figure 5.17 Schematic representation of a GLHI event which triggers octant 4.

After testing the trigger logic for these 3 triggers, the trigger status of the event was known. Based on the number of events which are accepted by either of these triggers with respect to the total number generated, we can calculate the trigger efficiency for the event sample under study. This efficiency can be plotted as a function of the p_T of any particle which is believed to be associated with the trigger. For example, we could estimate the efficiency of triggering on high p_T π^0's, η's, ω's etc., in a given rapidity range. For the purposes of this thesis, the particle of interest is a charmed particle. We wish to know how frequently an event containing charmed particles satisfies any of the aforementioned triggers. In the next section, we discuss the generator used to simulate the physics processes relevant for this trigger study.

5.4 Event Generation

The event generator chosen for performing a full event simulation was Pythia 5.7/Jetset V7.4[82]. Pythia generates various processes via LO mechanisms, as well as the underlying events associated with the spectator partons. The initial and final state partons develop parton showers via QCD radiation. Pythia/Jetset use the Lund string model for the fragmentation of the final state partons into colorless hadrons. The Jetset package handles the decays of unstable particles via an exhaustive list of decay modes and branching ratios extracted from the PDG tables. After the fragmentation and decays, we are left with a number of stable hadrons which are observed in the various detectors. A variety of physics processes are available to the user. For this analysis, only the minimum bias and charm production processes were used.

Pythia has a number of input switches and parameters by which the user can designate the process of interest and the kinematic regime. These main input parameters are the following:

- Process ID: The processes selected was either minimum bias events or LO charm hadroproduction.

- p_T^{MIN}, p_T^{MAX}: Minimum and maximum p_T of the hard subprocess. (Set to 0.0 and $\sqrt{s}/2$ respectively.)
- Y^{MIN}, Y^{MAX}: Minimum and maximum rapidity of the hard subprocess in the center of mass frame. (Set to $\mp$ 4.0 units of rapidity.)
- BEAM/TARGET particle types and momenta: We used 515 GeV/c π^- beam incident on a fixed proton target.

In addition to these, there are many other user-controllable parameters, such as choice of structure functions, Q^2 definition, fragmentation parameters, etc, which were left at the default values.

There were a few parameters which were adjusted in Pythia from their default values. These were,

- Effective minimum transverse momentum $p_\perp$ for multiple interactions. This parameter was reduced to 0.700 GeV.
- Width of primordial k_T distribution[19] This parameter was increased to 1.05 GeV.

The motivation for changing these parameters from their default values will be discussed in the next section. After running Pythia with a particular process, and a specified kinematic domain, the user had available a list of stable particles with which to work. For each particle, its momentum, production point and particle ID was stored within the event history. It was these final state particles which were fed into the aforementioned trigger simulation to evaluate the trigger bias.

---

[19] From this point onward, k_T is used loosely to refer to the gaussian width or the root mean square (RMS) of the intrinsic parton momentum ($\sqrt{< k_T^2 >}$).

5.5 Studies of the Pythia MC

In order to gain confidence in Pythia, we should be able to reproduce the features of the E706 data. To this end, we wish to be able to reproduce the p_T, rapidity, and multiplicity distributions of particles observed in the data using the Pythia MC. Since the bulk of the E706 data is QCD jet data, we wish to compare the Pythia QCD MC with the E706 data. Charm is a subset of all QCD diagrams, and is different only in that the charm quark mass is not neglected in the matrix elements. Consequently, we take the approach that if we can reproduce the relevant features of the E706 data with the Pythia QCD MC, then we can rely on Pythia to give reasonable predictions for the charm trigger efficiency.

5.5.1 $p_\perp$ *and* k_T

As alluded to previously, two of the default Pythia parameters were adjusted from their default values. The motivations for changing these parameters was to bring the Pythia simulation into better agreement with the data. The primary difference between Pythia and the data was in the overall event multiplicity. From the multitude of adjustable parameters available, one parameter was identified which had the largest observed effect on the event multiplicity, $p_\perp$.

The parameter, $p_\perp$ (PARP(81) in Pythia), gives the minimum value for which "hard" processes are described by QCD. For small values of $p_\perp$, QCD predictions become unreliable, and one must adopt a different prescription to describe particle production at high energy. With this in mind, Pythia invokes a description of low p_T processes which is **finite** as $p_T \to 0$, unlike LO QCD. Therefore, for collisions with $p_T > p_\perp$, the process is described via QCD cross section formulae, and for $p_T < p_\perp$, the low p_T description is used. Therefore, lowering $p_\perp$ permits a larger fraction of the interactions of the partons to be described via QCD $2 \to 2$ cross sections as opposed to the low p_T description. Since the QCD interactions produce more particles than the soft, low p_T description, reducing $p_\perp$ tends to increase the event multiplicity. Since spectator partons may also interact, this treatment

applies to them as well. The description of the low p_T phenomenon is by no means an easy topic, and is fairly controversial. We only wish to use this mechanism to improve the agreement of the observed spectra of final state particles in the MC with that of the data; the exact details of the mechanism is irrelevant, since it is only a model of what is going on, nothing more. Figure 5.18 shows the sensitivity of the track multiplicity[20] to lowering this parameter. The lower value of $p_\perp$=700 MeV/c produces about 50% more tracks than provided by the default choice of 1450 MeV/c. Later, we shall show comparisons of the Pythia MC ($p_\perp$=700 MeV) with the data. As an aside, it was checked that changing this parameter does not make any appreciable change in the characteristics of the charm particles produced in charm events.

The second modification to the default parameters of Pythia was to increase the primordial transverse momentum of the partons inside the colliding hadrons i.e. the k_T. The first indication that a higher value of k_T was warranted, occurred when comparing the MC trigger rate with the observed trigger rates in the E706 data. The trigger rates from the data were measured from a sample of minimum bias data which was recorded during the 1990 run. Since the trigger logic was recorded even for the minimum bias events, we could measure how often a minimum bias event would have fired a given trigger. In an analogous manner, Pythia minimum bias events were generated[21], and subjected to the software trigger simulation. The number of events satisfying the SLLO, SLHI, and GLHI were recorded, as well as a tally of the total number of events generated. Ratios of the number of events satisfying each trigger with respect to all events were formed, and compared to the measured trigger rates in the data. Figure 5.19(a) shows the fraction of events in

---

[20] These distributions represent the number of stable charged tracks which are within the E706 charged tracking acceptance.

[21] The minimum bias events were primarily gg interactions, with smaller contributions from qg, qq and low p_T processes[82].

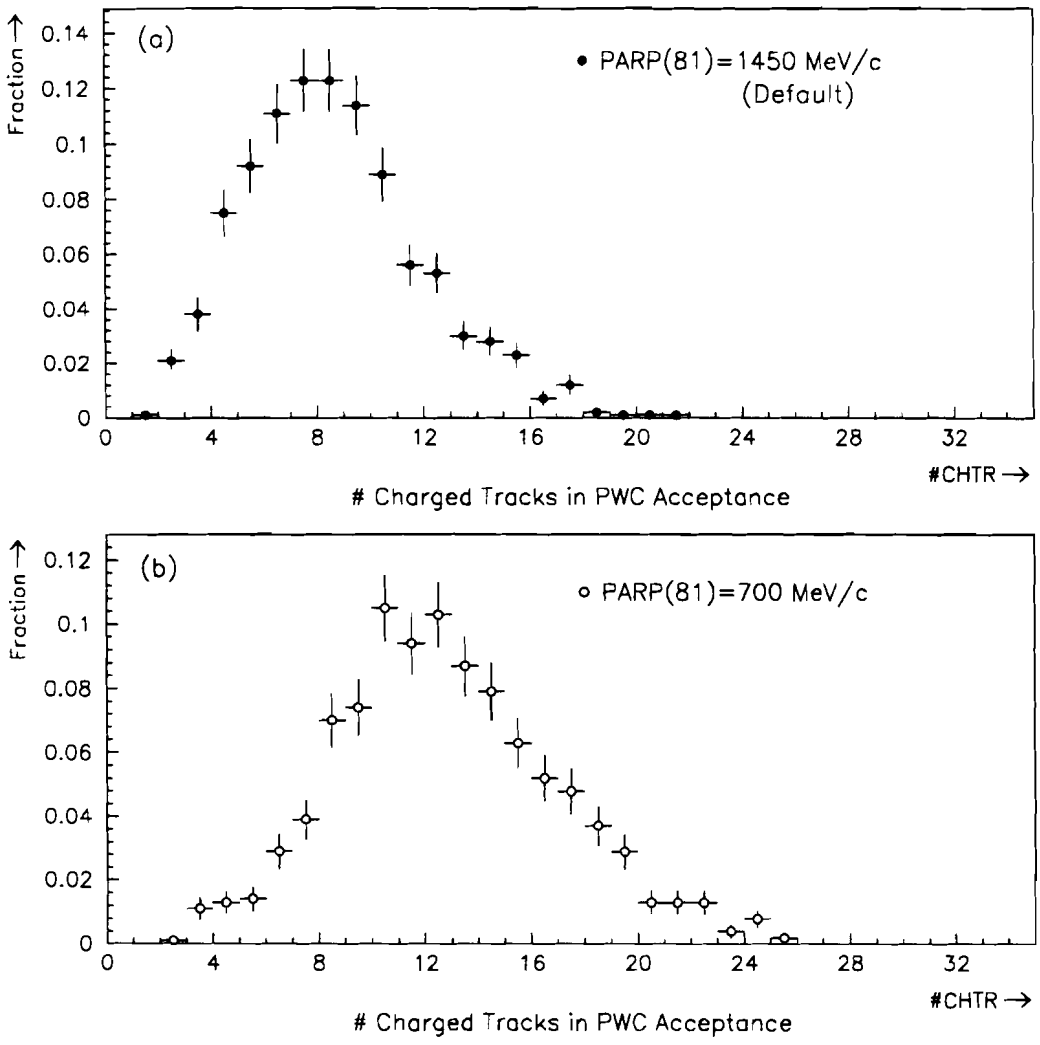

Figure 5.18 Comparison of the Pythia charged track multiplicity within the E706 PWC acceptance for (a) $p_\perp$=1450 MeV/c (default) and (b) $p_\perp$=700 MeV.

which any octant satisfies the SLLO as a function of the k_T used in the MC. The data trigger rate and its uncertainty are shown as a shaded band across the plot. From this plot, it is clear that the data favor a value of k_T ~1.05 GeV. Figure 5.19(b) shows the fraction of events satisfying the SLHI trigger for the data and MC. The same conclusions can be drawn as with the SLLO. It therefore appears that the data tend to favor a larger value of k_T in order for the Pythia MC to reproduce the trigger rates in the data. In summary, the Pythia simulation can be brought into better agreement with the E706 data provided we use a k_T ~1.05 GeV and $p_\perp$ ~700 MeV.

The second indication for using a higher value of k_T in Pythia was based on an article by Bellini[83] and references therein. In that article, it was indicated that the Pythia MC could be brought into better agreement with the various data on charm hadroproduction provided a larger value of $k_T \sim 1.0$ GeV was used. To investigate this further, a comparison was made between published E769 data[84] and Pythia for various choices of k_T. In Figure 5.20 we compare the p_T and x_F spectra from Pythia with that obtained from the E769 data. The E769 data were taken at an incident π^- beam energy of 250 GeV/c. The Pythia plots were generated using the same beam energy. The plots utilize the following parametrizations of the charm cross section,

$$\frac{d\sigma}{dp_T^2} \sim e^{-\beta p_T} \qquad \text{for} \sim p_T > 1 \text{GeV/c} \tag{5.9}$$

$$\frac{d\sigma}{dx_F} \sim (1 - x_F)^n \qquad \text{for } x_F > 0. \tag{5.10}$$

In Figure 5.20(a), we show the comparison of the β values obtained from Pythia, and how they compare with E769 data. In Figure 5.20(b), we show the fitted values for n. These comparisons tend to indicate that a higher value of $k_T \sim 1.0 \pm 0.2$ GeV/c would describe the data better than the default value of 0.45 GeV. Preliminary results from E791 have also indicated that a higher value of $k_T \sim 1$ GeV is necessary

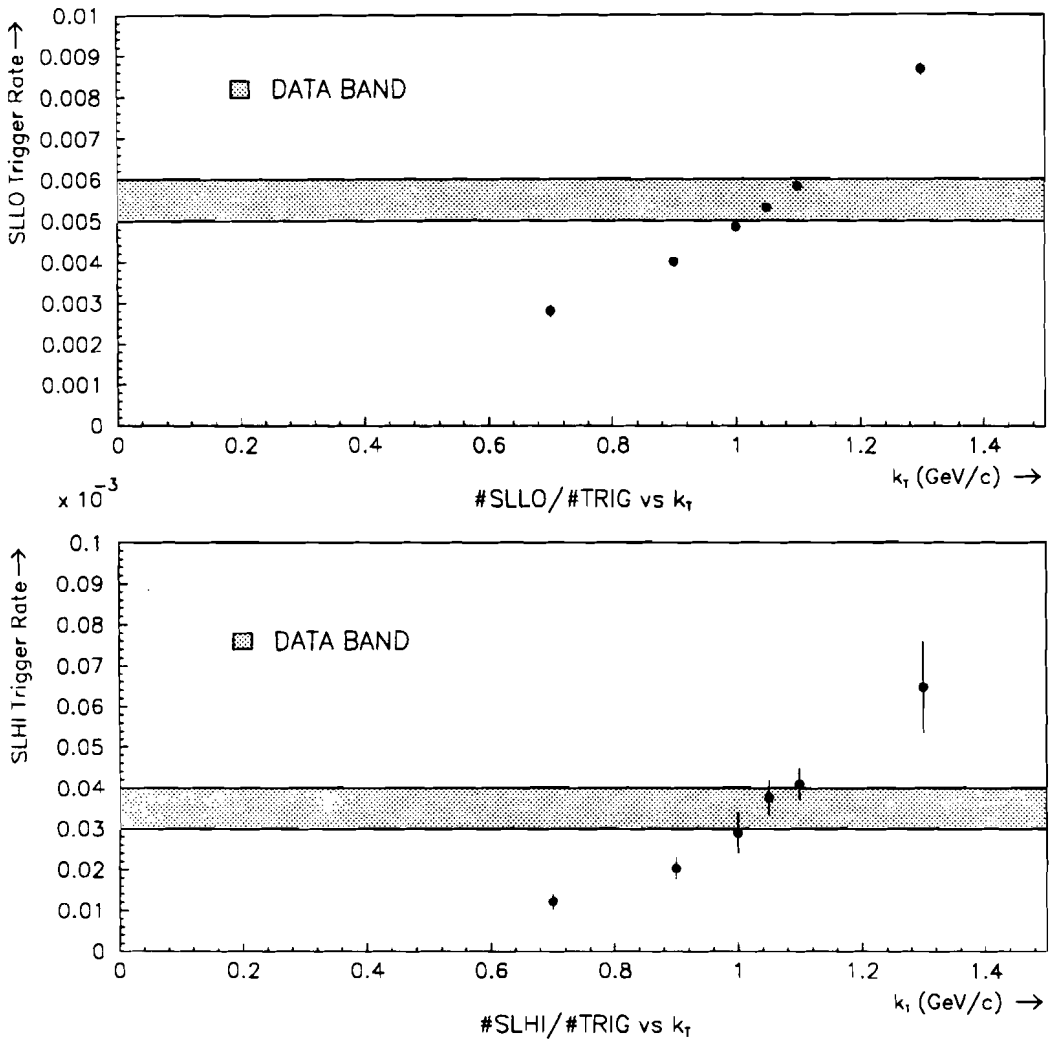

Figure 5.19 The fraction of events in which (a) the SLLO was satisfied, and (b) the SLHI was satisfied, as a function of the k_T used in the MC. The shaded band across the plot shows the SLLO and SLHI trigger rates as measured in the data. The width of the band is an estimate of the uncertainty.

in order to describe the correlation in $\Delta\phi$[22] between charm pairs, as well as the distribution in p_T^2 of $D\overline{D}$ pairs[85].

It is interesting, but not surprising that both the E706 data and the E769/E791 data on charm hadroproduction indicate that if Pythia is used to model these physics processes, a similar amount of k_T is required. Since both these samples have large gluon components at the Feynman level, one would hope that the two results are consistent. Both samples tend to prefer a $k_T \sim 1.0$ GeV in order to reproduce the features of the data.

5.5.2 Data vs Pythia for QCD 2 → 2 Events

In this section, various comparisons are made between the E706 1990 data and the Pythia MC. It is necessary that the MC reproduces the features observed in the data in order to claim that the MC gives reliable predictive power for estimating efficiencies. Consequently, it is necessary to demonstrate that the MC reproduces the relevant aspects of the data.

The procedure adopted for this study was to generate minimum bias events using Pythia, subject each event to the trigger simulation, and select any event which satisfies either the SLHI, GLHI, or 2 GAMMA trigger. The selected events were run through GEANT, which included a full detector simulation. An analogous sample was selected from the data, where we required that one of these aforementioned triggers must be satisfied. We now present comparisons between the MC and data on several different axes for these selected events. First we show comparisons involving primarily the charged tracks, and afterward some distributions involving photons.

First, we show in Figure 5.21 the multiplicity of reconstructed charged tracks for both the MC and data. The data tend to be somewhat broader than the MC,

---

[22] Here, $\Delta\phi$ refers to the angle between the 2 charm particles in the plane transverse to the beam direction.

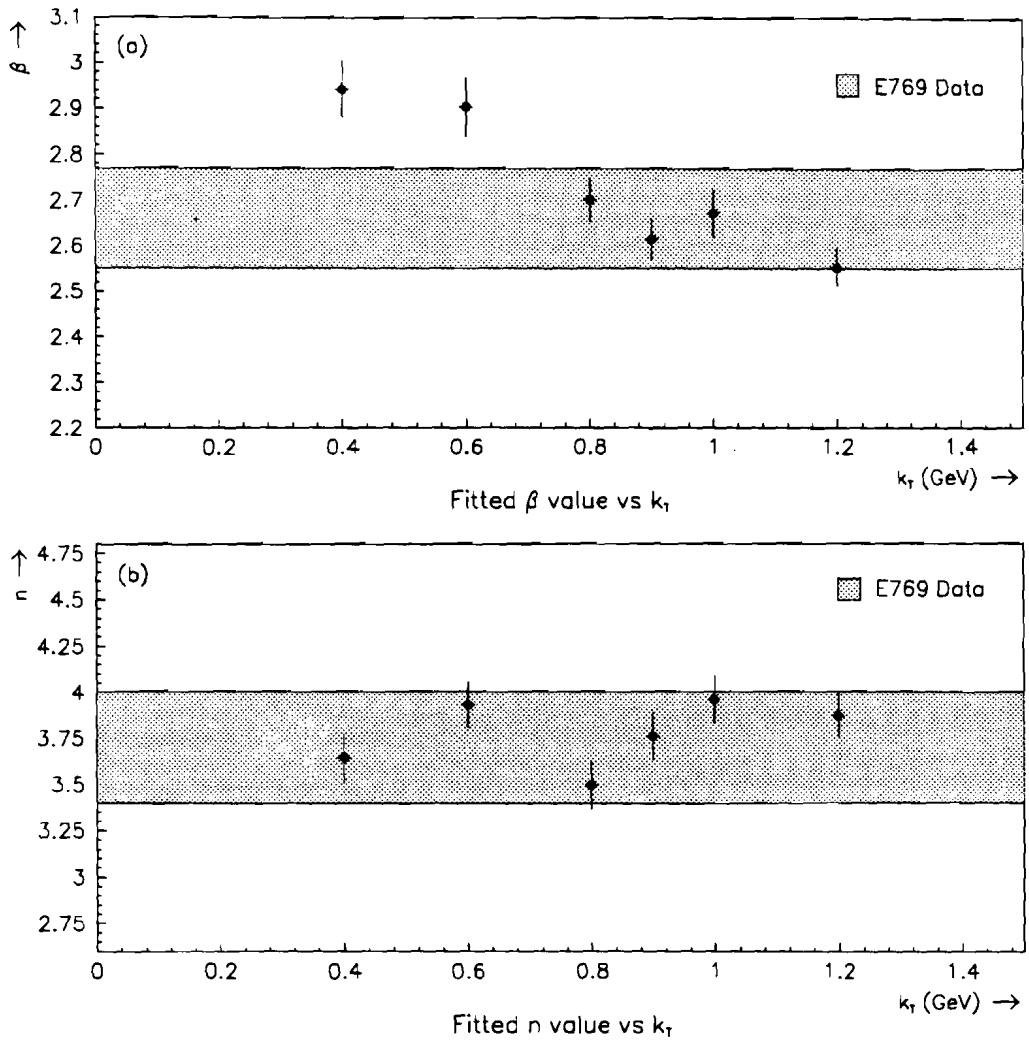

Figure 5.20 Comparison between the E769 data (shaded region), and the Pythia MC for the dependence of the charm cross section on (a) p_T, in the range 1-4 GeV/c, and (b) x_F, in the range 0.1-0.7.

but the overall agreement is satisfactory. Figure 5.22(a) shows the distributions in p_T, and (b) the ratio of the data to MC, for the charged tracks in these events. The ratio is fairly flat, with perhaps fractionally more low p_T tracks in the data than the MC. This could be a result of the nuclear effects which are not incorporated in the MC. The overall normalization in this ratio, and the forthcoming comparisons, are simply a reflection of the statistics in each sample. In Figure 5.23 is shown the comparison of the rapidity distributions of charged tracks between MC and data. The ratio of these distributions in Figure 5.23(b) indicates a slope which is consistent with the absence of nuclear (breakup) effects in the MC. Since the trigger rates are sensitive to the energy and position of particles at the face of the EMLAC, we show two additional distributions. In Figure 5.24 is shown the total momentum of charged tracks in the MC and data, along with the ratio. Again, the agreement is satisfactory, although not perfect. Finally, we show in Figure 5.25 the radial position of charged tracks at the face of the EMLAC. The agreement is reasonable, but degrades somewhat for $\sim R < 6$ cm. However, the inner radius of the EMLAC is at ~ 20 cm, so that the agreement is fairly nice within the fiducial volume.

Turning to photons, we are primarily interested in the triggering photon(s). Since most of the photons in QCD events arise from decays of π^0's, it is essential to compare the π^0 cross section as measured in the data, with that of the Pythia MC. In Figure 5.26 we show the measured π^0 cross section in the region from 0.6-5 GeV/c for minimum bias events. The data use the INTERACTION trigger[86] for the region up to about 2 GeV/c, and the PRETRIGGER from 2-5 GeV/c. Overlayed is the Pythia result using its own minimum bias events. Both the data and the MC are restricted to the center of mass rapidity range $-.75 < Y_{\pi^0} < .75$. One observes remarkably nice agreement over this p_T range, which spans approximately 6 orders of magnitude. Agreement in this variable is crucial, since it is primarily π^0's which trigger the apparatus.

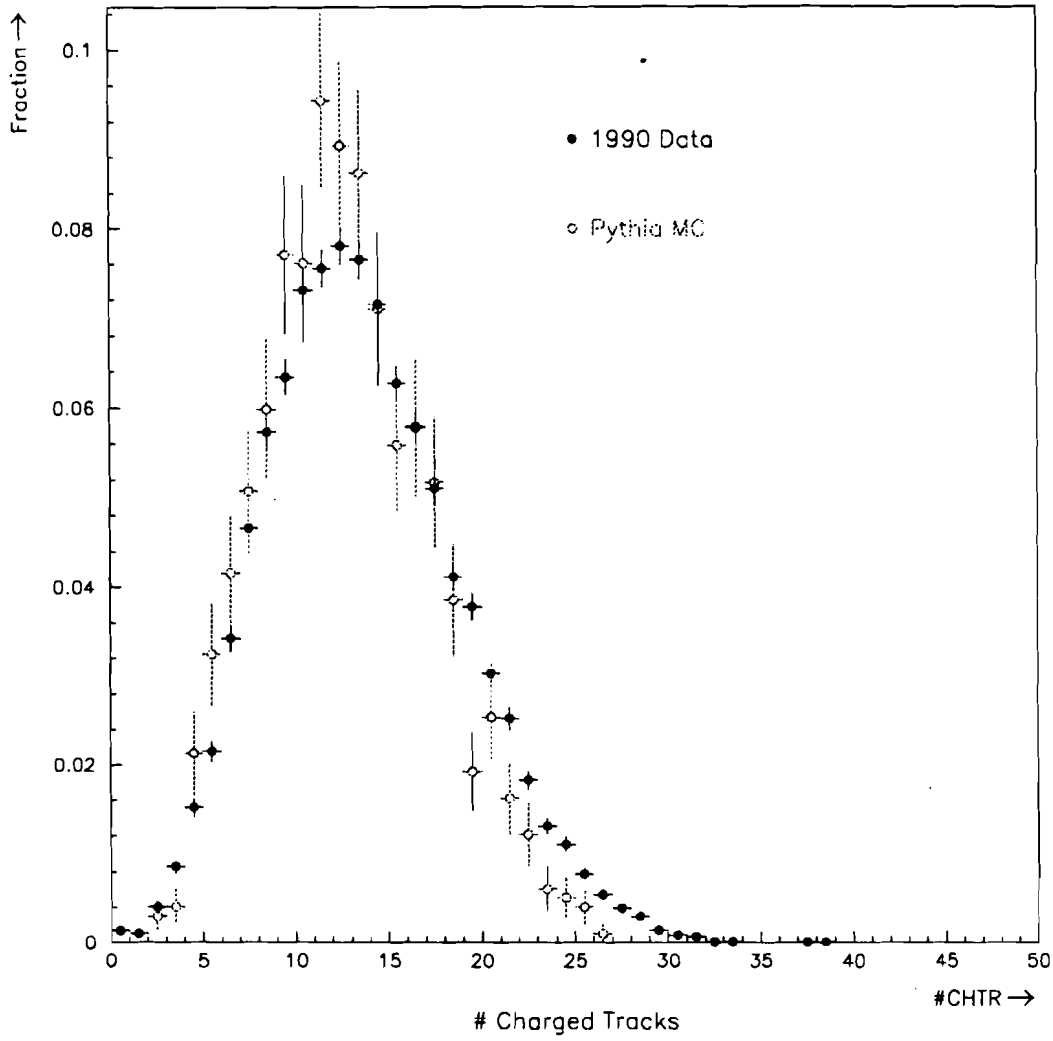

Figure 5.21 The multiplicity of charged tracks per event in the data and MC.

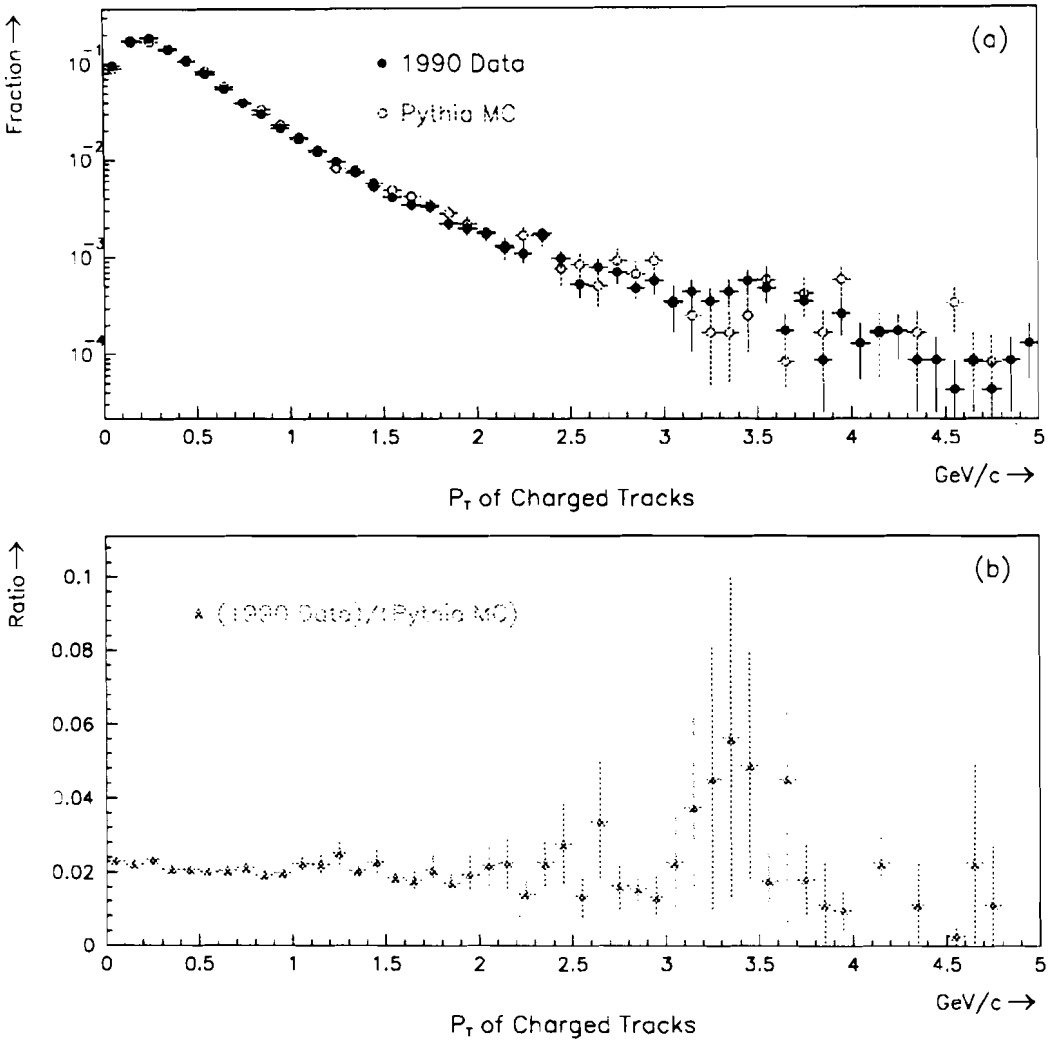

Figure 5.22 The comparison of the p_T distributions of the charged tracks in data and MC. Both are normalized to unit area. In (a) the two distributions are overlayed, and in (b) the ratio of DATA/MC is shown.

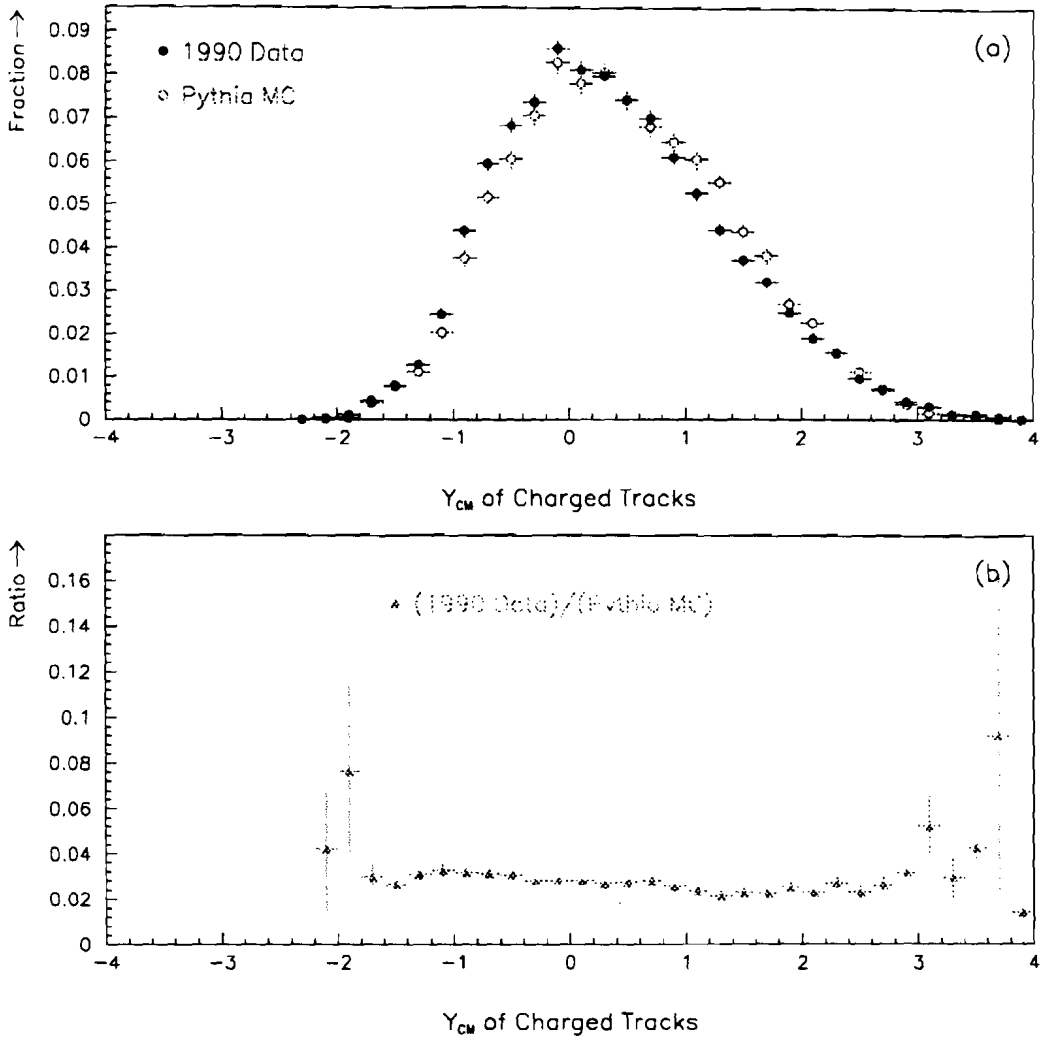

Figure 5.23 The comparison of the Y distributions of the charged tracks in data and MC. Both are normalized to unit area. In (a) the two distributions are overlayed, and in (b) the ratio of DATA/MC is shown.

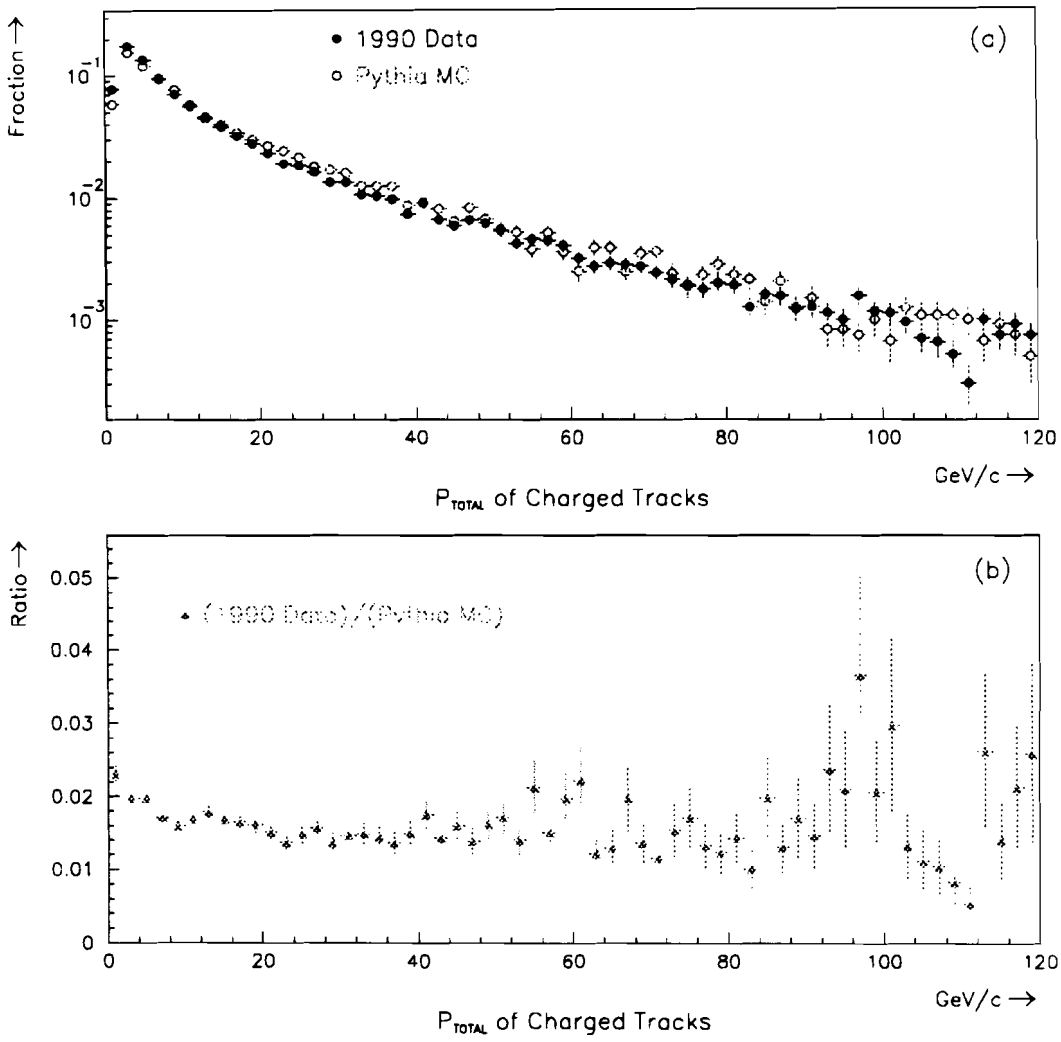

Figure 5.24 The comparison of the momentum distributions of the charged tracks in data and MC. Both are normalized to unit area. In (a) the two distributions are overlayed, and in (b) the ratio of DATA/MC is shown.

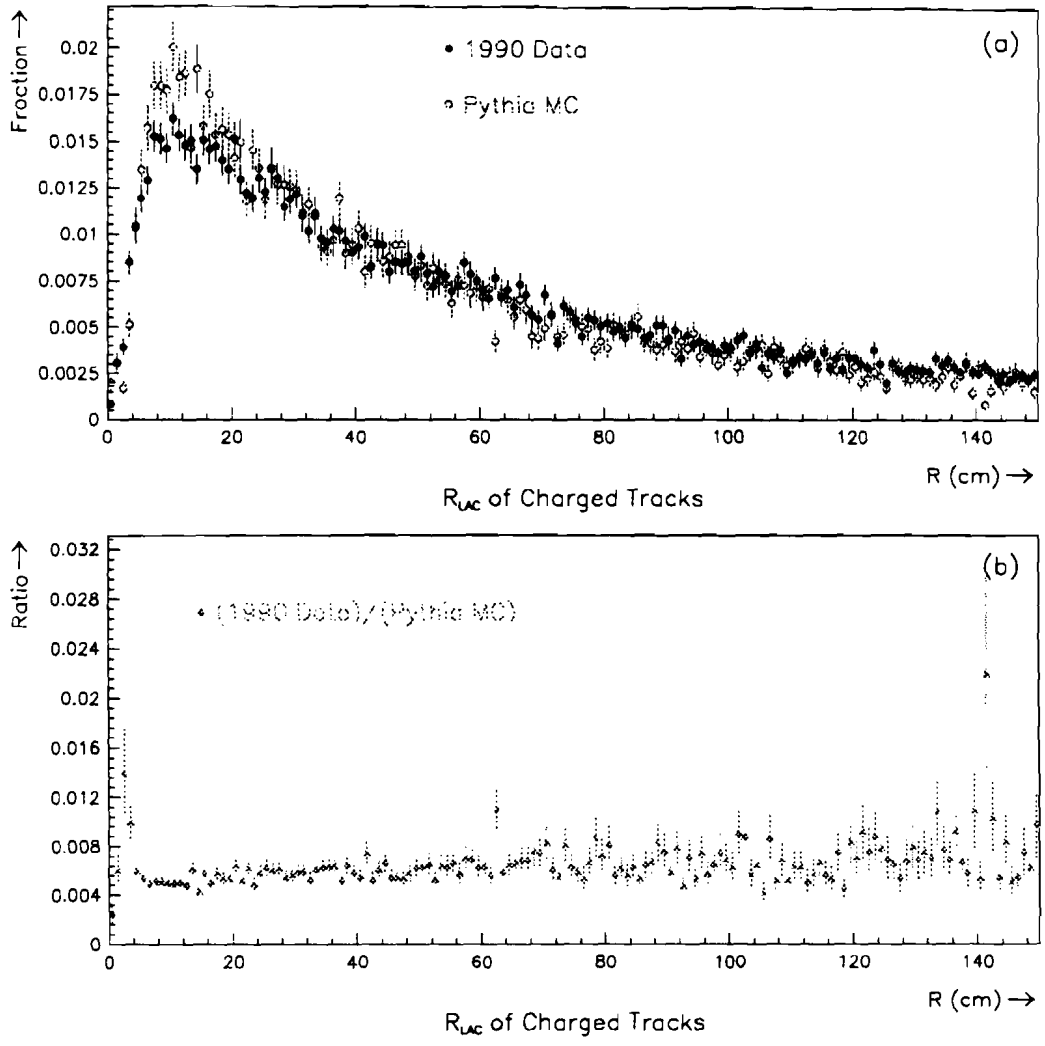

Figure 5.25 The comparison of the R position of the charged tracks at the face of the EMLAC in data and MC. Both are normalized to unit area. In (a) the two distributions are overlayed, and in (b) the ratio of DATA/MC is shown.

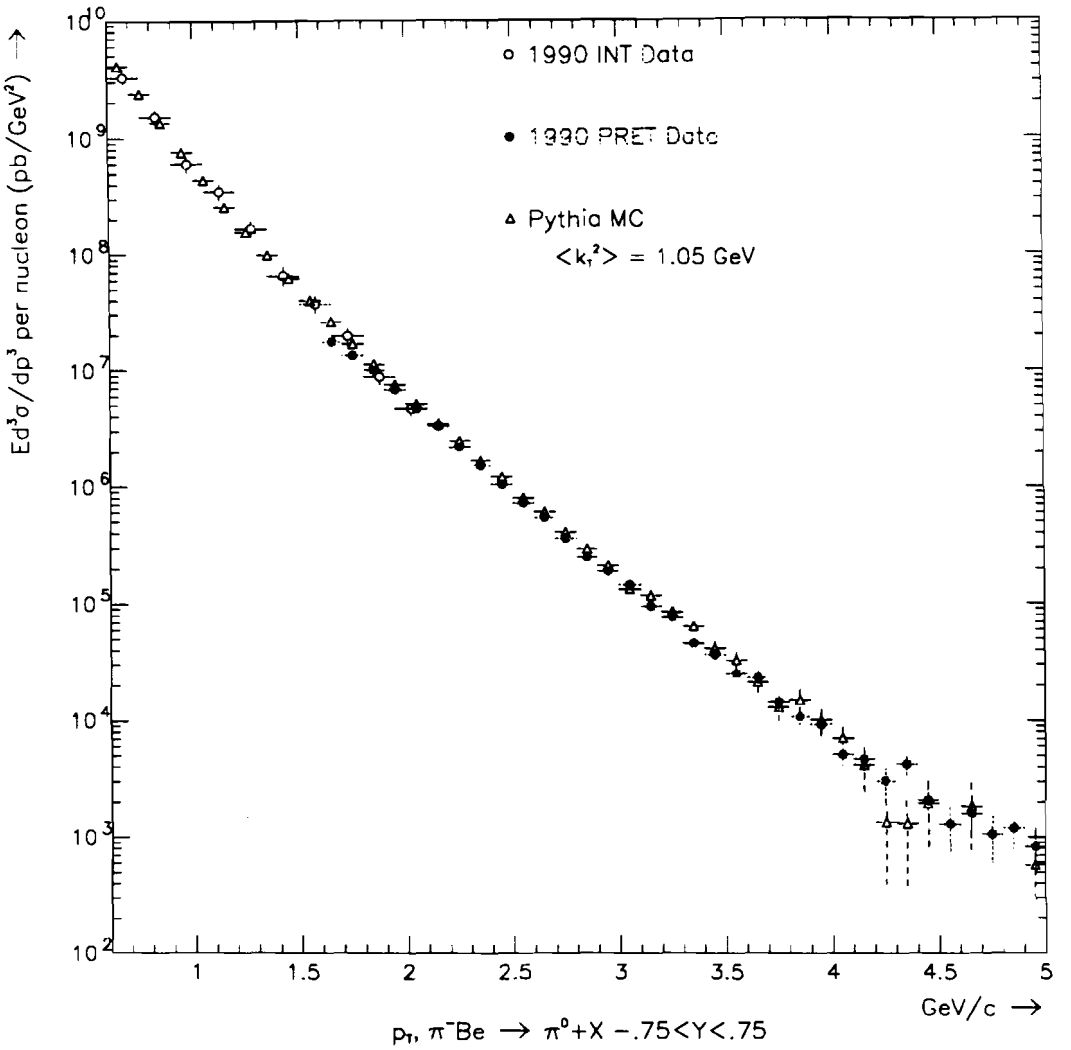

Figure 5.26 The invariant π^0 cross section per nucleon for data and MC. The MC is normalized to the data to compare shapes.

We now return our focus to the subset of events which were selected by one of the high p_T triggers. In Figure 5.27 is shown the transverse momentum of the highest p_T photon in the **triggered** events. Figure 5.27(a) shows the MC distribution and Figure 5.27(b) the corresponding data distribution. The effects of the LO and HI thresholds is evident in the data plot since only one run was used. For the MC, we averaged over all of the trigger (threshold) sets, so the effect is smeared out. Nevertheless, the two distributions are in reasonable agreement with one another, which suggests that the software trigger biases the events in a similar way as the online data trigger. One can also check that the trigger affects the rapidity distributions in the same way. Shown in Figure 5.28 is the rapidity distribution of the highest p_T photon in the data and the Pythia MC. The two distributions are seen to be in agreement with one another over the full rapidity range.

We now wish to investigate the correlation of other charged tracks in the event with the *trigger particle*[23]. Shown in Figure 5.29 is the difference in the azimuthal angle of charged tracks from the trigger particle. The distributions are split into subsets, with the criteria imposed on the charged tracks that (a) $p_T > 0$, (b) $p_T > 0.25$ GeV/c, (c) $p_T > 0.50$ GeV/c, and (d) $p_T > 1.00$ GeV/c. Within the level of statistics, the MC and data tend to agree fairly well. This indicates that the distribution of particles about the jet axes are similar between the MC and data. Finally, in Figure 5.30 is shown the number of charged tracks with $\Delta\phi$ within 1.0 radian of the trigger particle for the same p_T cuts imposed in Figure 5.29. The largest discrepancy is for the low p_T region, and the agreement improves as the p_T increases. Again, this is consistent with the notion that the MC does not simulate nuclear effects.

---

[23] By *trigger particle*, we simply mean the highest p_T photon above 1.25 GeV/c.

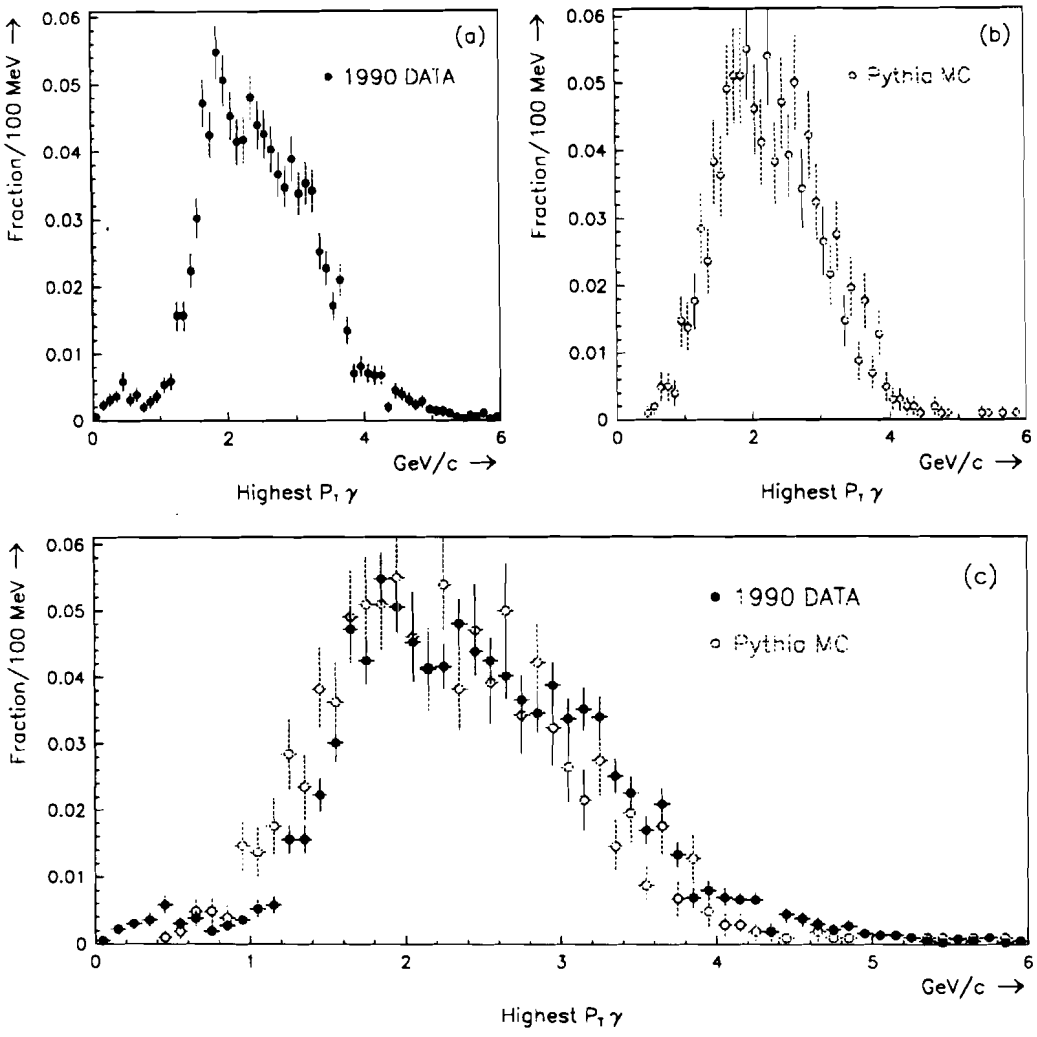

Figure 5.27 The highest p_T photon in an event which satisfied either the SLHI, GLHI, or 2 GAMMA trigger, for (a) Pythia MC and (b) Data. The overlay is shown in the bottom figure.

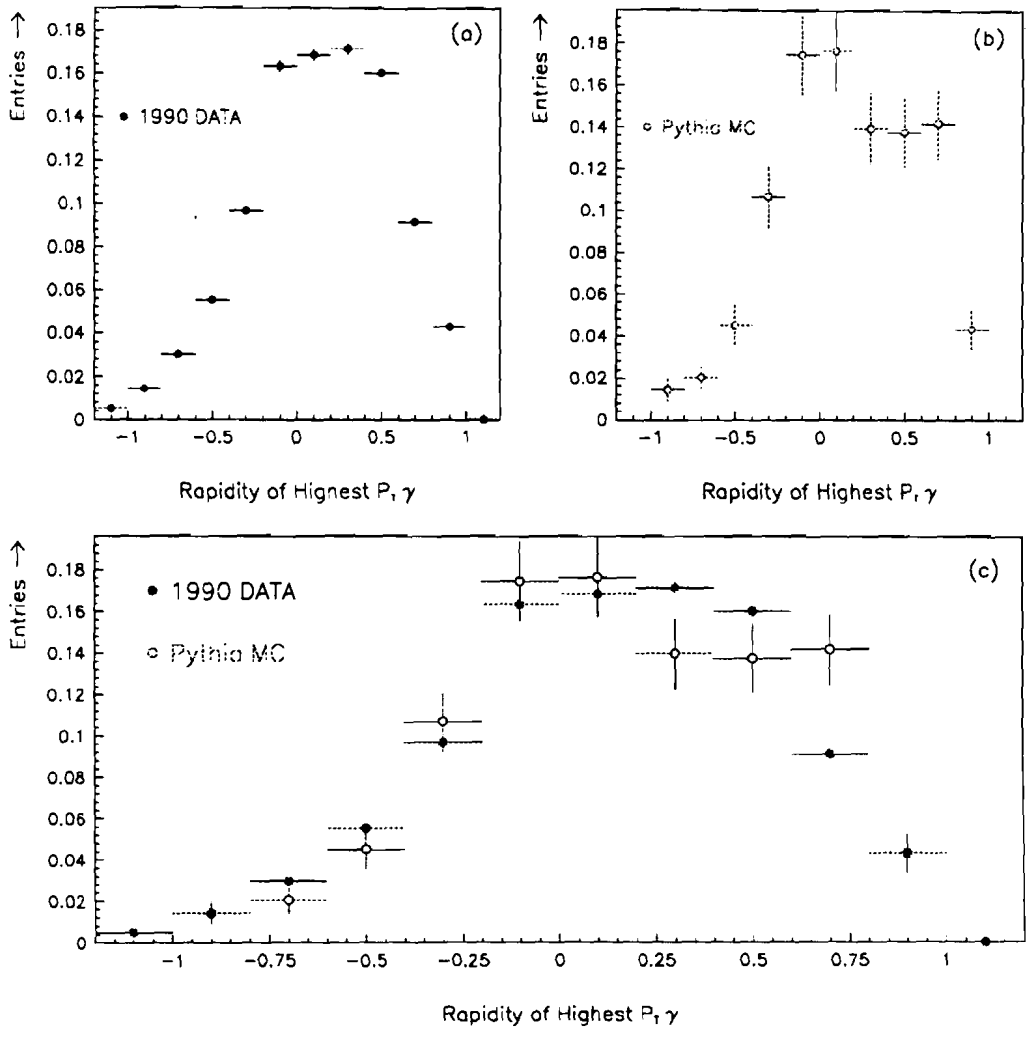

Figure 5.28 The rapidity spectrum of the highest p_T photon in an event which satisfies either the SLHI, GLHI, or 2 GAMMA trigger, for (a) Pythia MC and (b) DATA. The overlay is shown in (c).

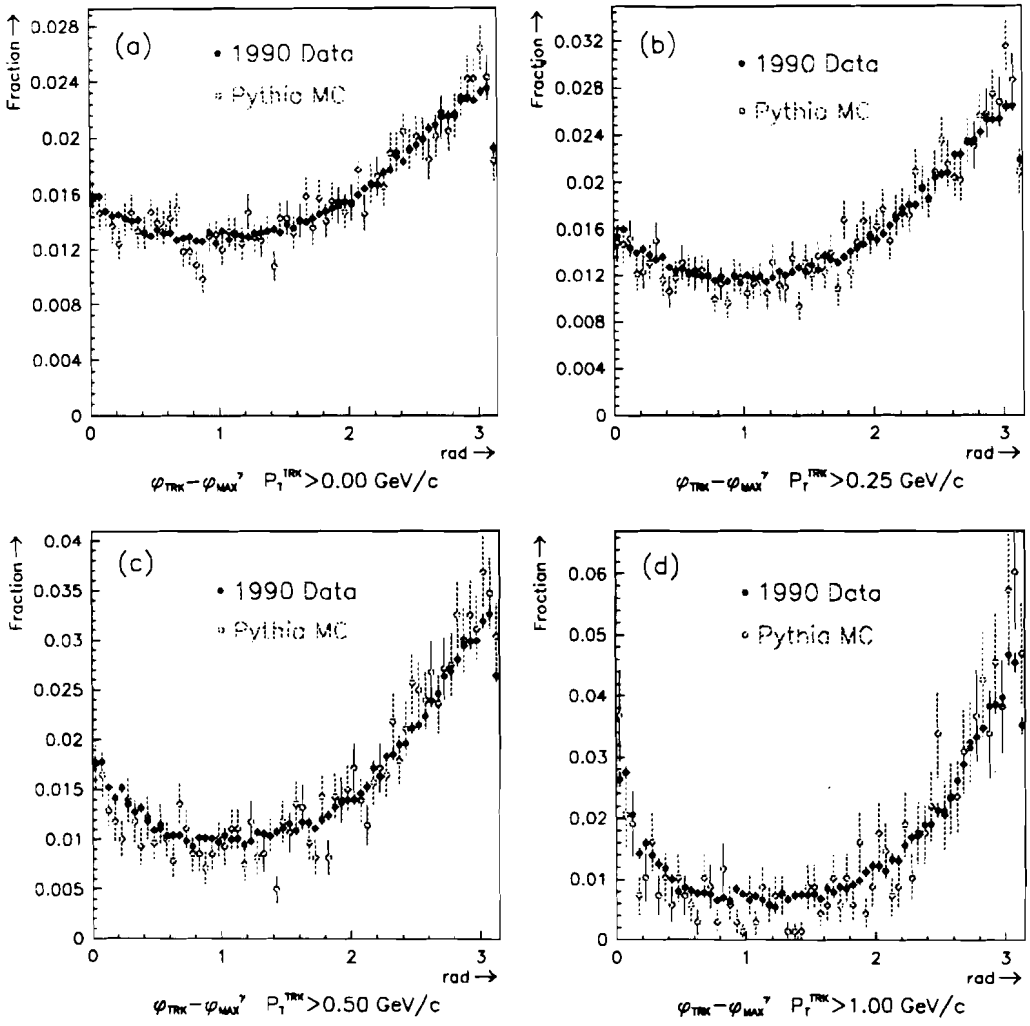

Figure 5.29 The difference in azimuth between the highest p_T photon and (a) all charged tracks, (b) charged tracks with $p_T > 0.25$ GeV/c, (c)charged tracks with $p_T > 0.50$ GeV/c, and (d) charged tracks with $p_T > 1.00$ GeV/c.

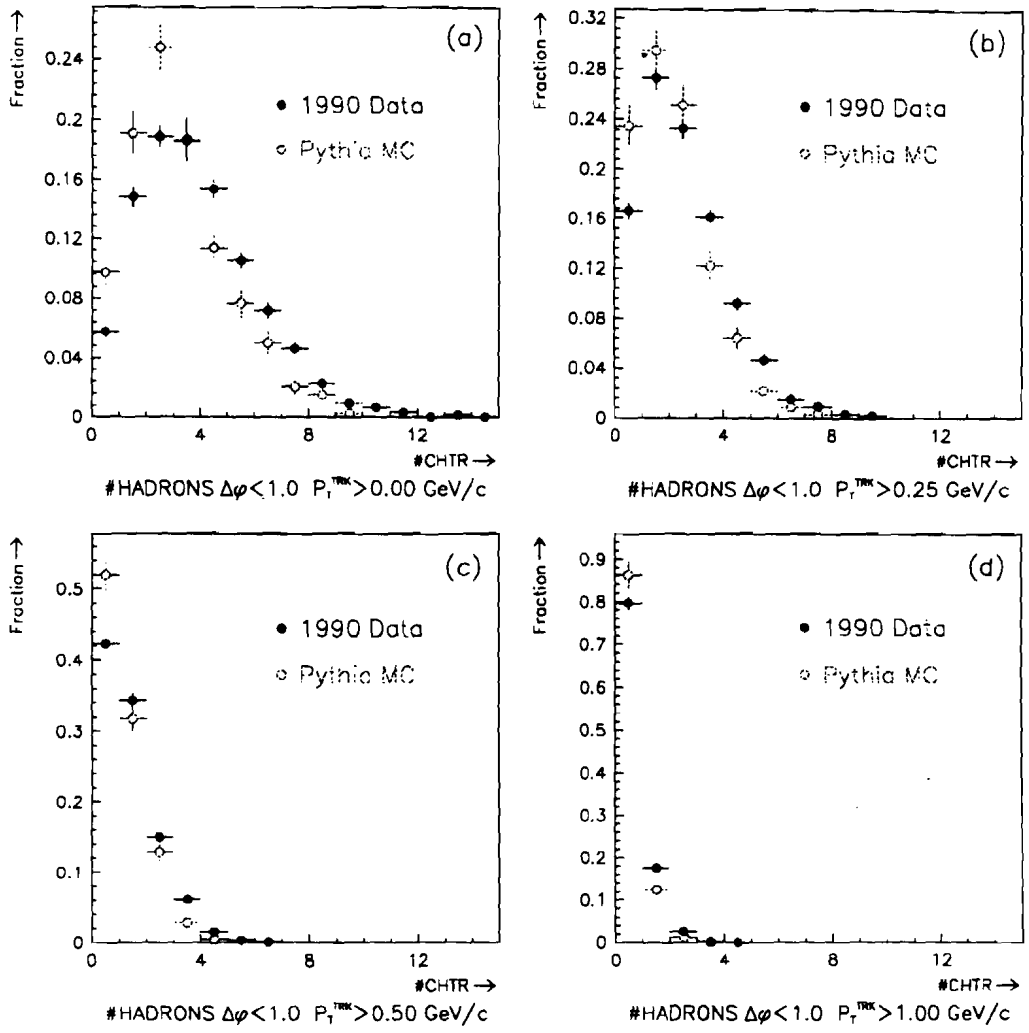

Figure 5.30 The number of charged tracks within $\pm$ 1 radian of the highest p_T photon. The count includes charged tracks with (a) $p_T > 0.0$ GeV/c, (b) $p_T > 0.25$ GeV/c, (c) $p_T > 0.50$ GeV/c, and (d) $p_T > 1.00$ GeV/c.

In the last set of comparisons relevant to this analysis, we wish to show the observed trigger rates of SLLO, SLHI, and the ratio SLHI/SLLO as a function of the trigger/run set number. As alluded to previously, the trigger p_T thresholds were adjusted during the course of the run, which necessitated distinct sets of turn-on curves for each set. Set 1 represents the latest running period in 1990, while set 6 represents the earliest. The most pronounced change in the trigger was a large increase in the threshold of the SLLO trigger from about 1.5 GeV/c to 2.5 GeV/c in going from set 2 to set 1. Figure 5.31(a) shows the SLLO trigger rate in both the MC and data as a function of the trigger set. From this plot, one finds that the SLLO fires about once in 200 events (except for trigger set 1, where it is about 1/2000 events) for both data and MC. In Figure 5.31(b) is shown the SLHI trigger rate versus the trigger set number. As expected, the SLHI fires at a much lower rate than the SLLO, with a typical rate of $\sim$ 1/30,000 events. Shown in Figure 5.31(c)-(d) is the ratio of the SLHI rate to the SLLO rate. The only difference from (c) to (d) is a factor of 10 magnification of the vertical scale. One can conclude from these figures that the trigger bias is reasonably reproduced with the tools which were developed for this analysis. In retrospect, we have shown that if we can match the multiplicity, p_T, and rapidity distributions fairly well, then the resulting trigger rate is also in reasonable agreement.

In light of these comparisons, we feel that the MC sufficiently reproduces the biases caused by the trigger. Therefore, we claim that the MC can be used to give some predictive power to estimate the trigger bias against charm events. Since charm is a subset of the QCD $2 \rightarrow 2$ diagrams, based on the previous comparisons, we expect that Pythia should provide a reasonable estimate of the trigger bias against charm events. In the next section we discuss the application of this simulation to charm.

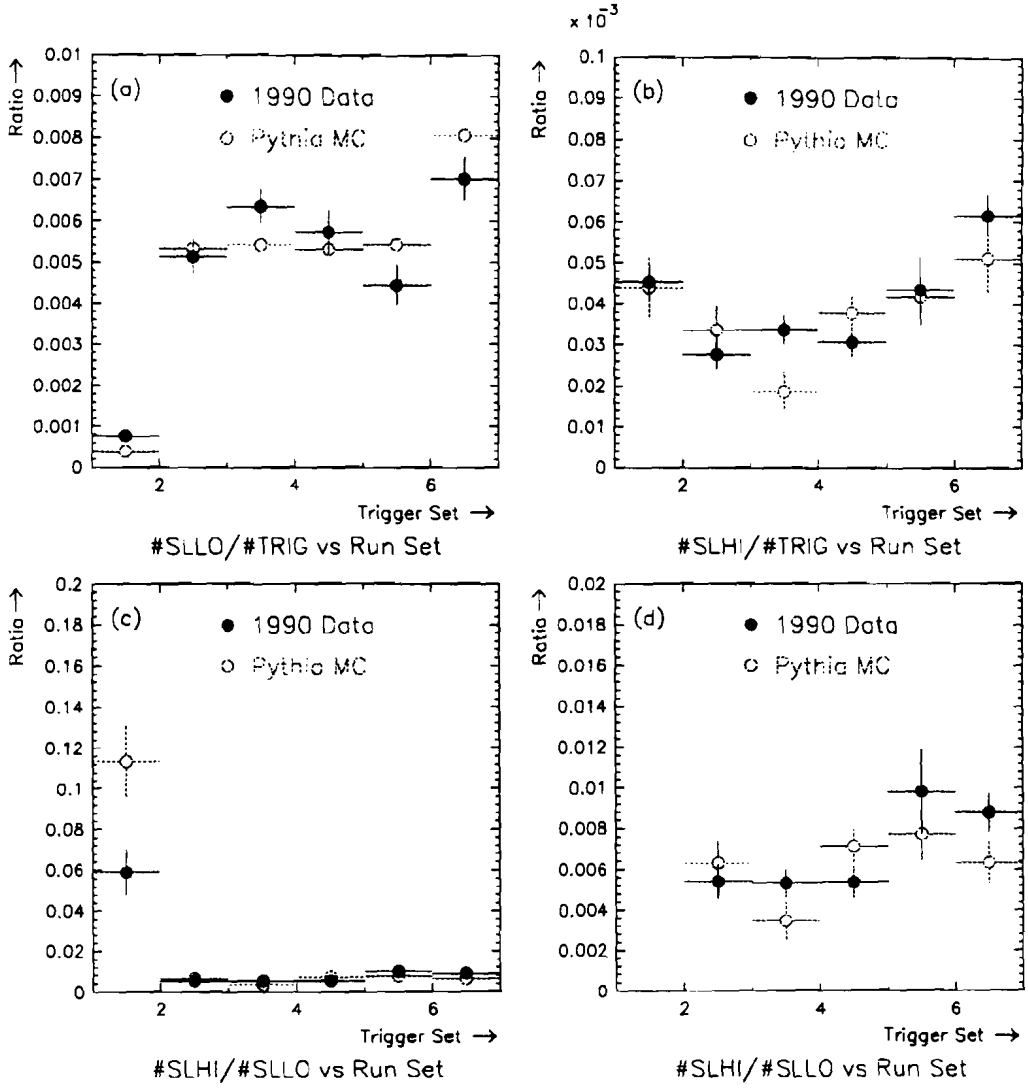

Figure 5.31 The fraction of events which satisfy (a) SLLO, and (b) SLHI trigger, versus the trigger set, for the MC and data. In (c) and (d), the ratio of SLHI/SLLO is plotted as a function of the trigger set.

5.6 Pythia and Charm Production

Pythia produces charm quark pairs via the leading order diagrams, as described in Chapter 1. The distribution functions of the pion and nucleon are described by the Owens Set 1, and DO Set 1.1 respectively. The majority of the contribution to charm hadroproduction is expected to come from gluon fusion at the E706 beam energy. The QCD radiation of the final state charm quarks is expected to simulate much of the NLO contributions. The charm quarks emit QCD radiation until some point at which they hadronize into charmed hadrons. The fractional momentum carried off by the charmed hadron with respect to the initial state charmed quark is given by the LUND parametrization[82]. The charmed hadrons' lifetimes, decay modes, and branching ratios are extracted from tables inside Jetset, which are updated using published values from the PDG book.

5.7 Charm Event Trigger Efficiency

Earlier in this chapter, we tried to convince the reader that the Pythia event generator, along with the trigger simulation developed by the author, could describe many of the relevant features of the data. We now wish to defend the previous statements regarding the indifference of the trigger to the parent parton of the jet. In other words, we wish to demonstrate that the trigger bias is similar, whether we are talking about light parton or charm quark jets. In Figure 5.32 is shown the efficiency for satisfying either the SLHI, GLHI or 2 GAMMA trigger as a function of the jet's transverse momentum. The two distributions correspond to events generated using (a) all QCD $2 \rightarrow 2$ processes, and (b) only leading order charm production. The jet p_T is defined by the vector sum of all the stable particles within a cone of size 1.0 about the jet axis[24]. One observes that the efficiency is

[24] The cone size is in $\eta - \phi$ space, and is defined by $R=\sqrt{\Delta\eta^2 + \Delta\phi^2}$, where $\Delta\eta$ and $\Delta\phi$ are the differences in rapidity and azimuth respectively, of each particle to the jet axis.

fairly similar over the relevant p_T range. It is not our intent to prove that charm quarks jets are the same as light parton jets, they're not. However, it would be quite surprising if the two were substantially different. Differences such as the charm quark mass, jet multiplicity, and jet definition can be expected to account for the small differences observed in Figure 5.32. From the figure, one can estimate that the average trigger efficiency is $\sim 10^{-3} - 10^{-2}$, independent of the parent parton. In the forthcoming sections, we will be more quantitative and precise in the determination of the trigger efficiency.

We now wish to turn our focus to the task of estimating the efficiency of triggering on charm events. In order to correct the data, we need to know the probability of triggering on a charm event which contains a $D^{\pm}$ meson which decays to $K\pi\pi$. In particular, we want to know the trigger efficiency as a function of the p_T of this $D^{\pm}$ meson. We have previously shown the trigger efficiency as a function of the charm jet p_T for all LO charm events (see Figure 5.32). We now investigate the subset of those events which have a $D^{\pm}$ which decays to a $K\pi\pi$. Furthermore, we plot the trigger efficiency versus the $D^{\pm}$ meson p_T, as opposed to the jet p_T. Whether we plot the trigger efficiency versus the jet p_T or the $D^{\pm}$ meson p_T, we expect the shapes to be similar, simply because the two variables are highly correlated. Shown in Figure 5.33 is a comparison of the trigger efficiency plotted as a function of the charm jet p_T, and versus the $D^{\pm}$ meson p_T. In both cases, the charm jet being considered is the one which yields a $K\pi\pi$ from a $D^{\pm}$ decay. The functional form is quite similar for both, except for a shift in the horizontal axis. Since the average efficiency must be the same, what is the significance of the shift? The shift is simply a result of the fragmentation of the charm jet into a charmed particle. In most models of the charm fragmentation function, including LUND, the stable charmed particle retains, on average, about 70% of the p_T of the charm quark. Therefore, the shift is simply a result of the difference in where the bulk of the statistics are located in p_T for each of the two distributions. For the **triggered charm events**, the *charm jets* have an average p_T $\sim$3 GeV/c, whereas for the $D^{\pm}$

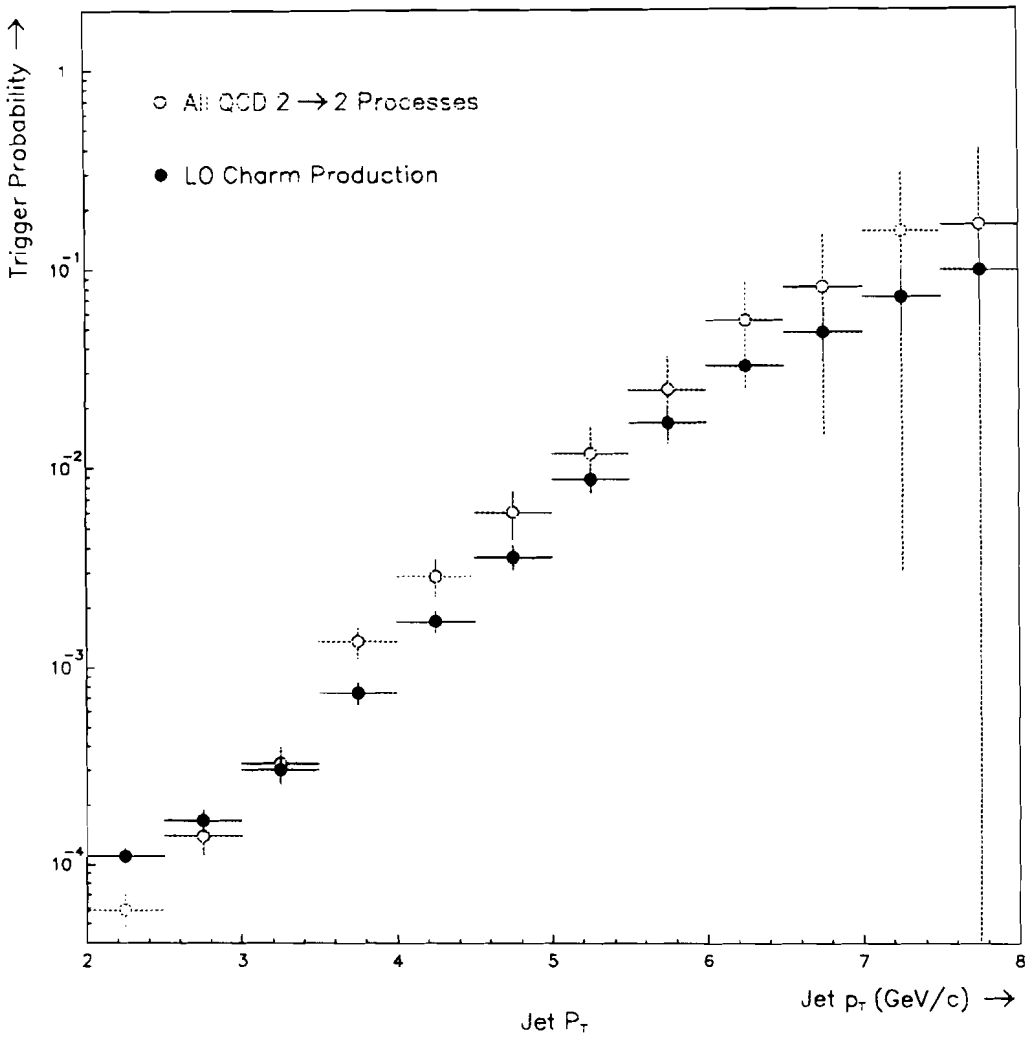

Figure 5.32 Trigger efficiency as a function of the jet p_T for all QCD jets (primarily light partons), and charm quark jets.

mesons, the p_T spectrum peaks around 2.1 GeV/c. Consequently one can see from Figure 5.33 that the average trigger efficiency is the same, as it must be.

In Figure 5.33 we have already given the reader an indication of the expected magnitude of the efficiency for triggering on charm events. As expected, the efficiency is fairly low, just as for any QCD jet. The trigger bias is predominantly against the transverse momentum of the jet, as indicated in Figure 5.33. However, due to the strong correlation between the jet p_T, and the charm meson p_T, the trigger is seen to be a strong function of the charmed hadron p_T. It is reasonable to ask whether or not the trigger introduces a bias onto the x_F spectrum as well[25]. In Figure 5.34(a) is shown the x_F spectrum for the full sample and the triggered sample, and in (b) the x_F ratio of the triggered sample to the full sample. The spectrum integrates over the full p_T range. The trigger efficiency is seen to be fairly flat with x_F, and we shall therefore integrate over it when estimating the trigger efficiency.

The procedure for correcting the data is now fairly straightforward. First we generate the charm events using Pythia. Next, we select those events which have a $D^{\pm}$ meson which subsequently decays into the $K\pi\pi$ channel. By generating the p_T distribution of this D meson for all events, and another for triggered events, we can extract the trigger efficiency as a function of the p_T of the D meson (which decays to $K\pi\pi$). We simply divide the **triggered** p_T distribution by the **full** p_T distribution, and this gives the desired trigger efficiency. In fact, we have already shown this in Figure 5.33. The points which show the trigger efficiency as a function of the p_T^D provide these trigger probabilities. The inverse of these trigger probabilities give the **average trigger weight** for each p_T bin.

---

[25] The x_F is defined by $x_F = p_z/(\sqrt{s}/2) = 2p_z/\sqrt{s}$, where p_z is defined in the center of mass system. The x_F gives the fraction of longitudinal momentum a particle carries with respect to the available center of mass (CM) momentum.

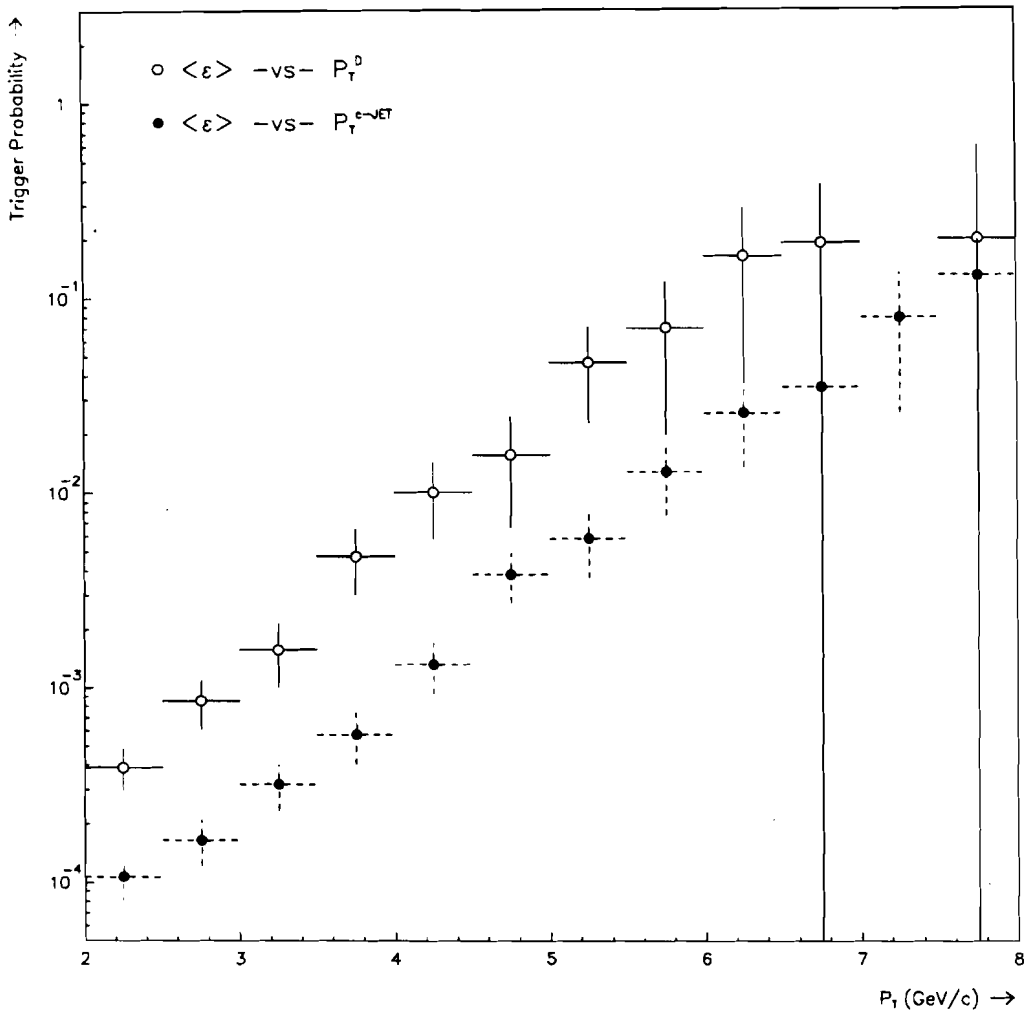

Figure 5.33 The trigger efficiency plotted as a function of the transverse momentum of the charm jet and the D meson. In both cases the jet(meson) selected is the one which produces a $K\pi\pi$ from a $D^{\pm}$ decay.

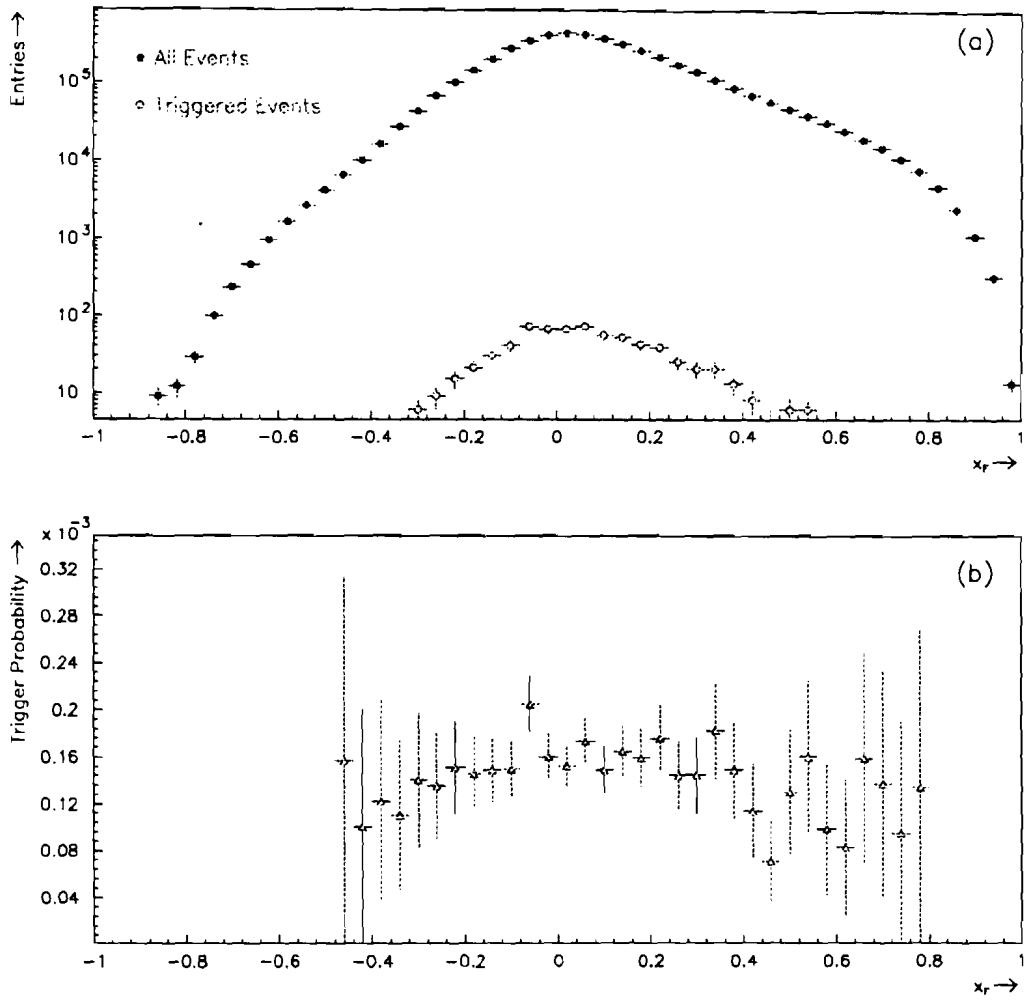

Figure 5.34 (a) Pythia x_F spectrum for all $D^{\pm}$ mesons, and those which satisfy the MC trigger. In both cases, we integrate over p_T. (b) The ratio of the x_F spectra of the triggered sample to the full generated sample.

5.8 Charm Reconstruction Efficiency

Now that the program to extract the trigger efficiencies has been outlined, we can begin to discuss the reconstruction efficiency. Given the sample of charm events in the data, we need to know the efficiency of finding the displaced vertices. The technique is to simply take a sample of MC events which are known to have $D^{\pm}$ mesons which have decayed to $K\pi\pi$, and measure how often the secondary vertex algorithm reconstructs the $D^{\pm}$ mesons. The procedure is straightforward, but there are important details which must be addressed before carrying it out. The first issue which we will address concerns the correlations which exist between the trigger and reconstruction efficiency. The second issue which must be addressed is the reliability of the MC to estimate the reconstruction efficiency. Just as was done with the trigger simulation, we must show that the MC reproduces the aspects of the data which are relevant to determining the reconstruction efficiency.

5.8.1 Correlations between Trigger and Reconstruction Efficiency

It is reasonable to ask whether or not the requirement that the observed D events trigger the apparatus, places a bias on the reconstruction efficiency of those events. In other words, does the sample of triggered $D^{\pm}$ events have a different average efficiency than a sample which is not required to trigger the apparatus? The answer is clearly, yes. The triggered sample has different kinematics on average than a non-triggered sample, as a result of the trigger. Therefore, in order to follow the same path as the data, we evaluate the charm reconstruction efficiency for the sample of MC events which were accepted by the software trigger. In this way, we expect that the reconstruction efficiency will encounter the same correlations which were present in the data.

To illustrate the correlations, we show in Figure 5.35 the momentum distribution of all D mesons, and only those which are accepted by one of the high p_T triggers. Clearly the trigger tends to select higher momentum charmed hadrons. It is not immediately clear whether or not the increase in the average momentum

of the $D^{\pm}$ mesons will make any change to the reconstruction efficiency. If the reconstruction efficiency is flat with momentum, then clearly there is no change. If however there is some momentum dependence, the average answer is expected to be affected. The correlations are not expected to be large, but their impact shall be accounted for by evaluating the reconstruction efficiency with respect to the triggered $D^{\pm}$ sample, not the full sample.

5.8.2 The MC Detector Simulation

Since the reconstruction efficiency is evaluated using a MC simulation of the apparatus, we must first show that the MC reproduces the effects of the data. In particular, any variable to which the reconstruction efficiency is sensitive must be reproducible with the MC. The actual evaluation of the reconstruction efficiency is fairly straightforward, and is reserved for Chapter 6. In the next section we discuss the detector simulation which is the foundation to estimating the reconstruction efficiencies.

In order to accurately estimate the reconstruction efficiency, a full detector simulation needed to be used. All of the detectors, and their response were simulated within the framework of GEANT. For the purpose of evaluating the efficiency for reconstructing the decay vertices of charmed mesons, only the tracking simulation was necessary. In this thesis, we only give a brief summary of the detector simulation. More details on the detector simulations can be found in the references[55, 87].

The GEANT simulation will take an input set of particles, along with their production points and momenta, and step it through the various detector elements. At each step, GEANT evaluates the probability for various processes to occur, based on the particle type and its momentum. Examples of some of the physics processes handled in GEANT are, photon conversions, bremsstrahlung, secondary interactions, multiple scattering and decays. Furthermore, as the particles pass through the detectors, they will generate hits when appropriate. The hits produced

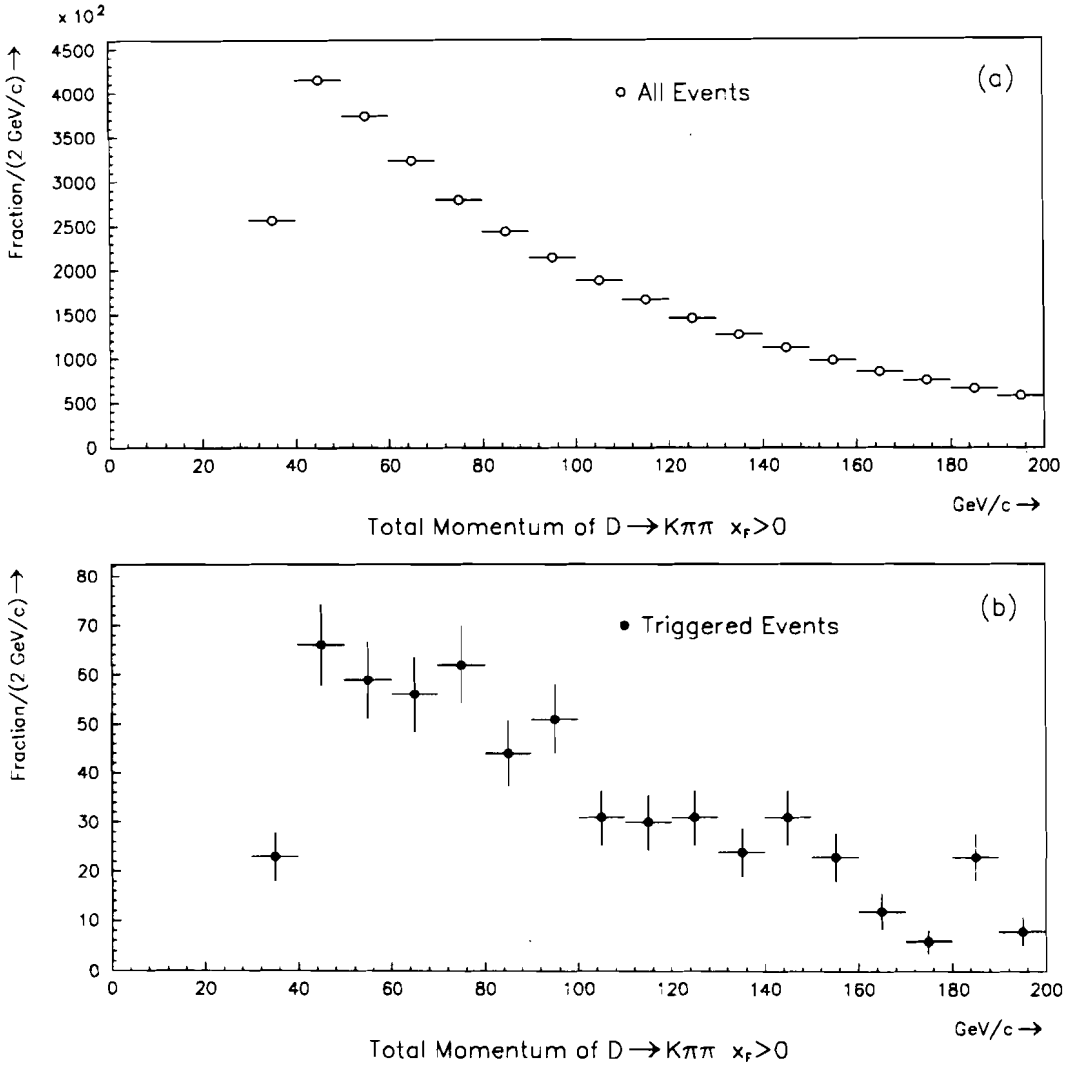

Figure 5.35 Momentum of D mesons with $x_F > 0$ which decay into $K\pi\pi$ for (a) full generated sample, and (b) sample of events which satisfy a SLHI, GLHI, or 2 GAMMA trigger.

in the various detectors are available to the user for further processing. The hit positions recorded by GEANT assume a perfect detector. It is now the job for the user to implement into the MC the relevant effects which are observed in the data. There are 3 main effects which must be simulated in the tracking chambers[87].

- Hit Clusters
- Chamber Efficiencies
- Noise Hits

Hit clusters are defined by any number of adjacent wires in the detector which register a hit. The primary sources of hit clusters are,

- Wide angle tracks which produce enough ionization on several adjacent detector elements, and
- Delta rays which produce adjacent hits through secondary ionizations.

In order to implement this effect in the MC, the ratio of double (2 hit cluster) to single hits was plotted as a function of the transverse coordinate. The same distributions were also generated for triples, quadruples, and quintuples (3, 4, and 5 hit clusters respectively). Each of these distributions exhibited a smooth parabolic shape, with its minimum at the center of the chamber, i.e. 0 degrees. This is the expected shape due to the sources mentioned above, since as one moves away from the center of the chamber, the angles of the tracks increase.

The second effect which needed to be simulated was the chamber efficiencies. The chamber efficiencies were measured from a set of high quality tracks in the data. For each track, we measured how often each plane registered a hit for the track in question. The frequency at which a hit was found on the track for each plane was a measure of the chamber efficiency. The chamber efficiencies were measured as a function of two variables, the position in the plane and the run number. Figure 5.36

shows the measured chamber efficiency for a single chamber of each subsystem[26]. Shown in the figures is the positional dependence for two of the efficiency run sets. The bins along the horizontal axis of these plots correspond to the 16 channel amplifiers common to all three subsystems. Although these figures show typical variations, larger variations do occur during the course of the run.

After simulating the hit clusters and the plane efficiencies, random noise was added. Distributions of the number of hits which were not associated with a track were used as input into the MC to simulate random noise. The noise hits were distributed randomly across each plane. After implementing the random noise, the noise distributions were measured in the MC in the same way as was done in the data. The input distributions were then tuned in order that the output of the MC agreed with the output of the data.

In order to check that the appropriate hit multiplicity was being generated for a given track, we looked at the hit distribution surrounding tracks in the SSD's and PWC's. Plotted in Figure 5.37 is the distance of all hits to each track in the event for the various detector elements. The peaks and valleys in these plots are caused by the granularity of the detectors, with each peak being separated by the appropriate strip width. The agreement is satisfactory, which is indicative that the average hit multiplicity generated per track is modelled reasonably well.

5.8.3 Comparisons between the Pythia MC and Data

For this analysis, it was pertinent that the MC reasonably reproduces the features in the data. In particular, the tracking simulation must be able to provide an estimate of the reconstruction efficiency for finding secondary vertices from charm decays. The inefficiencies are attributable to the following losses:

- Acceptance

[26] The subsystems we are referring to are the SSD, PWC, and STRAW chambers.

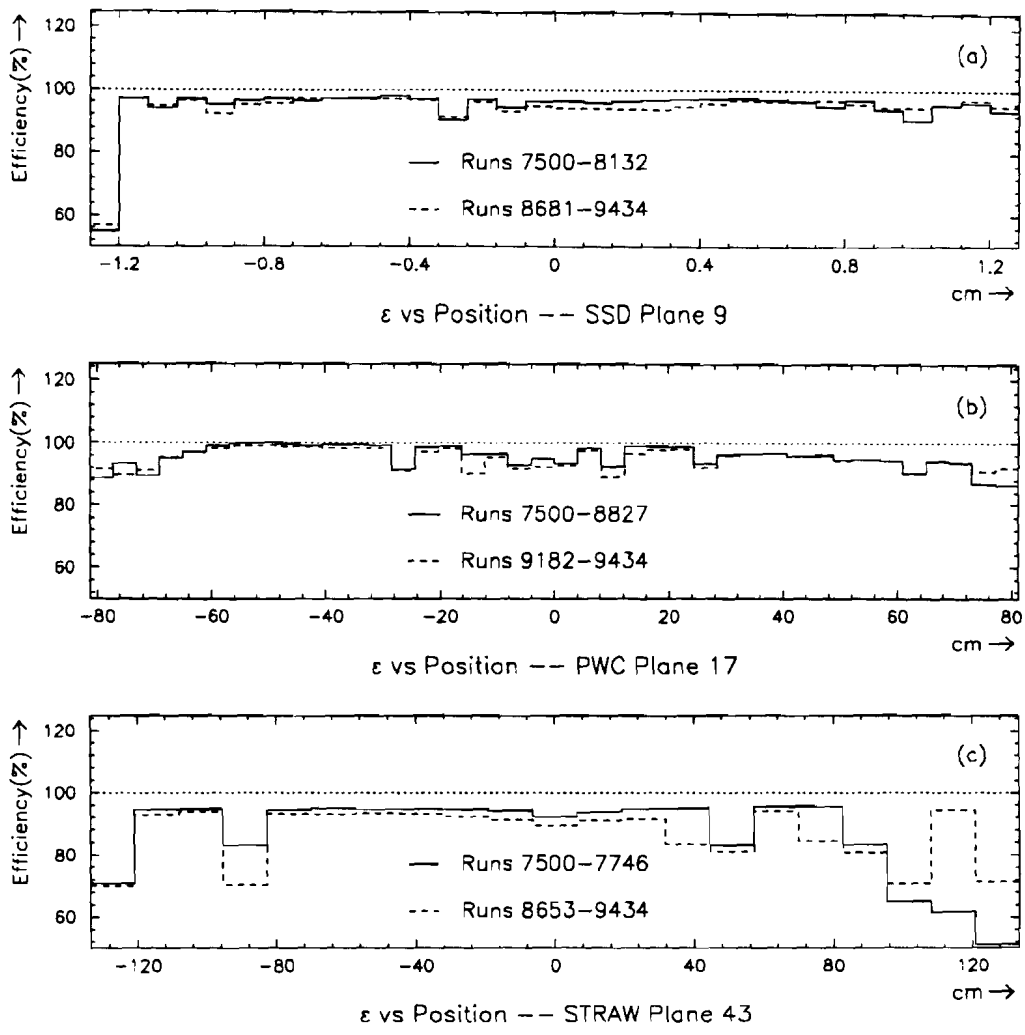

Figure 5.36 Hit efficiency as a function of position for (a) SSD Plane 9, (b) PWC Plane 17, and (c) Straw Plane 43. Two efficiency sets are shown to give an indication of the variations among various sets.

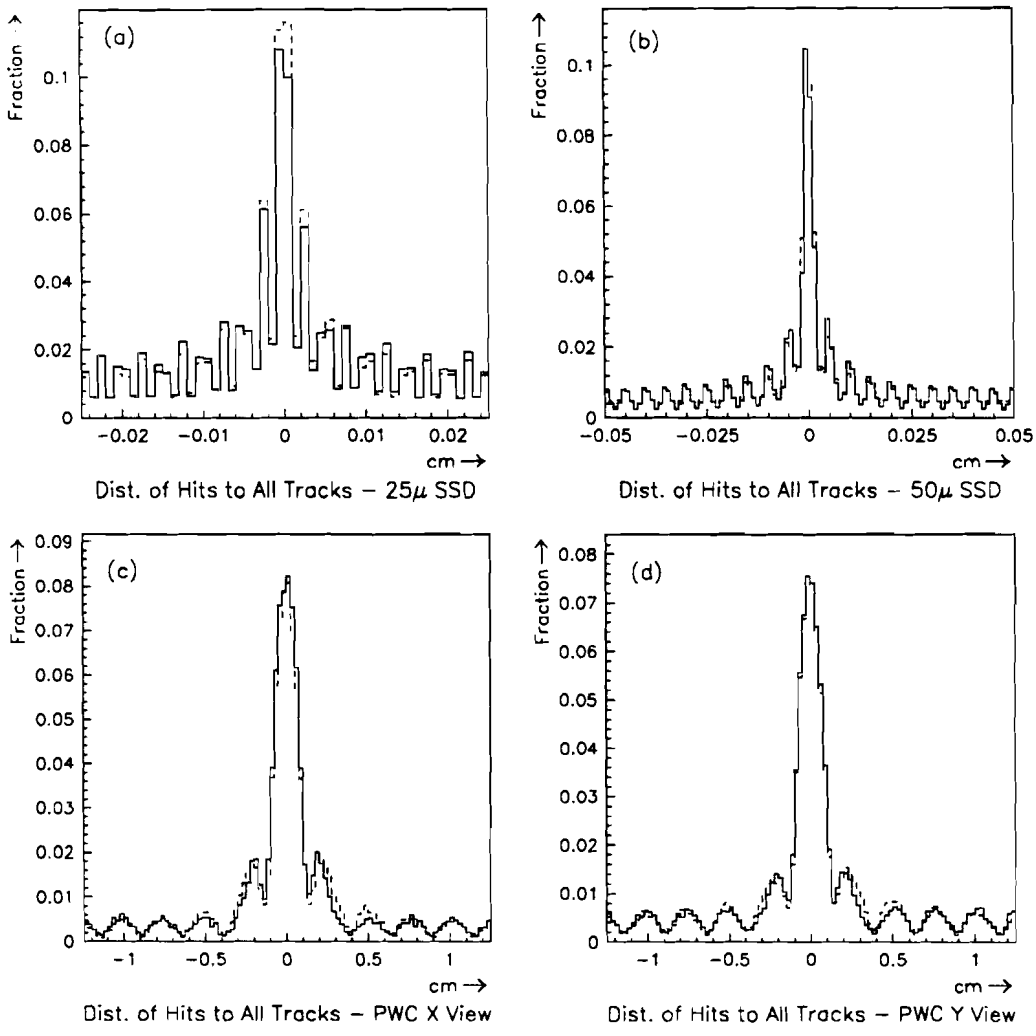

Figure 5.37 Distance of all hits to all tracks for (a) the 25μ SSD planes, (b) the 50μ SSD planes, (c) the X View PWC's, and (d) the Y view PWC's. The solid line id the DATA and the dashed is the MC.

- Tracking Efficiency
- Overall Event Activity
- Detector Resolution

The acceptance is modelled within the framework of GEANT, where the geometry of all the detector elements are specified. Any losses in the data due to the geometry should be accounted for provided the acceptance of the detector is modelled correctly.

The tracking efficiency is dictated primarily by the chamber efficiencies. The level of agreement between the MC and data can be tested by comparing the number of hits on the reconstructed tracks. Shown in Figure 5.38 is the number of hits on reconstructed PWC and SSD tracks in the data and MC. The level of agreement is quite nice, which indicates that the chamber efficiencies are reasonably implemented.

The overall event activity is the most difficult to reproduce. The event activity is measurable in terms of various multiplicity distributions, such as hits and tracks. Clearly, the number of hits should be highly correlated with the number of tracks, provided the MC incorporates all of the data effects. In Figure 5.39 we show the number of reconstructed tracks in the PWC and SSD systems. The agreement is fairly nice, but the data tend to be slightly broader than the Pythia MC. In Figure 5.40, we make the additional comparison between the MC and data of the number of SSD tracks which are associated with the primary vertex ($\sigma < 100\mu$). The data distribution appears to have a slightly higher mean value than does the MC, but otherwise, the agreement is reasonable.

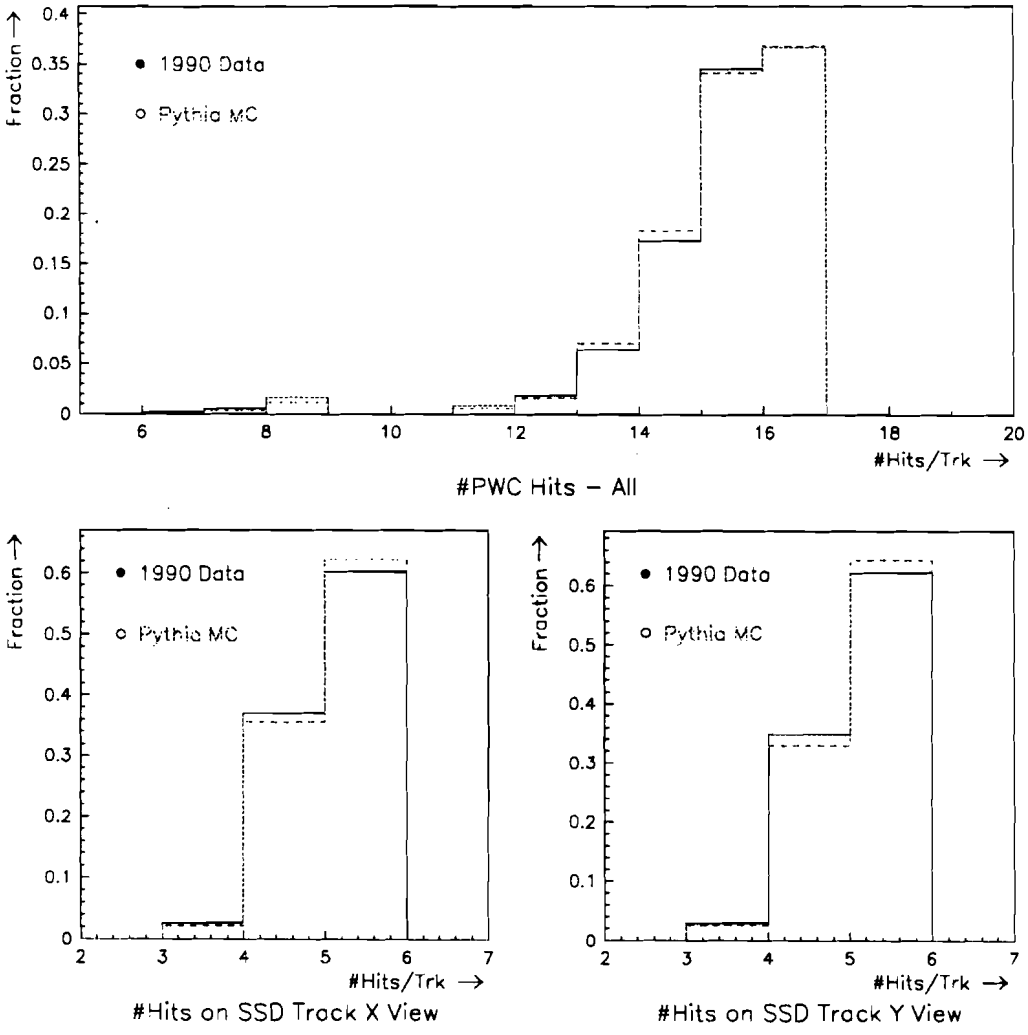

Figure 5.38 The number of hits on the reconstructed tracks in the PWC, SSD X view and SSD Y view. The solid points are the DATA and open points are the MC.

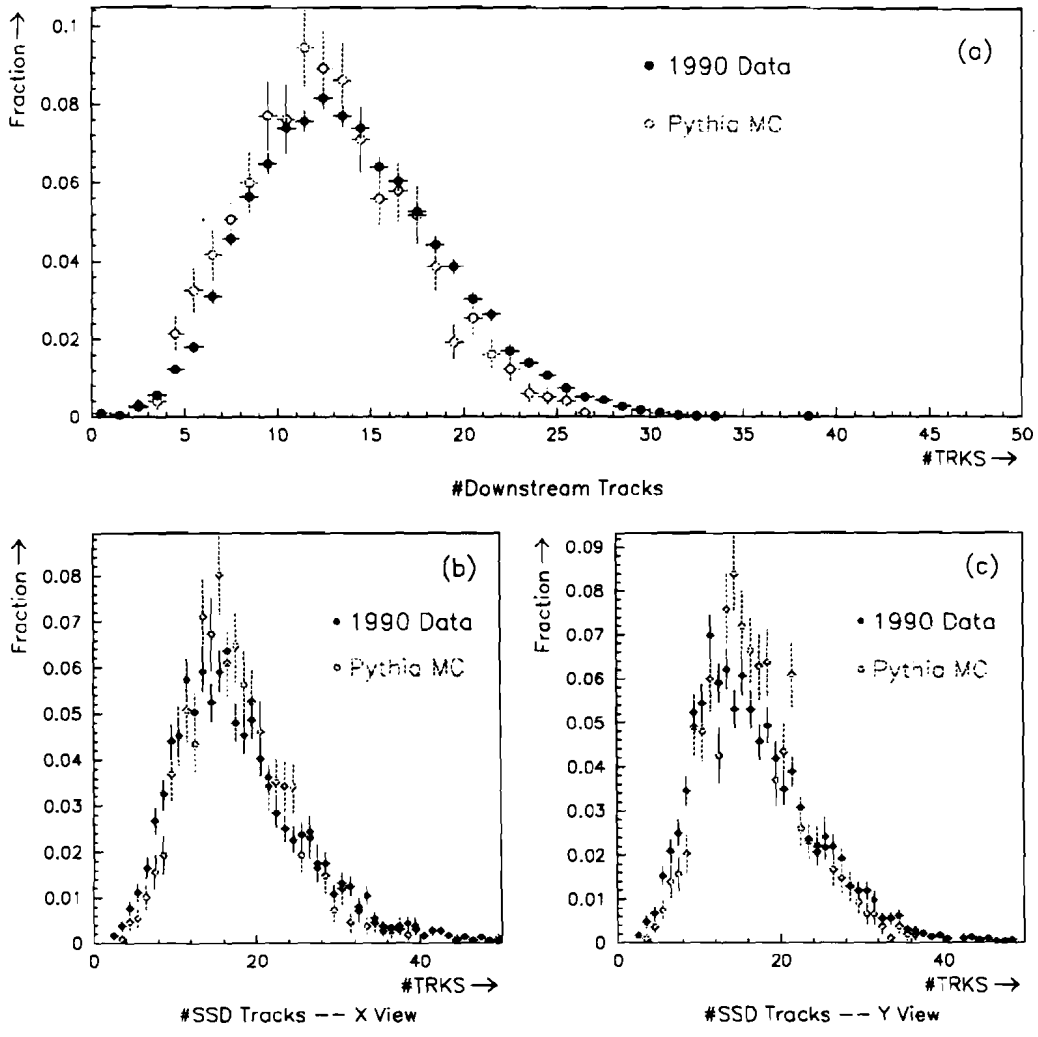

Figure 5.39 Number of reconstructed tracks in (a) the downstream system, (b) the SSD X view, and (c) the SSD Y view. Solid dots are the DATA and open dots are the PYTHIA MC.

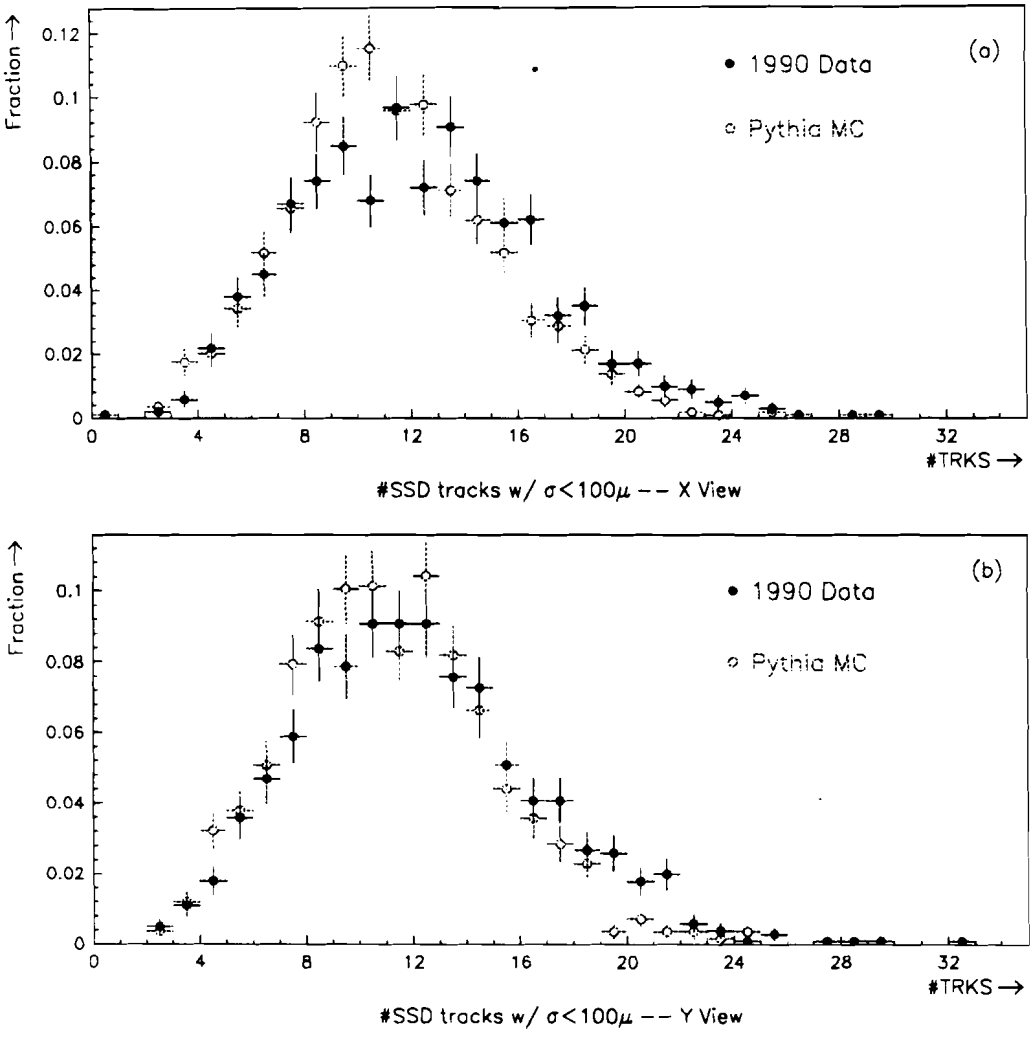

Figure 5.40 Number of SSD tracks within 100μ of the primary vertex for (a) the SSD X view, and (c) the SSD Y view. Solid dots are the DATA and open dots are the PYTHIA MC.

In Figure 5.41, we compare the hit multiplicity between the data and MC. In all three distributions, the peaks tend to match up fairly well, but the data tends to have more entries in the tails. Since the number of tracks does not exhibit this large of a difference, these extra hits are most probably due to occasionally large hit clusters which are not well modelled in the MC. These large clusters may have to do with the electronics i.e. cross talk, a noisy amplifier, etc., or perhaps physics processes which are not modelled correctly in the MC. This will have to be addressed when estimating the systematic error in the reconstruction efficiency.

Finally, in Figure 5.42 and Figure 5.43, we show the average number of SSD links for each downstream track as a function of the track momentum. These plots also provide a measure of the complexity of the events. The overall agreement indicates that the MC reproduces the same linking uncertainties/ambiguities as the data. This statement is important since the secondary vertex algorithm does discriminate upon linking information (see Chapter 4).

The final comparisons are related to the resolution of the detectors. For our purposes, the most important comparison to be made is with regard to the SSD resolution. A measure of the SSD resolution is provided by the impact parameter distribution to the primary vertex[27]. In Figure 5.44, we compare the impact parameter distribution of the physics links for the X and Y views. The MC tends to be slightly narrower than the data in both views (~5-7%).

---

[27] This assumes that we integrate over similar momentum distributions i.e. see Figure 5.24.

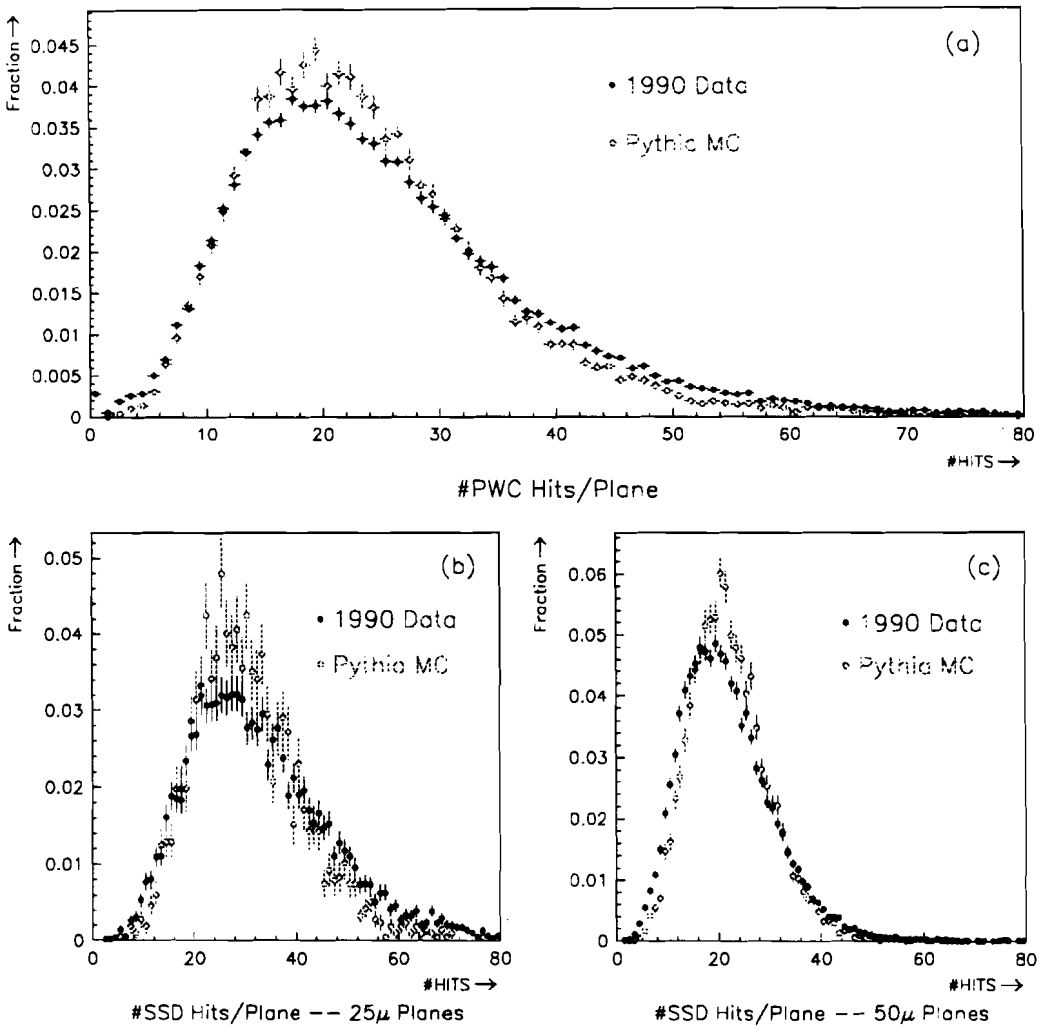

Figure 5.41 Total number of hits in (a) the PWC's, (b) the SSD X view, and (c) the SSD Y view. Solid dots are the DATA and open dots are the PYTHIA MC.

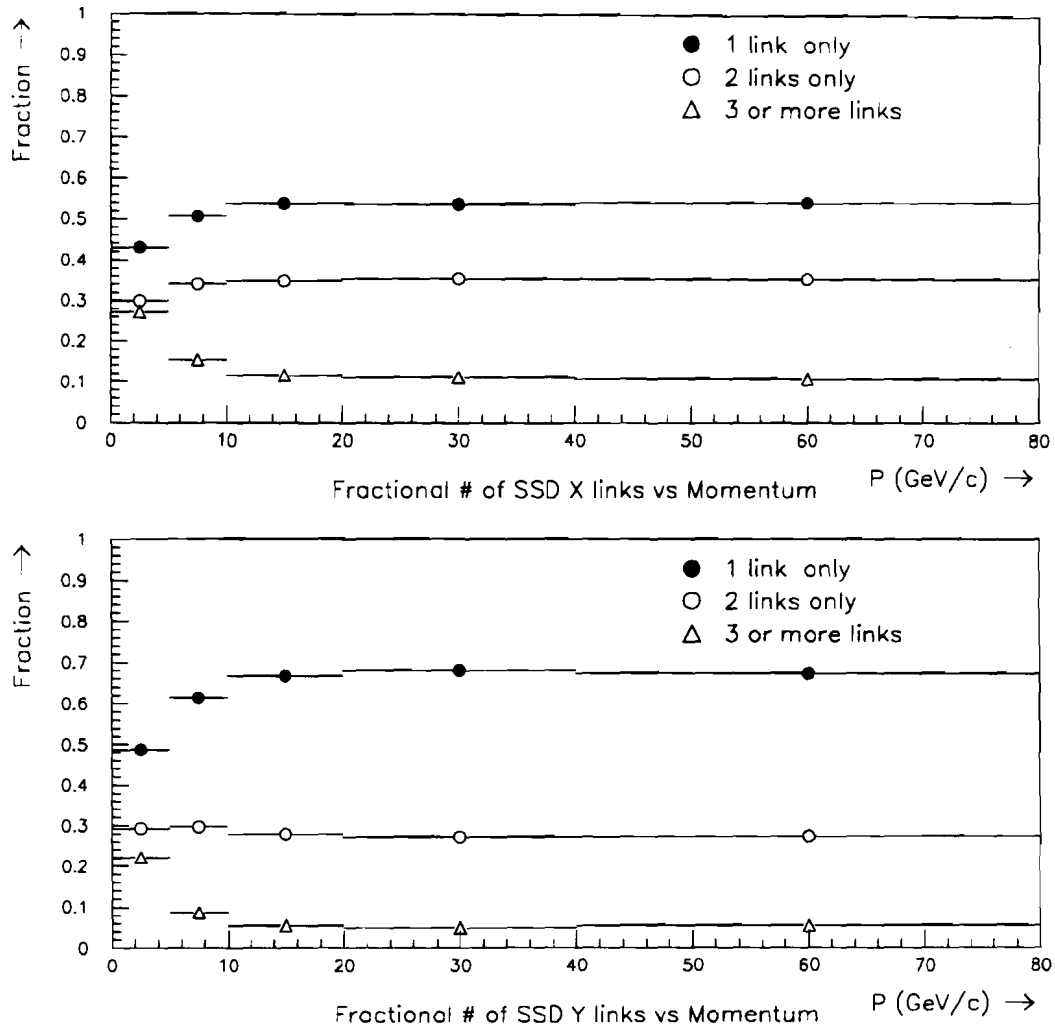

Figure 5.42 Relative population of downstream tracks having 1, 2, and 3 or more links as a function of the track momentum in the (a) X View, and (b) Y View for the DATA.

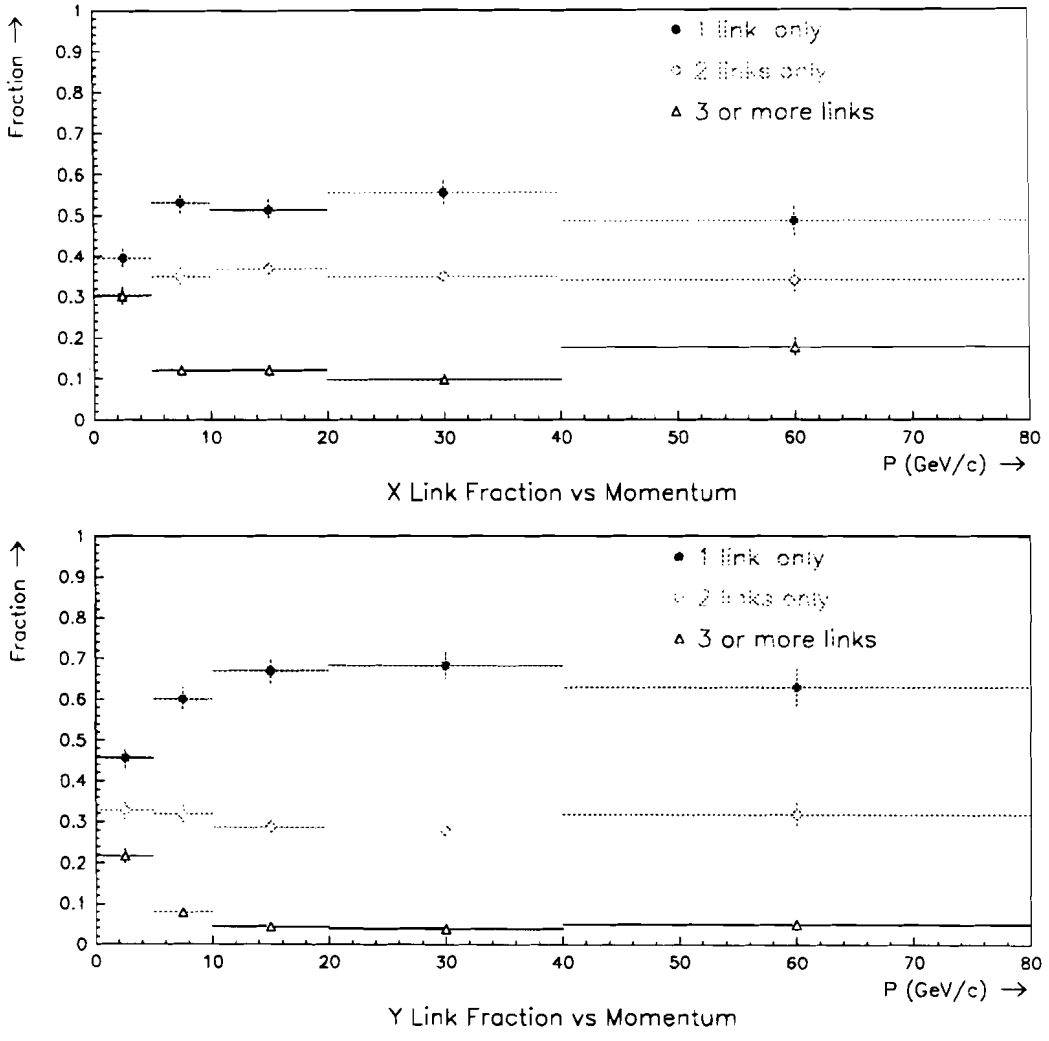

Figure 5.43 Relative population of downstream tracks having 1, 2, and 3 or more links as a function of the track momentum in the (a) X View, and (b) Y View for the PYTHIA MC.

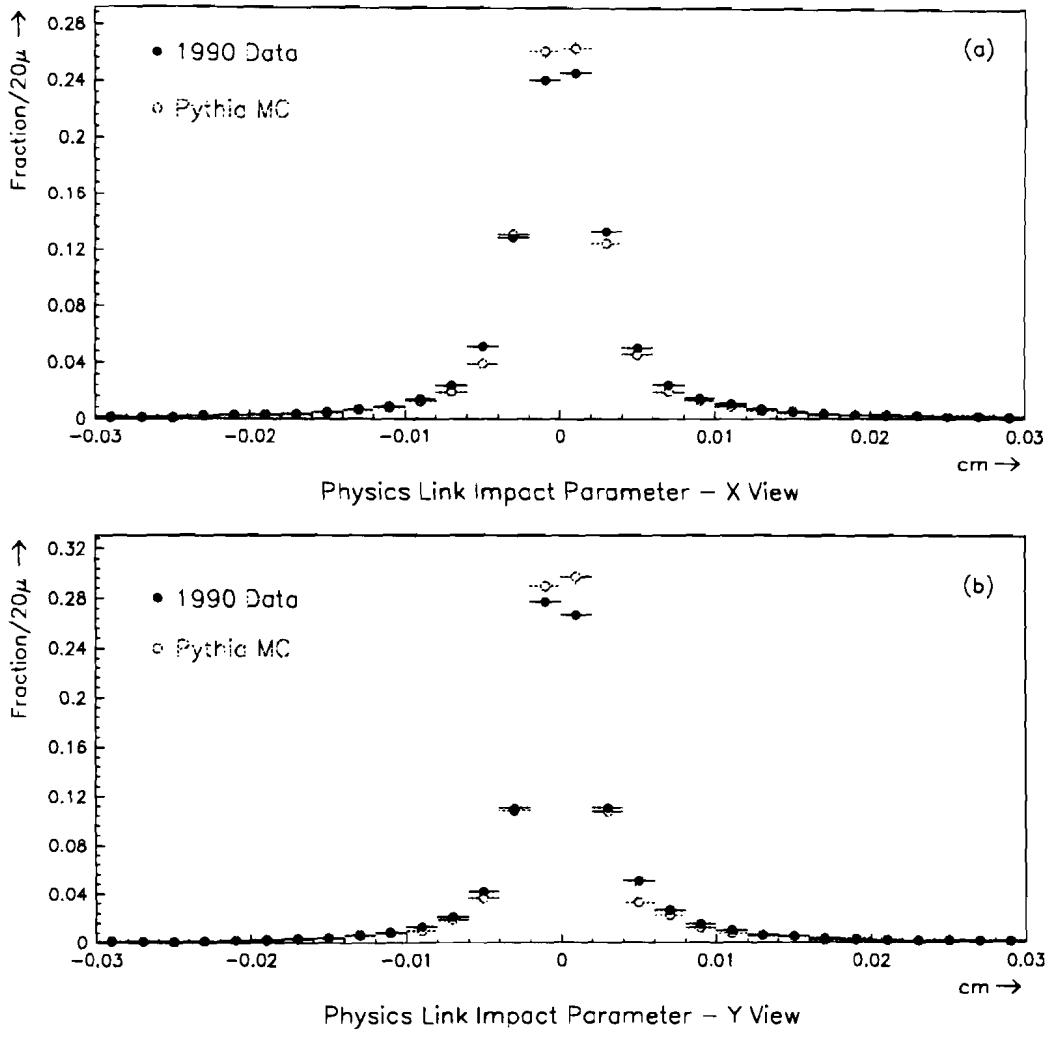

Figure 5.44 Impact parameter distribution of physics links in the X and Y views.

In summary, we have shown that the MC can be used to estimate the efficiency for charm events with reasonable accuracy. In the first section of this chapter, we showed that the MC reproduces the kinematical features of the data. In particular, it was shown that the MC reproduces the kinematical spectra of hadrons and their multiplicities. It was then shown that the **data trigger rates for the LO and HI threshold triggers could be reproduced with the MC**, provided we tuned some of the adjustable parameters in Pythia. In the last section of this chapter, we discussed the tracking simulation in the MC, and presented various comparisons with the data. The comparisons tended to be in general agreement, with some differences in the tails of the distributions. Based on these results, we expect that the MC should provide a reliable estimate of the efficiency of observing charmed hadrons in high energy collisions.

Chapter 6 Data Analysis

6.1 Overview

The data from which this analysis was performed was collected during the 1990 Fermilab fixed target run of E706. The data were collected via collisions of a 515 GeV/c π^- beam incident on copper and beryllium targets. As mentioned previously, the data sample was processed using the SGI farms at Fermilab, and written in the form of compressed data summary tapes (DSTs). The full data sample was subdivided into 6 sets, reflecting changes in the trigger during the course of the run. Table 6.1 summarizes the total event yield in each of the respective data sets.

Table 6.1 1990 Data Run Sets

Run Set	Run Number Range	Number of DST Events
1	9181-9434	5,904,433
2	8989-9180	4,051,049
3	8629-8988	5,839,137
4	8240-8628	3,931,743
5	8055-8239	2,864,491
6	7594-8054	4,966,478

This analysis utilizes only the SLHI, GLHI and TWO GAMMA triggers, which represented ~80% of the total data sample. The data are measured over the p_T range from 1-8 GeV/c and $x_F > -0.2$. In this chapter, we shall develop the ingredients necessary for calculating the $D^{\pm}$ cross section. In the next, and final chapter, we shall present the final physics results.

6.2 Cross Section Measurement

In this section we present the cross section formula used to calculate the total $D^{\pm}$ cross section. The $D^{\pm}$ cross section is expressed as,

$$\sigma(D^{\pm}) = \frac{1}{L} \times \int dp_T \, dx_F \, \frac{1}{\epsilon(x_F, P_T)} \cdot \frac{dN(D^{\pm}(x_f, p_T))}{dx_F \, dP_T} \qquad 6.1$$

where L is the integrated luminosity, $\frac{dN(D^{\pm}(x_f,p_T))}{dx_F \, dP_T}$ is the number of observed events in a particular x_F and p_T bin, and $\epsilon(x_F, P_T)$ is the efficiency for observing those events. The integrated luminosity L, is a product of the number of live triggerable beam particles with the number of targets per unit area. It may be expressed as

$$L = \rho \cdot l \cdot N_a \cdot (LTB) \qquad 6.2$$

where ρ is the density of the target material, l is the target length, N_a is Avogadoro's number, and LTB is the live triggerable beam. The LTB is the amount of beam (BEAM1) recieved during which time the trigger was ready to accept an event. The LTB is expressed as follows:

$$LTB = BEAM1 \otimes \overline{BH} \otimes (\text{live fraction}) \qquad 6.3$$

where BEAM1 is the live beam count, $\overline{BH}$ is the anticoincidence with the beam hole counter (see Chapter 2), and the *live fraction* is the fraction of the beam incident on target, during which time the trigger was *live*. The *dead times* were a result of the various aspects of the TRIGGER LOGIC, including the CLEAN INTERACTION definition, PRETRIGGER definition, veto wall cuts, early p_T vetoing, and SCRKILL (periodic power supply noise). All of these counts were extracted from the experimental scalers which were read out at the end of each spill. Typically, the live time was about 50%.

The efficiency $\epsilon(x_F, P_T)$, is expressed as a product of the reconstruction efficiency and the trigger efficiency as follows,

$$\epsilon(x_F, P_T) = \epsilon_{REC}(x_F, P_T) \times \epsilon_{TRIG}(x_F, P_T). \quad 6.4$$

In this equation, it is understood that the reconstruction efficiency is evaluated with respect to a sample which satisfied the software trigger simulation.

In general, if one has enough statistics, each observed event can be weighted by the inverse of its efficiency. Due to the small size of the charm sample, we choose to integrate over x_F, and rely on the MC to provide distributions which are in reasonable agreement with the data. This produces some uncertainty in the efficiencies, due to any differences between the MC and data x_F spectrum. However, we expect the sensitivity to this difference to be small on the scale of the other uncertainties involved in the cross section calculation. With this approximation, the integrated $D^{\pm}$ cross section can be expressed as,

$$\sigma(D^{\pm}) = \frac{1}{L} \times \sum_i \frac{N_i(D^{\pm}(p_T^i))}{\epsilon(p_T^i)} \quad 6.5$$

where the sum runs over all p_T bins. $N_i(D^{\pm}(p_T^i))$ is the number of observed $D^{\pm}$ events in each p_T bin, and $\epsilon(p_T^i)$ is the efficiency for observing a $D^{\pm}$ event in the i^{th} bin. Using this prescription, we weight the number of events in each p_T bin by (the inverse of) an **average efficiency** for observing an event in the given p_T bin. In the limit of small statistics, this is a common approach to correcting one's data.

Therefore, in order to calculate the $D^{\pm}$ cross section, we need to know four quantities. They are,

- The trigger efficiency for each p_T bin;
- The reconstruction efficiency for each p_T bin;
- The number of events in each p_T bin; and
- The integrated luminosity.

In the forthcoming sections, we discuss how each of these quantities were obtained. Once we have acquired the values for these variables, we will be in a position to calculate the charm cross section.

6.3 Trigger Efficiency

This topic was discussed at great length in Chapter 5. For the benefit of the reader, we will briefly summarize the procedure for extracting the trigger efficiency. The trigger efficiency is estimated by producing charm pairs via LO diagrams using the Pythia MC. Events which contain a $D^{\pm}$ decáying in the mode of interest ($K\pi\pi$), are subjected to a software simulation of the E706 online trigger. In that process, the stable particles in the event which reach the EMLAC deposit a parametrized amount of energy into the EMLAC, which was based on full shower studies using GEANT. Based on the amount of trigger p_T deposited in the EMLAC, a probability was calculated that the event would fire either the SLHI, 2 GAMMA, or the GLHI trigger. Based on this probability, the event was either accepted or rejected. The trigger efficiency is simply the ratio of the number of events accepted by the trigger to the total number generated. The trigger efficiency is primarily a function of the jet p_T, but we may also parametrize it as a function of the D meson p_T, since the two are highly correlated (see Figure 5.33). This is convenient, since, in the data events, we measure the kinematics of the charmed hadron with fairly high precision. Therefore, we can simply weight the number of observed charm events in a given p_T bin, by the associated probability that such an event would fire the trigger. The probability is simply the trigger efficiency determined from the MC.

6.3.1 Forcing decays in Pythia

Within the framework of Pythia/Jetset, the user may force the decay of a particle or antiparticle into a given mode. This is done by simply *turning off* all decay modes, except for the one of interest. This may be done for the particle, antiparticle, or both particle and antiparticle. For this analysis, we utilized this mechanism. The approach taken was to generate two samples of events. In the first sample of events, we required that all D^+'s decay into $K^-\pi^+\pi^+$, with no restriction on the other charm decay. In the second sample the D^- was forced to decay into the mode $K^+\pi^-\pi^-$, while the partner charm particle's decay was unrestricted. This

procedure is typically ~10 times faster than running with all decay modes available, due to a branching ratio of ~9.1% for $D \to K\pi\pi$. Forcing one of the charged species to decay into $K\pi\pi$ does not pose a problem, since in the data, each of the events of interest is observed to contain a $K\pi\pi$ as well. Consequently, there is no bias in generating events in this manner.

6.3.2 Pythia D^+ *vs* D^-

Since two samples have been generated, each enriched with either $D^+ \to K^-\pi^+\pi^+$ or $D^- \to K^+\pi^-\pi^-$, one is inclined to ask whether or not the efficiencies depend on the charge. In this case, we are referring to either the trigger efficiency or the reconstruction efficiency. Naively, one expects that if the detector does not treat positively and negatively charged particles differently, the efficiencies should be the same for both species. However, **if** the efficiency is different for positively and negatively charged D mesons, one must combine the two MC samples in the same proportions as the data, in order to get the correct average. In other words, if there is a different efficiency for D^+ and D^- mesons, the average efficiency depends on the relative contributions of the two samples to the total.

One might ask how a difference in efficiency between D^+ and D^- mesons may emerge. A difference in the average efficiency may emerge if the production dynamics are different for D^+ and D^- mesons. For example, if one's efficiency depends on momentum and the average momentum of D^- mesons is higher than D^+ mesons, the average efficiency may be different for the two charge states. Therefore, a difference in the average efficiency may be a result of the production characteristics of the two charge states, rather than an acceptance issue. The degree to which the average efficiency is different would depend on how different the production spectra are between the two charge states. Since we have the two samples in hand, a definitive comparison can be made as to whether the efficiency is independent of the charge state.

The reason for introducing this topic (of differences between D^+ and D^- mesons) is because production asymmetries have in fact been observed between D^+ and D^- mesons. Most notably, is the observed asymmetry in x_F between D^+ and D^- mesons in π^- nucleon collisions[88, 89]. Recall that x_F is the fraction of the available CMS energy which the charm particles carries along the beam (Z) axis ($x_F = 2p_z/\sqrt{s}$). The asymmetry α, defined by,

$$\alpha = \frac{N_{D^-} - N_{D^+}}{N_{D^-} + N_{D^+}} \qquad 6.6$$

shows a strong rise with increasing x_F, but is fairly flat with p_T^2. The most popular explanation for this asymmetry has to do with the interactions of the final state charmed quarks with the valence quarks in the beam. Since a D^- meson can be formed with one of the valence quarks of the π^- beam, whereas a D^+ cannot, there tends to be a production asymmetry between the two species. This effect tends to increase as the rapidites (or x_F) of the charm quarks increase, where they have a larger probability of interacting with the valence quarks of the beam.

This effect has been implemented into the Pythia event generator, and while it qualitatively reproduces the effect, it tends to overestimate the asymmetry by about a factor of 2. In other words, the Pythia simulation tends to have too large of an excess of D^- over D^+ in the positive x_F region, as compared to the data measurements. Published data from E769[89] and WA82[88] indicate a ratio of $D^-/D^+ \sim 1.2$, whereas Pythia gives a result closer to 1.4[1]. Therefore, weights were applied to bring the ratio in Pythia down to that which has been measured by other experiments.

---

[1] This average interates over the positive x_F region only.

6.3.3 Estimate of the Trigger Efficiency

The method is fairly straightforward to extract the trigger efficiency for the given sample of events (D^+ or D^-). We simply combine the two distributions with a weight such that the integral over the positive x_F region gives $D^-/D^+ = 1.2$. We then divide the p_T distribution of the *triggered* D sample by the *full* sample. Again, these p_T distributions refer to that of the D mesons which decayed to $K\pi\pi$. Before combining the distributions it is worth checking to see if in fact there is any observable difference in the trigger efficiency between D^+ and D^- events. Shown in Figure 6.1 is a comparison of the trigger efficiency as a function of the transverse momentum for D^+ and D^- mesons. The plot covers the p_T range from 1-8 GeV/c. One observes that events contaning D^- mesons tend to trigger the apparatus $\sim 10\%$ (on average) more efficiently than D^+ mesons. This effect was traced back to the Pythia event generator yielding a slightly stiffer p_T distribution for D^- mesons than D^+ mesons. In Figure 6.2, we compare the D^- and D^+ p_T spectra, and show the corresponding ratio of D^- to D^+. One observes a positive slope in Figure 6.2(b), indicating that the D^- mesons are slightly stiffer in p_T than D^+ mesons. Since the decay products of these mesons will exhibit the same trend, the D^- mesons will trigger the apparatus slightly more efficiently than the D^+ mesons. Since this effect has not been experimentally corroborated, we include it in our systematic uncertainty in the trigger efficiency. As discussed above, we combine the D^+ and D^- samples so that the ratio of D^- to D^+ is equal to 1.2 in the positive x_F region. The resulting trigger efficiency after combining the positive and negative D mesons is presented in Table 6.2. This table provides the corrections which are to be applied to the data sample in order to account for the losses due to the trigger. In the next section, we shall discuss the sources of systematic error in the trigger efficiency.

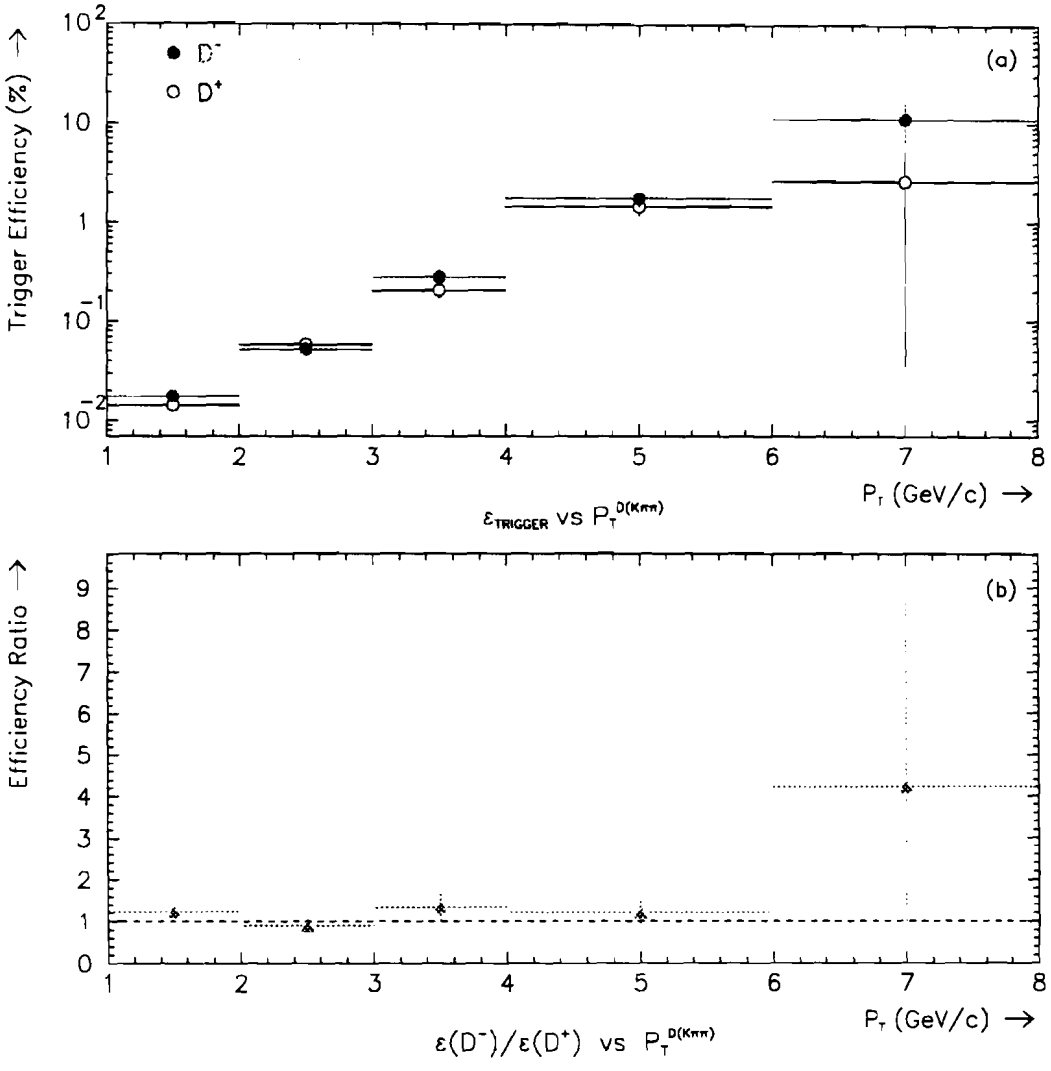

Figure 6.1 The trigger efficiency of D^+ and D^- mesons, which decay to $K\pi\pi$, as a function of their transverse momentum.

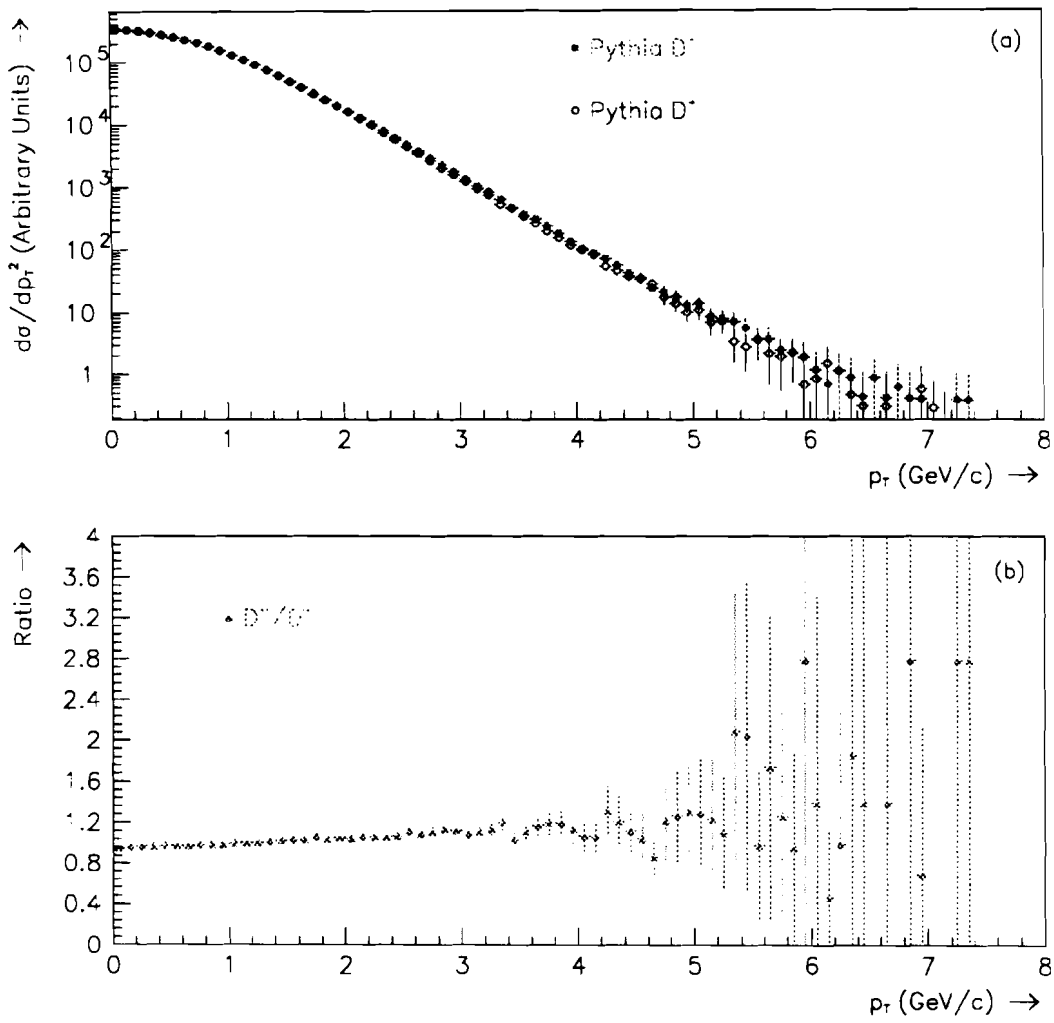

Figure 6.2 (a) Comparison of the D^- and D^+ p_T distribution from Pythia, and (b) the ratio of D^- to D^+ as a function of p_T.

6.3.4 Systematic Studies of the Trigger Efficiency

One might ask how stable is the trigger efficiency to variations in the MC. There are a number of parameters which can be adjusted which will influence the result, at both the event generator level (Pythia/Jetset), as well as in the trigger simulation. We would like to obtain an estimate of our sensitivity to reasonable variations in the input parameters. In particular, we want to vary the parameters to which the trigger may be sensitive. In chapter 4, we saw a strong sensitivity to the amount of primordial k_T used in the event generation. We found that Pythia would reproduce our data fairly well, provided it was supplemented with an intrinsic k_T of 1.05 GeV (see Figure 5.19). Preliminary results from the higher statistics sample of charm from E791 lean toward a k_T value of at least 1.0 GeV as well (within the framework of Pythia). The effect of varying k_T is to alter the p_T spectrum of the charm quarks in the event. Therefore, a variation in the k_T provides a measure of the sensitivity of the trigger to the p_T spectrum of the jets in the event. Lowering the k_T below $\sim$1.0 GeV would render the Pythia results inconsistent with the E791 data, as well as with the E706 jet data (see Figure 5.19). Based on Figure 5.19, we allow the k_T to vary between 1.0 and 1.1 GeV, and we measure the deviation of each from the central value. The spread of each with respect to the central value is a measure of the systematic uncertainty due to variations in the p_T spectrum of the charm jets. Alternate to varying the k_T, we could change the input structure functions of the colliding hadrons, or vary the fragmentation functions of the final state partons. In either case, the effect is to either stiffen or soften the p_T spectrum of the final state particles which emerge from the interaction. We choose to keep with the default structure functions and fragmentation functions in Pythia, and vary the k_T about the central value of 1.05 GeV.

This sensitivity to k_T is demonstrated in Figure 6.3(a), where we measure the trigger efficiency using a k_T=1.0, 1.05, and 1.10 GeV. The ratios of the higher and lower k_T values to the nominal value (as a function of p_T) are shown in Figure 6.3(b). One observes variations on the order of $\pm$10-15% with respect to the default value

of k_T. This provides a scale for the size of the systematic uncertainties due to the jet p_T spectrum.

Clearly the trigger efficiency depends on the amount of p_T present prior to the hard scatter. The next issue we wish to address is whether or not an incident, non-zero beam slope has a significant impact on the trigger rate. To investigate this further, we modelled the effect of the beam slope in the MC. The slope distributions of beam tracks were measured in the data (based on groups of runs), and fed into the MC using a gaussian approximation for the shape of the beam. Figure 6.4(a-b) shows the input distributions for the X and Y slope distributions based on the measurements from the 1990 data[2]. From these distributions, X and Y view beam slopes were chosen at random, and were subsequently used to define a new axis by which the scattering takes place. By rotating the scattering axis, the particles produced by Pythia gain or lose p_T with respect to the unrotated coordinate system. Since the trigger p_T is measured with respect to the unrotated coordinate system, the particles which acquire additional p_T are more likely to cause a trigger than if they hadn't recieved the extra p_T from the beam. Shown in Figure 6.4(c) is the calculated p_T of the beam (with respect to the unrotated system) for each event, based on the generated beam slopes and a 515 GeV/c beam. A long tail of events is observed, which extends beyond 1 GeV/c in transverse momentum. The issue we wish to address is whether or not the additonal p_T of the beam changes the trigger rate. Shown in Figure 6.5(a-b) is a comparison of the trigger efficiencies with and without the beam p_T effect. The two distributions are observed to be consistent with one another, indicating that the beam does not influence the trigger rate substantially.

---

[2] The offsets and widths are related to the configuration and settings of the magnets in the secondary beamline.

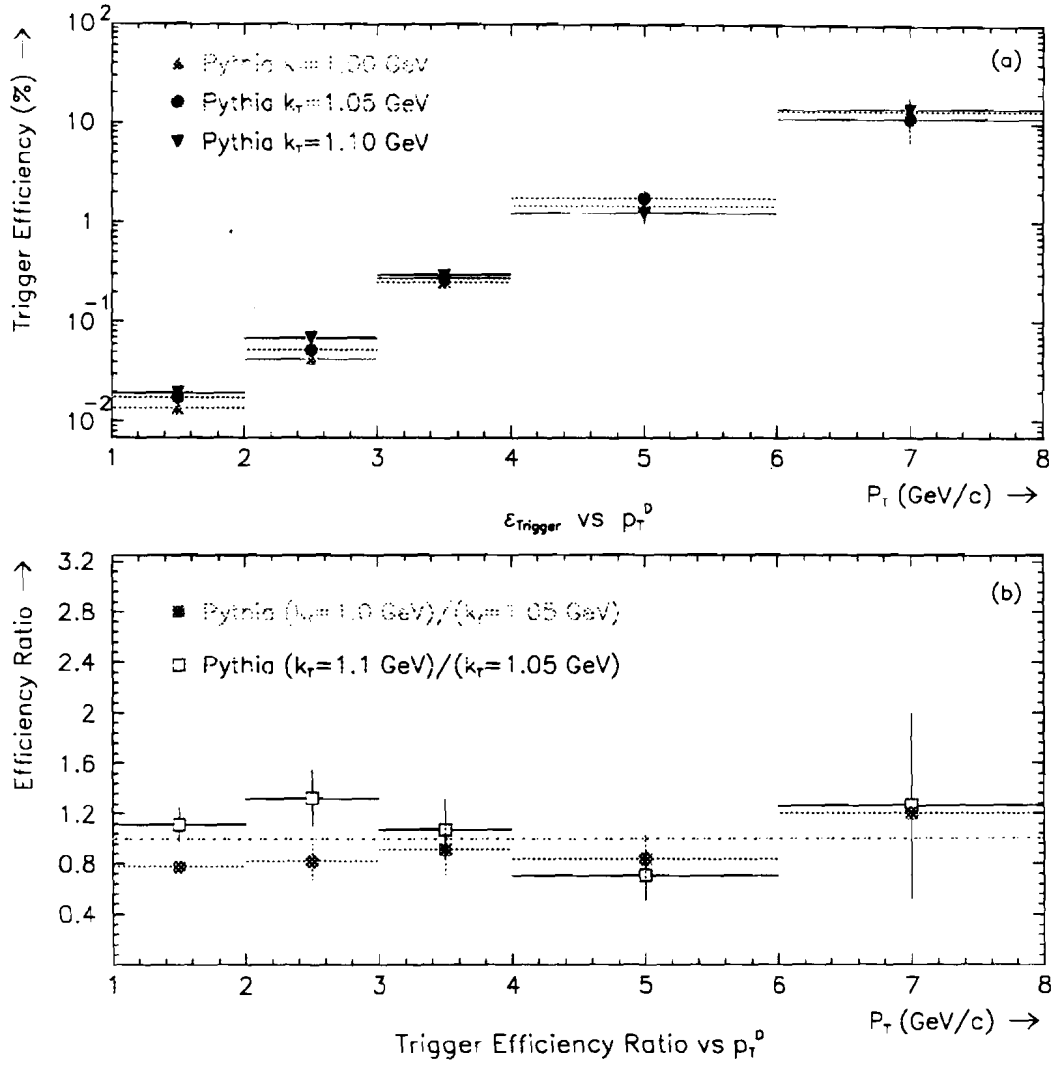

Figure 6.3 (a) The trigger efficiency as a function of the D($K\pi\pi$) p_T for three values of k_T; k_T = 1.0 GeV, k_T = 1.05 GeV, and k_T = 1.10 GeV, and (b) the ratios k_T = 1.0 GeV/k_T = 1.05 GeV, and k_T = 1.10 GeV/k_T = 1.05 GeV.

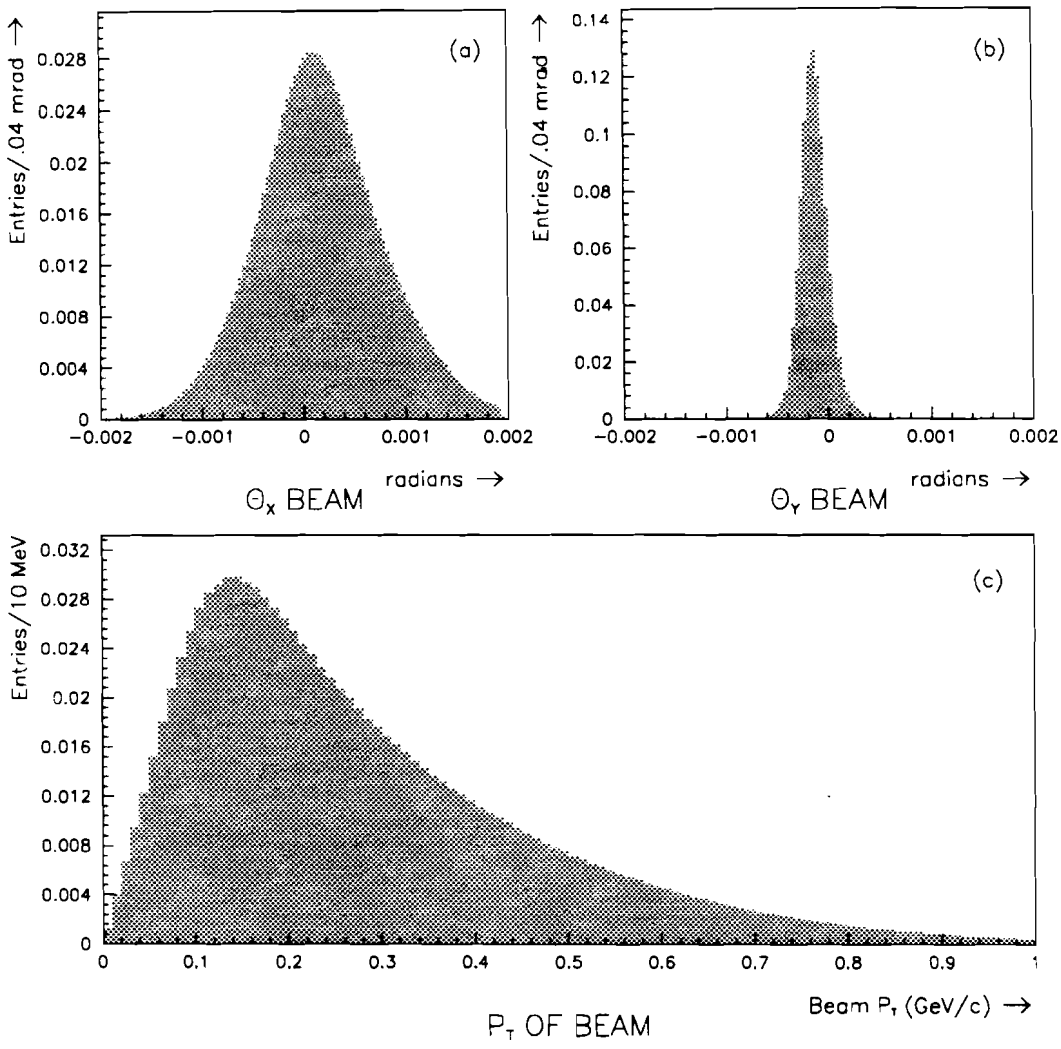

Figure 6.4 The beam slope distributions as implemented into the MC for (a) the X view and (b) the Y view, based on the 1990 data measured beam slopes. In (c) is shown the corresponding p_T of the beam based on a 515 GeV/c incident momentum.

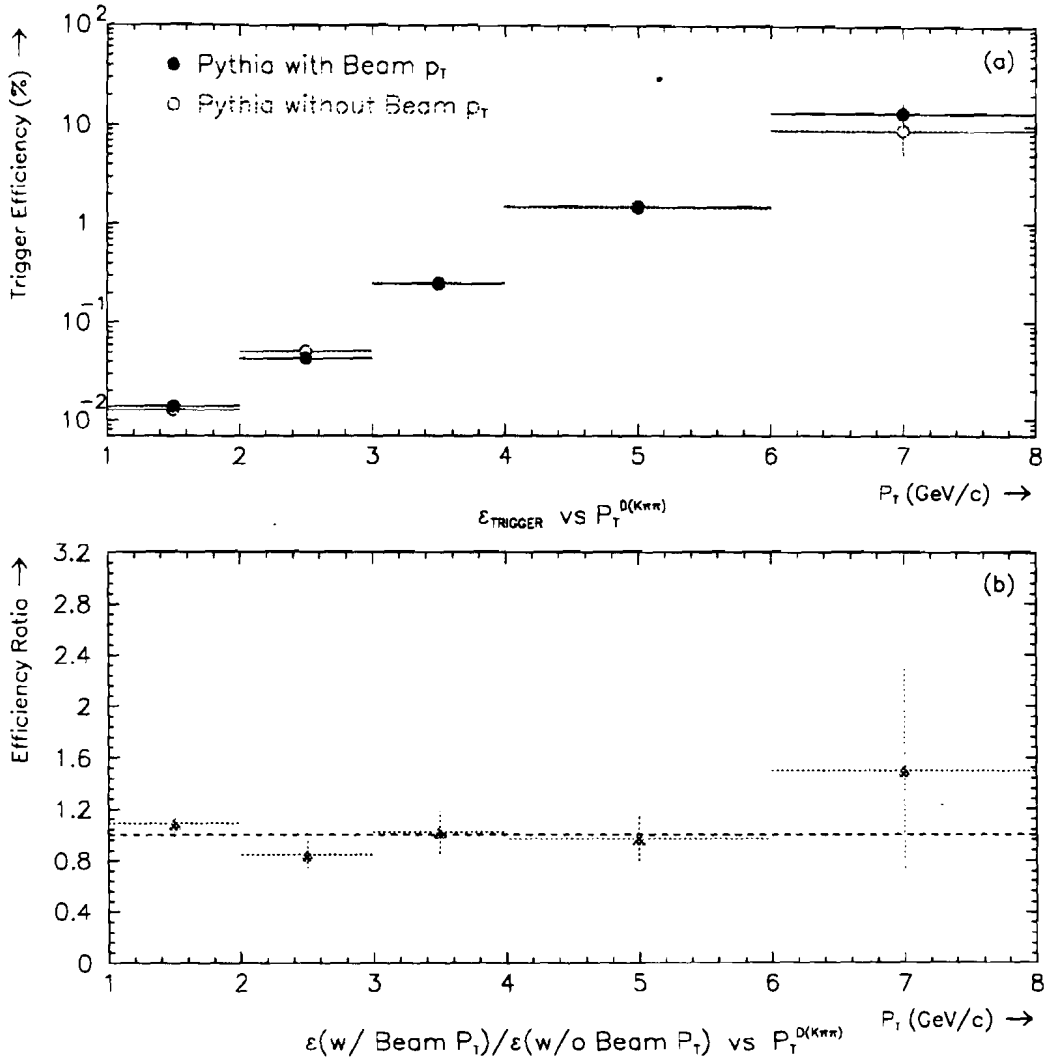

Figure 6.5 Comparison of the trigger efficiency with and without additional p_T due to the slope of the beam particle. In (a) the two efficiencies are overlayed, and in (b), we show the ratio of the two.

Summary of Trigger Efficiencies

Based on these figures, we have a good feel for how the trigger efficiency behaves as a function of p_T. The trigger efficiency rises with p_T, as expected, based on the thresholds of the EMLAC. The inverse of the trigger efficiency provides a weight which is to be applied to each p_T bin in the data to correct for the trigger losses. In the lowest p_T bin (1-2 GeV/c), this amounts to a weight of ~10,000 ! In other words, only ~1/10,000 such events produced are expected to trigger the EMLAC. We obtained an estimate of the uncertainties in the trigger efficiencies by changing the input p_T spectrum of charm particles (changing k_T). We found that these variations tend to produce uncertainites at the level of ~10-15%. There appeared to be some differences between the trigger efficiencies of D^- and D^+ mesons at the level of $\sim \pm 10\%$. The additional p_T provided by the nonzero beam slope did not appear to have a large impact on the observed trigger rates.

In order to check the overall normalization, we compared the trigger rates between the Pythia QCD MC and the E706 jet data (see Figure 5.31). There it was shown that the MC reproduced the trigger rates which were observed in the data, provided we used a $k_T \sim 1.05$ GeV in the MC (see Figure 5.19). We also showed in Figure 5.32 that charm quark jets trigger the EMLAC quite similarly to the jets initiated by light partons. At high p_T, where the E706 trigger operates, one does not expect a large difference between light parton and charm quark jets, and no large difference is observed. Based on these arguments, we feel confident that the overall magnitude of the trigger corrections properly reflects the losses induced by the trigger. In light of the studies presented in this section, the systematic errors are taken to be $\pm 15\%$.

We now summarize the results for the trigger efficiency in tabular form. Table 6.2 shows the estimated trigger efficiency for $D^{\pm}$ mesons, along with the

Table 6.2 $D^{\pm}$ Trigger Efficiency

p_T bin (GeV/c)	Trigger Eff (%)	Stat. Err (%)	Syst. Error (%)
1-2	0.0159	0.0015	0.0024
2-3	0.0552	0.0065	0.083
3-4	0.238	0.040	0.036
4-6	1.59	0.29	0.29
6-8	7.2	4.3	1.1

error estimates. The results were obtained by adding the D^+ and D^- samples together with a weight such that $D^-/D^+ = 1.2$.

In Figure 5.34, we showed that the trigger did not significantly alter the shape of the x_F spectrum. In other words there is no strong trigger bias against x_F, it is primarily against p_T. Therefore, we can use this same efficiency estimate whether we integrate over all x_F, or restrict ourselves to $x_F > 0$.

We now we turn our attention to making an estimate of the software reconstruction efficiency.

6.4 Estimation of the Reconstruction Efficiency

In order to extract the reconstruction efficiency, one must not only have developed the programs to find displaced vertices, but one must also be able to extract the small charm signal from the large combinatoric background. Before presenting the results for the reconstruction efficiency, we shall discuss some of the issues related to the extraction of the charm signal from the background. Since the reconstruction efficiency includes the losses due to the software analysis cuts, it is beneficial to discuss this aspect of the analysis prior to presenting the results for the reconstruction efficiency.

6.4.1 Extraction of the Charm Signal

Over the past few years, hadroproduction of charm at fixed target experiments has played an increasing role in providing an understanding of QCD. This has been made possible primarily by the implementation of silicon microstrips which allow precise measurements of the decay positions of displaced (secondary) vertices. We refer the reader to Chapter 4 for the discussion of the algorithm used to reconstruct secondary vertices.

Extracting charm signals from hadroproduction experiments has traditionally been quite difficult. These difficulties arise from (a) the small production cross section relative to the total hadronic cross section ($\sim$ 1/1000) and (b) small branching ratios to specific final states. With the advent of silicon detectors, it is now possible to fully reconstruct specific final states via displaced vertices. Despite the additional secondary vertex information, one is still faced with other backgrounds. The severity of the backgrounds depend on the details of the apparatus. The primary backgrounds to reconstructing charmed hadrons in specific final states are,

- Secondary Interactions;
- Combinatorial Background;
- Weak decays of strange mesons; and
- Weak decays of charmed mesons, which are not in the mode of interest.

In the 1990 run, E706 utilized a nuclear target consisting of 1.6 mm of copper followed by $\sim$4.96 cm of beryllium (see Chapter 2 Figure 2.3). Due to the large amount of material in the target region, the background was primarily due to secondary interactions and the resulting combinatorics. Although air gaps were present in the 1990 target configuration, this cut was not used because of the statistical loss of events. In the absence of any cuts applied to the raw secondary vertex information, the charm signal was not recognizable.

In general if one wishes to extract a small signal from a large background, one must reduce the background entries by a large amount and the signal events by only a small amount. In order to accomplish this goal, one must have some tool for discriminating the signal events from the background events. These tools are manifested in the form of **cuts** which are applied to all of the secondary vertex events. If the cuts result in a non-negligible loss of signal events, one must have a mechanism by which to estimate the loss and correct for it. For this thesis the losses due to various cuts were estimated using the monte carlo event and detector simulation.

6.4.2 Software Cuts

In this section we describe the cuts used to improve the signal to background (S/B) for the charm events. In this analysis the $D \rightarrow K\pi\pi$ mass was formed from either 3 track vertices or from 2 track vees which had additional tracks *attached* to it. Recall that each vertex/vee had a list of **extra track candidates** which were consistent with coming from the vertex/vee in question (see Chapter 4). Neither the vees or vertices were refit with any of the extra track candidates. For the case of vees, a 3 track combination can be made with the 2 tracks from the vee plus any one of the additional *extra track candidates*. The motivation for accepting vees in this category was to minimize the algorithm's inefficiencies. In other words if we use the vees, it is only necessary to have 2 out of the 3 decay tracks tagged as secondary tracks rather than all three. Most of the cuts were common to both the vee and vertex samples. The **cuts on the 3 track vertices** were,

$$\sigma_R \leq 50\mu \tag{6.7}$$

$$S > 6 \tag{6.8}$$

$$\frac{\delta^i_{SEC}}{\delta^i_{PRIM}} \leq 0.4 \qquad i=1,2,3 \tag{6.9}$$

$$\prod_{i=1}^{3} \frac{\delta^i_{SEC}}{\delta^i_{PRIM}} \leq 0.005 \tag{6.10}$$

$$\#\text{BEST LINKS} \geq 3. \qquad 6.11$$

Similarly, the **cuts applied to the vee sample** were the following:

$$\sigma_R \leq 50\mu \qquad 6.12$$

$$S > 6 \qquad 6.13$$

$$\frac{\delta^i_{SEC}}{\delta^i_{PRIM}} \leq 0.4 \qquad i=1,2 \qquad 6.14$$

$$\prod_{i=1}^{2} \frac{\delta^i_{SEC}}{\delta^i_{PRIM}} \leq 0.002 \qquad 6.15$$

$$\#\text{BEST LINKS} \geq 3 \qquad 6.16$$

$$\frac{\delta^3_{SEC}}{\delta^3_{PRIM}} \leq 0.4 \quad or \quad \delta^3_{SEC} < 30\mu. \qquad 6.17$$

In addition to these mathematical constraints, the vees were also required to satisy the following criteria:

- At least 1 track in the vee must not be used in any other vertex in the event.
- All SSD links must be distinct from one another.

In 6.7 and 6.12, σ_R is the **impact parameter of the parent momentum vector to the primary vertex**. A schematic representation of this variable is shown in Figure 6.6. The solid lines represent tracks eminating from the primary vertex, and the dashed lines are those coming from the D decay. The shaded regions are approximate locations of the 1990 targets. The reader should note that the vertical scale is magnified by a factor of 60 as compared to the horizontal scale[3].

[3] To provide a reference scale, the widest angle track in Figure 6.6 has a polar angle of about 6 degrees.

The parent momentum vector is defined as the vector sum of the momenta of the decay tracks, and is constrained to pass through the secondary vertex. Among the forementioned cuts, this is the most powerful in reducing background. In 6.8 and 6.13, S is defined as the **longitudinal significance of separation** from the primary vertex to the secondary vertex. The longitudinal significance of separation is simply the measured separation divided by the expected error. Mathematically, S is defined by,

$$S = \frac{(Z_{SEC} - Z_{PRIM})}{\sqrt{\sigma^2_{Z_{SEC}} + \sigma^2_{Z_{PRIM}}}}$$

where Z_{SEC} and Z_{PRIM} are the Z coordinates of the secondary and primary vertex, and $\sigma^2_{Z_{SEC}}$ and $\sigma^2_{Z_{PRIM}}$ are their respective variances. The variables δ^i_{SEC}, and δ^i_{PRIM} are simply the impact parameters of each decay track to the secondary and primary vertex respectively. In 6.17, δ^3_{SEC} (δ^3_{PRIM}) always refers to the **extra track candidate** which was attached to the vee.

We now wish to give some insight into why these cuts were chosen. As mentioned previously, the σ_R cut is the most powerful for reducing the background. The reason for this is fairly simple. For the $D \rightarrow K\pi\pi$ decay, the momentum vector formed from the $K\pi\pi$ should be equal (within resolution) to that of the parent D meson. Consequently, if the D meson was produced at the primary vertex, the parent momentum vector should extrapolate back to it, as indicated in Figure 6.6. There is clearly a resolution issue involved, which reflects the errors in the momenta of the decay tracks, as well as the uncertainty in the positions of the primary and secondary vertices. Provided these errors are small, a tight cut on σ_R can provide a large suppression to the background events, with only minimal loss to the signal. The explanation for the background rejection is easy to understand. Background produced from secondary interactions of primary particles in the target material usually results in some amount of **unseen momentum**. By **unseen momentum**, we mean any particle which is not fully reconstructed in the tracking system. The

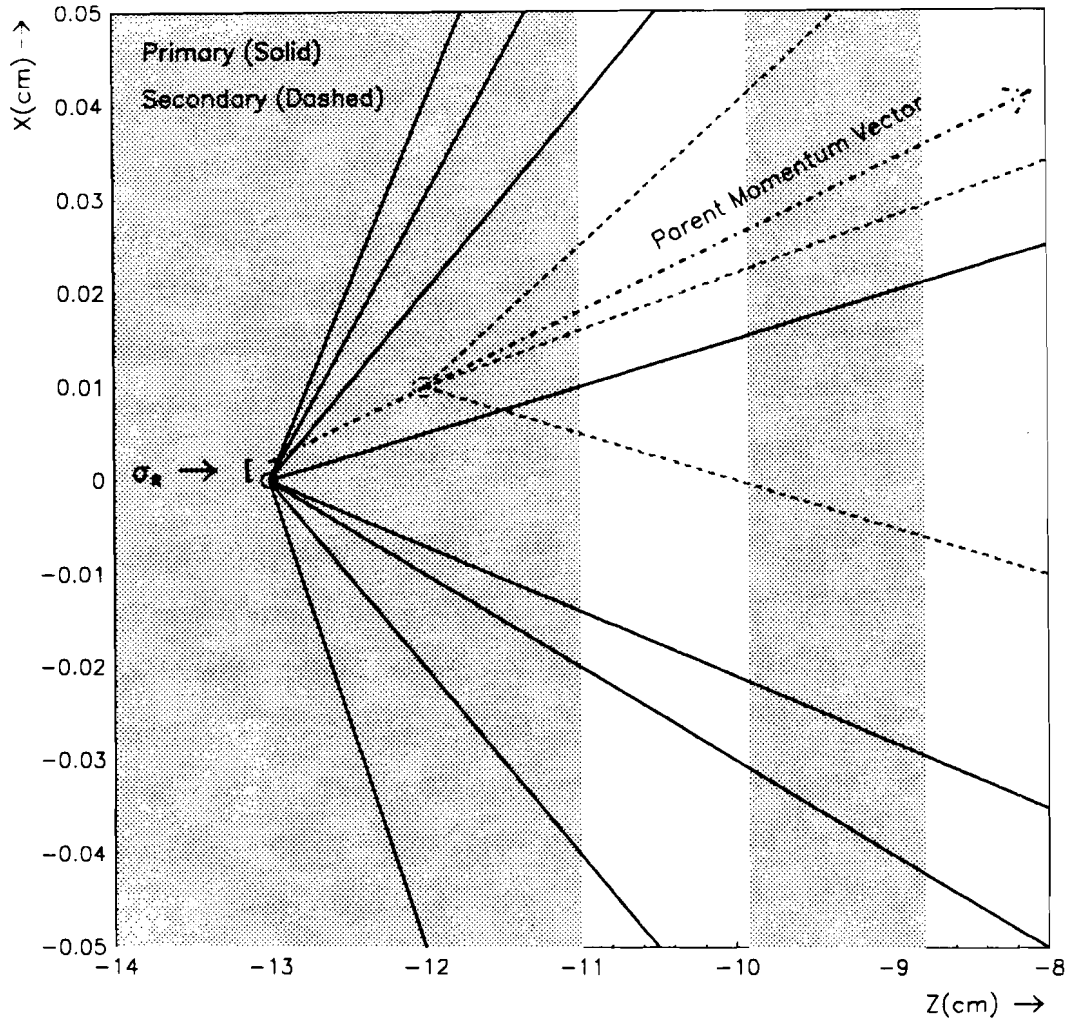

Figure 6.6 Schematic representation of the σ_R variable. Solid line are tracks from the primary vertex, dashed lines are secondaries, and the dot-dashed is the momentum vector sum of the secondary tracks.

missing momenta may be a result of acceptance losses, electrical neutrality, or both. A consequence of the missing momentum is that the momentum vector of the observed secondary tracks do not point back to the primary vertex very well. In other words, the resolution in σ_R is smeared to a great extent due to the missing momentum. The same argument can be made regarding other charm decays, (such as $D^{\pm} \rightarrow K^{\mp}\pi^{\pm}\pi^{\pm}\pi^{0}(\pi^{0})$, or $D^{\pm} \rightarrow K^{\mp}\pi^{\pm}e^{\pm}\nu$), where one or more of the decay particles are not observed in the tracking system. Again, the missing momenta will smear the σ_R distribution beyond what is expected if all the decay products had been observed. Finally, it should also be clear that a tight σ_R cut will reduce the combinatorial background, since there is no reason for background vertices to have a narrow σ_R distribution. Based upon these arguments, it is clear that the σ_R cut is a powerful tool for discriminating signal versus background.

To give the reader a feel for this variable, we show in Figure 6.7(a) the calculated value of σ_R for all 3 track vertices in the 1990 data. In Figure 6.7(b) is shown the integrated fraction of 3 track vertices with σ_R below a given value. From the plot, one finds that only 5.7% of these 3 track vertices have $\sigma_R < 50\mu$, almost a factor of 20 reduction in the background ! Since these vertices are primarily background events, one has a flavor of how the σ_R variable looks for the background events. Later, we shall show the corresonding plots for MC charm events.

The significance of separation cut (6.8, 6.13) was used to ensure that the secondary vertex in question was well separated from the primary vertex in the event. We require a minimum significance of separation of at least 6 for the candidate charm events. Typically, the longitudinal error of the secondary vertex is $\sim 500\mu$, and the primary vertex about 300 μ, so that a significance cut of 6 tends to require that the decay vertex is at least 4 mm downstream of the primary vertex.

Further cuts are imposed upon the ratio of the impact parameter of the secondary tracks to the secondary vertex relative to the primary vertex. For three track vertices, we require that each track comes at least 2.5 times as close to the

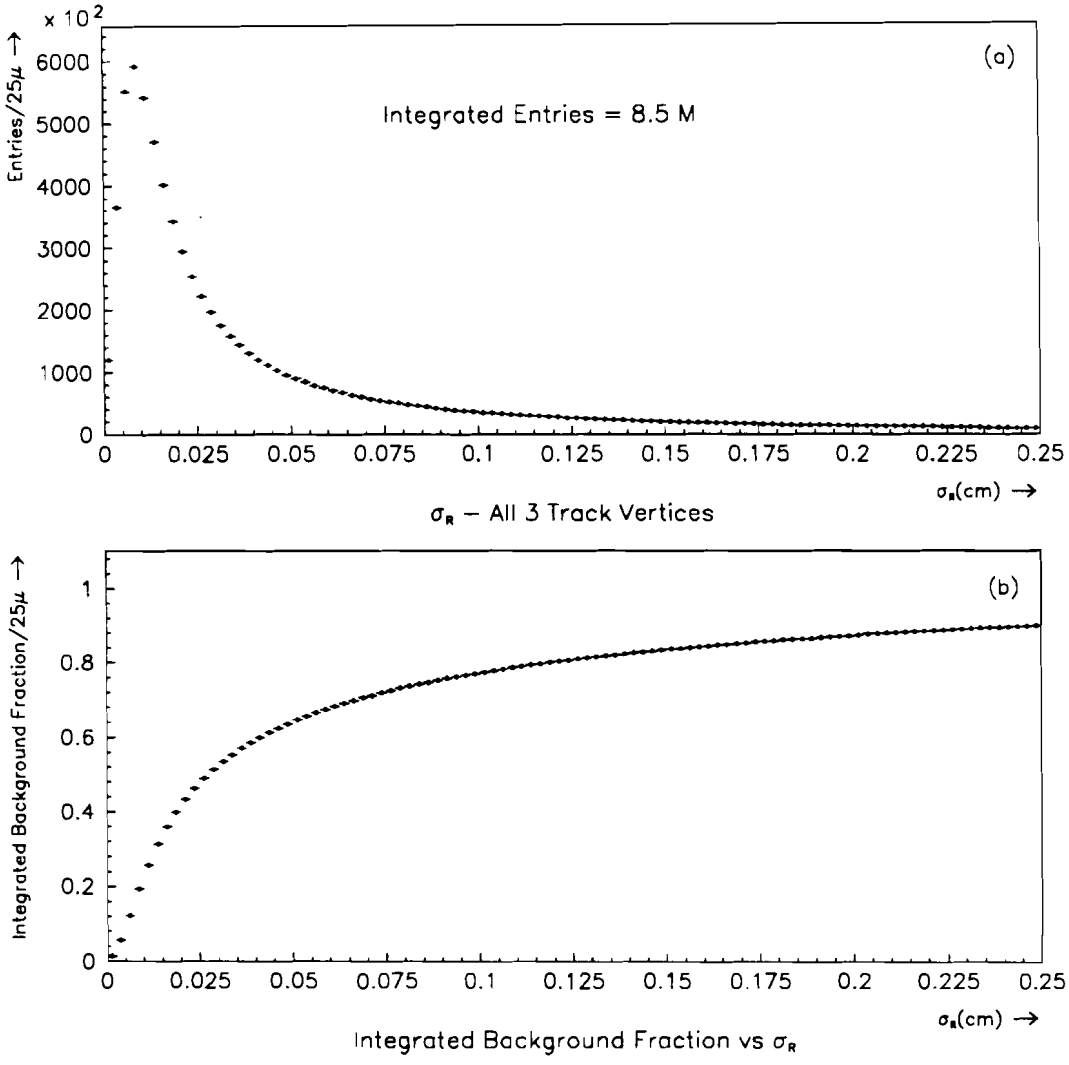

Figure 6.7 (a) The distribution of σ_R for all 3 track vertices (and vees with additional tracks) in the 1990 data. In (b) is shown the running integral of (a), normalized to the total number of events (including overflows).

secondary vertex as it does to the primary vertex (6.9, 6.14). For the vee sample, the requirement is only placed on the 2 tracks used in the fit. The third track in the vee i.e. the attached track, must have **either** $\delta^3_{\rm SEC}/\delta^3_{\rm PRIM} \leq 0.4$ or $\delta^3_{\rm SEC} < 30\mu$. In other words, the third track may point back to the primary vertex, but it should also have a small impact parameter to the secondary vertex as well. Along the same lines, a cut is applied on the product of the impact parameter ratios as defined in 6.10 and 6.15. For the 3 track vertex case, this cut requires that, **on average**, each decay track be about 5.8 times closer to the secondary vertex than the primary.

In both the vees and vertices, we require that at least 3 of the 6 SSD links (3X + 3Y) are the **best links** of their respective downstream tracks. Vertices composed primarily of **extra links** are usually a result of combinatorics among the downstream and upstream tracks. If one assumes that the probability of choosing the best link correctly is at least 80%, the forementioned cut removes less than 5% of the sample. Based on the plots shown in Figure 5.42 and Figure 5.43, this estimate is reasonable.

Two additional cuts were applied to the vees which were not used for the vertices. The first cut required that no vertex in the event contain both of the tracks from the vee. This cut was implemented to reduce the combinatorial background among the tracks produced in secondary interactions. The final cut applied to the vees was the constraint that the 3 SSD links in each view must be unique. This differs from the 3 track vertex case, where we require that only 5 of the 6 SSD tracks must be unique. In other words, we allow two of the SSD tracks to *overlap* in either the X or Y view. If 2 tracks overlap in the X or Y view, only 1 SSD track is formed. However, the two tracks are eventually split apart by the magnetic field of the analysis magnet, and the two tracks become distinct in the downstream system. As a result, the two downstream tracks link to the same SSD track.

Clearly, one loses true signal events as a result of these analysis cuts. Additional losses are incurred as as result of the acceptance of the spectrometer, chamber

efficiencies, and the reconstruction software. We rely on the monte carlo to estimate the losses due to these sources. The MC incorporated all of the important physical processes (GEANT) and detector effects. In order for the MC to provide an accurate estimate of the reconstruction efficiency, it must reproduce the features of the data which are responsible for the losses. In Chapter 4, we presented some comparisons between the MC and data. First, we showed that the hit and track multiplicities were in fair agreement with one another. Also, we showed that the linking ambiguities were reproduced, based on the average number of SSD links for each downstream track. Finally, we showed that the SSD track resolution was reasonably accounted for by the MC. Based on the overall agreement in these variables, we could be fairly confident that the MC will reproduce the losses in the reconstruction programs. As mentioned earlier, the MC must also account for losses due to the analysis cuts. In order to investigate this further, we performed a study of the impact of the analysis variables on the K^0_S signal. Since this sample involves a high statistics mass peak, we can make a clean comparison between MC and data, as to how well the analysis variables are reproduced. These studies are presented in the next section.

6.4.3 Data and MC Comparison of K^0_S *Events*

In order to provide a more direct comparison of the secondary vertex results, we turn to the abundant K^0_S signal present in the 1990 data. The K^0_S signal was reconstructed from the sample of vees generated by the charm reconstruction package, and is therefore subject to many of the biases which enter into the charm analysis. A comparison of the features of the $K^0_S \to \pi^+\pi^-$ signal between the MC and data will give an indication of how reliable the MC is in predicting the losses due to the analysis cuts. In this section we shall compare some of the variables upon which the reconstruction efficiency depends. Some of these variables enter at the reconstruction level, and others are related to the forementioned analysis cuts. In both cases, the MC should reproduce the data distributions in order to claim that the losses are appropriately accounted for.

The first step was to generate a sample of K^0_S events using the Pythia MC. In order to do this study in a timely manner, it was required that every event contain at least one K^0_S which decayed in front of the SSD chambers. Therefore, this sample is 100% pure with K^0_S which decayed in the Target/SSD region. The fraction of **data events** which have a K^0_S decaying in that same region is only about 1/50 events. Therefore, the data plot tends to have more background than does the MC distribution. To bypass this, we perform a sideband subtraction for both the MC and data. Both the MC and data were put throught the same reconstruction chain, and the outputs compared.

First in Figure 6.8, we show the K^0_S signal obtained from the two samples. In Figure 6.8(a-b), the raw signal plot is shown, and in Figure 6.8(c) are the background subtracted plots. The mass resolution of the K^0_S ($\sim$ 3 MeV) is seen to be reasonably well accounted for by the MC simulation. In order to make sure that we are comparing similar spectra of K^0_S's, we show in Figure 6.9(a) the energy distribution of the reconstructed K^0_S's and in Figure 6.9(b) we compare the reconstructed decay distance from the primary vertex. From these plots, we conclude that the samples are quite similar, so that a valid comparison can be made. In addition, these plots also indicate that the acceptance is modelled correctly, since the MC reproduces the losses at low energy and short decay distances.

The variables which we shall compare are those to which the secondary vertex finding is sensitive. We have already shown in Figure 5.42 and Figure 5.43 the uncertainties due to the number of SSD links was well reproduced by the MC. We also showed (in Chapter 4) that the hit and track multiplicities were in fairly good agreement, so that the losses due to the overall event confusion should be accounted for by the MC. Another variable which must be reproduced by the MC is the impact parameter distribution of the decay tracks (π^+ and π^- for the K^0_S case) to the reconstructed decay vertex. In Figure 6.10(a-b) we compare the X and Y view impact parameter distributions, and in Figure 6.10(c) we show the radial (spacial) distribution. Since the impact parameters of the two tracks are measured

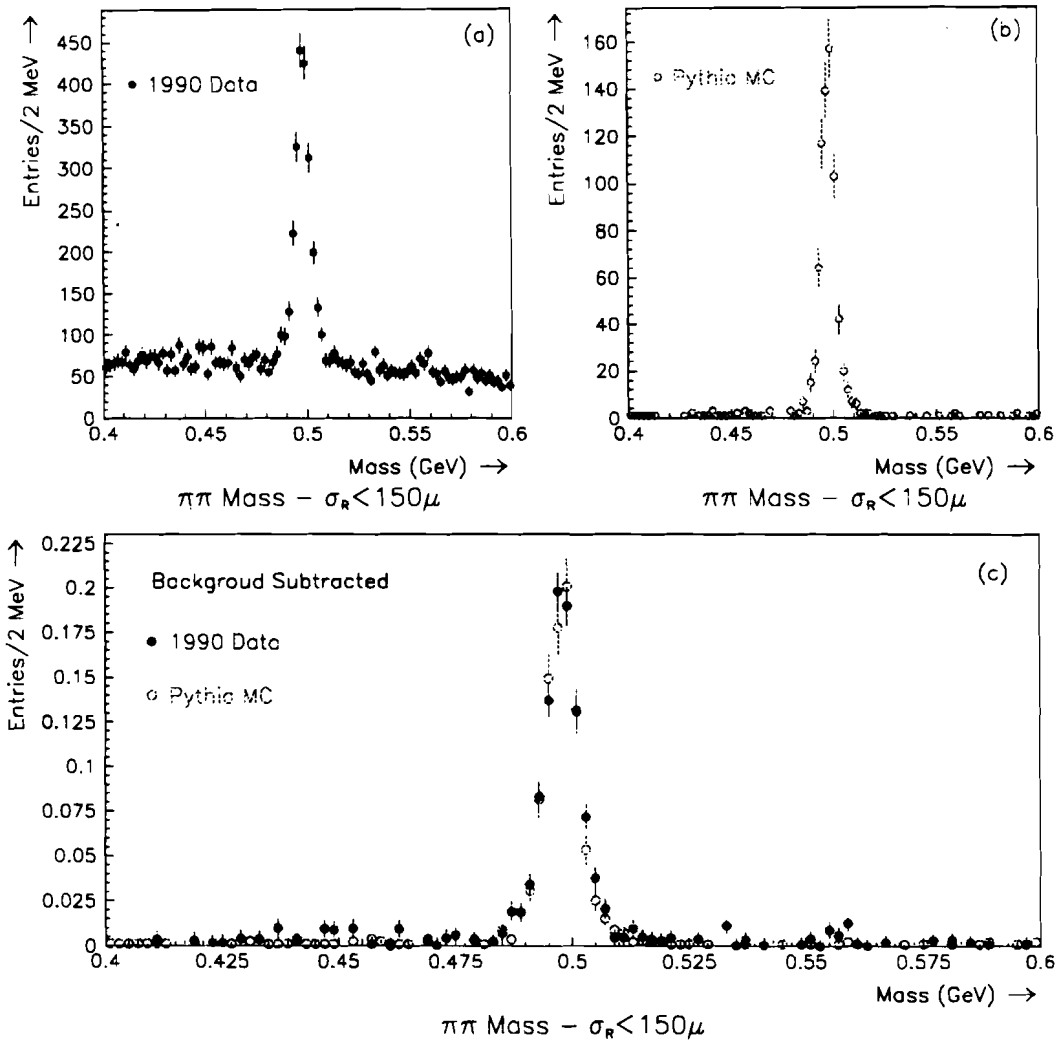

Figure 6.8 The K^0_S sample obtained from (a) ~2% of the 1990 data, and (b) the (Pythia) MC and detector simulation. In (c), a background subtraction is done, and the mass distributions are superimposed onto one another.

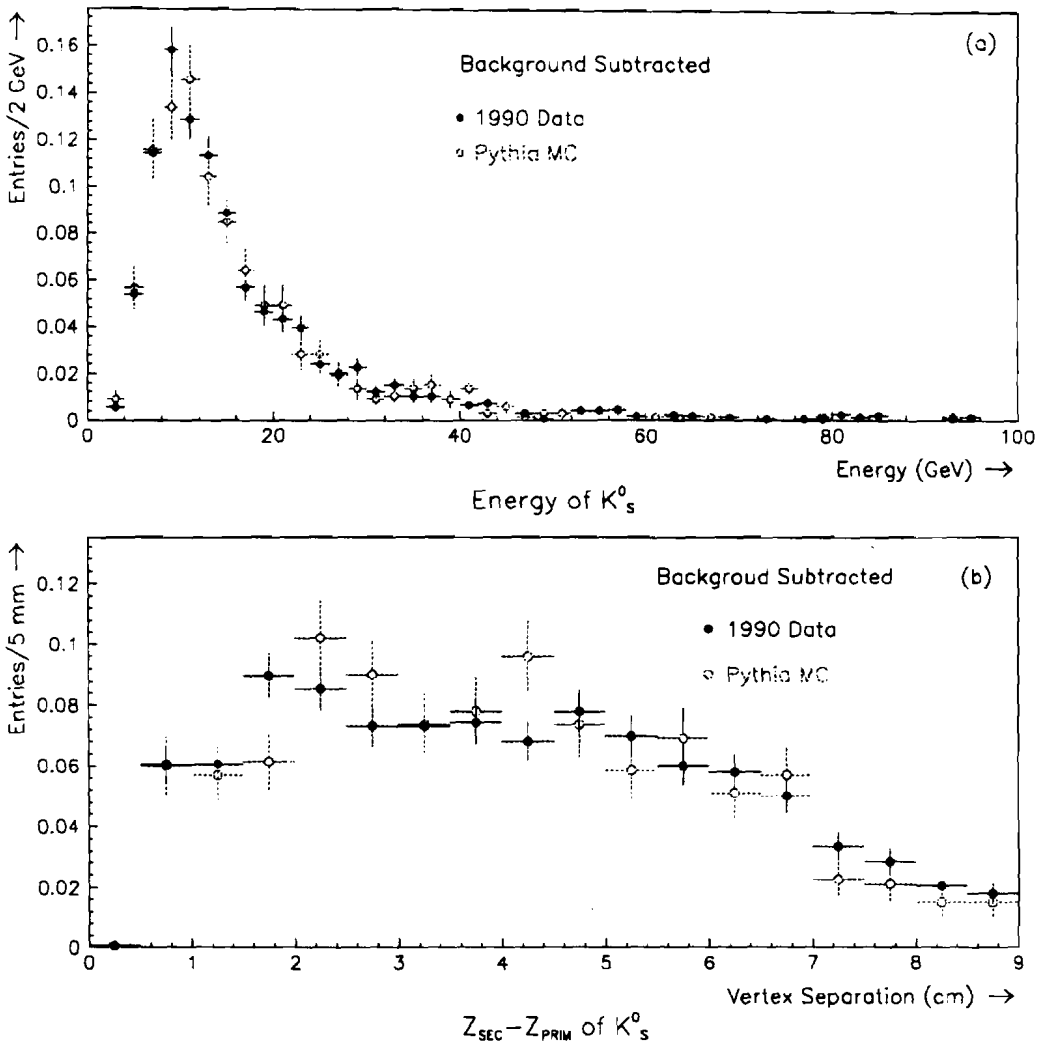

Figure 6.9 The reconstructed (a) energy of the K^0_S, and, (b) decay distance from the primary vertex in the event. Both plots are background subtracted.

with respect to the weighted vertex Z_W (see 6.8), the tracks do not pass through the secondary vertex. The MC distribution is seen to be consistent with that observed for the data. Many of the cuts related to secondary vertex finding are related to the resolution. The agreement in this variable suggests that the losses due to the tracking resolution are reproduced reasonably well by the MC. Furthermore, the losses due to any cuts which are related to the impact parameter, should be reasonably accounted for (such as the cuts defined in 6.9 and 6.14).

Further comparisons can be made regarding the parameters of the reconstructed vee. As alluded to previously, in forming vees, 2 independent measurements are made of the decay position of the K^0_S, one in the X view, and the other in the Y view. The difference between the measured Z location in the X and Y views provides a measure of the 2 track longitudinal resolution. In Figure 6.11(a), we show the difference in the Z location of the decay vertex as measured in the X and Y views. In Figure 6.11(b), we form a significance by dividing the measured separation by the expected error, on an event by event basis. Figure 6.11(c) shows the χ^2_{VEE}, where χ^2_{VEE} was defined in 6.3. All three distributions are reproduced by the MC within the available level of statistics. This gives us additional confidence that the resolution losses are accounted for by the MC.

In the final set of figures related to these samples, we wish to compare the σ_R variable mentioned above. Recall that σ_R is the **impact parameter of the momentum vector (of the decay tracks) to the primary vertex** (see Figure 6.6). Like the charmed mesons, K^0_S's are generally produced at the primary vertex, so that one expects a σ_R distribution which is fairly narrow. Since the width of the σ_R distribution reflects the vertex resolution, as well as the momentum resolution, this comparison is particularly sensitive to any resolution differences between the data and MC. The relative agreement in σ_R for the K^0_S sample will provide us with an indication of the expected level of agreement in this variable for the $D^\pm$ sample. Since a σ_R cut of 50μ is used in the $D^\pm$ analysis, we would like to see what fraction of events pass this cut for both MC and data. In Figure 6.12,

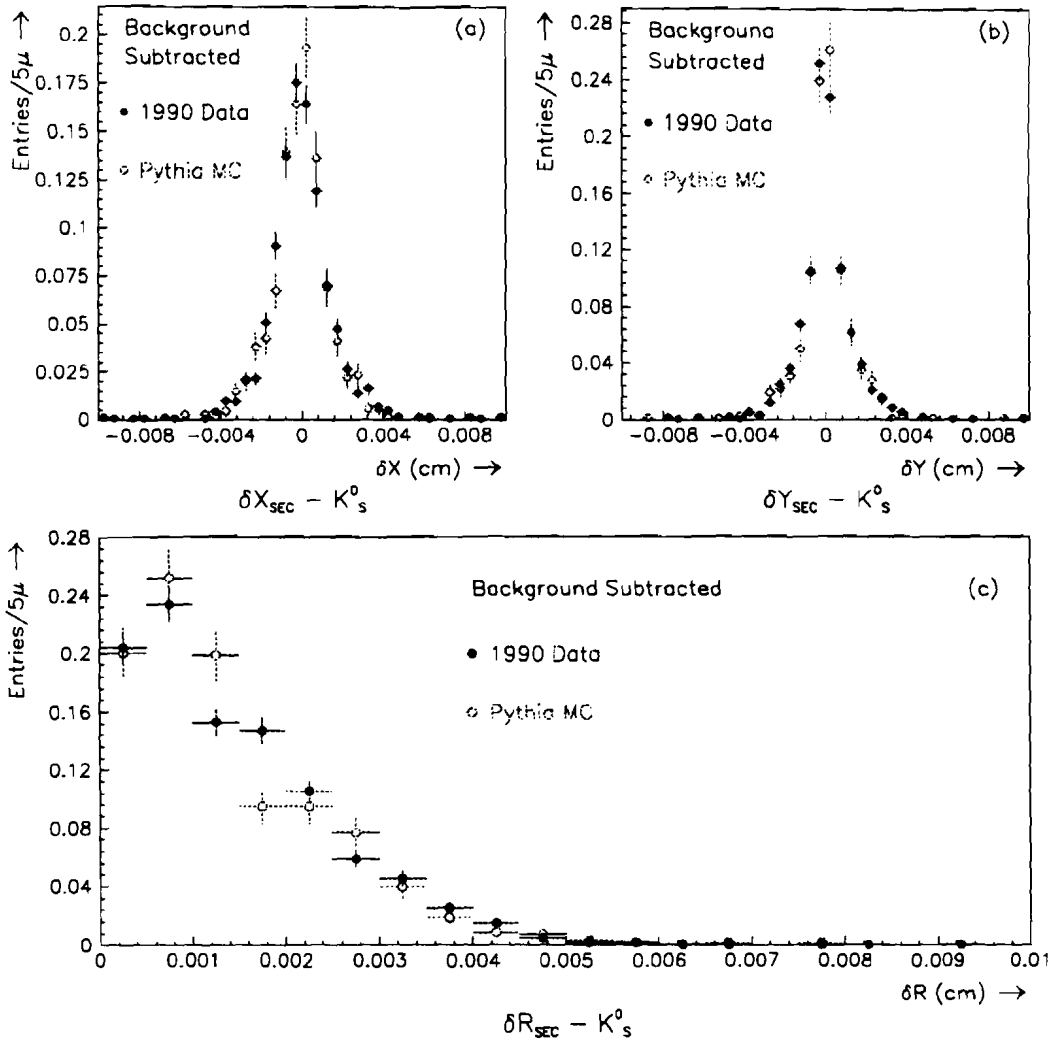

Figure 6.10 Comparison of the impact parameter distribution of the $\pi^-\pi^+$ tracks to the decay vertex along (a) the X view, (b) the Y view, and (c) the radial direction.

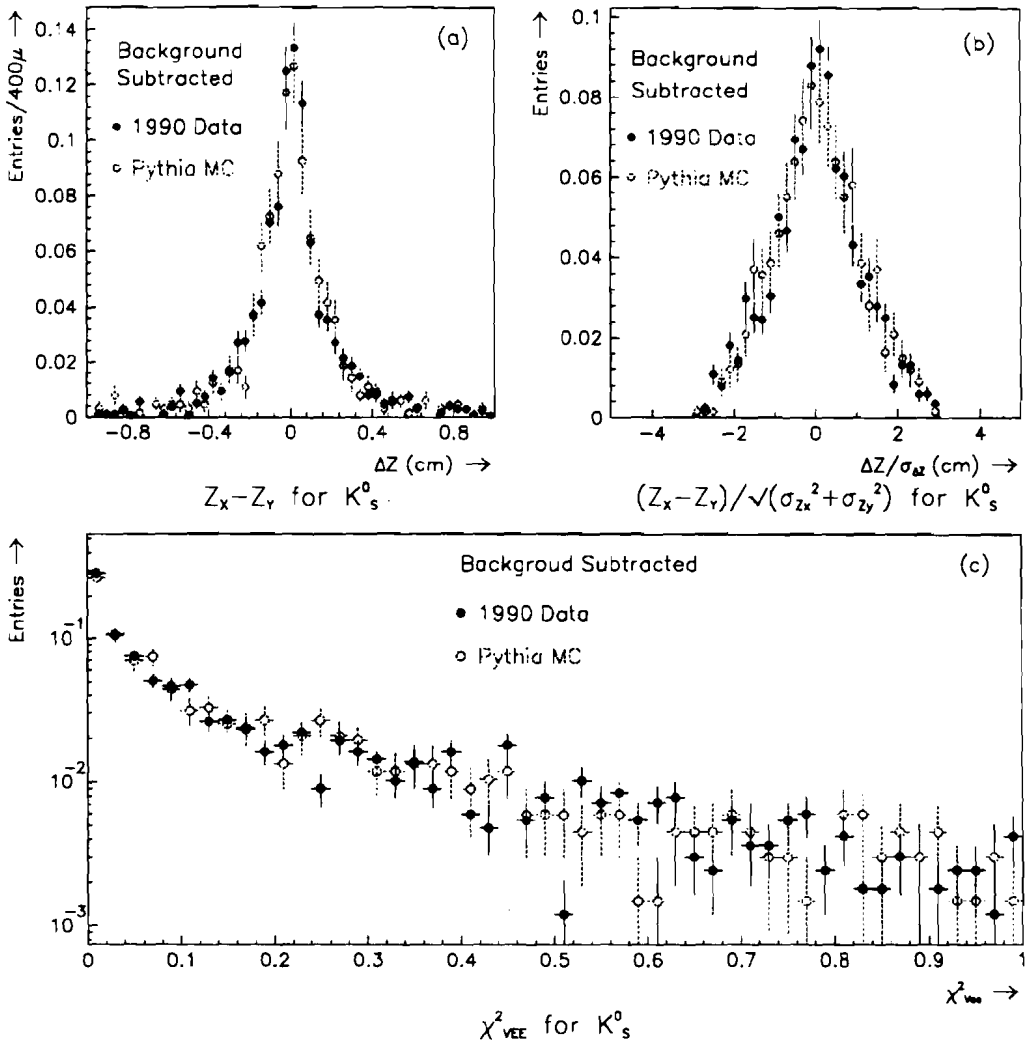

Figure 6.11 Comparison between the MC and data for (a) the ΔZ, (b) $\Delta Z/\sigma_{\Delta Z}$, and (c) χ^2_{VEE} of the secondary vertex (vee).

we compare background subtracted distributions of σ_R, integrated over all decay distances (see Figure 6.9(b)). We observe that the MC tends to show fairly nice agreement with the data. This indicates that the MC can be used to estimate the loss of signal events due to a given value of σ_R^{CUT}.

Since the average decay length of the charm particles is much smaller than strange particles, we provide one last comparison. First, we divide the K_S^0 sample into 4 bins, each differentiated by the decay length. The subsamples consist of decays which have a decay distance D within (a) $0 < D < 1.5$ cm, (b) $1.5 < D < 3.0$ cm, (c) $3.0 < D < 6.0$ cm, and (d) $6.0 < D < 12.0$ cm. For each subsample, we plot the number of events which survive a given σ_R cut, as a function of the σ_R cut used. The number of events is then normalized to the total number observed with $\sigma_R < 200\mu$ (see Figure 6.12). Figure 6.13(a-d) shows the comparisons of the *survival fraction* as a function of σ_R^{CUT}. The bins in D are indicated below their respective plots. From these figures, one finds that the MC provides a fairly accurate description of the losses incurred due to a given σ_R cut. Based on a σ_R cut of 50μ, the fraction rejected by the MC and data appears to be similar to within ~5%. (We neglect the last bin in D because charm particles rarely decay that far from their production point.). For a 3 track vertex, i.e. $D \rightarrow K\pi\pi$, we expect these distributions to reach unity faster, since the 3 track vertex has a better resolution than a 2 track vertex. In addition, there is more resolution smearing in the K_S^0 vertex than the $D^{\pm}$ vertex due to multiple scattering[4]. We therefore expect that the relative uncertainty in the correction due to the σ_R cut not to be more than ~5%.

---

[4] The momentum of the decay tracks from the K_S^0 are significantly lower than those from the $D^{\pm}$'s.

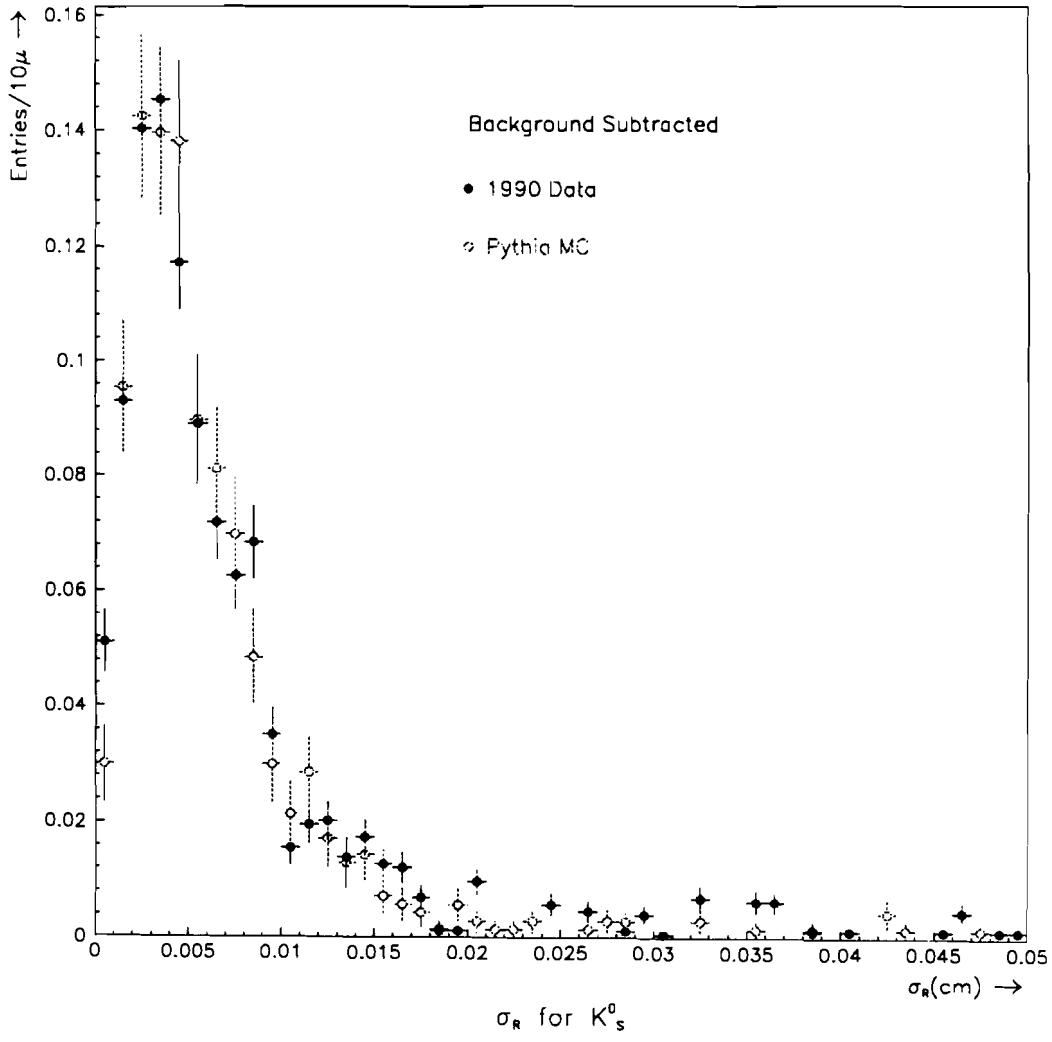

Figure 6.12 Comparison of the K^0_S σ_R distribution for 1990 data and MC.

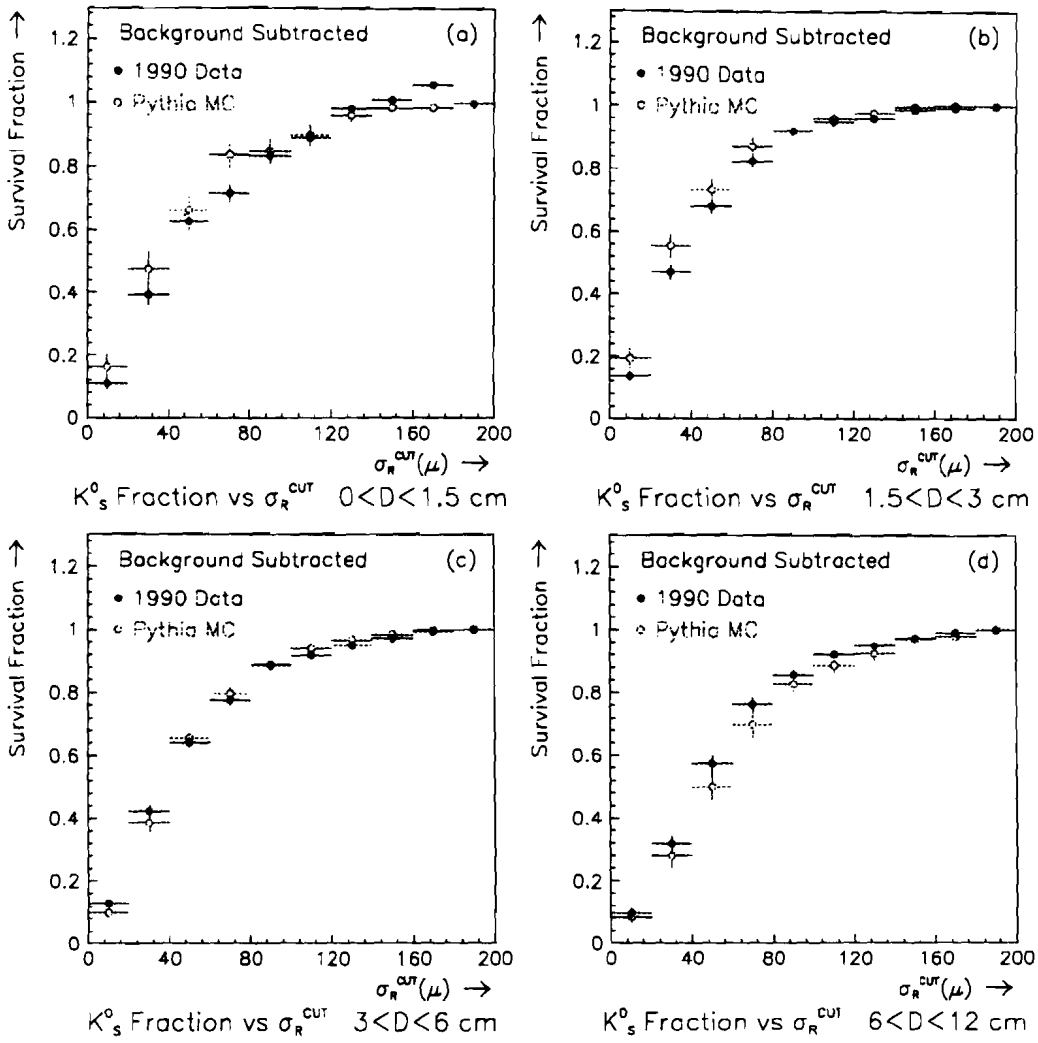

Figure 6.13 Comparison of the survival fraction of K^0_S signal events as a function of σ_R^{CUT} in four bins of the decay distance D.

In summary, we have shown that the MC and data are in reasonably good agreement with respect to hit and track multiplicities, linking uncertainties and resolution. In addition, we have shown that several of the distributions upon which the reconstruction program and analysis cuts are based, can be reproduced by the MC as well. Based on the overall agreement with respect to these variables, we conclude that the MC will provide a reasonably accurate estimate of the $D^{\pm}$ reconstruction efficiency. In the next section, we present the results for the $D^{\pm}$ reconstruction efficiency.

6.4.4 Calculation of the $D^{\pm}$ *Reconstruction Efficiency*

In this section we describe the technique used to calculate the $D^{\pm}$ reconstruction efficiency[5]. Since the reconstruction efficiency is sensitive to the input spectrum i.e. the momentum, it is necessary to calculate the reconstruction efficiency with respect to a triggered (momentum biased) sample of $D^{\pm}$ mesons. A sample which is not required to satisfy the E706 software trigger will undoubtedly have a different momentum distribution[6], and therefore, a different average efficiency. Due to the limited statistics of the triggered sample, a second larger sample of $D^{\pm}$ mesons was generated, with no trigger requirement imposed. Each of these events was then weighted so that the resulting momentum (p_T and p_{TOTAL}) matched the triggered spectrum. In this way, we hope to roughly impose the effect of the trigger onto an unbiased sample of $D^{\pm}$ events. We therefore have two samples with which to work with in evaluating the reconstruction efficiency. The first is the true, triggered sample, and the second is an unbiased sample which was weighted to replicate the triggered sample. Apriori, we expect the reconstruction efficiencies obtained from these two samples to yield similar results. In the forthcoming plots, we shall overlay the results from the two samples.

---

[5] From this point onward, reconstruction efficiency refers to the product of the acceptance and the efficiency due to all software and analysis cuts.

[6] See Figure 5.35, for example.

First, we show in Figure 6.14(a), the reconstruction efficiency as a function of the p_T (of the $D^{\pm}$ meson), integrating over the region $-.2 < x_F < 1.0$. The solid points are the efficiency measured with respect to the triggered events, and the open points are the weighted events. One observes that the triggered and weighted events are in fair agreement with one another. In Figure 6.14(b-e), we compare the reconstruction efficiency as projected onto other axes, including x_F, p_{TOTAL}, Z_{PRIM}, and charge. Again, the two samples are in reasonable agreement with one another. Since the points in the weighted distribution are mostly within the statistical errors of the triggered distribution, and the two curves exhibit the same trend, we shall assume that the weighted distribution is a reasonable approximation to the triggered distribution. Therefore, the reconstruction efficiency is extracted from the weighted distribution as opposed to the triggered distribution.

In order to eventually compare to other experiments, we will need the reconstruction efficiency integrated over the region $0 < x_F < 1$ as well. These plots are shown in Figure 6.15. As before, the triggered and weighted samples are overlayed for comparison. The two samples appear to be in fair agreement with one another.

σ_R for $D^{\pm}$

Earlier in this chapter we stressed the importance of the σ_R cut. We showed in Figure 6.7 the σ_R distribution for all of the 3 track events from the 1990 data[7]. We now show in Figure 6.16 the σ_R distribution for reconstructed $D^{\pm}$ mesons in the MC. Since the MC reproduces the resolution in the data fairly well (see Figure 6.13 and Figure 6.10), we expect that the $D^{\pm}$ σ_R distribution in the data looks similar to the MC. Upon comparing Figure 6.16 to Figure 6.7, one observes that nearly all of $D^{\pm}$ events are contained within the first 2 bins of Figure 6.7, i.e. $\sigma_R \leq 50\mu$. From

[7] To be more precise, it was only those 3 track events which had a net charge of ± 1.

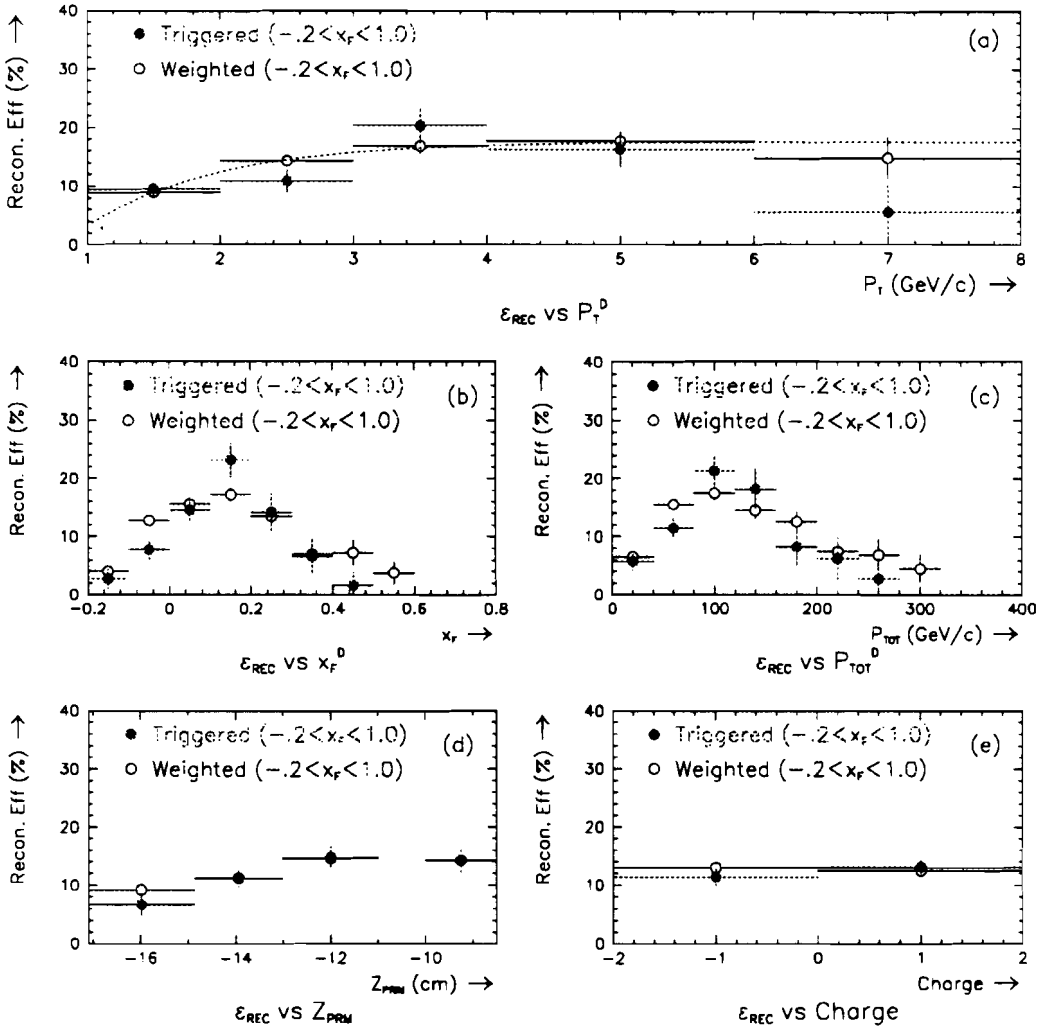

Figure 6.14 Reconstruction efficiency as a function of (a) p_T, (b) x_F, (c) PTOTAL, (d) Z_{PRIM}, and (e) charge. All figures integrate over the region $-.2 < x_F < 1.0$. The dotted curve in (a) is a fit to the weighted distribution.

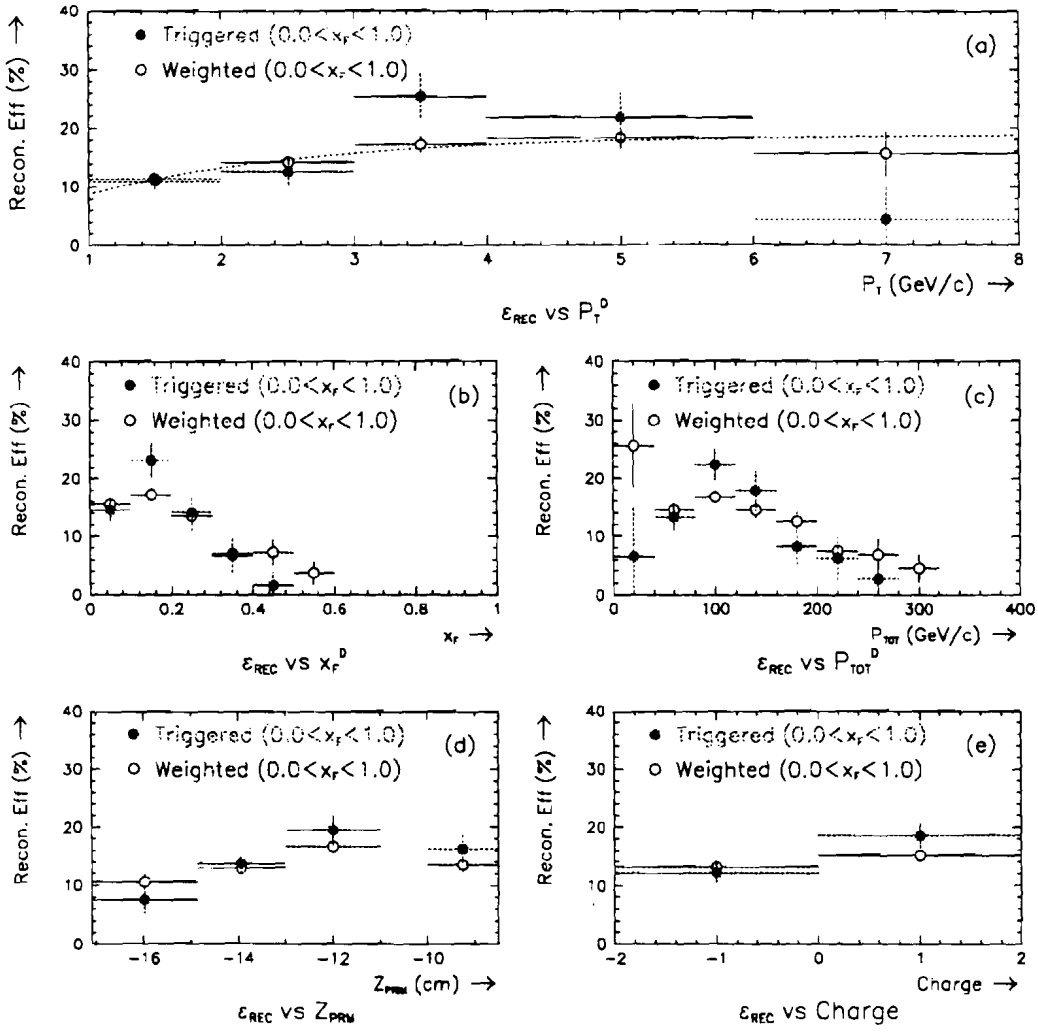

Figure 6.15 Reconstruction efficiency as a function of (a) p_T, (b) x_F, (c) p_{TOTAL}, (d) Z_{PRIM}, and (e) charge. All figures integtrate over the region $0.0 < x_F < 1.0$.The dotted curve in (a) is a fit to the weighted distribution.

this comparison, it should be clear that σ_R is a powerful discriminator for rejecting background events, with minimal loss of signal events. Also shown in Figure 6.16 is the comparison between the class of charm events which were formed from 2 and 3 track vertices. There is some indication that the 3 track vertices have better resolution than 2 track vertices, as one would expect, due to the additional track used in the vertex determination.

Systematic Uncertainty in the Reconstruction Efficiency

In order to estimate the systematic uncertainty in the reconstruction efficiency, two additional versions of the MC preprocessor[8] were prepared. One version introduced more hits than the default version, and the other reduced the hit multiplicity. The changes in the hit multiplicities were based upon the variations in multiplicity observed in the data. The effect of changing the event multiplicity propagates into producing more tracks, more event confusion, and therefore results in a degradation of the track and vertex resolution. Therefore, we expect that increasing the event multiplicity decreases the reconstruction efficiency, and lowering the event multiplicity results in an increase in the reconstruction efficiency. Based on these studies, we found variations in the reconstruction efficiency at the level of $\sim \pm 10\%$ with respect to the default preprocessor. We therefore assign a systematic uncertainty of $\pm 10\%$ to the reconstruction efficiencies due to the detector simulation.

Summary of Reconstruction Efficiency

We now summarize in tabular form the reconstruction efficiency which will be used for correcting the observed spectrum of $D^{\pm}$ mesons. Table 6.3 gives the estimated efficiencies, integrated over the region $-.2 < x_F < 1.0$. Also indicated are the statistical and systematic errors. This table corresponds to the fitted results from Figure 6.14(a), evaluated at the center of each bin. Similarly, Table 6.4 provides the reconstruction efficiency integrated over the region $0.0 < x_F < 1.0$. These numbers reflect the fitted results from Figure 6.15(a).

[8] The MC preprocessor was the software package which introduced the detector effects into the generated events i.e. noise, efficiencies, etc.

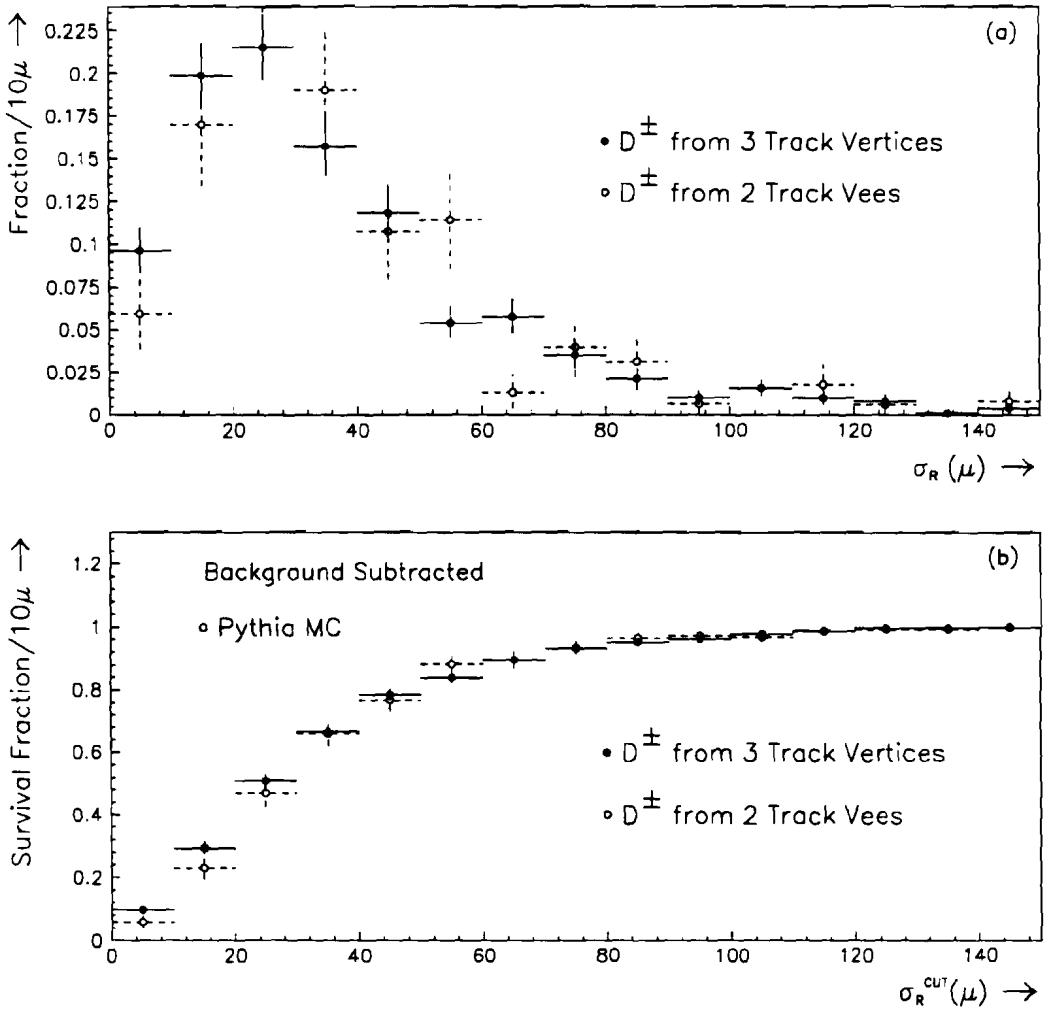

Figure 6.16 (a) The distribution in σ_R for reconstructed $D^{\pm}$ mesons, and (b) the integrated fraction of events surviving a particular σ_R cut, as a function of σ_R^{CUT}.

Table 6.3 $D^{\pm}$ Reconstruction Efficiency integrated over $-.2 < x_F < 1.0$

p_T bin (GeV/c)	Recon Eff (%)	Stat. Err (%)	Syst. Error (%)
1-2	8.9	0.6	0.9
2-3	14.6	0.9	1.5
3-4	16.4	1.2	1.6
4-6	17.4	1.5	1.7
6-8	17.6	3.7	1.8

Table 6.4 $D^{\pm}$ Reconstruction Efficiency integrated over $0.0 < x_F < 1.0$

p_T bin (GeV/c)	Recon Eff (%)	Stat. Err (%)	Syst. Error (%)
1-2	11.3	0.8	1.1
2-3	14.6	1.1	1.5
3-4	16.5	1.5	1.7
4-6	17.8	1.8	1.8
6-8	18.5	4.1	1.9

6.5 Charm Signals in the 1990 Data

6.5.1 $D^{\pm} \rightarrow K^{\mp}\pi^{\pm}\pi^{\pm}$

In this section we show the signals obtained in the 1990 data. All analysis cuts have been applied, including trigger type and target fiducial cuts (see Figure 4.1). First, we show in Figure 6.17 the $K\pi\pi$ invariant mass spectrum for all events in the range $-0.2 < x_F < 1.0$ and $p_T > 1.0$ GeV. A clear signal at ~1.869 GeV is observed which contains about 110 events. In forming the $D^{\pm}$ invariant mass, the kaon is always assigned to be the particle which has a charge opposite to that of the

parent[9]. Based on the resolution observed in the MC, the signal region was defined to be from 1.80 to 1.94 GeV.

We now split the data into various p_T bins in the range from 1-8 GeV/c. These data are shown in Figure 6.18. The ability to observe D mesons with a p_T as high as ~6-8 GeV/c is a unique feature which E706 exhibits, due to the high p_T trigger. Other experiments devoted to charm generally have low bias triggers, and are therefore dominated by the low p_T events.

Based on these data, we make an estimate of the number of events in each p_T bin. In each bin, the statistical error was found to dominate any systematic errors resulting from various assumptions of the background shape. Therefore, we only show the statistical errors for each p_T bin. The numbers of events are given in Table 6.5 below.

Table 6.5 Estimated number of $D^{\pm}$ Data Events in the range $-.2 < x_F < 1.0$

p_T bin (GeV/c)	Number of Events	Stat. Err
1-2	42	12
2-3	45	9
3-4	17	5
4-6	6	3
6-8	2	1.4
Total 1-8	112	17

[9] In the $D \rightarrow K\pi\pi$ decay, the K must have opposite charge to the parent D meson.

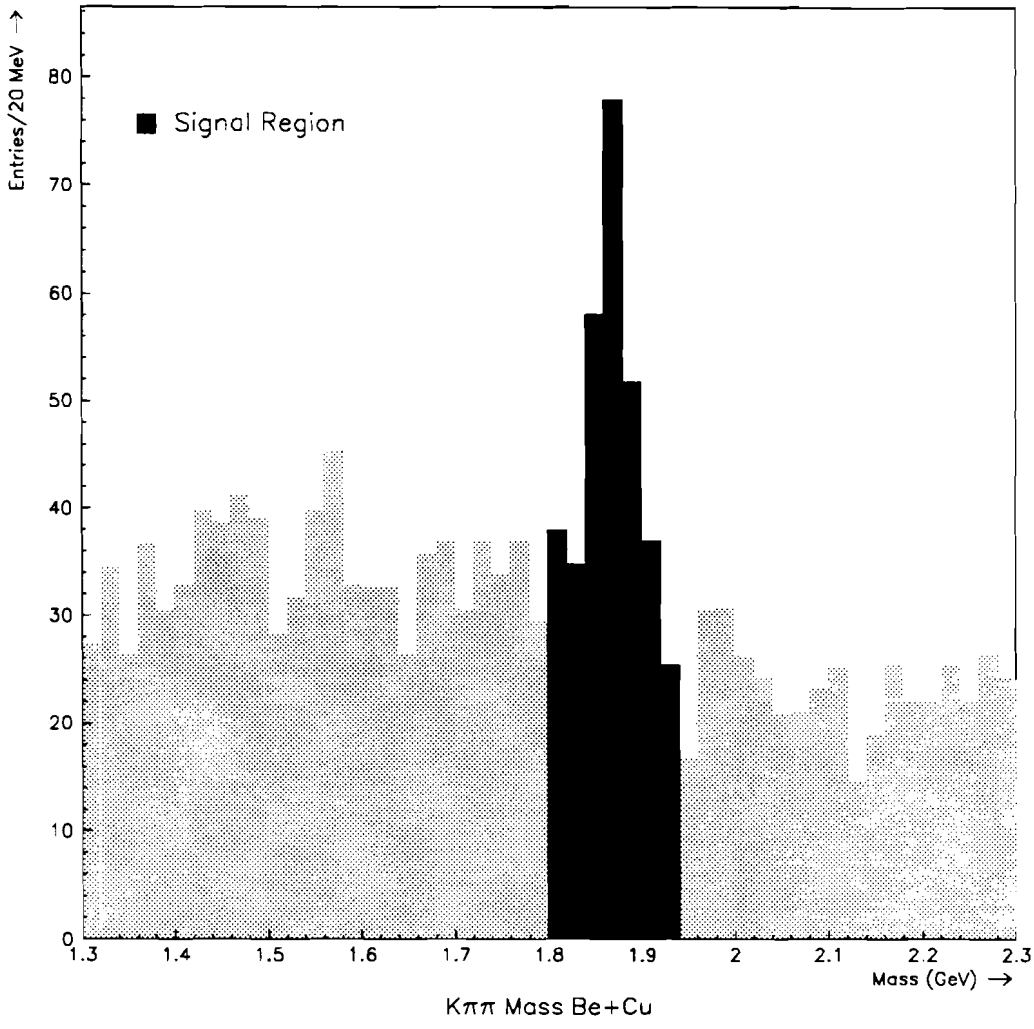

Figure 6.17 The $K\pi\pi$ invariant mass spectrum with all reconstruction cuts applied for the full 1990 data sample. The spectrum covers the range $p_T > 1$ GeV/c and $-0.2 < x_F < 1.0$.

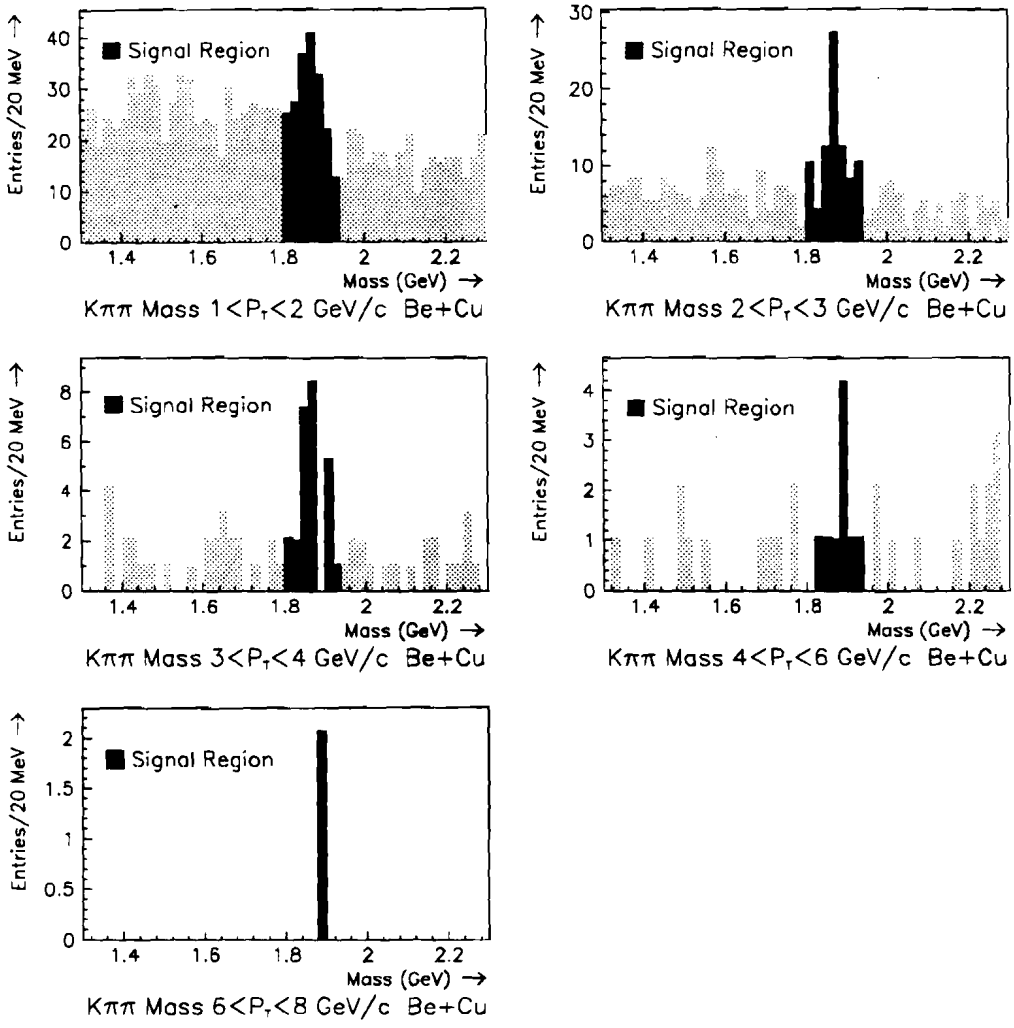

Figure 6.18 The $K\pi\pi$ invariant mass spectrum in several p_T bins. The p_T bins are, (a) 1-2 GeV/c, (b) 2-3 GeV/c, (c) 3-4 GeV/c, (d) 4-6 GeV/c, and (e) 6-8 GeV/c. The events are integrated over the x_F region from -0.2 to 1.0.

In order to compare our results to other available data, we provide the analogous figures, except we restrict our x_F range from 0.0 to 1.0. Figure 6.19 and Figure 6.20 show the $K\pi\pi$ invariant mass spectra for the full data sample and in various p_T bins, respectively. Shown in Table 6.6 are the estimates for the number of entries in each p_T bin, along with the statistical errors.

Table 6.6 Estimated number of $D^{\pm}$ Data Events in the range $0.0 < x_F < 1.0$

p_T bin (GeV/c)	Number of Events	Stat. Err
1-2	41	11
2-3	31	8
3-4	13	5
4-6	5	3
6-8	0	0
Total 1-8	90	15

These data integrate over all three triggers used in this analysis. That is, the events from the SLHI, GLHI, and TWO GAMMA make up the signals which were shown. It is worthwhile to show the signals which were obtained for each of the triggers independently. In addition to showing the invariant mass plots for each of these three triggers, we also plot the overlap between the SLHI and GLHI triggers. These data are shown in Figure 6.21(a-d). The mass plots shown in the figure are the signals obtained in the SLHI, GLHI, TWO GAMMA, and SLHI⊗GLHI, respectively. As one expects, there is a strong overlap between the SLHI and GLHI. For the MC events satisfying the software trigger simulation, we found that $\sim$ 50% satisfied the SLHI, $\sim$55% satsified the GLHI, $\sim$25% satisfied the TWO GAMMA, and the overlap between the SLHI and GLHI was $\sim$30%. Within the statistical errors, the distribution of events among the triggers is in reasonable agreement between the MC and data.

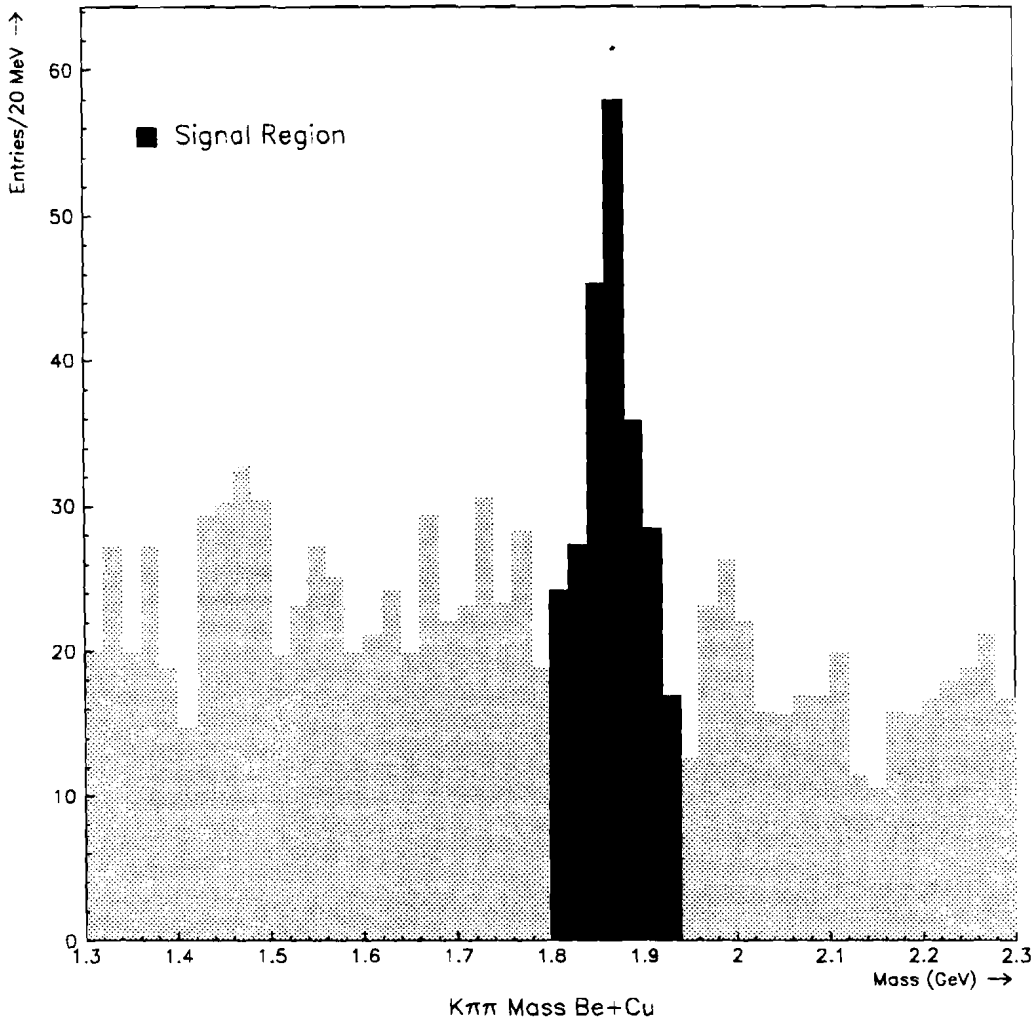

Figure 6.19 The $K\pi\pi$ invariant mass spectrum with all reconstruction cuts applied for the full 1990 data sample. The spectrum covers the range $p_T > 1$ GeV/c and $0.0 < x_F < 1.0$.

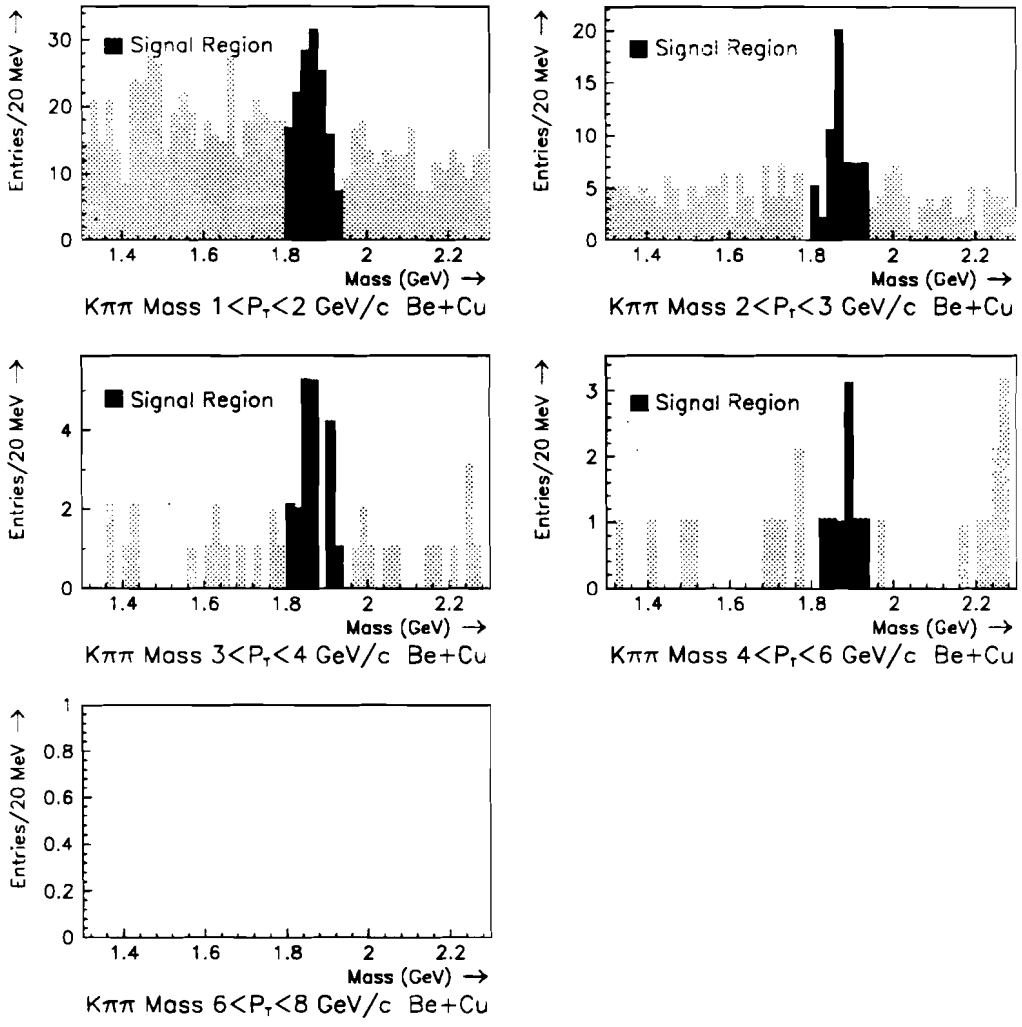

Figure 6.20 The $K\pi\pi$ invariant mass spectrum in several p_T bins. The p_T bins are, (a) 1-2 GeV/c, (b) 2-3 GeV/c, (c) 3-4 GeV/c, (d) 4-6 GeV/c, and (e) 6-8 GeV/c. The events are integrated over the x_F region from 0.0 to 1.0.

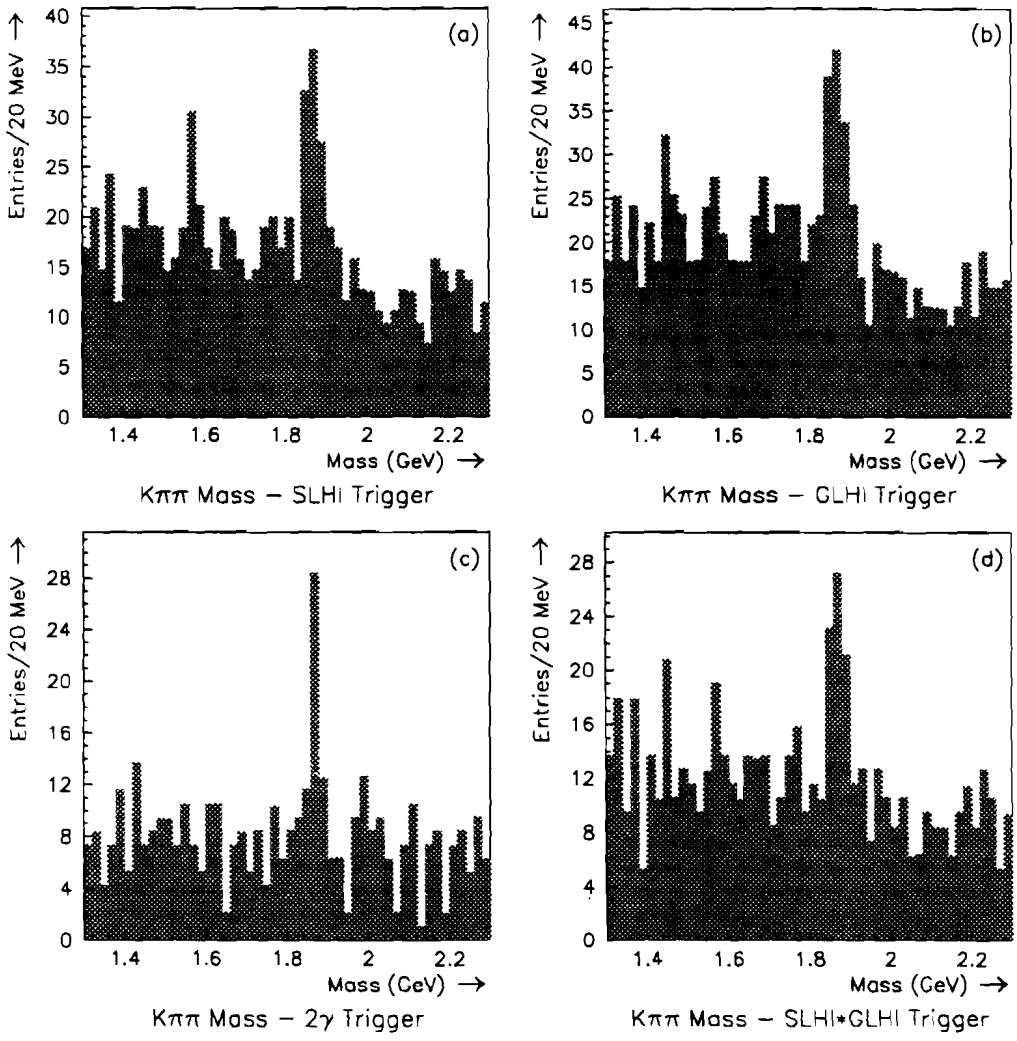

Figure 6.21 $K\pi\pi$ invariant mass distributions for (a) SLHI trigger, (b) GLHI trigger, (c) TWO GAMMA trigger, and (d) SLHI⊗GLHI overlap.

To illustrate the beauty (no pun intended) of the charm events observed in the data, we present an event display of a typical high p_T charm event. In Figure 6.22 and Figure 6.23, are shown the X and Y view projections of such an event. The light colored tracks which are emerging from $Z \sim -11.3$ cm are the primary vertex tracks, and those eminating from $Z \sim -9.8$ cm are the decay tracks of the $D^{\pm}$ meson. The five shaded figures from left to right are two copper targets, 2 beryllium targets, and the first silicon detector. The $D^{\pm}$ in this event has a transverse momentum of $\sim$4.1 GeV/c.

Although it is the $D^{\pm}$ charm meson which is used for this analysis, it is reasonable to ask whether other charm signals were observed as well. In the next section, we present some of the other charm signals which were observed in the 1990 Data.

6.5.2 D^0 *and* $D^{*\pm}$ *Decays*

In addition to observing the decays of the charged D meson, we also observed the decays of the neutral D meson. Shown in Figure 6.24 is the $K^-\pi^+$ and $K^+\pi^-$ invariant mass spectrum for 2 prong vertices in the 1990 data. The cuts used are very similar to those used for the $D^{\pm}$ sample. The combinatoric background is seen to be larger for the D^0 than for the $D^{\pm}$ signal. This is a consequence of the shorter lifetime of the D^0 coupled with the increasing combinatoric background as a function of decay distance. In addition, the combinatoric background to 2 track vertices is larger than for 3 track vertices. In any case, we observe a clear enhancement at the mass value associated with the D^0 charmed meson.

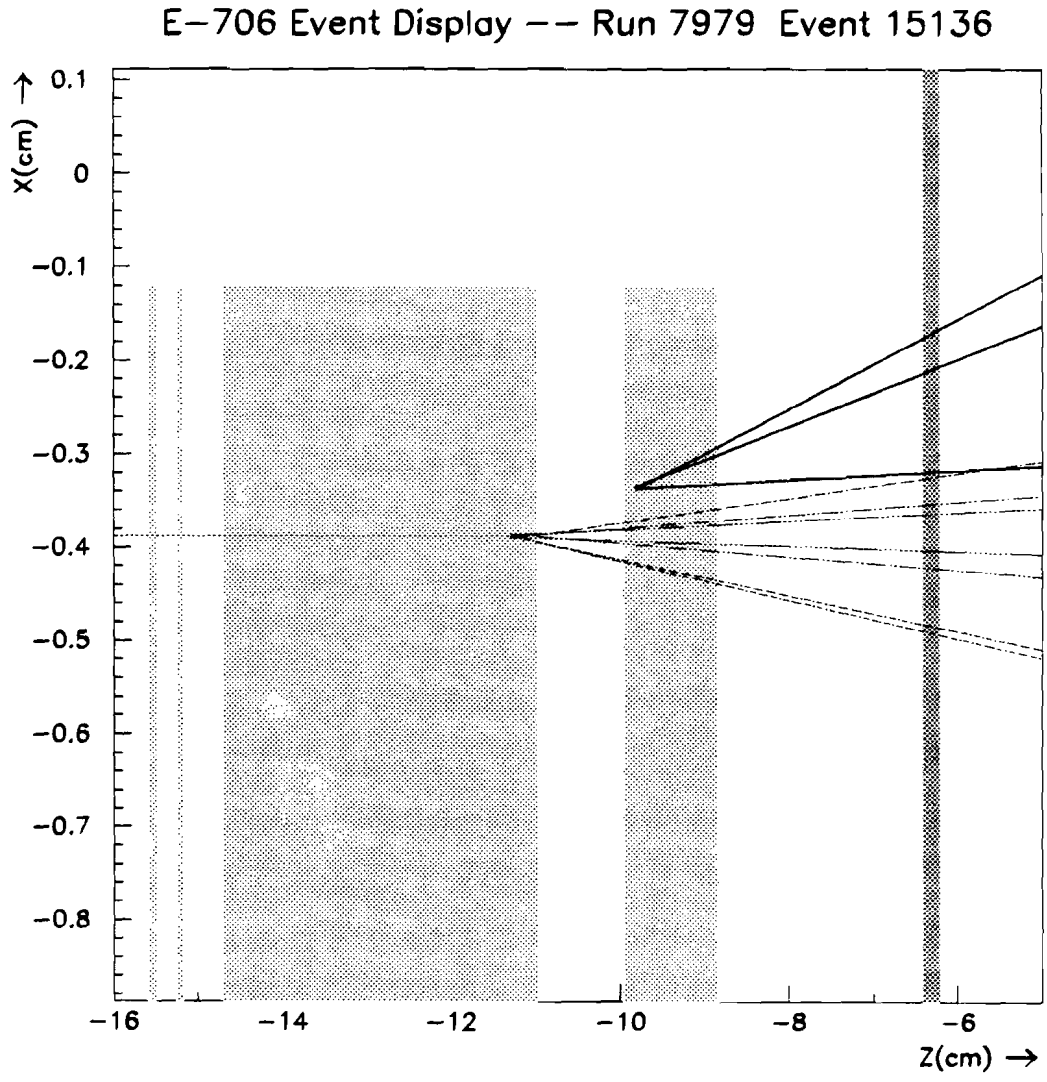

Figure 6.22 Event display in the X view of a high p_T $D^{\pm}$ meson decaying downstream of the primary vertex. The light colored tracks are primary vertex tracks, and the dark tracks are the decay tracks from the charmed meson.

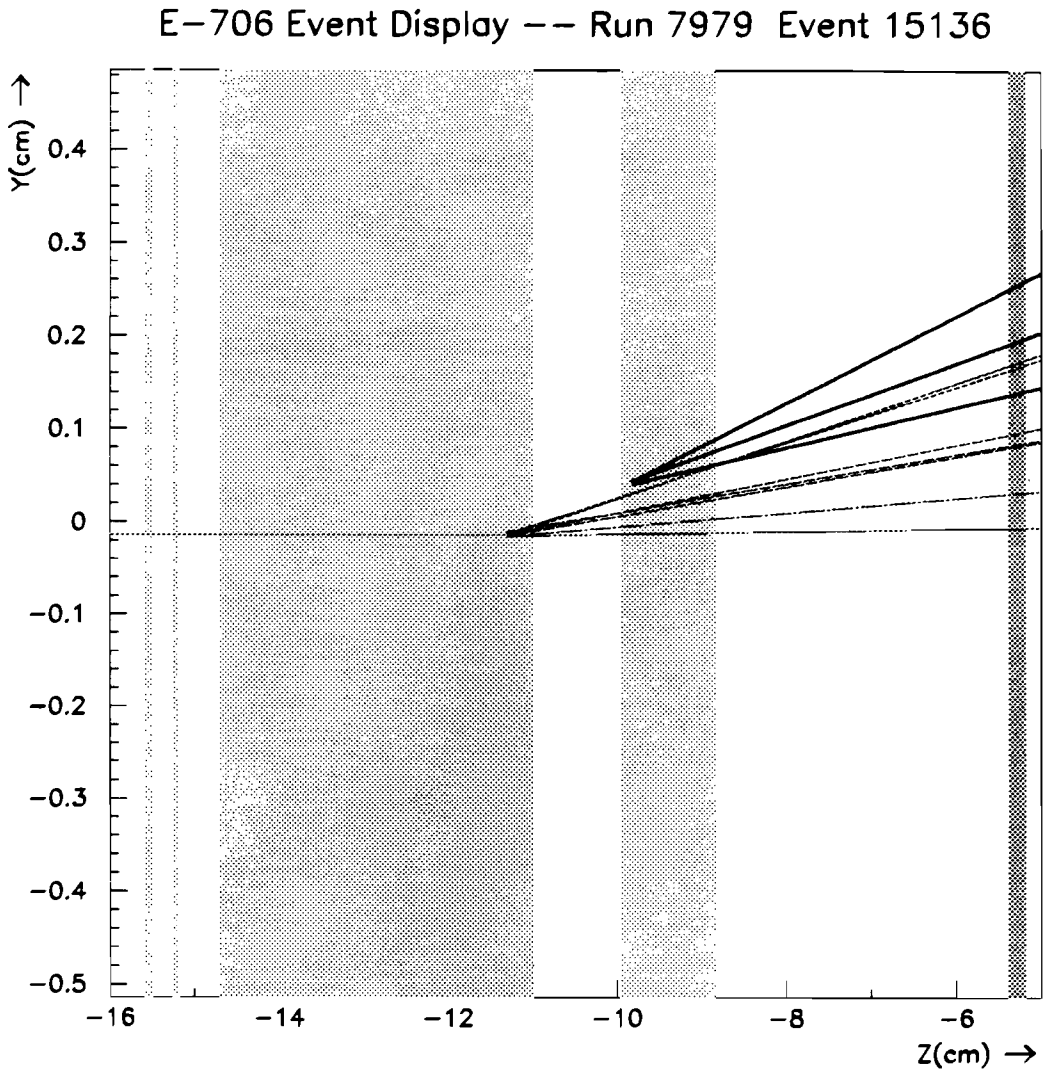

Figure 6.23 Event display in the Y view of a high p_T $D^{\pm}$ meson decaying downstream of the primary vertex. The light colored tracks are primary vertex tracks, and the dark tracks are the decay tracks from the charmed meson.

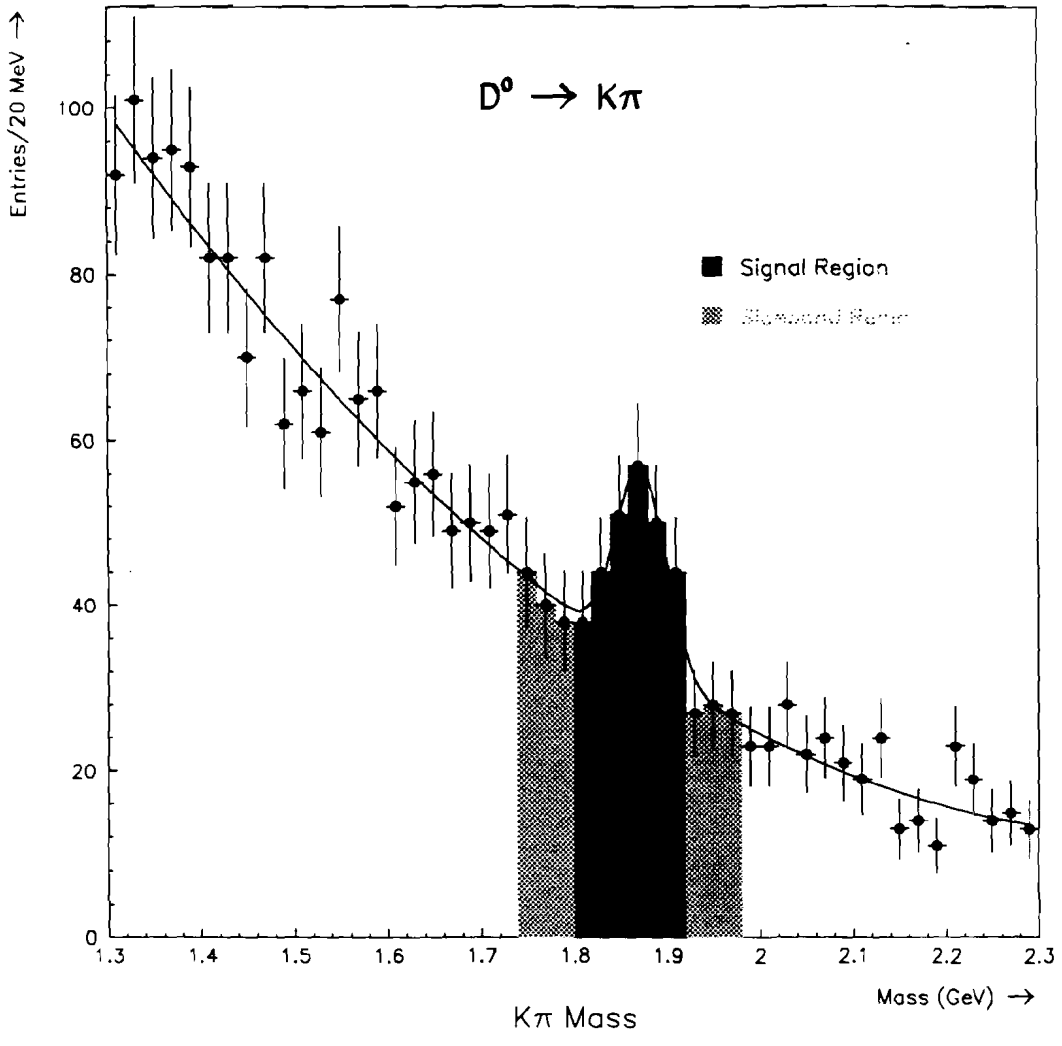

Figure 6.24 $K^-\pi^+$ and $K^+\pi^-$ invariant mass distribution for 2 track secondary vertices in the 1990 data.

Since a substantial fraction of D^0's have previously been observed to come from the decay of the excited charm state $D^{*\pm}$, we can look for the signature of these states in our data. The common procedure is to take advantage of the kinematics of the $D^{*\pm} \rightarrow D^0\pi_s^{\pm}$ decay[10], in which the available CM energy is very small. In other words, since the D^0 (1865 MeV) and the $\pi^{\pm}$ (140 MeV) account for nearly all of the $D^{*\pm}$ (2010 MeV) mass, there is very little energy available to split the D^0 and $\pi_s^{\pm}$ apart. This is easily seen when writing the invariant mass formula,

$$M^2_{D^{*\pm}} \simeq M^2_{D^0} + M^2_{\pi_s} + 2 * E_{\pi_s} * E_{D^0} * (1 - \cos\theta) \qquad 6.18$$

where, θ is the opening angle between the D^0 and the $\pi_s^{\pm}$. Since the first two terms on the right hand side are nearly equal to the left hand side, the third term on the right is quite small. Therefore, the topological signature for the $D^{*\pm}$ decay is a displaced D^0 vertex, along with a soft $\pi^{\pm}$ which travels almost collinearly with the reconstructed D^0 meson i.e. $\theta \sim 0$. Since the $D^{*\pm}$ decays immediately, i.e. at the primary vertex, the soft $\pi^{\pm}$ meson eminates from the primary vertex, whereas the D^0 travels some distance before it decays. The signature of this decay is realized when making a plot of the $K\pi\pi_s - K\pi$ mass difference, where we are looking for the D^0 in the decay mode $D^0 \rightarrow K\pi$. If the three tracks involved are from the decay $D^{*\pm} \rightarrow D^0\pi^{\pm}$, then the plot of this difference exhibits a narrow peak at $\sim$ 145 MeV. It is narrow because the error in the mass difference is essentially equal to the error in the momentum measurement of a soft pion[11], which is very precise (see Figure 3.13). In addition to the peak being very narrow, it is also near the lower edge of the available phase space. Therefore, not only does one have a very narrow peak, but the background is low as well. Without further ado, we show in

---

[10] Here, the subscript *s* is used to indicate that the pion is a generally a low momentum (soft) pion.

[11] The error from the K and π momentum measurement cancels out in the difference.

Figure 6.25(a) the mass difference plot for the cases when the $K\pi$ invariant mass is in the D^0 mass region, and when it is in the sidebands. A narrow peak at $\sim$ 145 MeV is observed for the case where the $K\pi$ formed a D^0, but no such peak is observed when the $K\pi$ invariant mass falls in the sidebands (see Figure 6.24 for the signal and sideband definitions). In Figure 6.25(b) is the sideband subtracted plot of the mass difference. The clean peak at $\sim$145 MeV is the signature of the $D^{*\pm} \rightarrow D^0\pi^{\pm}$ decay.

From Figure 6.24, we estimate $\sim$ 80 D^0 events in the signal region. In Figure 6.25, we find about 28 events in which the D^0 comes from a $D^{*\pm}$. Therfore, one finds that roughly 35% of D^0 mesons in the data sample come from $D^{*\pm}$ decays. This is only a raw number, which would need to be corrected for various losses in order to quote a physical measurement.

Since the physics analysis is based only upon the $D^{\pm}$ signals, we shall not spend any more time on the D^0 and D^* signals. We now turn to a discussion of the integrated luminosity.

6.6 Integrated Luminosity

As mentioned earlier, the luminosity is extracted from the scaler information and the target parameters. In general, each octant of the EMLAC had slightly different *live times*, and therefore, the LTB varies slightly from octant to octant. For this analysis, it will suffice to obtain a single number which represents the integrated luminosity for the entire 1990 run. Table 6.7 shows the integrated luminosity which E706 recieved during the 1990 run.

Table 6.7 Integrated Luminosity for the 1990 run

Beam/Target	Energy (GeV)	Number of Events	Sensitivity (events/pb)
π^-Be	515	$\sim$16 M	8.9
π^-Cu	515	$\sim$ 3 M	1.4

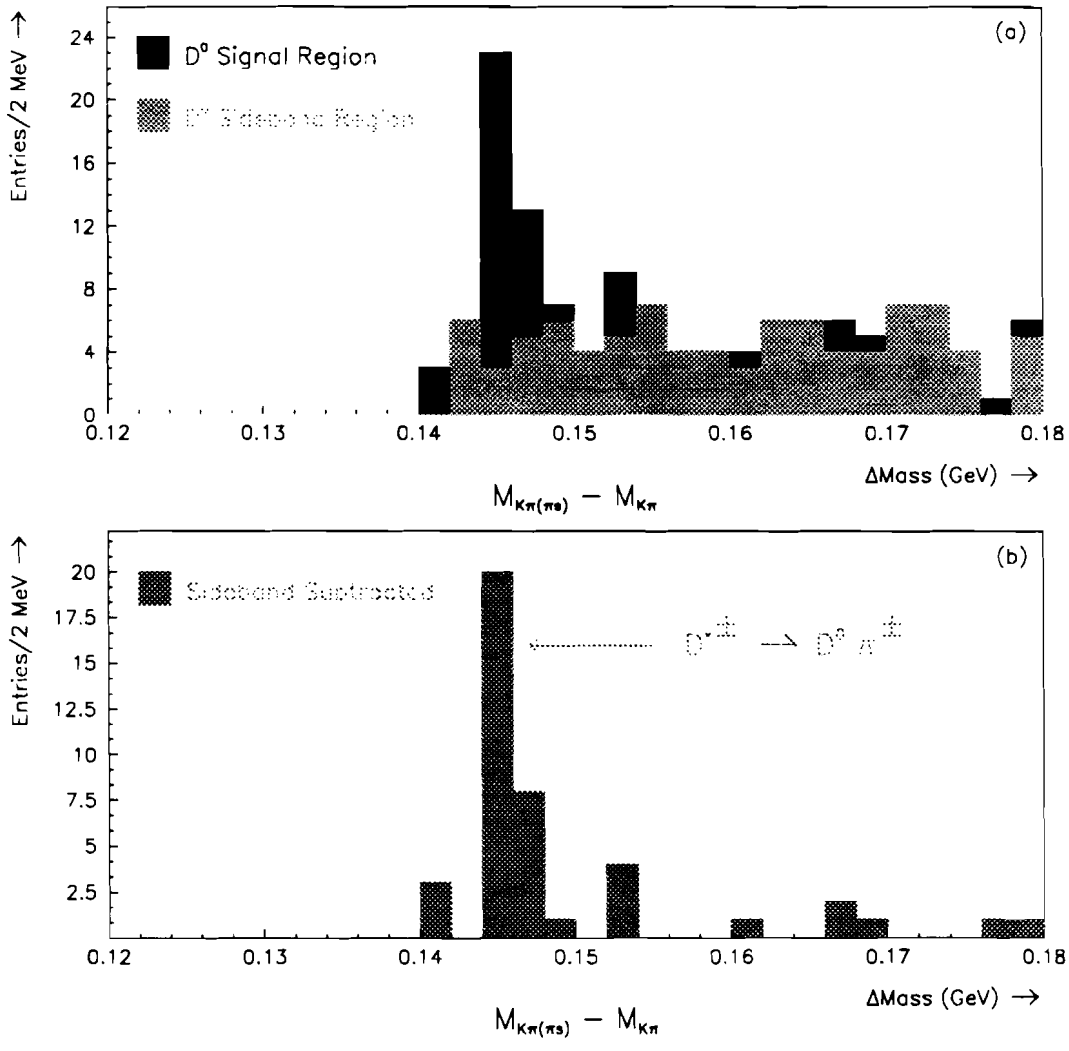

Figure 6.25 Mass difference $K\pi\pi_s - K\pi$, for $K\pi$ events in the signal and sideband regions of the D^0. Here, π_s refers to the soft pion which emerges from the $D^{*\pm}$ decay, $(D^{*\pm} \rightarrow D^0\pi_s)$.

As discussed in Chapter 4, the target was not centered on 0.0, which resulted in some fraction of the LTB to miss the target. Since the experimental scalers include all triggerable beam particles, a correction was added to account for the fraction of triggerable beam particles which were not hitting the target. This estimate was obtained by using the interactions which occured in the silicon strip detectors. Due to the relatively large transverse size of the SSD wafers (see Figure 2.3), they intercepted nearly all of the triggerable beam particles. In this case, one simply measures the fraction of vertices in the silicon chambers which satisfy the transverse fiducial cut (see 1) with respect to the total. Based on this study[90, 24], it was found that $\sim$ 73% of the triggerable beam particles passed the transverse fiducial target cut. We therefore applied a weight of 1.37 to the data events, in order to account for the loss of triggerable beam particles. The error in this correction was determined by performing the same analysis on both the upstream (beam) SSDs, and the downstream SSDs independently. The two results were found to be within $\pm$2% of each other, which gives a scale of the uncertainty in this correction.

The final correction which was applied was a correction to account for beam absorption in the target. Based upon the absorption lengths of beryllium and copper, one can calculate the fraction of beam which interacts in a given length of material[12]. Due to the absorption of beam along the length of the target, the amount of beam decreases monotonically as we move from upstream to downstream in the target. We take the approach of applying an average correction for the copper and beryllium pieces separately[24]. These corrections are shown in Table 6.8.

We now have all of the pieces needed to calculate a cross section. We have the number of events, their efficiency, and the corresponding luminosity. In the next chapter, we present the cross section results.

---

[12] The number of beam particles remaining after traversing a series of targets is given by, $N(z) = N(0) * \prod_{i=1}^{N_T} \exp(-\delta z_i/\lambda_i)$, where N_T is the number of targets, δz_i is the thickness of each target, and λ_i is the corresponding absorption length for each target.

Table 6.8 Average π^- Beam Absorption Corrections for the 1990 Data

Target	Correction
π^-Be	1.054
π^-Cu	1.007

Chapter 7 Results and Conclusions

7.1 Overview

In this chapter, we present the final physics results related to the charm sample. In the last chapter, we presented the signals, their efficiencies and the integrated luminosity. In this chapter, we present the differential cross sections in p_T, as well as the integrated result. The results shall be compared to the NLO theoretical predictions and the Pythia MC. The data shall also be compared to other recent data on charm hadroproduction. In the last section, we investigate the dependence of the charm cross section on the number of nucleons in the nucleus.

7.2 Differential Cross Section

In this section, we shall be presenting the invariant $D^{\pm}$ differential cross section per nucleon, integrated over rapidity, and averaged over azimuth. Mathematically, this may be expressed as,

$$\frac{d^2\sigma}{dp_T^2} = \frac{1}{2\pi p_T \Delta p_T} * \sigma_{D^{\pm}}(p_T) \qquad 7.1$$

where

$$\sigma_{D^{\pm}}(p_T) = \frac{1}{L} \times \frac{N(D^{\pm}(p_T))}{\epsilon(p_T)}. \qquad 7.2$$

is the cross section produced in a given p_T bin.

Table 7.1 Summary of cross section variables for $-0.2 < x_F < 1.0$

p_T bin (GeV/c)	Number of Events	Recon. Eff. (%)	Trigger Eff. (%)
1-2	42 ± 12	$8.9 \pm 0.6 \pm 0.3$	$0.0160 \pm 0.0018 \pm 0.0032$
2-3	45 ± 9	$14.6 \pm 0.9 \pm 1.5$	$0.0543 \pm 0.0077 \pm 0.011$
3-4	17 ± 5	$16.4 \pm 1.2 \pm 1.6$	$0.255 \pm 0.049 \pm 0.051$
4-6	6 ± 3	$17.4 \pm 1.5 \pm 1.7$	$1.61 \pm 0.35 \pm 0.32$
6-8	2 ± 1.4	$17.6 \pm 3.7 \pm 1.8$	$9.17 \pm 5.4 \pm 1.8$

Table 7.2 Summary of cross section variables for $0.0 < x_F < 1.0$

p_T bin (GeV/c)	Number of Events	Recon Eff (%)	Trigger Eff (%)
1-2	41 ± 10	$11.3 \pm 0.8 \pm 1.1$	$0.0160 \pm 0.0018 \pm 0.0032$
2-3	31 ± 8	$14.6 \pm 1.1 \pm 1.5$	$0.0543 \pm 0.0077 \pm 0.011$
3-4	13 ± 5	$16.5 \pm 1.5 \pm 1.7$	$0.255 \pm 0.049 \pm 0.051$
4-6	5 ± 3	$17.8 \pm 1.8 \pm 1.8$	$1.61 \pm 0.35 \pm 0.32$
6-8	-	-	-

The number of signal events and efficiencies for each p_T bin are summarized in Table 7.1 and Table 7.2 for the $x_F > -0.2$ and $x_F > 0$ samples respectively.

First we show in Figure 7.1 the $D^{\pm}$ cross section per nucleon as a function of the $D^{\pm}$ transverse momentum in the x_F range from -0.2 to 1.0. If the cross section is parametrized with a simple exponential fit,

$$\frac{d\sigma}{dp_T^2} \sim e^{-\beta * p_T} \qquad 7.3$$

we obtain $\beta = 2.59 \pm 0.13$ GeV^{-1}. The analogous plots are shown in Figure 7.2 where we have restricted the data to the positive x_F region only. Using the same

functional form for the differential cross section (7.3), we find $\beta = 2.57 \pm 0.14$ GeV^{-1}. The data are observed to have similar slopes, for both the positive and negative x_F regions.

The data points for Figure 7.1 and Figure 7.2 are provided in Table 7.3 and Table 7.4 respectively.

Table 7.3 $D^{\pm}$ Cross Section integrated over $-0.2 < x_F < 1.0$

p_T bin (GeV/c)	XS (μb/GeV^2)	Stat. Err (μb/GeV^2)	Syst. Error (μb/GeV^2)
1-2	0.46	0.13	0.12
2-3	5.3E-02	1.1E-02	1.5E-02
3-4	2.9E-03	0.9E-03	0.9E-03
4-6	5.1E-05	2.5E-05	1.5E-05
6-8	2.6E-06	1.8E-06	1.8E-06

Table 7.4 $D^{\pm}$ Cross Section integrated over $0.0 < x_F < 1.0$

p_T bin (GeV/c)	XS (μb/GeV^2)	Stat. Err (μb/GeV^2)	Syst. Error (μb/GeV^2)
1-2	0.36	0.09	0.08
2-3	3.6E-02	0.9E-02	0.8E-02
3-4	2.2E-03	0.9E-03	0.6E-03
4-6	4.1E-05	2.5E-05	1.1E-05
6-8	-	-	-

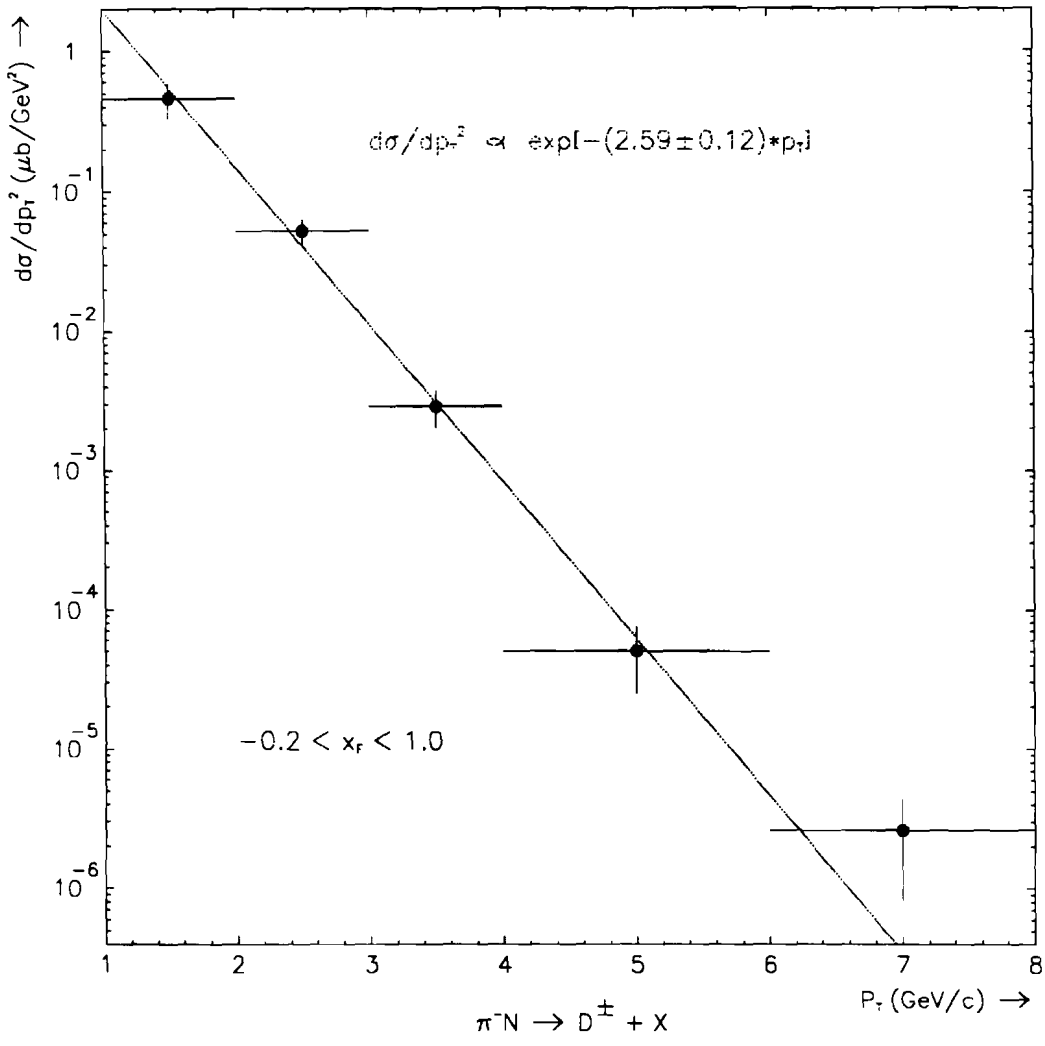

Figure 7.1 Inclusive cross section per nucleon for $D^{\pm}$ production in 515 GeV/c π^--Nucleon collisions, as a function of p_T, and integrated over the region $-0.2 < x_F < 1.0$.

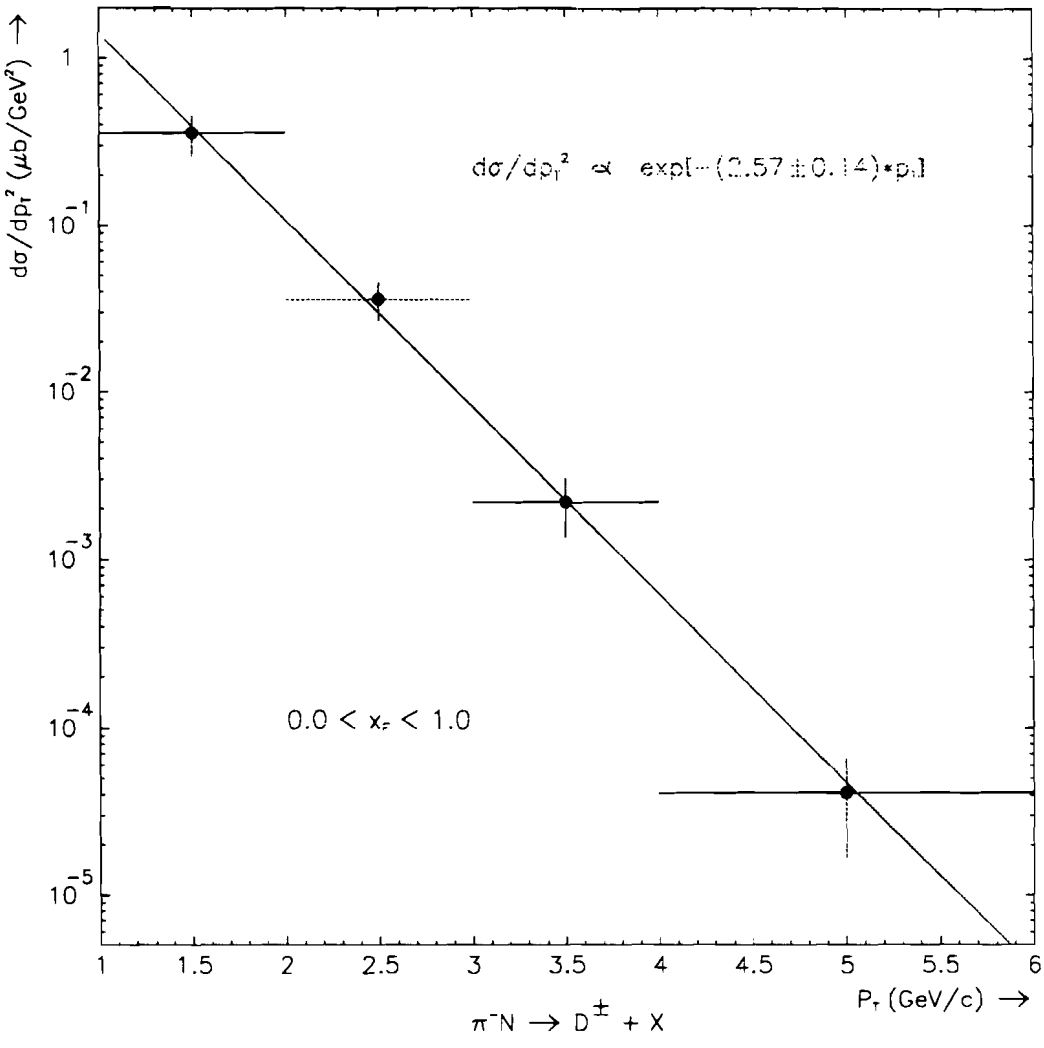

Figure 7.2 Inclusive cross section per nucleon for $D^{\pm}$ production in 515 GeV/c π^--Nucleon collisions, as a function of p_T, and integrated over the region $0.0 < x_F < 1.0$.

7.3 Comparison of Differential Cross Section with NLO

We now wish to compare our differential results to the NLO predictions. The NLO predictions include the LO $2 \rightarrow 2$ and NLO $2 \rightarrow 3$ matrix elements, in which a pair of charm quarks are among the partons in the final state (see Figure 1.5). The momentum distribution of the partons inside the colliding hadrons are described by the SMRS set 2 PDF[1] for the pion[37], and the HMRSB PDF for the nucleon[38]. In order to compare the NLO result with data, the final state charm quarks must be fragmented into stable charmed hadrons. This procedure utilizes the Peterson fragmentation function[45] to account for the hadronization process. The NLO calculations are also supplemented with an intrinsic k_T for the incoming partons. Previous measurements from E769 and WA82 have indicated that a high value of k_T is needed in order to bring the NLO predictions into agreement with the data[47]. We therefore compare our data with the NLO calculations, using several values of k_T. These values are input as the mean k_T^2 ($< k_T^2 >$) which is equal to the square of the gaussian width of the k_T smearing. The values used are $< k_T^2 > = 0.5$, 1.0, 2.0, and 3.0 GeV^2. These comparisons are shown in Figure 7.3(a-d). The data are seen to be in reasonable agreement with the NLO prediction, when they are supplemented with a $< k_T^2 > \sim 1$ GeV^2.

7.4 Comparison of Differential Cross Section with Pythia (LUND)

In this section, we compare our results to the Pythia/LUND MC. The MC utilizes a $k_T = 1.05$ GeV, as was discussed in Chapters 5 and 6. In Figure 7.4(a), we compare our full x_F sample, with the Pythia MC covering the range $-1.0 < x_F < 1.0$. Also shown in Figure 7.4(a) is the Pythia prediction with x_F restricted to the positive region. The shape of the MC distribution does not appear to change significantly between the forward and backward regions. This is consistent with what we observed in the data (see Figure 7.1 and Figure 7.2). In Figure 7.4(b), we compare the Pythia MC with the data, both being restricted to the region $x_F > 0$. In both cases, the Pythia MC is in reasonable agreement with the data.

---

[1] PDF is short for *parton distribution function.*

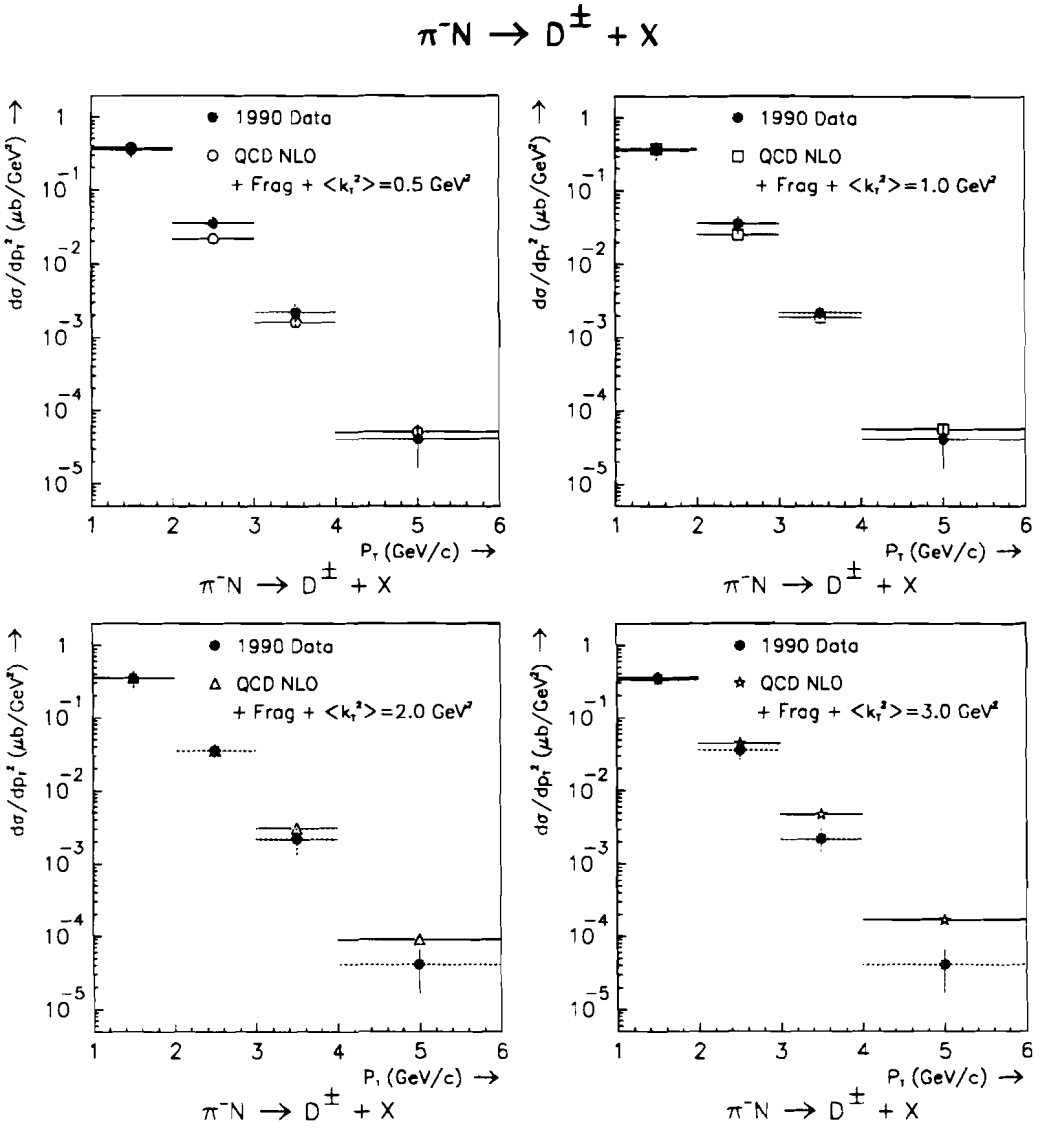

Figure 7.3 Comparison of the E706 $D^{\pm}$ cross section with the NLO predictions using the values of $< k_T^2 >$ equal to, (a) 0.5 GeV^2, (b) 1.0 GeV^2, (c) 2.0 GeV^2, and (d) 3.0 GeV^2. The NLO calculations use SMRS set 2 PDF for the pion, and HMRSB PDF for the nucleon, and the Peterson fragmentation function with $\epsilon_c = 0.06$ for the fragmentation of the charm quarks.

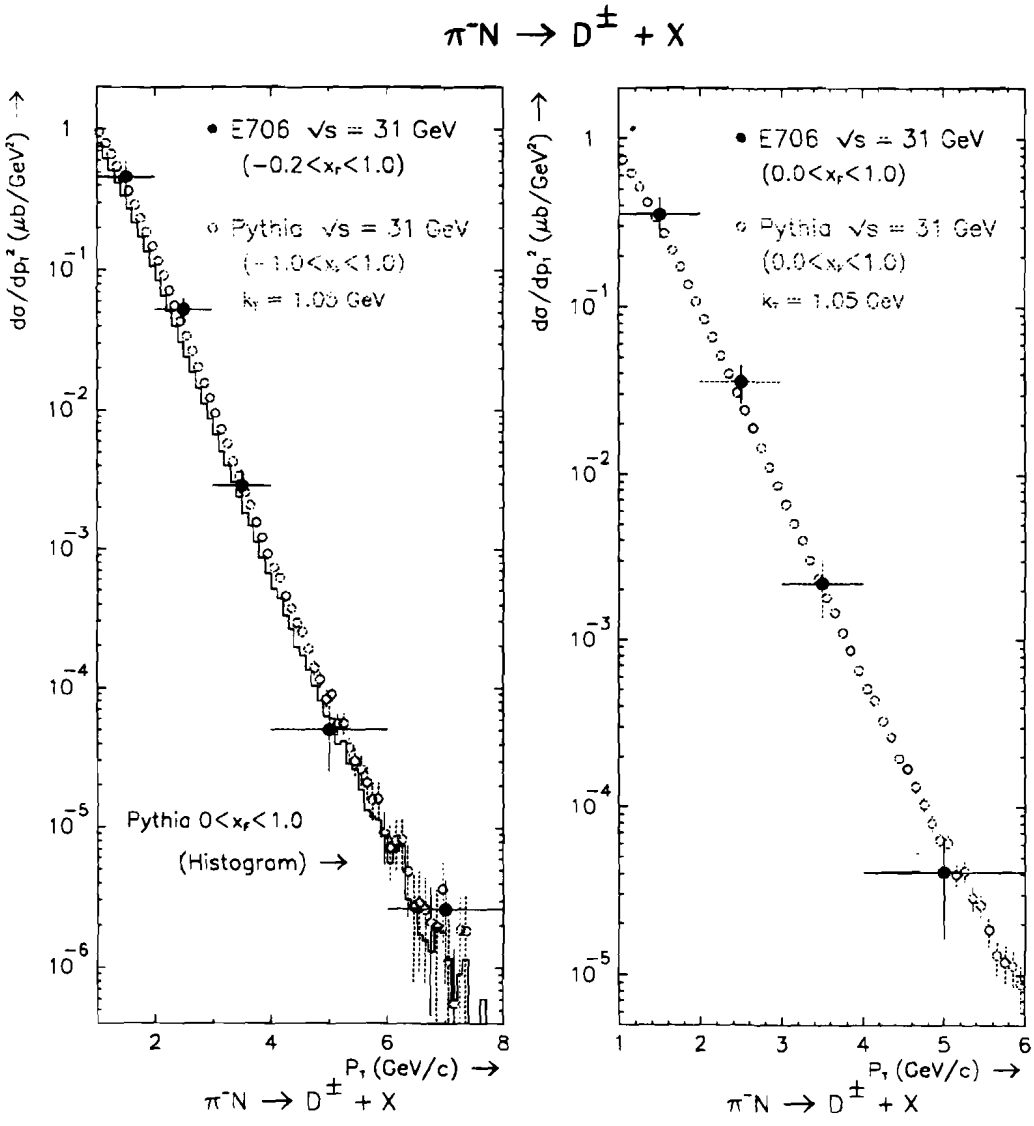

Figure 7.4 Comparison of the Pythia MC with the E706 data, where the data are integrated over (a) $-0.2 < x_F < 1.0$, and (b) $0.0 < x_F < 1.0$.

7.5 Comparison with Previous Measurements

We now compare the E706 data ($\sqrt{s}$ = 31 GeV), with the E769 data[84] ($\sqrt{s}$ = 22 GeV). These data are shown in Figure 7.5, where we overlay the two data samples. In Figure 7.5(a), we utilize the full E706 data sample ($-0.2 < x_F < 1.0$), and in Figure 7.5(b), we restrict our data to the positive x_F hemisphere. One can appreciate from this figure the large coverage in p_T which the E706 data span. One would expect that the E706 data are slightly stiffer than the E769 data, due to the larger CM energy. The E769 data can be fit to the same exponential form as in 7.3, which is found to give $\beta = 2.66 \pm 0.12$ GeV^{-1}. The E706 data is observed to have a similar slope to that which was reported by E769. Based on the Pythia MC, one would expect the E706 data to be slightly stiffer than the E769 data, due to the higher CM energy. From the Pythia MC, the expected difference in the value of β was found to be 0.1 i.e. the 515 GeV/c beam gave a value of β that was 0.1 higher than the 250 GeV/c beam. Although our data are consistent with this difference, the statistical errors are also about the same size as the measured difference. Within the error of the measurement, the data appear to be in reasonable agreement with what one would expect based upon the published measurements from E769.

7.6 Total $D^{\pm}$ Cross Section

In this section, we make an estimate of the total $D^{\pm}$ cross section. In order to obtain the total $D^{\pm}$ cross section, we will need to account for the cross section which our experiment is unable to observe. In particular, we will need to have an estimate of the fraction of the $D^{\pm}$ cross section which is below a p_T of 1 GeV/c. Since our data agreed fairly well with the Pythia MC, we shall extrapolate our data using the Pythia spectrum. From the generated MC spectrum, it is found that we need to apply an extrapolation of 2.08 ± 0.1 to account for the cross section below a p_T of 1.0 GeV/c. In order to get the total cross section, we simply integrate over the differential distribution. In general, this integral may be written as,

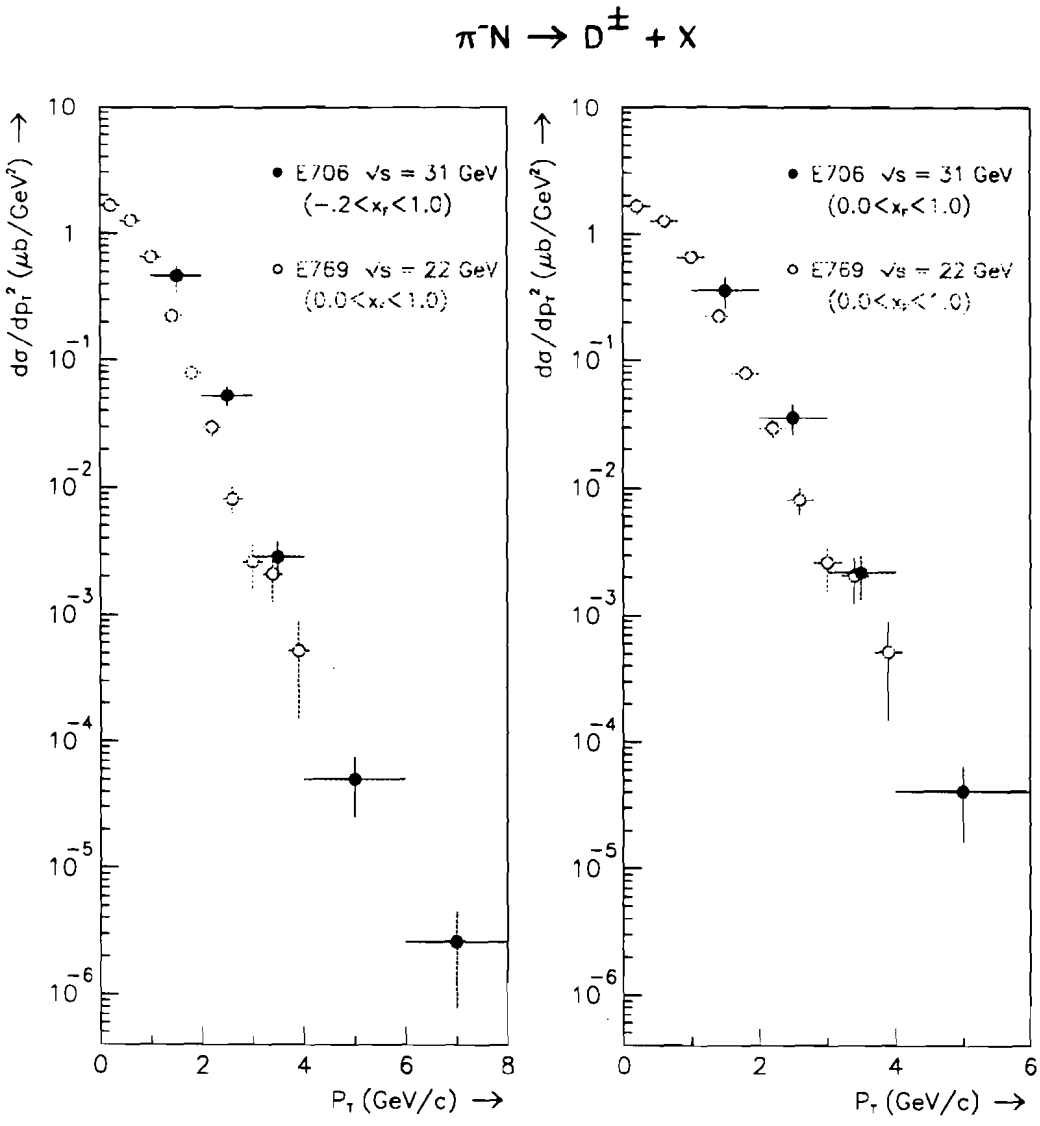

Figure 7.5 Comparison of the E706 data with the E769 data. The E706 data covers the x_F range from (a) -0.2 to 1.0, and (b) 0.0 to 1.0. The E769 data cover only the positive x_F region.

$$\sigma = \int_0^{\infty} \frac{d\sigma}{dp_T^2} 2\pi p_T dp_T, \qquad 7.4$$

where $d\sigma/dp_T^2$ is the cross section as shown in Figure 7.1 (Figure 7.2). Since we have a small number of data points, we may rewrite 7.4 as,

$$\sigma = 2\pi \sum_i^N \frac{\Delta\sigma}{\Delta p_T^2} p_T \Delta p_T. \qquad 7.5$$

In 7.5, Δp_T is the width of the p_T bin, and p_T is the transverse momentum, evaluated at the center of each bin. The sum runs over all p_T bins in the distribution.

We are now in a position to calculate the $D^{\pm}$ total cross section in the range $p_T > 1$ GeV/c, and $-0.2 < x_F < 1.0$. Using Table 7.3, and 7.5, we estimate the $D^{\pm}$ cross section to be,

$$\sigma(D^{\pm}) = 5.2 \pm 1.3(\text{stat}) \pm 1.2(\text{syst})\ \mu b \qquad p_T > 1\ \text{GeV/c},\ x_F > -.2 \qquad 7.6$$

If we extrapolate our data to account for the cross section below $p_T = 1.0$ GeV, we obtain an integrated result covering the full p_T range and $x_F > -0.2$. In this kinematic region, we find an integrated $D^{\pm}$ cross section,

$$\sigma(D^{\pm}) = 10.9 \pm 2.6(\text{stat}) \pm 2.4(\text{syst})\ \mu b \qquad x_F > -.2\ . \qquad 7.7$$

We may take this one step further, and also use Pythia to estimate the fraction of the $D^{\pm}$ cross section with $x_F < -0.2$. Since the cross section is strongly peaked near $x_F = 0.0$, we expect this fraction to be fairly small, and so the extrapolation is not too large. Upon examination of the x_F spectra for $D^{\pm}$ mesons, we find that 91% and 96% of D^+ and D^- mesons have $x_F > -0.2$ respectively. Taking the inverse of each, we arrive at correction factors of 1.10 and 1.04 for D^+ and D^- mesons respectively. We use the average value of the two as an estimate of the correction, and take the deviation from the average as an indication of the error. We therefore apply a correction of 1.07 ± 0.03 to the cross section in 7.7, which provides a measurement of the **total $D^{\pm}$ cross section** of,

$$\sigma(D^{\pm}) = 11.7 \pm 2.8(\text{stat}) \pm 2.6(\text{syst})\ \mu\text{b}. \qquad 7.8$$

The systematic errors include uncertainties due to the trigger corrections, reconstruction efficiency, luminosity, and branching ratio for $D \rightarrow K\pi\pi$.

In order to compare to other experiments which have only presented their results in the positive x_F region, we simply correct the $x_F > 0$ subsample of $D^{\pm}$ mesons for the (unobserved) cross section with $p_T < 1$ GeV/c. Using Table 7.4, and 7.5, we find

$$\sigma(D^{\pm}) = 8.2 \pm 1.9(\text{stat}) \pm 1.5(\text{syst})\ \mu\text{b} \qquad x_F > 0 \qquad 7.9$$

for the total $D^{\pm}$ cross section with $x_F > 0$. This result is compared with previous data in Figure 7.6, where we show the integrated $D^{\pm}$ cross section per nucleon for $x_F > 0$ in π^--Nucleon collisions. For each data point, the vertical line is obtained by adding the statistical and sytematic uncertainties in quadrature. For the E706 data point, the triangles above and below indicate the statistical error. The measurements in Figure 7.6 have been corrected to utilize the most recent estimate of the $D \rightarrow K\pi\pi$ branching fraction (9.1 ± 0.6 %). Also shown in the figure is the NLO prediction for charm production. The NLO results have been scaled assuming a constant fragmentation rate for $c \rightarrow D^{\pm}$ over this energy range. This assumption is consistent with previous measurements of the ratio of the $D^{\pm}/D^0$ cross sections[91, 92, 51, 53]. The E706 data are seen to be in nice agreement with the trend of the previous measurements. While the overall normalization of the theory is fairly uncertain, the shape appears to be fairly stable. Apart from the overall normalization of the theory, the four most recent measurements, including E706, appear to be in reasonable agreement with the theoretical expectations.

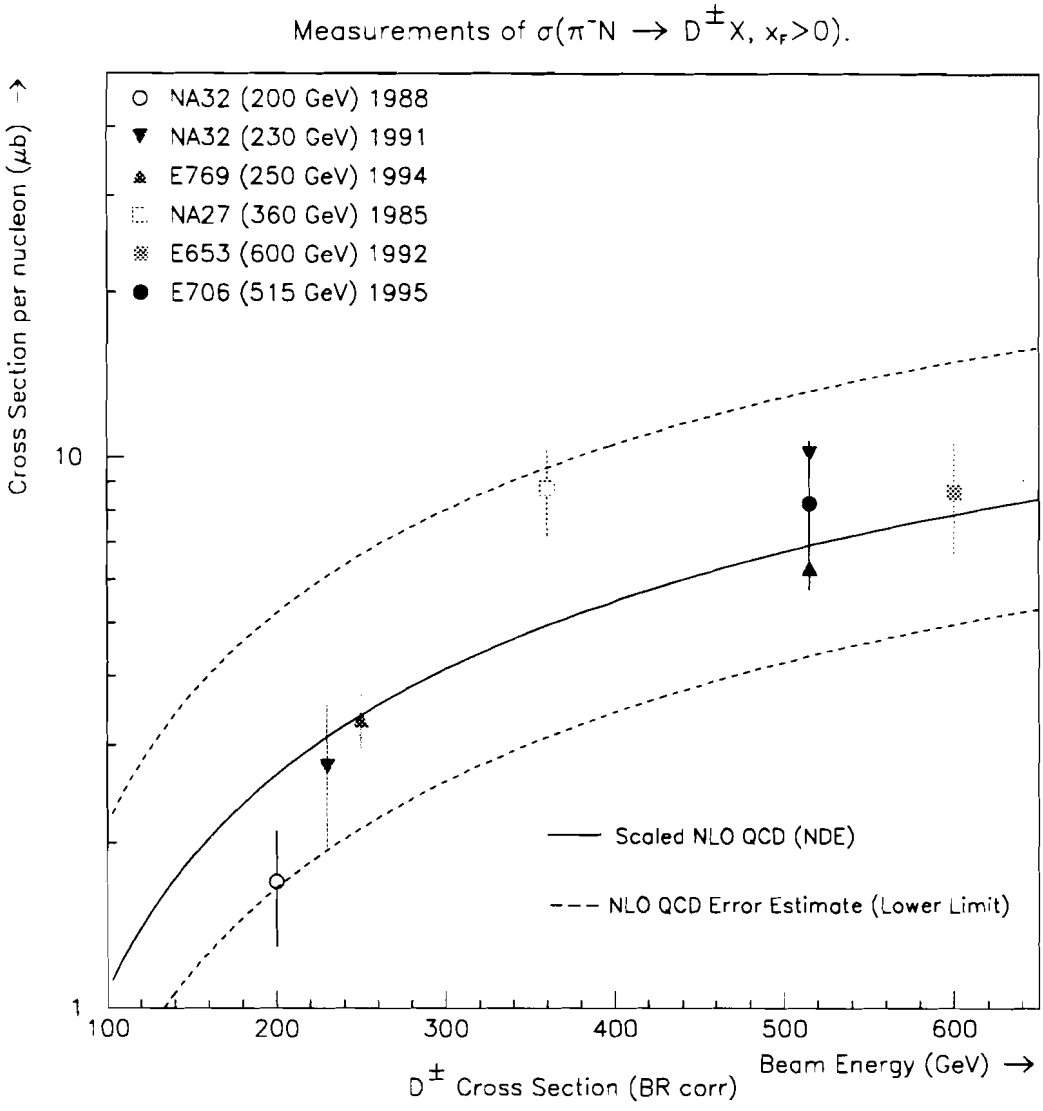

Figure 7.6 Comparison of the E706 $D^{\pm}$ cross section ($x_F > 0$), with other recent experimental results measured at different beam energies. Also shown is the NLO prediction, scaled to the data points.

We now wish to calculate the fraction of the $D^{\pm}$ cross section having $x_F > 0$. Using 7.9 and 7.8, we find,

$$\frac{\sigma(D^{\pm}, x_F > 0)}{\sigma(D^{\pm}, \text{all } x_F)} = 0.70 \pm 0.14 \qquad 7.10$$

The error assumes that systematic uncertainties cancel, and we are therefore dominated by the statistical error in the additional cross section with $x_F < 0$. The result indicates that the average x_F of charmed particles in π^--Nucleon collisions is greater than 0.0. Since charm production is dominated by gluon fusion, this implies that the gluon structure function is harder in pions than protons. This result is consistent with theoretical expectations[39], where one finds the **charm cross section ratio**,

$$\frac{\sigma_c(x_F > 0)}{\sigma_c(\text{all } x_F)} \sim 0.625 \qquad 7.11.$$

This result was found to be nearly independent of the charm quark mass (in the range from 1.2-1.8 GeV), and beam energy (between 100 and 1000 GeV).

7.7 Inclusive charm cross section

In order to estimate the inclusive charm cross section, we must account for the fraction of charm quarks which do not fragment into $D^{\pm}$. This implies we must account for the contributions of D^0 and D_s mesons, as well as Λ_c baryons to the total charm cross section. Based on available data measurements[91, 92, 51, 53], we have,

$$D^{\pm}/(D^0 + \overline{D^0}) = 0.47 \pm 0.07. \qquad 7.12$$

This result is consistent with what one would expect based on the relative number of spin states of D^* and D mesons (3:1), and the published branching ratios for $D^* \rightarrow D$ mesons. From this analysis, one expects[46],

$$D^{\pm}/(D^0 + \overline{D^0}) \simeq 0.43 \qquad 7.13$$

Since the data are in agreement with the theoretical estimate, we shall use the latter in the extrapolation.

One must also account for the D_s and Λ_c contribution to the total cross section. Based on the available data ([93], [94] and references therein), we use the estimates,

$$\sigma(D_s)/\sigma(D^0 + D^+) \sim 0.2$$

$$\sigma(\Lambda_c^+)/\sigma(D^0 + D^+) \sim 0.25$$

Therefore, in order to get the total $c\bar{c}$ cross section from the $D^{\pm}$ single inclusive cross section, we must divide by 0.43 ± 0.05[2] (for the D^0, $\overline{D^0}$ contribution), multiply by 1.45 ± 0.15 (for the D_s and Λ_c contributions), and divide by 2 (to go from the inclusive $D^{\pm}$ to the $c\bar{c}$ cross section). Extrapolating our total $D^{\pm}$ cross section (see 7.7), with these factors yields,

$$\sigma(c\bar{c}) = 19.7 \pm 5.8 \pm 5.6 \ \mu b \qquad 7.14$$

These results are plotted in Figure 7.7 along with the theoretical predictions. The error estimates on the NLO prediction were obtained by varying the renormalization scale, but keeping the factorization scale fixed, and therefore the uncertainties in the theory are to be taken as a lower limit. Additional uncertainties of similar magnitude arise when varying the factorization scale as well as from choice of input structure functions[46]. The theoretical prediction, apart from an overall normalization, appears to be in reasonably good agreement with the measurements of NA32, E769, and E706. The E653 and NA27 measurements reside somewhat higher than the other three measurements, but are not inconsistent with the theoretical predictions.

---

[2] Here we have made a rough estimate of the error based on the uncertainties of the $D^* \rightarrow D$ branching ratios.

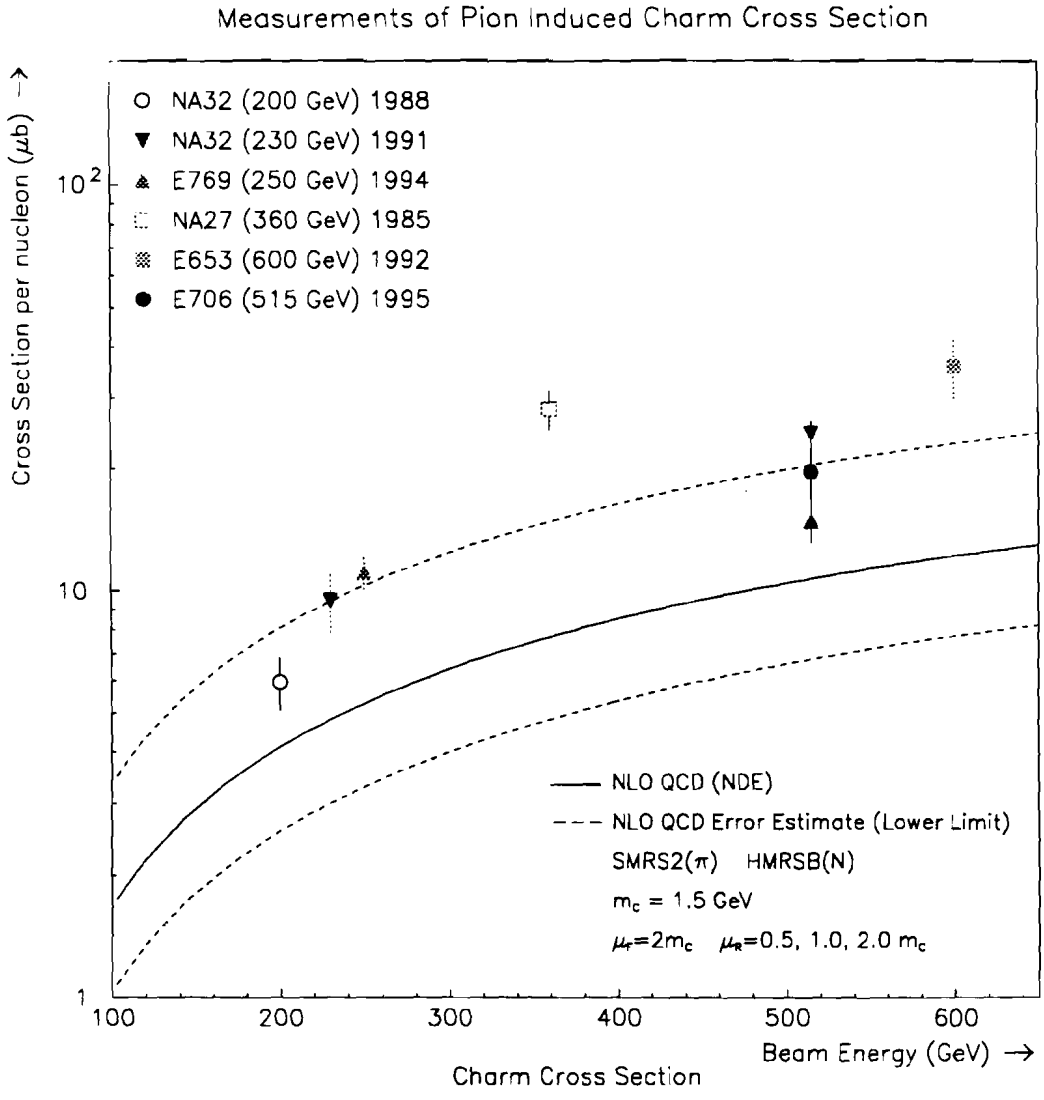

Figure 7.7 Total Charm Production Cross Section per nucleon for the process $\pi^- N \rightarrow c\bar{c} + X$ as a function of incident π^- energy. Also shown are the NLO theoretical predictions.

7.8 Inclusive $D^{\pm}$ Production vs π^0 Production

It is interesting to compare the ratio of the production cross sections of charmed to light mesons as a function of their transverse momenta. The probability of producing a pair of charm quarks from a minimum bias inelastic collision is ~ 0.001. Therefore, modern day experiments which operate with minimum bias triggers must record a huge sample of data in order to obtain a moderate sample of reconstructed charm decays. One would expect that as the Q^2 of the collision increases, the probability of producing a pair of charm quarks increases. Since the transverse momentum is related to the momentum transfer Q^2, it is interesting to compare the p_T distribution of the $D^{\pm}$ mesons to that of the π^0. Shown in Figure 7.8 is the ratio of the $D^{\pm}$ cross section to the π^0 cross section as a function of their respective p_T. Also shown in the figure is the expectation as obtained from the Pythia MC. The two are seen to be in reasonable agreement with one another. One can observe that the fractional charm cross section increases by more than an order of magnitude in going from $p_T \sim 1$ GeV/c to $p_T \sim 4 - 5$ GeV/c. This in fact was one of the attributes of E706 triggering on high p_T phenomenon. In doing so, we actually increase the charm fraction in the data by about an order of magnitude. Based on the integrated number of data events, and the $D^{\pm}$ sample collected, we found that $\sim 1/100$ events contain a pair of charm quarks.

7.9 Nuclear Effects

In this last section, we investigate the dependence of the charm production cross section on the number of nucleons. Since the 1990 configuration of E706 featured beryllium and copper targets, a measurement of the nuclear dependence can be made. One often assumes that the cross section scales in the following way:

$$\sigma = \sigma_0 * A^{\alpha} \qquad 7.15$$

Here, σ_0 is the cross section per nucleon, and σ is the total cross section on a target of atomic number A. Using 7.15, it is fairly straightforward to show that,

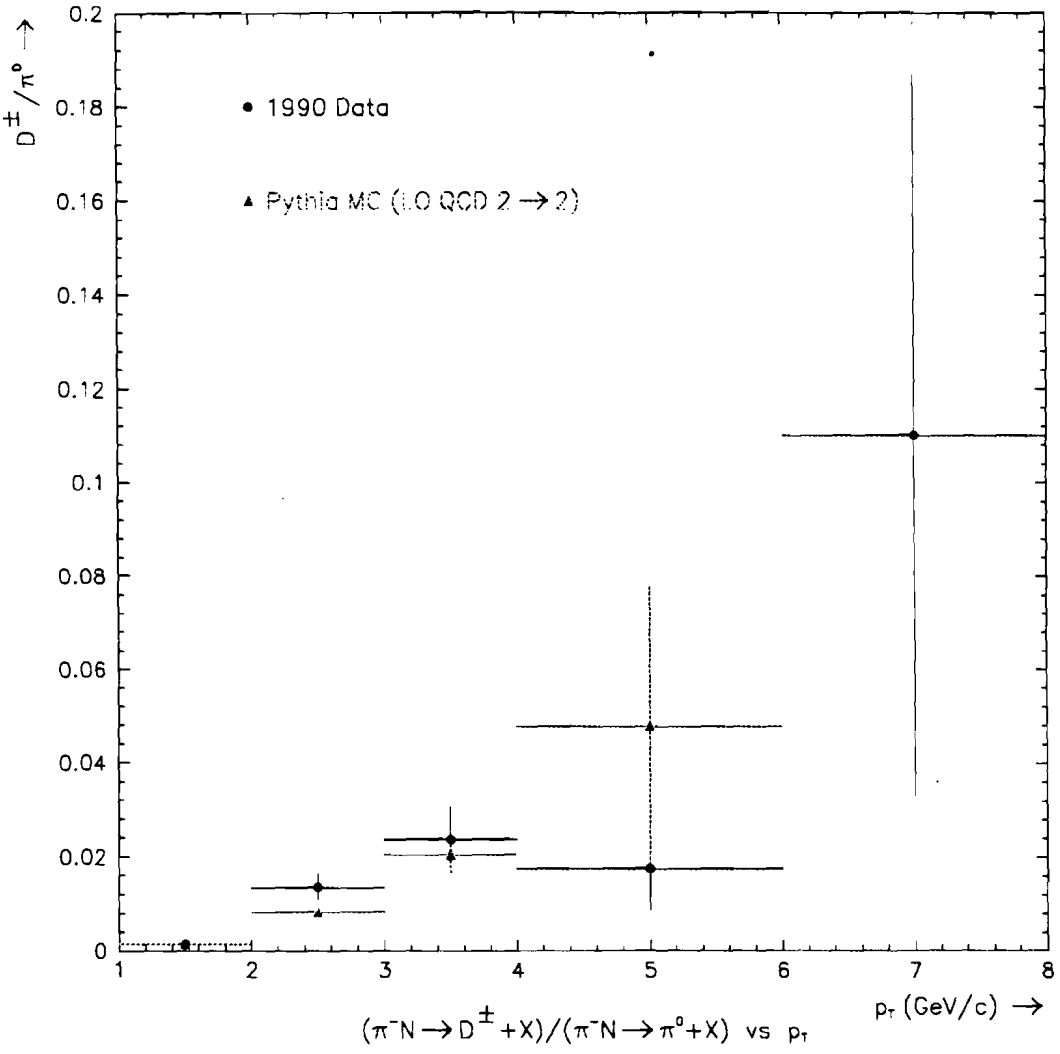

Figure 7.8 Ratio of the $D^{\pm}$ to π^0 cross section as a function of their respective p_T. The figure shows the 1990 data results, and the expectation from the Pythia MC.

$$\alpha = 1 + \frac{\ln(\sigma_{Cu}/\sigma_{Be})}{\ln(A_{Cu}/A_{Be})} \qquad 7.16$$

where σ_{Cu} and σ_{Be} are the cross sections per nucleon for copper and beryllium, and A_{Cu} and A_{Be} are their atomic numbers respectively.

For diffractive scattering, the cross section grows as R^2, where R is the nuclear radius. Since the radius scales as $R \sim A^{1/3}$, one finds that $\alpha = 2/3$ for diffractive scattering. For high p_T inclusive meson production, one finds that $\alpha \sim 1.10$, whereas for direct photon production, one finds $\alpha \sim 1.0$[81]. A model which qualitatively describes these observed values of α has to do with rescattering of the partons as they emerge from the hard scatter. Since the fragmentation of the partons is expected to occur at the scale of nuclear distances ($\sim$ 1 fm)[95, 96], it is reasonable to assume that the partons traverse the nuclear environment prior to hadronization. Due to the steeply falling production cross section with p_T, any additional (strong) rescattering will tend to stiffen the observed p_T spectrum of the final state particles. While direct photons also traverse the nuclear environment, they are not subject to (strong) rescattering, and so one expects $\alpha = 1$ for direct photons.

In light of these observations, it is interesting to know whether or not charm quarks, like light partons, also exhibit a nuclear effect. Recent data on the nuclear dependence of fully reconstructed D mesons indicate a value which appear to be consistent with $\alpha = 1.0$. Those results are summarized in Table 7.5[3]

Table 7.5 Nuclear Effects in $\pi^- N \rightarrow D + X$

Experiment	Beam Momentum (GeV)	Mesons studied	α	x_F range
WA82[97]	340	D^0, D^+	0.92±0.06	> 0.0
E769[98]	250	D^0, D^+	$1.0 \pm 0.05 \pm 0.02$	> 0.0
E769[98]	250	D^*	$1.0 \pm 0.007 \pm 0.02$	> 0.0

[3] Charge conjugate states are implied.

We shall now take a look at the E706 data. Shown in Figure 7.9 is the $K\pi\pi$ invariant mass distribution for the copper and beryllium targets.

In forming the ratio of the copper to beryllium cross section, many of the factors cancel out. The only factors which do not cancel are the numbers of events, the luminosities for each target (see 2), and the reconstruction efficiencies. The trigger efficiencies may be slightly different between beryllium and copper, but those differences are expected to be negligible compared to the statistical uncertainties. We therefore can rewrite α as,

$$\alpha = 1 + \frac{\ln(R_{Cu}/R_{Be})}{\ln(A_{Cu}/A_{Be})} \qquad 7.17$$

where,

$$R_{Cu} = \frac{N_{Cu}}{< \epsilon_{Cu} > * L_{Cu}} \qquad 7.18$$

$$R_{Be} = \frac{N_{Be}}{< \epsilon_{Be} > * L_{Be}} \qquad 7.19.$$

In these equations, N_{Cu} (N_{Be}) is the number of reconstructed $D \rightarrow K\pi\pi$ events in the copper (beryllium) targets, $< \epsilon_{Cu} >$ ($< \epsilon_{Be} >$) is the average reconstruction efficiency, and L_{Cu} (L_{Be}) is the integrated luminosity. In the luminosity term, the overall beam count is common to the beryllium and copper targets, and therefore the beam count and its error nearly cancel in the ratio. The cancellation is not perfect in that a small fraction of the triggerable beam particles may cross the transverse fiducial boundary along the length of the target. In this case, the nominal length used in the luminosity calculation is not the true length of target which the beam particle passes through. Since the beam has a preference to fan out, the downstream end of the target sees slightly less beam particles than the upstream end. This effect was determined to be $\sim$1%, and hence negligible on the scale of other errors in this A dependence measurement[90].

The various numbers needed for the calculation of α are summarized in Table 7.6.

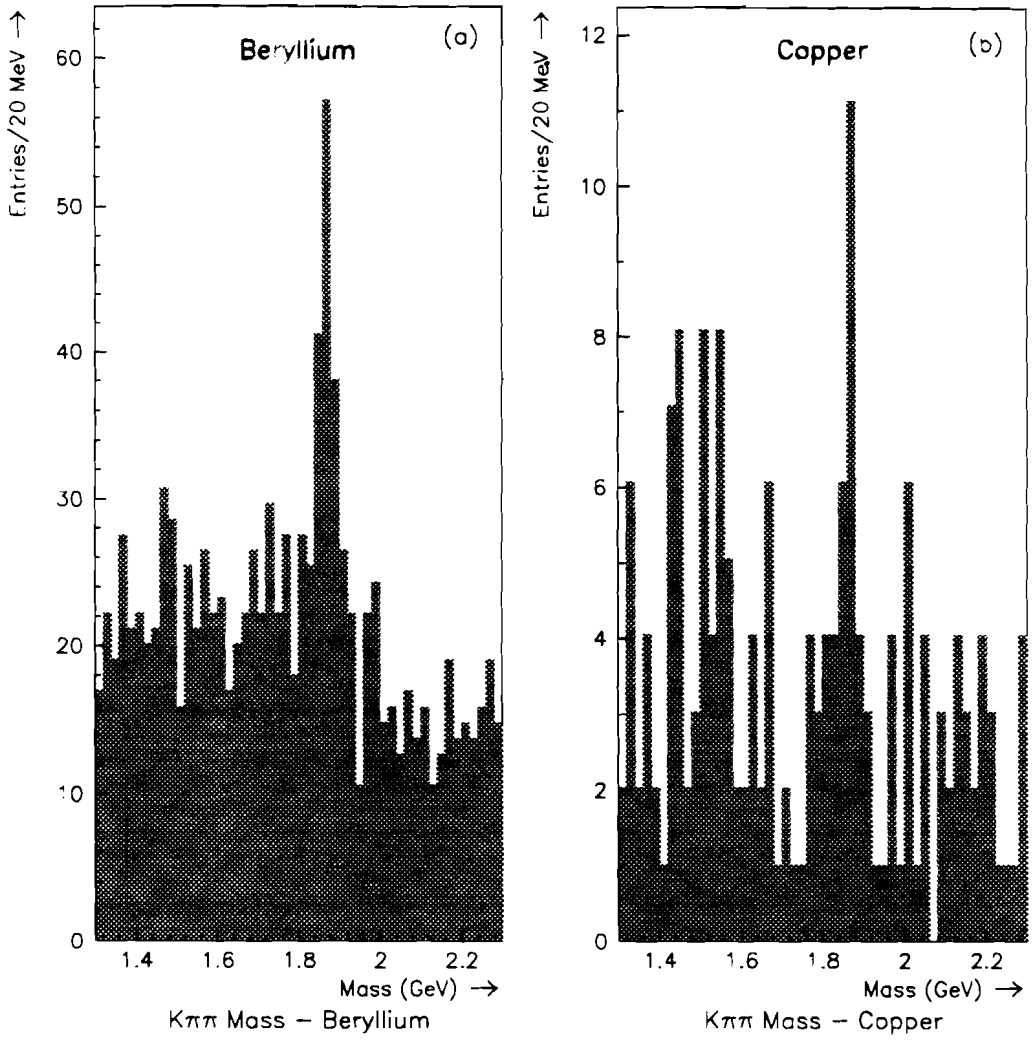

Figure 7.9 $K\pi\pi$ invariant mass distribution for events produced in the beryllium and copper targets.

Table 7.6 Parameters for calculating A dependence

Target	Copper	Beryllium
Number of events	19.7 ± 6	104 ± 15
$< \epsilon >$ (%)	9.15	13.3
Luminosity (pb^{-1})	1.4	8.9
Atomic number	63.546	9.012

Upon inserting the numbers from Table 7.6 into 17, we arrive at,

$$\alpha = 1.28 \pm 0.33$$

The A dependences for the $D^{\pm}$ and D^0 are shown in Figure 7.10 where we plot the values of α measured at the various beam energies. Unfortunately, due to low statistics, the error on α is quite large. Within errors, the result is consistent with the scaling of the charm cross section with the number of nucleons i.e. A^1.

7.10 Conclusions

In this thesis, we have utilized the ~ 10 pb^{-1} of data collected during the E706 1990 fixed target run to measure the production characteristics of charm particles. The sample of ~100 events (after analysis cuts) was observed to span the kinematical range $1 < p_T < 8$ GeV/c and $-0.2 < x_F < 1.0$. The remarkable coverage in p_T of the charmed particles was a consequence of the high luminosity in conjunction with the high p_T trigger. The bias introduced onto the charm sample was evaluated using the Pythia event generator and a MC simulation of the online trigger. Using the sophisticated detector simulation, the losses due to the trigger and reconstruction were corrected for, which allowed for a cross section determination.

We have compared our differential p_T distribution with the NLO predictions and have found reasonably good agreement, provided the NLO prediction is

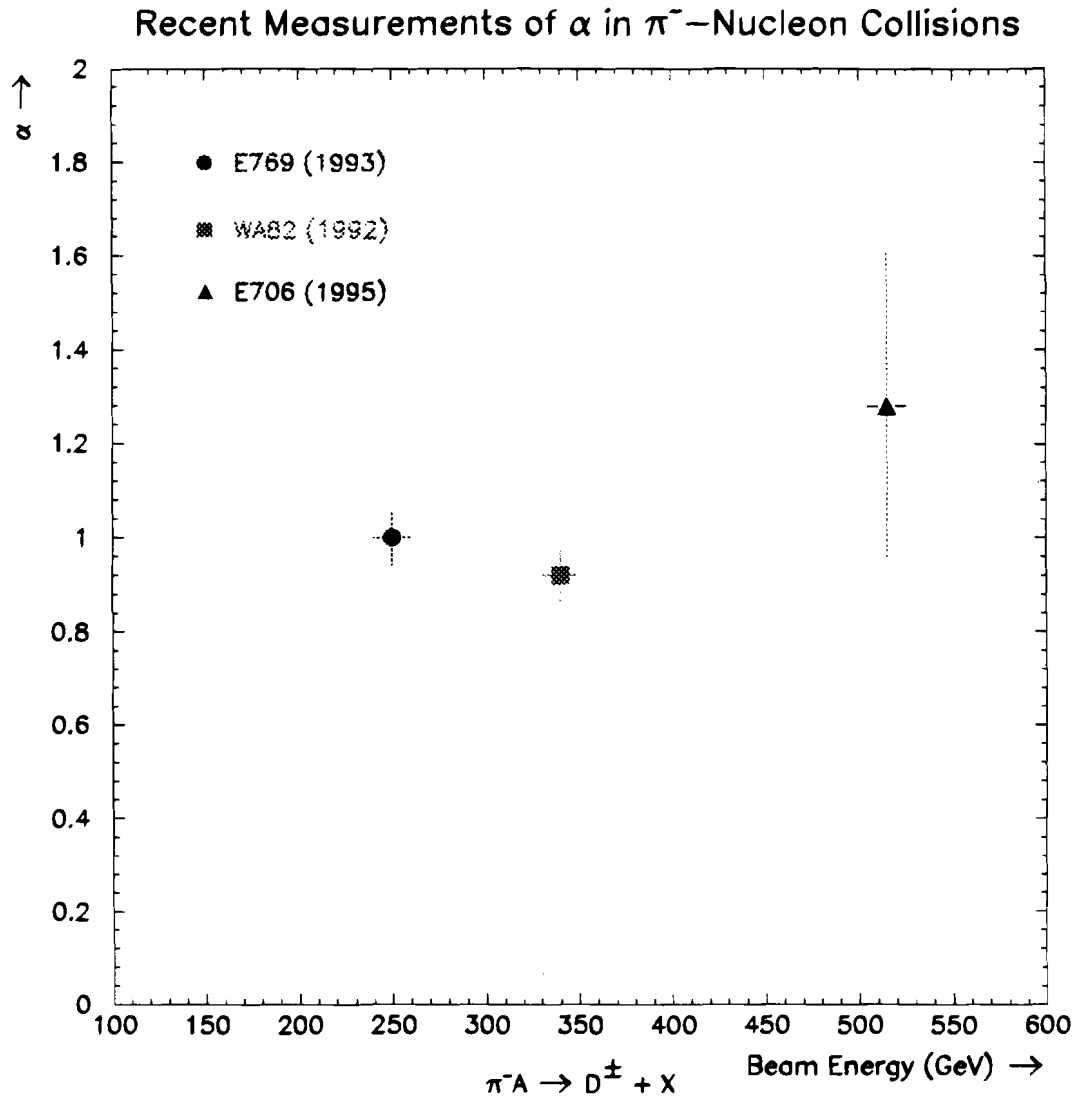

Figure 7.10 Measurement of the nuclear dependence parameter, α, for various experiments.

supplemented with a mean k_T^2 ($< k_T^2 >$) of ~ 1 GeV^2. Having to use such a high value of $< k_T^2 >$, may be an indication that even higher orders in the perturbative expansion are warranted. We also compared our results to the Pythia prediction, and found fair agreement when Pythia is supplemented with a $k_T \sim 1.0$ GeV^2. In addition, our data were compared to the published results of E769, where we found that the E706 data is slightly stiffer in p_T, as one would expect, but the difference is within 1σ of the statistical uncertainty. The coverage in p_T of the E706 data was seen to extend beyond what was reported by E769, making the E706 data truly unique.

From the differential cross section, we obtained an estimate of the integrated $D^\pm$ cross section per nucleon. There we found a total $D^\pm$ cross section per nucleon, $\sigma(D^\pm) = 11.7 \pm 2.8(\text{stat}) \pm 2.6(\text{syst})$ μb. The $D^\pm$ cross section in the forward x_F region was found to be $\sigma(D^\pm) = 8.2 \pm 1.9(\text{stat}) \pm 1.5(\text{syst})$ μb. By assuming a constant fragmentation rate of $c \rightarrow D^\pm$, we were able to obtain a total charm cross section of $\sigma(c\bar{c}) = 19.7 \pm 5.8 \pm 5.6$ μb. The errors include the uncertainties due to the extrapolation. The E706 result was seen to be consistent with the trend of the previous measurements. The data of NA32, E769 and E706 tend to agree with a particular normalization of the charm cross section, whereas the E653 and NA27 data tend to suggest a slightly higher total cross section. All five measurements are consistent with the theoretical predictions, due to fairly large systematic uncertainties in the theory. While the NLO predictions increase the total charm cross section by about a factor of 2.5, the theoretical uncertainties do not appear to improve in going from LO to NLO[46]. Based on these observations, one would be inclined to go beyond NLO.

We also compared the relative production rates of $D^\pm$ mesons to π^0's as a function of the transverse momentum. There it was seen that the $D^\pm$ production relative to the π^0 cross section rises from $\sim 1/400$ at $p_T \sim 1$ GeV/c, to about $1/50$ at $p_T \sim 4-5$ GeV/c. The results from the E706 data were observed to be reproducible with the Pythia MC.

Finally, we measured the nuclear dependence of charm production using the beryllium and copper targets. From that analysis, we found $\alpha = 1.28 \pm 0.33$. Within the error, the result is consistent with the scaling of the charm cross section with the number of nucleons.

REFERENCES

[1] M. A. Tuve, N. Heydenberg and L. Hafsted. The Scattering of Protons by Protons. *Phys. Rev. 50*, page 806, 1936.

[2] M. Gell-Mann. *Phys. Lett. 8*, page 214, 1964.

[3] G. Zweig. CERN report 8182/Th 401, 1964.

[4] J. D. Bjorken. *Phys. Rev. 179*, page 1547, 1969.

[5] E. D. Bloom et al. *Phys. Rev. Lett. 23*, page 930, 1969.

[6] M. Breidenbach et al. *Phys. Rev. Lett. 23*, page 935, 1969.

[7] I. J. R. Aitchison and A. J. G. Hey. *Gauge Theories in Particle Physics.* IOP Publishing Ltd, 1989.

[8] R. P. Feynman. *Phys. Rev. Lett. 23*, page 1415, 1969.

[9] C. G. Callan and D. Gross. *Phys. Rev. Lett. 22*, page 978, 1969.

[10] F. Abe et al. Observation of top quark production on $p\bar{p}$ collisions. **FERMILAB-Pub-95/022-E**, 1995.

[11] S. Abachi et al. Observation of top quark. **FERMILAB-Pub-95/028-E**, 1995.

[12] H. Yukawa. *Proc. Phys. Math Soc. Japan*, 17:48, 1935.

[13] F. Halzen and A. Martin. *Quarks and Leptons.* John Wiley and Sons, 1984.

[14] D. Perkins. *Introduction to High Energy Physics.* Addison-Wesley, 1987.

[15] J.G.H. de Groot et al. *Z. Physik C1*, page 143, 1979.

[16] B. Andersson, G. Gustafson, G. Ingelman, and T. Sjöstrand. *Phys. Rep. 97*, page 31, 1983.

[17] G. Marchesini, I.G. Knowles, M.H. Seymour, and B.R. Webber. *HERWIG Reference Manual*, v5.7 edition.

[18] J. F .Owens. *Rev. of Mod. Phys. 59*, page 465, 1987.

[19] T. Ferbel and W. R. Molzon. *Rev. of Mod. Phys. 56*, page 181, 1984.

[20] E. Braaten E. L. Berger and R. D. Field. *Nucl. Phys. B239*, page 52, 1984.

[21] M. Fontanaaz ad D. Schiff P. Aurenche, R. Baier. *Phys. Lett. B140*, page 87, 1984.

[22] M. Fritzsch and P. Minkowski. *Phys. Lett. B69*, page 316, 1977.

[23] Brajesh Choudhary. *A Study of High Transverse Momentum Direct Photon Production in Interations of 500 GeV/c π^- and Proton Beams on a Beryllium Target.* PhD thesis, University of Delhi, 1991.

[24] N. Varelas. *π^0 Production at High Transverse Momenta from π^- Collisions at 520 GeV/c on Be and Cu Targets.* PhD thesis, University of Rochester, 1994.

[25] R. K. Ellis, H. Georgi, M. Machacek, H. Politzer and G. Ross. *Phys. Lett. B78*, page 281, 1978.

[26] R. K. Ellis, H. Georgi, M. Machacek, H. Politzer and G. Ross. *Phys. Lett. B152*, page 285, 1979.

[27] S. Gupta and A. Mueller. *Phys. Rev. D20*, page 118, 1979.

[28] H.M. Georgi, S.L. Glashow, M.E: Machacek, D.V. Naonpoulos. Charmed particles from two-gluon annihilation in proton-proton collisions. *Annals of Physics*, 114:273–289, 1978.

[29] B. L. Combridge. Associated production of heavy flavour states in pp and $p\bar{p}$ interactions. *Nucl. Phys. B151*, pages 429–456, 1979.

[30] V. Barger, F. Halzen, and W.Y. Keung. Central and diffractive components of charm production. *Phys. Rev. D25*, pages 112–119, 1982.

[31] S. Dawson P. Nason and R. K. Ellis. *Nucl. Phys. B303*, page 607, 1988.

[32] R.K. Ellis and C. Quigg. A pinoteca of cross sections for hadroproduction of heavy quarks. **FN-445** 2013.000.

[33] S.J. Brodsky. The intrinsic charm of the proton. *Phys. Lett.*, pages 451–455, 1980.

[34] S. Dawson P. Nason and R. K. Ellis. *Nucl. Phys. B327*, page 49, 1988.

[35] S. Dawson P. Nason and R. K. Ellis. The total cross section for the production of heavy quarks in hadronic collisions. FERMILAB-Pub-87/222-T, 1987.

[36] M. Mangano *private communication.*

[37] P.J. Sutton, A.D. Martin, R. Roberts, and J. Stirling. *Phys. Rev. D45*, page 2349, 1992.

[38] P. Harriman, A.D. Martin, R. Roberts, and J. Stirling. *Phys. Rev. D37*, page 798, 1990.

[39] M. L. Mangano and P. Nason and G. Ridolfi. *Nucl. Phys. B405*, page 405, 1993.

[40] D.W. Duke and J.F. Owens. Q^2-dependent parametrizations of parton distribution functions. *Phys. Rev. D30(1)*, page 49, 1984.

[41] D.W. Duke and J.F. Owens. Q^2-dependent parametrizations of pion parton distribution functions. *Phys. Rev. D30(5)*, page 943, 1984.

[42] P. N. Harriman et al. Parton distributions extracted from data on deep inelastic scattering, prompt photon production, and the Drell-Yan process. *Phys. Rev. D42*, page 798, 1990.

[43] P. J. Sutton et al. Parton distributions extracted forthe pion extracted from Drell-Yan and prompt photon experiments. Preprint RAL-91-058, 1991. Rutherford Appelton Laboratory.

[44] D.F. Geesaman, J. Morfin, C. Sazama, W.K. Tung, editor. *Hadron Structure Functions and Parton Distributions.* World Scientific, 1990.

[45] C. Peterson et al. *Phys. Rev. D27*, page 105, 1983.

[46] S. Frixione, M. Mangano, P. Nason, and G. Ridolfi. Charm and botton production: Theoretical results versus experimental data. *Nucl. Phys. B431*, pages 453–483, 1994.

[47] S. Frixione, M. Mangano, P. Nason, and G. Ridolfi. Testing QCD in Charm Production. **CERN-TH-7377/94**, 1994.

[48] Zhongxin Wu. The Feynman-X Dependence of $D^{\pm}$ Mesons in π^--Nucleon Interactions. PhD thesis, Yale University, 1991.

[49] J. A. Appel. Hadroproduction of charm particles. *Annu. Rev. Nucl. Part. Sci.*, 42:367–399, 1992.

[50] M. Dameri. A review on the experimental status of charm hadroproduction. *Frascati Physics Series*, 1:167–180, 1993.

[51] S. Barlag et al. Production properties of D^0, D^+, D^{*+} and D_s^+ in 230 GeV/c π^- and K^--Cu interactions. *Z. Phys. C49*, page 555, 1991.

[52] A. Wallace et al. Beam Flavor Dependence in the Hadroproduction of $D^{\pm}$ and $D_s^{\pm}$ Mesons. **FERMILAB Conf-94/184**, 1994.

[53] M. Aguilar-Benitez et al. Inclusive Properties of D Mesons in 360 GeV/c π^-p Interactions. *Phys. Lett. B161*, page 400, 1985.

[54] K. Kodama et al. Charm meson production in 600 GeV/c π^-emulsion interactions. *Z. Phys. C49*, page 555, 1991.

[55] R. Roser. *Eta Production at High Transverse Momentum by Negative 520 GeV/c Pions Incident on Beryllium and Copper Targets.* PhD thesis, University of Rochester, 1994.

[56] L. DeBarbaro. *Omega Production at High Transverse Momentum by Negative 518 GeV/c Pions Incident on Beryllium and Copper Targets.* PhD thesis, University of Rochester, 1995.

[57] V. Abramov et al. **FERMILAB-Pub-91/62-E**, 1991.

[58] S. Kartik. *Phys. Rev. D41*, page 1, 1990.

[59] I Kourbanis. *The A-dependence of Leading Particle Production by 800 GeV Protons.* PhD thesis, Northeastern University, 1989.

[60] C Yosef. *Production of High Transverse Momentum π^0 Mesons in Interactions of 530 GeV/c proton and π^- Beams on Beryllium and Copper Targets.* PhD thesis, Northeastern University, 1990.

[61] D. D. Skow. *A Study of High Momentum Eta Meson Production.* PhD thesis, University of Rochester, 1990.

[62] L. Sorrell. **The E706 Trigger System**, Sept. 21, 1994. E706 Note 201.

[63] FNAL Computer Department, Fermilab, Batavia, Ill. *VAXONLINE Users Guide.* PN-252.

[64] E. Engels et al. *Nucl. Instru. and Meth. A253*, pages 523–529, 1987.

[65] S. Mani. *A Silicon Microvertex detector for studying QCD jets associated with direct photons.* PhD thesis, University of Pittsburgh, 1986.

[66] P.D.D.S. Weerasundara. *A Study of Large Transverse Momentum Direct Photon plus Away-Side Jet Production using 500 GeV/c proton and π^- Beams Incident on a Beryllium Target.* PhD thesis, University of Pittsburgh, 1993.

[67] Nanometric Systems Inc., Oak Park, Illinois. *MultiWire Proportional Chamber Readout System.*

[68] K. Hartman. *Hadronic Production of π^0 Pairs and Associated Event Structure at 530 GeV.* PhD thesis, Pennsylvania State University, 1990.

[69] D. Brown. *A Comparison of High Transverse Momentum Direct Photon and Neutral Pion Events in Negative Pion and Proton-Nucleus Collisions at 31.5 GeV Center of Mass Energy.* PhD thesis, MIchigan State University, 1992.

[70] C. Bromberg et al. *Nucl. Instru. and Meth. A307*, pages 292–297, 1991.

[71] W. Desoi. *Construction and Performance of a Liquid Argon Calorimeter for Use in E-706 at the Fermi National Accelerator Laboratory.* PhD thesis, University of Rochester, 1990.

[72] C. B. Lirakis. *A Study of High Transverse Momentum η Production in 530 GeV/c Hadronic Interactions.* PhD thesis, Northeastern University, 1990.

[73] A. Sinanidis. *Particles Produced in Association with High Transverse Momentum Single Photons and π^0s in Hadronic Collisions.* PhD thesis, Northeastern University, 1989.

[74] R. Benson. *Characteristics of Forward Energy Production in Proton-Nucleus and Pion-Nucleus Collisions at 530 GeV/c.* PhD thesis, University of Minnesota, 1989.

[75] G.O. Alverson and E.L. Pothier. E706 Internal Note 139, 1985.

[76] R. Brun et al. *ZEBRA User's Guide.* Cern Computer Center Program Library, DD/EE/85-6 Q100, or FNAL Software Note PU-0046.

[77] J.P. Mansour. *High Transverse Momentum π^0 Production from π^- and p Beams at 530 GeV/c on Be and Cu.* PhD thesis, University of Rochester, 1989.

[78] W. Dlugosz. *The Production of High p_T π^0 Mesons in 515 GeV/c π^--Nucleon Collisions.* PhD thesis, Northeastern University, 1994.

[79] L. De Barbaro and F. Lobkowicz. E706 Internal Note 167, 1988.

[80] F. Carminati. Geant, detector description and simulation tool. **CERN Program Library Long Writeup W5013**, 1993.

[81] Lee Sorrell. *Measurement of the Nuclear Dependence of Direct Photon and Neutral Meson Production at High Transverse Momentum by Negative 515 GeV/c Pions Incident on Beryllium and Copper Targets.* PhD thesis, Michigan State University, 1995.

[82] T. Sjöstrand. Pythia 5.7 and jetset 7.4 physics manual. **CERN-TH.7112/93**, 1993.

[83] G. Bellini. Hadro and photoproduction of charm at fixed target. **FPRINT-94-31**, 1994.

[84] E769 Collaboration. Feynman-x and Transverse Momentum Dependence of $D^{\pm}$ and D^0, $\overline{D^0}$ Production in 250 GeV/c π^--Nucleon Interactions. *Phys. Rev. Lett. 69*, page 3147, 1992.

[85] S. Kwan for the E791 Collaboration. Testing QCD in Charm Hadroproduction. Physics Seminar at Fermilab, June 1995.

[86] J. Kuehler. *An Analysis of π^0 Mesons Produced in Minimum Bias 515 GeV/c π^--Nucleon Collisions.* PhD thesis, University of Oklahoma, 1995.

[87] W. Chung. *A Study of the Event Structure in High P_T Direct Photon and π^0 Production by 515 GeV/c π^- and 800 GeV/c Proton Beams Incident on Nuclear Targets.* PhD thesis, University of Pittsburgh, 1995.

[88] WA82 Collaboration. Study of D^+ and D^- Feynman's x distributions in π^--nucleus interactions at the SPS. *Phys. Lett. B305*, page 402, 1993.

[89] E769 Collaboration. Enhanced Leading Production of $D^{\pm}$ and $D^{*\pm}$ in 250 GeV $\pi^{\pm}$-Nucleon Interactions. *Phys. Rev. Lett. 72*, page 812, 1994.

[90] G. Ginther *private communication.*

[91] K. Kodama et al. *Phys. Lett. B284*, page 461, 1992.

[92] S. Barlag et al. *Z. Phys. C39*, page 451, 1988.

[93] M. P. Alvarez et al. *Z. Phys. C60*, page 53, 1993.

[94] S. Aoki et al. Charm Production by 350 GeV/c π^- Interactions in Nuclear Emulsion. *Prog. Theor. Phys. 87*, page 1305, 1992.

[95] Peter Renton. *Electrweak Interactions.* Cambridge Univ. Press, 1990.

[96] Steven Weinberg. *Subatomic Particles.* W, H. Freeman and Company, 1990.

[97] M. Adamovich et al. *Phys. Lett. B284*, page 453, 1992.

[98] G. Alves et al. *Phys. Rev. Lett. 70*, page 722, 1993.